Raman spectroscopy for skin cancer diagnosis and characterisation of thin supported lipid films

Marta Larraona Puy, Lic.

Thesis submitted to the University of Nottingham
for the degree of Doctor of Philosophy

March 2012

Abstract

Raman spectroscopy is a powerful tool in oncological imaging. Optical biopsies in which an accurate diagnosis of the tumour areas is spectroscopically performed are especially interesting for application to skin cancer treatments. In the first part of this dissertation a study on automated Raman spectral imaging allowed accurate diagnosis and delineation of the borders of a common type of skin cancer, basal cell carcinoma (BCC). Automated detection and imaging of BCC in skin sections excised during surgery was performed by combining Raman micro-spectroscopy with supervised multivariate mathematical algorithms based on linear discriminant analysis (LDA). The model allowed 90±9% sensitivity and 85±9% specificity in BCC detection. Raman spectral images based on the LDA model were created and compared with the gold-standard of the conventional histopathological diagnoses resulting in excellent agreement. Additional studies on the ability of the model in discriminating between BCC and hair follicles produced accurate diagnoses. In this thesis instrumental implementation and design of a Raman spectral imaging prototype aiming to reduce the acquisition time required to build the Raman spectral images was developed.

High sensitivity variants of Raman spectroscopy such as surface enhanced Raman spectroscopy (SERS) are known to enable optical detection down to single molecules and can be applied to thin supported lipid research. The combination of SERS with a complementary topographic technique simultaneously synchronised adds to the chemical information the morphology of the sample surface. In the second part of this thesis simultaneous atomic force microscopy (AFM) and SERS characterisation of thin (≈15-20 nm) supported films of arachidic acid and cationic phospholipids on sapphire/silver substrates was successfully achieved. Supports were fabricated with nanosphere lithographic procedures and allowed enhancement of the weak Raman signals from the amphiphilic films by a maximum factor of $\times 10^8$.

List of Publications

Part of the work described in this dissertation has been a topic of the following publications:

- C. S. Sweetenham*, M. Larraona-Puy* and I. Notingher, **Simultaneous surface-enhanced Raman spectroscopy (SERS) and atomic force microscopy (AFM) for label-free physicochemical analysis of lipid bilayer**, *Appl Spectrosc*, 2011, **65** (12), 1387. *Equal contributors.

- M. Larraona-Puy, A. Ghita, A. Zoladek, W. Perkins, S. Varma, I. H. Leach , A. A. Koloydenko, H. Williams and I. Notingher. **Discrimination between basal cell carcinoma and hair follicles in skin tissue sections by Raman micro-spectroscopy**, *J Mol Struct* 2011, **993**(1-3), 57-61.

- M. Larraona-Puy, A. Ghita, A. Zoladek, W. Perkins, S. Varma, I. H. Leach , A. A. Koloydenko, H. Williams and I. Notingher. **Development of Raman micro-spectroscopy for automated detection and imaging of basal cell carcinoma**, *J Biomed Opt* 2009, **4**(5): 054031.

Acknowledgements

This work was funded by the UK National Institute for Health Research (NEAT FSG004), the University of Nottingham Hospitals Charity, and the Engineering and Physical Sciences Research Council (Bridging the Gap grant EP\E018580\1).

First I would like to thank my supervisor, Dr. Notingher, for his guidance and brilliant ideas along all these years which made this thesis a reality.

Secondly, my gratitude to all the colleagues involved in the different projects I have participated on starting from Dr. Sweetenham and Dr. Zoladek, who built the combined AFM-SERS and the Raman micro-spectroscopic instrument for skin measurements, respectively. Their help and support along my PhD have been fundamental from a professional and personal point of view. Also special thanks to Adrian Ghita, who collected the majority of the Raman spectral database for the skin cancer project. Thanks to Drs. Leach, Perkins, and Varma from the histopathology and dermatology departments of the Nottingham University Hospital NHS Trust for their help and patience. Also a very special mention to Dr. Koloydenko, expert in biomedical statistics, for his important contribution to the rigour of this study and his helpful answers to all my statistical questions. Another especial mention to Robert Chettle and Andrew Stuart from the electronics workshop of the School of Physics and Astronomy of the University of Nottingham for their support with the design and implementation of the electronic circuits of the wide-field Fourier-transform Raman spectroscopic instrument. Also I need to acknowledge the staff from the workshops and stores of the school of Physics for their hands on approach to my daily technical problems.

I would also like to show my appreciation to the members of the Nanoscience group, from the experts in Raman spectroscopy (Pop, Faris, Kenny, Christian), polymers (James S., Mike, Kevin, James B., Zoe, Dave), AFM and STM (Julian, Adam, Andy, Sam, Rich, Philip, Nick, Alex, Pete, Luis, Rosanna, Maria). Without their help, ideas, motivation, and PhD-related plus personal support none of the work presented in this thesis would have been possible.

Thanks as well to all those who, as well as my supervisor, helped in the correction and improvement of this draft: Prof. Moriarty and Dr. Sharp from the Nanoscience group for their helpful suggestions and careful follow-up of the projects, and again from the Nanoscience team Dr. Smith, Dr. Sweetman, Dr. Stannard, Dr. Sweetenham, Julian Stirling and Faris Sinjab. From the outside world, thanks to Dr. Widera, Kate Rothery and again Dr. Koloydenko.

My gratitude to Prof. Barth (Stockholm University) for his support and the opportunity of joining his infrared group while waiting for my viva examination.

Last but not least thanks to my examiners, Profs. Stone and Moriarty for their interest in my work and their key comments which have been incorporated into this final version.

On a personal note I would like to thank my family, especially my parents, Irene, and Nick, my "Turkish sisters" Isin and Bahar, and my volleyball and non-volleyball friends, from Nottingham, Seville, and Madrid.

For the Spanish reader:
Nada me pone tan contento como llegar a una relación con mi trabajo en la que pueda sentirme satisfecho. (Aurelio Alvea (1943), my first intelectual guide).

For the English reader:
We should dream bigger, reach higher,[...] and speak up.
(Justine Musk in "The art of being an ambitious female").

Everyone bitten by the "passion-and-curiosity-for-science bug" should do science. It is true that as a gender we are under-represented (at least in Physics). But the female scientist shares the same motivation (*science is fascinating*) and therefore should not be put off by statistics or stereotypes.

A career in science is a process of dynamic regeneration, continuous learning, and recycling/reorientation of ideas to tackle unsolved scientific questions. Ideally, anyone dreaming to become a scientist should be given a methodological hand.
As a female scientist I agree that the time for male domination of the scientific community is over. And I just encourage whoever might end up reading this note (no matter the gender) to pursue their dreams.

Be ambitious, be passionate, be patient and systematic, have dialogues and not monologues and fight with words. For becoming a scientist you do not need an exclusive rare skill, but time for observation and reflection. Anyone should be given the opportunity to become a scientist if they see the beauty and magic underneath. It should be an unwritten human right.

Contents

List of Figures

List of Tables

Chapter 1

Introduction

This introduction includes the motivation and aims of this thesis, the development of the main hypotheses behind this research, the novelty and expected contributions of this study, and an outline of each chapter.

Motivation and aims

This thesis covers two important applications of Raman spectroscopy (RS) in biology and medicine.

Firstly, the potential of RS as an analytical tool in skin cancer diagnosis is studied. The aim is to obtain 2D images containing the diagnosis of skin tissue sections excised during surgery. This diagnosis will be based on the chemical information extracted from the Raman spectra of the samples. The images will be produced automatically by applying a supervised classification method based on linear discriminant analysis (LDA), aiming at maximum detection of the cancer regions.

Secondly, this thesis investigates the ability of surface enhanced Raman spectroscopy (SERS) to characterise thin supported lipid films when combined with a topographic technique such as atomic force microscopy (AFM). The chemical information provided by the spectroscopic study will be added to the morphological information from the AFM images. Having complementary simultaneous data from different regions of these thin lipid films should allow an improved understanding of their properties.

In the first study of this thesis, the initial questions to be answered are "do conventional skin cancer treatments need to be improved?" and "is the use of RS advantageous when compared to conventional methods?". This thesis focuses on a

particular type of skin cancer, namely, basal cell carcinoma (BCC), which is the most common type of cancer in humans.

For difficult and recurrent cases of BCC, Mohs micrographic surgery (MMS) is considered the most appropriate treatment. In practice, however, clinicians are unable to use MMS in all required cases due to time, cost, and other practical considerations. The main limitation of MMS is that it relies on histopathology. Histopathological evaluation of skin tissue sections excised during skin cancer surgery is a subjective and time-consuming technique in which tissue biopsies are stained and visually examined by clinical specialists. Automated evaluation of skin tissue sections based on a spectroscopic technique would be advantageous in terms of time, and diagnostic objectivity. A model based on the spectroscopic differences in the Raman spectra within these sections can be used to produce images that incorporate the medical diagnosis as an alternative to histopathology. Hence, the first specific aim of this thesis is *to create a model based on RS which automatically produces images and includes the diagnosis of the skin tissue sections.*

Taking into consideration previous studies on skin cancer diagnosis with RS, new questions can be formulated such as "is the proposed method a real advantage in terms of diagnostic accuracy for BCC detection?", or "is the gold-standard histopathological evaluation of a trained specialist more reliable if subjectivity is minimised by, for example, multiple independent examinations by different histopathologists?" Situations in which the subtle chemical information provided by RS would be more accurate than gold-standard histopathology in BCC diagnosis correspond to challenging samples in which healthy skin components such as hair follicles are misdiagnosed as BCC and *vice versa* due to their similar morphology. In these cases, diagnosis based on the chemical "fingerprints" rather than on visual appearance would represent a break-through and a valuable tool in order to aid the medical specialists to reach a final diagnosis. Hence, a study on the ability of the RS method to discriminate between hair follicle and BCC is included in this thesis.

In order to complete the study on the performance of RS as an optical tool in skin cancer diagnosis a discussion on the time required to produce the Raman spectral images is needed, i.e. is the Raman spectral imaging method sufficiently fast to be introduced in a real medical scenario?. If not, which approach should be chosen to accelerate data acquisition?. In this thesis an initial step is taken towards the development of a novel Raman spectral imaging technique. The new spectral imaging technique combines the faster speeds of large-area sample illumination

with the high recording speeds and sensitivity of the most recent generation of 2D photodetectors plus the advantages of Fourier transform spectrographs.

The second study described in this thesis is the development of SERS for characterisation of thin supported lipid films. Supported lipid films play an important role in bio-nanotechnology, having a wide range of applications. These films have been widely used as models of the cell membrane mimicking biological processes such as cell-cell adhesion or membrane trafficking under tightly controlled conditions. Supported thin lipid films also enable the incorporation of proteins to create highly specific sensors, and have been applied to bio-functionalisation of inorganic materials [1]. A "dual" simultaneous characterisation of these thin lipid films would increase the control over such interfacial platforms promoting an improved detection of the slight chemical and morphological changes that the system experiences under different experimental conditions. "Dual" characterisation in this thesis refers to "chemical" and "topographic" characterisation, which are performed by an integrated system combining vibrational spectroscopy and scanning probe microscopy. The ultimate aim of this work is *to achieve simultaneous "dual" characterisation of supported lamellar lipid arrangements with SERS and AFM.*

Hypotheses

The main hypotheses formulated by this thesis are:

1. *Automated spectral imaging of BCC using RS in combination with mathematical models can be introduced as an alternative to histopathological evaluation of MMS-excised tissue sections.*

2. *Discrimination between hair follicle and BCC can be accurately obtained with the RS automated method and applied to MMS-excised tissue sections of difficult, ambiguous diagnosis.*

3. *A fast Raman spectral imaging instrument combining wide-field Fourier transform Raman spectroscopy and charged coupled devices (CCDs) can be designed and built cost-effectively for its future application to skin oncological research.*

4. *"Dual"(chemical and topographic) characterisation of thin supported lipid films can be achieved by combining AFM and SERS.*

Novelty and expected contributions

In the last two decades the number of investigations testing the performance of Raman spectroscopy to solve biomedical problems has exponentially increased, as researchers take advantage of the high chemical specificity of this non-invasive technique. RS has been successfully applied in oncology, where it has been able to detect early stages of cancer in tissues and cells [2–4]. Raman spectral images of different types of tumours including BCC have been produced [5].

Methods which find patterns in the Raman spectra to create spectral clusters (e.g. k-means clustering) are commonly used to produce the Raman spectral images. However, these images need to be assigned to a biological component (eg. healthy tissue, fat, hair, cancer, etc.) after the image has been produced, which normally implies human intervention. Furthermore, creating Raman spectral images using exclusively pattern recognition clustering methods has the disadvantage that only the information present in a specific sample is used. Classification methods based on previously built multivariate models can be used to create Raman spectral images where the diagnosis can be read directly from the Raman spectral maps.

In Raman spectral imaging, classification methods usually require spectral data reduction. Several studies using unsupervised methods for spectral data dimensional reduction followed by classification algorithms have been reported [6, 7]. However, this thesis suggests a novel approach to Raman spectral imaging of skin tissue sections. The classification algorithm is based on the information collected from a large number of samples, which is used to build a Raman spectral database and not solely on the information from the particular specimen to be diagnosed. A supervised method for dimensional reduction of the spectral data is used, giving biological meaning to the information introduced into the classification model. This approach will produce automatically Raman spectral images with the diagnosis, i.e the clusters shown in such Raman spectral images are already labelled as cancer or healthy tissue, and do not need *a posteriori* evaluation.

Testing such models in samples where the diagnosis is challenging, to produce Raman spectral images in order to discriminate between BCC and hair follicles is an innovative step towards the introduction of RS in daily clinical practice.

The principle of achieving Raman spectral imaging combining wide-field sample illumination, Fourier transform interferometry, and CCDs has been previously patented [8], but as yet not put into practice. Fast acquisition in the Raman micro-spectroscopic instrument originates from the simultaneous illumination of large areas of the sample (wide-field illumination) and use of fast CCDs. Wide-field Raman spectroscopy (WFRS) without interferometers allows the collection

of Raman signals from a limited spectral bandwidth; spectroscopic information outside this spectral band is not recorded. However, when WFRS is combined with a Fourier transform interferometer full spectra could be recorded, which is essential to detect the subtle and spectrally spread chemical differences between the Raman spectra of BCC and healthy skin components.

Finally, the novelty of achieving a "dual" characterisation of thin supported lipid films with AFM and SERS is adressed. SERS is preferred over conventional RS due to its ability to enhance the weak Raman signal from the thin lipid films. A wide range of non-simultaneous AFM and spectroscopic studies have been reported on thin supported lipid films [9, 10]. Nevertheless, SERS studies on nanometre thick lipid films commonly include dyes which are strong Raman scatterers (eg. rhodamine or acridine orange) within the membranes, masking the spectra of the pure lipid layers [11]. The studies which do include the signal from the lipids are normally performed using high applied voltages [12], which might not be desirable in certain experiments with thin lipid films. The novelty of this work is that it aims to record simultaneous AFM images and SERS spectra from these thin supported lipid films without introducing labels or external voltages to the system.

Outline

- **Chapter Two** describes the two applications in biology and medicine which would be investigated by RS. This chapter is divided into two parts. The first includes a brief background into the biology of healthy skin, skin cancer, and current diagnostic procedures. Previous works in the field of optical diagnosis on skin cancer are reviewed. The interest in using RS to study this particular medical problem is addressed. In the second part, the scientific relevance of thin supported lipid films is discussed, and a review of previous techniques used for characterisation of these systems is presented.

- **Chapter Three** is an introduction to the theoretical basis of the experimental techniques used in the investigations. The theory of Raman scattering is explained in detail. The components of the Raman spectroscopic instrument are described from a theoretical point of view. The chapter contains a brief overview of Raman spectral imaging, SERS, AFM, and the main methods for the synthesis of the thin lipid films.

- **Chapter Four** introduces the practical aspects of the techniques of this thesis including descriptions of the instruments, calibration issues, and general sample preparation methods. The Raman spectra of the main compounds

used in this thesis are presented. The analysis of the Raman-active modes of such spectra and their correspondent assignment is also included.

- **Chapter Five** presents a Raman micro-spectroscopic (RMS) study of BCC, with the objective of automating imaging and producing accurate diagnosis of tumour borders.

- **Chapter Six** continues the skin cancer project presented in Chapter Five, focusing on overcoming the main limitations of the earlier work. Two studies are presented, the first examining samples of difficult diagnosis including hair follicles. Also reported is the development of a fast novel Raman spectral imaging prototype.

- **Chapter Seven** is a study of the simultaneous characterisation of thin supported lipid films by AFM and SERS. This chapter consists of experimental work supported by theoretical calculations. Topics covered are substrate optimisation, lipid layer(s) fabrication, and optical and topographic characterisation of the supported lipids.

- **Chapter Eight** concludes this thesis, discussing the results presented and possibilities for future work.

Chapter 2

Background and related work

2.1 Skin cancer and optical techniques in oncological diagnosis/imaging.

2.1.1 Healthy skin and basal cell carcinoma (BCC)

Healthy human skin is composed of three different layers: epidermis, dermis and subcutis (Figure 2.1). **Epidermis** is the outermost layer, with a thickness ranging

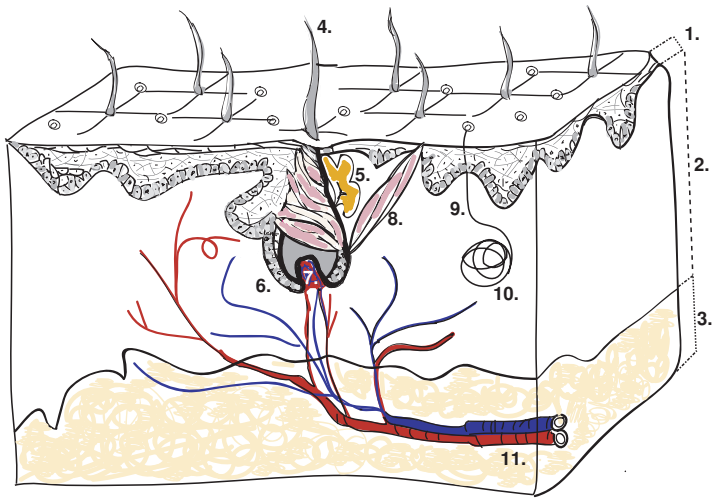

Figure 2.1: Skin cross-section. 1. Epidermis. 2. Dermis. 3. Subcutis. 4. Hair shaft. 5. Sebaceous gland. 6. Hair bulb. 7. Dermal papilla. 8. Arrector muscle. 9. Sweat duct. 10. Sweat gland. 11. Capillary system.

from 0.1 to 1.4 mm depending on its location on the body. The majority of cells forming the epidermis are *keratinocytes*, cells specialised in producing the fibrous structural protein "keratin". A main role of keratin is to protect the integrity of epithelial cells from stresses that can cause cell rupture or death [13]. Also other cells can be present in the epidermis, such as melanocytes [14] (which

synthesise the melanin pigment with a key role in photoprotection) or Merkel cells [15] (essential in the cutaneous nerve response). Epidermis is divided into four sublayers. From the outside to the interior, the layers are named *stratum corneum*, *stratum granulosum*, *stratum spinosum*, and *stratum basale* [16] (see Figure 2.2).

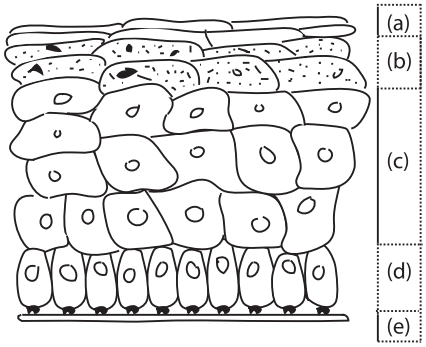

Figure 2.2: Sublayers of the epidermis: (a) *stratum corneum*, (b) *stratum granulosum*, (c) *stratum spinosum*, and (d) *stratum basale*. In addition, (e) corresponds to the basal membrane.

Cell division of keratinocytes occurs at the *stratum basale* or basal cell layer. In healthy tissue, division implies the formation of two secondary cells from a parental basal cell. One of these secondary cells will remain undifferentiated into the basal layer, therefore retaining its capacity to divide. The other secondary cell starts the differentiation and migrates towards the outer sublayers. In this process, the cell gradually experiences morphological and biochemical changes: the cell flattens, loses its nucleus, and increases its keratin production. [17] Indeed, the classification in sublayers of the epidermis previously mentioned is primarily based on the state of differentiation of the new generation of keratinocytes within them. The extreme case corresponds to the *stratum corneum* or horny layer, composed of sheets of mature keratinocytes with no nuclei.

Dermis is separated from the epidermal basal cell layer by the basal membrane. The thickness of dermis is in the range of 0.6 to 3 mm depending on the location on the body. The majority of the cells are fibroblasts, although other cells such as lymphocytes or macrophages can also be present. Fibroblasts produce proteins such as collagen and elastin, and glycosaminoglycans. Collagen (type I) is the most abundant protein and the major structural component of dermis.

Finally the deepest layer of the skin is the **subcutis**. It has a thickness of up to 3 cm and it is mainly composed of loose connective tissue and fat. In this study, subcutaneous tissue is not analysed as the skin tissue sections investigated reach no further than the dermis.

Other components commonly present in skin are sebaceous glands, sweat ducts and glands, and hair follicles [16]. Hair follicles are tubular invaginations of the

epidermis extending deep into the dermis that surrounds the root of the hair. The terminal expanded part of the follicle is called the hair bulb. At the base of the follicle there is a projection named the dermal papilla containing capillaries that irrigate the cells in the bulb. Those cells are mitotically active, overcoming differentiation and keratinisation and thus generating the hair fibre or hair shaft [18]. The hair shaft is a long filament in the centre of the follicle extended above the surface of the epidermis. It consist of keratotic protein (65-95%), water, lipids, melanin pigment granules, and trace elements [18, 19]. In this study the term "hair" is used to refer to the hair shaft in order to differentiate this structure from the hair follicle.

Cancer is a type of uncontrolled tissue growth in which the balance between cell division and cell differentiation is disrupted [17]. In the case of skin cancer, each basal cell from the *stratum basale* generates two new secondary cells which do not lose the property of dividing. The division process is repeated for the secondary cells, with the number of basal cells increasing exponentially. As the growth continues, larger amounts of cells that cannot be eliminated by mechanisms of self control (e.g. programmed cell death or *apoptosis*) accumulate in the tissue disrupting its normal function and organisation. Cancerous tissues present biochemical differences compared to their healthy analogues. For example, cells presenting dysplasia (cancer in its earlier stages) have an increased nucleus-to cytoplasm ratio, deficiencies in their DNA structure, higher metabolic activity, and alterations in lipid and protein levels [4]. Cancerous tissue also contains an increased number of blood vessels that allow tumour proliferation, which is the consequence of alterations in specific protein production [17]. The current study focuses on detecting these slight biochemical changes with Raman micro-spectroscopy in a specific type of skin cancer.

Skin cancer is a growing source of concern, not only for being the most frequent of all types of cancers (and the commonest of all malignancies) [20] but also due to its increasing incidence rate. Each year there are more new cases of skin cancer than the combined incidence of breast, prostate, lung, and colon cancers [21]. In the UK and USA more than 100,000 and 1,000,000 cases respectively are diagnosed annually [21, 22]. About 80% of skin cancer cases worldwide are basal cell carcinomas (BCC). This type of skin cancer belongs to the keratinocyte or non-melanoma family, and primarily arises from the *stratum basale* sublayer of the epidermis. Less often it can also develop from the outer region of the hair bulb. BCC commonly occurs in areas of skin exposed to the sun such as the head or the neck [23]. Ultraviolet radiation present in the sunlight produces structural alterations in the DNA of the exposed skin cells. These alterations are rapidly

repaired by self regulation mechanisms in the healthy individuals. A deficient repair may lead to disordered cell growth [20] explaining the direct relation between prolonged sun exposure and high BCC incidence rates.

BCCs can be classified according to their growth into: nodular-ulcerative, superficial, infiltrative, morphoeic, micronodular, and basosquamous [24]. In the current study only nodular (the most common) and morphoeic (with very aggressive growth pattern and high recurrence) BCCs were analysed.

2.1.2 Mohs micrographic surgery (MMS)

For large, rare or recurrent BCCs, those growing into the surrounding skin tissue and in critical areas (e.g. the high risk zone of the face: nasolabial folds, eyelids and periauricular areas), it is widely accepted that the most suitable treatment is MMS [21].

MMS was developed in 1940s by Frederick Mohs and originally designed as a three-step process: tumour removal, tissue fixation, and margin excision sectioning. Its objective is to remove the tumour with histological margin control, in order to obtain simultaneously maximum confidence in the completeness of the excision and minimise loss of surrounding normal tissue.

Today the procedure includes additional steps. Firstly, the skin from the area in which the tumour manifests itself externally is surgically removed. Note that such partial removal does not eradicate completely this type of contiguous tumour, whose borders may be spread into deeper regions of the skin in a finger-like manner. Then, the excised tissue block is divided into sectors which are labelled, their orientation being recorded. All tissue sectors are frozen, horizontally sectioned, and stained with hematoxilyn and eosin (H&E). Each of these thin stained layers is examined under a microscope by expert histopathologists in order to detect the presence of residual tumour. Any evidence of tumour is located on a Mohs map. According to histological findings the process is repeated in the positive sectors until the sample is clear of tumour [25]. Some of the stages of the procedure are shown in Figure 2.3.

It is widely accepted that MMS is the current most effective method for removal of aggressive BCC in terms of maximum conservation of healthy skin and minimum tumour recurrence rates [26–28]. While 5-year recurrence rates for BCC treated by MMS are 1.4% for primary tumours and 4% for recurrent tumours [29], for standard excision, where no margin evaluation is carried out, this rate reaches 3.2% to 10% for primary tumours and more than 17% for recurrent BCCs [30]. It has also been reported that at shorter follow-up periods (18 months) MMS

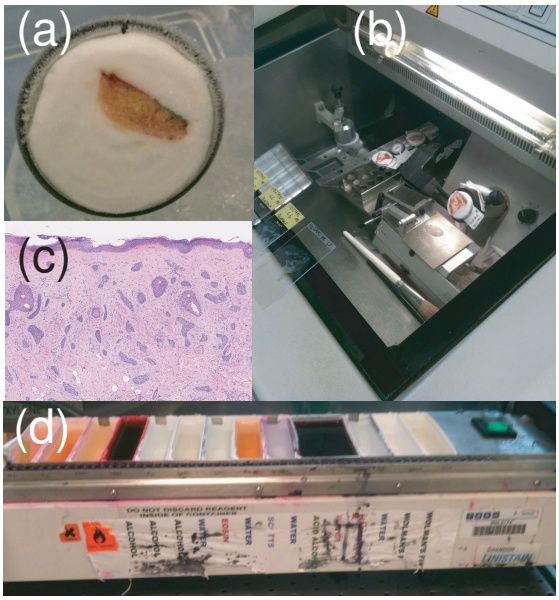

Figure 2.3: Stages of MMS: (a) Thick frozen excised tissue block. Its edges are colour-labelled to record its orientation. (b) Horizontal sectioning of frozen tissue. Images (c) and (d) belong to the staining process. (d) is the machine with the different chemicals for the fixing and staining protocol, and (c) is a typical stainned tissue, (see also Figure 2.4). Images courtesy of Dr. Leach (c) and Dr. Kong (rest).

was considerably more successful than surgical excision especially for recurrent tumours (0% versus 3%) [27].

However, in many cases traditional methods such as surgical excision, cryosurgery, curettage, and electrodessication rather than MMS are applied to high-risk BCC despite its lower effectiveness based solely on availability and cost considerations [31–33]. Focusing on UK as an example of current worldwide situation it has been reported that there are less MMS centres and specialised surgeons than the number recommended by the National Institute for Health and clinical excellence guidelines according to clinical needs [34]. The main reason for the inefficiency of service provision are the time consuming and costly procedures required to obtain and evaluate tissue sections during MMS, as well as a need for specialised staff including trained technicians for frozen tissue preparation. All these drawbacks arise from the fact that current MMS relies on sequential histopathological evaluation of the excised tissue sections.

Histopathology is a subjective, non-automated, time-consuming technique. Trained specialists diagnose the presence or absence of cancer by reading the histological slides acquired from a biopsy specimen. Diagnosis relies on the experience of the trained histopathologist, which is prone to inter-observer variability [35,36]. In practice the interpretation of MMS sections is mostly performed by the surgeon, and might be subject to diagnostic errors.

Inter-observer differences have been widely reported since histopathology has become a routinely clinical technique [18]. To express the diagnostic accuracy of a method in cancer detection, results are normally expressed in terms of its sensitivity and specificity. While the sensitivity is related to how precise the technique is in detecting true tumour, the specificity shows how accurately it identifies the healthy tissue. In a study on 48 samples evaluated by 20 pathologists, overall sensitivity was 87% (range, 55-100%) and specificity 94% (range, 83–100%) [19]. In another study on 592 histopathological slides using two pathologists, inter-observer agreement was found in 93% of cases [37]. These rates vary depending on the difficulty of the samples being studied and the efficiency of sample preparation, especially the sectioning procedure [38].

An automated reliable low-cost method for BCC detection and imaging in MMS-excised skin sections alternative to current histopathology would allow a wider use of MMS according to clinical needs. This would be a significant advance in the treatment of BCCs.

2.1.3 Staining methods for histopathological diagnosis

The most common sample preparation for histophatological evaluation includes tissue freezing, sectioning, fixation, and staining with hematoxylin and eosin ($H\&E$). $H\&E$ stains cell nuclei in blue/purple/black (hematoxylin) depending on the thickness of the section and the formulation of haematoxylin used. Mucins and some areas of the cytoplasm may take a delicate blue depending on the cell type. The majority of components of the cell cytoplasm are stained in pink/red (eosin) [39]. Connective tissue and red blood cells show a range of pinks and reds.

An example of a stained tissue section can be seen in Figure 2.4 where the darker purple band at the edge of the section corresponds to the epidermis. Dermis is the paler pink area. White regions appearing in the dermis correspond to fat. White areas enclosed into darker purple rings represent sebaceous glands (white inner circle) associated to hair follicles (dark purple external ring).

Other methods used to stain MMS fresh-frozen tissue sections are toluidine blue (TB) and methylene blue (MB) [40]. TB and MB tend to accumulate in the mitochondria of carcinoma cells to a greater extent than in normal cells. TB is technically easier and responds faster than $H\&E$ [41]. An early study comparing $H\&E$ and TB staining methods in MMS excised tissue sections recommended the latter for BCC identification [42]. TB was found to be helpful in discriminating basaloid cells around hair follicles from false apparent cases of BCC [42]. TB also visualises stromal change, which might be an indicator of residual BCC. Despite

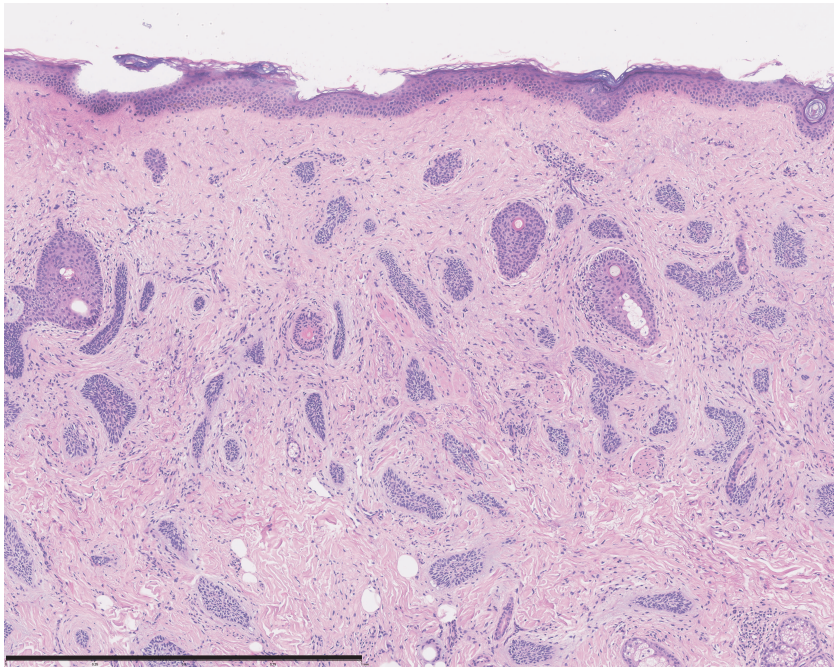

Figure 2.4: Example of an $H\&E$ stained slide of skin tissue. Cell nuclei adopt blue to purple colour due to haematoxylin dye, and cell cytoplasm pink due to eosin. Collagen regions are pink, while epidermis, hair follicle, and tumour regions are coloured in purple. White regions correspond to the fat, which remain unstained. Scale bar = 1 mm.

all of these advantages TB is only used by 16.8% of Mohs' surgeons surveyed [43]. The main reason for not using TB is that $H\&E$ is the standard staining technique taught in histopathologist training [42, 43]. If staining methods are to be used in Mohs centres, investment in histopathological training with alternative methods to traditional $H\&E$ such as TB seems reasonable. However, TB evaluation is still associated with major problems such as subjectivity, the need of specialised staff, and long waiting times to produce the final diagnosis.

2.1.4 BCC diagnosis with optical techniques

Many optical techniques have been suggested for detection and imaging of BCC. In order to identify the chemical alterations which take place in tumorous regions, chemically specific methods are required. Techniques such as fluorescence microscopy and vibrational spectroscopies (e.g. infrared or Raman spectroscopy) rely on the spectra generated when photoillumination is performed. The use of spectroscopic techniques is especially interesting in the discrimination of BCC and healthy tissue when healthy skin structures mimic morphologically BCC, as the mentioned spectra contain chemical information from the sample.

Many studies based on fluorescence imaging which aim to distinguish BCC from normal tissue and to focus on BCC border delineation have been reported [44–47].

A common contrast agent used in these fluorescence studies is aminolevulinic acid, which accumulates the protein protoporphyrin IX inside the skin tumour tissue [48].

Despite its molecular specificity, fluorescence imaging has several intrinsic disadvantages when compared to vibrational spectroscopy: it requires chemical labelling and it has broader spectra. Chemical labelling implies the introduction of external fluorescent molecules called *exogenous* fluorophores. If autofluorescent molecules from the tissue itself (*endogenous* fluorophores) are used instead, the limitation arises from the fact that the number of these fluorophores is limited. The broadband nature of fluorescence spectra from the tissue is due to its complex composition. The fluorescent bands of the biomolecules present in the tissue overlap to produce featureless fluorescent spectra [46]. These wide bands hide the subtle spectral details required for reliable discrimination between healthy skin and BCC. In addition, fluorescence images lack meaningful quantitative information as required in automated imaging. These images provide purely qualitative information as they depend on emission intensity spectra, which vary greatly with sample preparation procedures.

Common fluorophores require ultraviolet light to be excited, which may lead to sample photobleaching of the fluorophores. Photobleaching refers to the photodamage and destruction of endogenous fluorophores whose autofluorescence is to be measured. All these drawbacks may explain the low sensitivity reported in fluorescence studies on diagnosis of BCC. A comparison between this technique and histopathological mapping by Stenquist *et al* in 2006 reported that good correlations were only observed in less than 50% of patients [45].

Despite the intrinsic disadvantages of fluorescence, advanced fluorescence microscopic techniques have been recently applied to BCC discrimination, e.g. multiphoton laser scanning microscopy (MLSM) [48–50]. In MLSM the excitation of fluorophores is obtained by a non-linear multiphoton process. Among the family of MLSM two photon excitation microscopy (TPEM) is the most widely used technique. Briefly, a high-energy ultra-short pulsed laser is focused on the sample via a microscope objective in order to confine the maximum number of exciting photons in time and space. Two quasi-simultaneous photons of wavelength λ exciting a fluorophore would combine to produce the same effect as a single photon of half the wavelength ($\frac{\lambda}{2}$) striking the fluorophore. This allows the use of harmless near infrared (NIR) light to excite fluorophores that otherwise would require highly damaging ultraviolet photons. This is the case of collagen, keratin, melanin or elastin, among other autofluorescent substances present in the skin. Therefore,

MLSM reduces photobleaching and allows higher imaging depth useful in case of thick samples.

In combination with TPEM, second harmonic generation (SHG) has been used [48]. In SHG, when a high laser beam of wavelength λ interacts with a highly polarisable material with non-centrosymmetric structural configuration, such as collagen or muscle fibres, a signal of $\frac{\lambda}{2}$ wavelength is produced [50]. Lin *et al* [50] studied the discrimination of nodular BCC from dermis by the combination of MLSM and SHG [50]. They reported lower SHG and higher MLSM signals in the cancer stroma than in normal dermis. Increased multiphoton signal in the cancer areas was explained by the autofluorescence contribution of the tumour cells. SHG signal in the samples was associated primarily to the collagen fibres, containing mainly structural information. Lower values of SHG signal in BCC regions were attributed to collagen disruption or deficiency. Indeed, monitoring the collagen structural changes in tumorous tissue with SHG has been reported as a reliable technique to explain the stage of development of the cancer. This is due to the fact that in earlier stages BCC is often surrounded by a collagen-rich case, which acts as a natural barrier for tumour spreading. As the tumour grows this collagen barrier is disrupted [51].

Optical coherence tomography (OCT) has also been successfully applied to BCC imaging [52,53]. OCT uses low-coherence interferometry to produce cross-sectional images of biological samples [54]. OCT skin cross-sections contain morphological information from the samples with penetration depths of the order of 0.5-1.0 mm by recording the small reflected signal from the skin layers after illumination with ultra-short laser pulses or low-coherence light sources [52]. This technique is particularly suitable for *in vivo* imaging of deep tissues. However, MMS-excised tissue sections are as thin as 20 μm.

The study carried out in this thesis aims to produce reliable images with the diagnosis of the skin sections and thus morphological information from the skin specimens needs to be complimented by chemical information. Hence, in the current thesis spectroscopic techniques are preferred to OCT.

Vibrational spectroscopy techniques achieve high chemical specificity and tumour discrimination accuracy presenting spectra with sharp meaningful peaks. An early study with infrared micro-spectroscopy showed 93% sensitivity in discrimination among epidermis, BCC, squamous cell carcinoma, and melanocytic lesions [47]. BCC/epidermis discrimination was based on the higher nucleic acid concentration of BCC. However, infrared spectroscopy has a major limitation: it requires preparation of thin frozen sections as this technique is based on the absorption of infrared radiation by the sample which, if strong, could lead to no detected

signal. Water strongly absorbs infrared light and biological tissue is water-rich. This is a major limitation especially for *in vivo* applications. For *in vitro* studies this trade-off implies an upper limit in the thickness of the samples to be measured which represents an intrinsic disadvantage for imaging MMS-excised tissue blocks [55, 56]. Tissue sections must be thinner than 10 μm to avoid complete absorption of the incident radiation.

2.1.5 Raman micro-spectroscopy (RMS) on skin and oncological detection/imaging

Raman micro-spectroscopy (RMS) is able to obtain both high chemical specificity and high resolution images on thick tissue specimens, as the Raman signal is produced by inelastic scattering (and not absorption) of monochromatic light by the molecules of the sample. This technique could be used both on biological tissue sections and excised tissue blocks.

Success in detection of the slight biochemical changes appearing in cells presenting dysplasia with RMS has been reported [4]. The potential of RMS to detect and diagnose human cancers both *in vivo* and *in vitro* has been demonstrated for a large number of cancer types including skin [2, 5, 7, 57–59], breast [60], oesophagus [61], lung [62], cervix [3], and prostate [63].

Early studies compared Raman spectra from normal, healthy human stratum corneum with other skin tissues such as callus tissue or hyperkeratotic psoriatic plaques [64]. RMS has also revealed the spectral differences between hair follicle, hair, sweat ducts, capillaries, sebaceous glands, and dermis [65, 66].

The capability of Raman spectroscopy to detect biochemical alterations in skin tissue caused by BCC was first demonstrated by Gniadecka *et al* [2]. Several protein and lipid alterations characteristic of BCC tissue were reported [2, 59] such as the alterations of the amide bands attributed to the conformational changes of proteins (essentially changes in the collagen). Further experiments showed 97% sensitivity and 98% specificity on BCC detection with the use of principal component analysis for dimension reduction, along with a neural network classifier for spectral clustering [7]. More recent work also demonstrated the ability to diagnose skin tumour *in vivo* using Raman spectroscopy combined with fibre optics [58].

Quantitative Raman spectroscopic images can be built by representing the intensity of a certain spectral peak, score or weight obtained with a multivariate spectral analysis method for each individual location in the 2D region where Raman spectra were acquired. As RMS does not require sample preparation, specimens

are not subject to chemical or structural alterations introduced by preparation protocols. Consequently, RMS is an objective and quantitative method that can be used continuously with the same level of accuracy, making it ideally suitable for automatic implementation and biochemical imaging. Many studies have applied RMS to tumour imaging in order to create spectral maps of tissue sections containing cancerous cells. Images of tumours in the brain [67], gastrointestinal tract [68], lymph [69], lung [62], oesophagus [6], and skin [5] have been produced. The majority of these studies applied unsupervised methods for imaging, such as the intensities of the scores of a selected number of principal components or k-means clustering.

Unsupervised methods examine the Raman spectra searching for patterns but they do not have any predictive power as classification algorithms do. Images obtained by unsupervised methods do not provide an automated diagnosis but require additional expert evaluation for the classification. To make classification easier k-means clustering can be used to find the similarities in the spectra from a tissue biopsy prior to applying the classification algorithm.

As a last remark, the reason for choosing spontaneous over stimulated Raman spectroscopy is justified. Although spontaneous (linear) Raman spectroscopy is optimal for *in vitro* samples such as the ones presented in this thesis, for future *in vivo* applications this might not be the case. In such cases the long acquisition times of Raman spectroscopic mapping experiments and the weakness of the Raman spectroscopic signals of some biological scatterers may be prohibitive. Variants of linear Raman such as coherent anti-Stokes Raman scattering (CARS) have been applied to investigations on BCC specimens to overcome these limitations. However, CARS rises new problems: CARS spectra carry information only from a narrow specific spectral band and have high background, which complicates data interpretation [70]. CARS studies on MMS sections tend to be complementary to other methods. An example is the work of Vogler *et al* [51] in which different techniques (SHG, TPE, RS, and CARS) are used to characterise the tumour areas. In this case CARS was used to image the spatial distribution of lipids in the tumour. This technique was found able to detect fat reservoirs in the BCC tissue, however accurate diagnosis remains difficult.

2.2 Supported lipids and techniques for their characterisation.

2.2.1 Supported lipid layers (SLLs): relevance and applications.

The second part of this thesis is focused on the study of thin supported lipid films. One of the major applications of thin supported lipid films is as *biomimetic* systems. The development of *biomimetic* systems or nature-like artificial models to replicate biological scenarios such as the cell surface is an important current topic in nano-biotechnology. Supported artificial planar lipid bilayers (SPLB) are well established biomimetic systems that accurately mimic the cell membrane environment [71]. Basically, an SPLB consists of a planar solid substrate covered by a lipid bilayer, either coupled to the solid or separated from it by a nanometre thick layer of water or polymer. The latter systems are called "free bilayers" and allow dynamical studies of the cell membrane. Real membranes are made of mixtures of lipids and incorporate proteins.

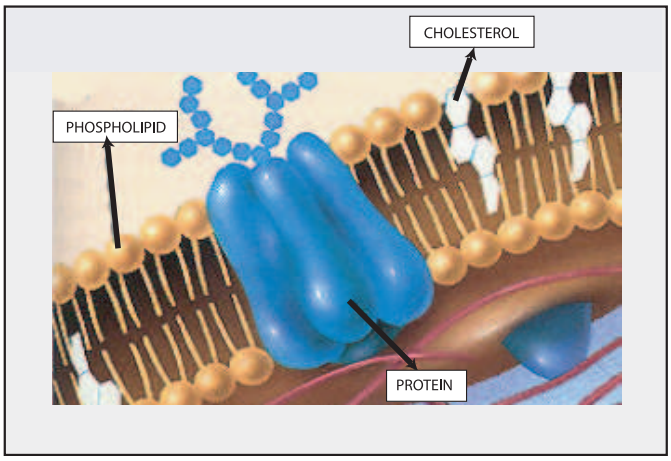

Figure 2.5: Detail of the cell membrane. Adapted by permission from Garland Science: ref. [72], © (2002).

SPLBs can incorporate proteins under non-denaturing conditions, enabling studies on cell-adhesion, locomotion, cell-cell recognition, immunological response, and cell transduction [1,73–75]. In such biological processes, binding between a specific protein within the membrane and its counterpart molecule of the cell occurs at the cell membrane interface. This and similar scenarios can be successfully reproduced by SPLBs, also allowing the fabrication of selective biosensors [1, 76]. In SPLB technology a conductor is generally chosen as the solid support and the bilayer acts as an insulator. The proteins incorporated in the bilayer (playing the role of

receptors) allow the electrical/optical detection of their counterpart ligands of the binding cells [73].

Another biologically relevant application of SPLBs is their success in mimicking the so-called cell membrane *microdomains* or *rafts* under well controlled conditions. Rafts are believed to play a central role in the workings of the cell membrane, responding to external stimuli by changing their dimensions and composition. Rafts feature in biological processes such as signal transduction [75], membrane trafficking or cell death [1]. Lateral lipid reorganisation and raft dynamics during these processes can be studied in the SPLB framework by vibrational spectroscopy techniques [10, 77, 78].

Research on the ability of supported lipid structures to biofunctionalise inorganic and polymeric materials has been reported [79, 80].

In some applications such as sensing or drug delivery, multilamellar lipid arrangements present advantages over single bilayers, when more bilayers imply higher rate of success [81]. When the effect of the substrate on the experimental results with single bilayers is significant, mutilayers may be a more suitable choice [82]. Multilamellar lipid structures can also mimic more accurately certain natural environments such as the methylakoid membranes of chloroplasts in plant leaves [83]. However, using a larger number of bilayers (more than 30) limits the properties that can be measured to the average values of the whole lipid structure, and do not allow the study of individual bilayers. A compromise might be to deposit up to a maximum of 10 bilayers [82].

2.2.2 The amphiphilic bilayer.

As shown in Figure 2.6 a lipid bilayer consists of an ensemble of amphiphilic molecules, each of these molecules formed by a polar or hydrophilic head and a non-polar or hydrophobic tail. The arrangement of the lipids within the bilayer is such that the free energy of the system immersed in an aqueous environment is minimised. Polar heads represented as empty circles in Figure 2.6 face the water molecules while the hydrophobic tails (or double black traces in Figure 2.6) are oriented inwards towards the inner part of the membrane.

In this thesis different amphiphiles have been used to create the supported amphiphilic layers, namely arachidic acid (AA), 1,2-dipalmitoyl-*sn*-glycero-3-phosphocholine (DPPC), and 1,2-dipalmitoyl-*sn*-glycero-3-ethylphosphocholine (EPC or cationic DPPC). AA belongs to the family of fatty acids; it is not a lipid but a simpler amphiphilic molecule. Fatty acids are carboxylic acids where the hydrophilic headgroup (-COOH) is bonded to a hydrophobic single alkyl chain

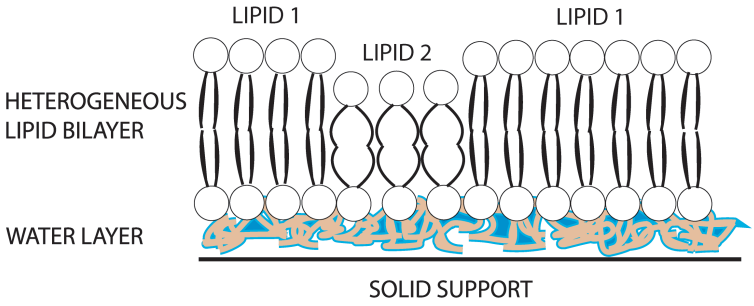

Figure 2.6: Representation of a supported lipid bilayer.

(i.e only formed by hidrogen and carbon atoms). AA is a saturated fatty acid with a long chain of 20 carbons, $C_{20}H_{40}O_2$. The carboxylic head group from AA dissociates in water and becomes negatively charged forming carboxilates (COO^-). Also it is assumed that the first one or two methylene groups are also in the water [84]. Phospholipids are more complex biomimetic systems than fatty acids and closer models to real cell membranes. Phospholipids differ from fatty acids in the number of alkyl chains (they have two instead of one) and in the nature of their polar head group. Phospholipids consist of a hydrophobic tail of two hydrocarbon chains, and a hydrophilic head such as phosphatildylcholine (PC) or phosphatidylethanolamine. Head groups can be charged, or overall neutral but incorporate charge separation. In the latter case they are termed *zwitterionic*. PCs are an example of zwitterionic head groups with a positively charged choline and a negatively charged phosphate (PO_3) [85]. In reality PCs are partially charged due to some acidic impurities. This increases the electrostatic repulsion that they experience when supported on negatively charged substrates such as mica, sapphire or metal oxide layers [85]. DPPC and EPC are neutral and cationic examples, respectively, of phospholipids with PC as a headgroup.

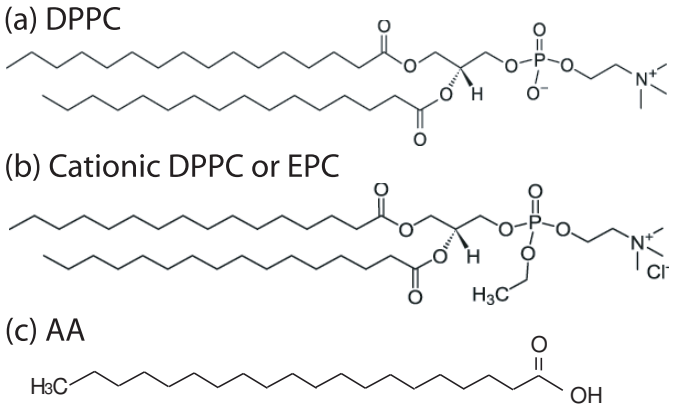

Figure 2.7: Structure of three selected amphiphiles: two phospholipids, (a) DPPC and (b) cationic DPPC, and a fatty acid (c) arachidic acid (AA).

2.2.3 Techniques for characterisation of supported lipid layers.

The establishment of supported lipid layers as good biomimetic models for a wide range of applications created the need for reliable techniques for characterisation of these systems. Structural studies with X-ray diffraction [86], and neutron scattering [87, 88] on thin lipid films have been performed for several decades already. However, the use of these techniques might be limited by the low contrast of the lipid films. A solution to improve the contrast between organic materials in neutron scattering is to use isotopic labelled lipids or deuterated water as a medium for the hydrogenated lipids.

Thin lipid film characterisation at nanometre scale can be achieved by electron microscopy, but radiation damage and the introduction of extra charges into the system are major complications [89, 90]. Furthermore, strict sample preparation requirements limit the applicability of transmission electron microscopy and scanning electron microscopy to hydrated multilamellar supported architectures.

When working with supported lipids the properties of the substrate in which the lipids lay might influence the choice of the optimal characterisation technique. Substrates are frequently made of glass [91], mica [92], sapphire [93], alkanethiol-coated surfaces (hybrid membranes) [94], or even more exotic materials such as ultraflat graphene [95]. Surface plasmon resonance (SPR) [96] and electrochemical investigations [94] have been reported in which thiols were used to anchor the lipids to the metal substrate. Nevertheless, the model loses biological relevance as hybrid membranes impose constrains in the dynamics of the system. In contrast, phospholipid bilayers decoupled from the substrates by a nanometer thick water layer or polymer cushion enable dynamic studies in a nature-like environment [1, 88, 97].

Atomic force microscopy (AFM) can be applied to aqueous environments and it is able to resolve down to subatomic features [98]. AFM has been successfully applied to image artificial and natural cell membranes for the last decade [99,100]. It allows topographic characterisation of the sample (in tapping and contact mode), and measures the mechanical properties and interaction forces within the system (force spectroscopy mode) [97,101]. AFM images have been produced on monolayers [97], hydrated bilayers [102], and multilamellar lipid structures [100]. However, AFM studies alone do not give a complete picture of the lipid layer architecture as they lack chemical information.

Studies by fluorescence microscopy provide chemical information from the sample, and their application to thin lamellar lipid research has been widely cove-

red [76, 103]. Dense and well ordered phases within the lamellar structures are difficult to observe by fluorescence microscopy because they have a low density of fluorophores [104]. Different phases better incorporate certain fluorophores and therefore optimisation has to be performed for each model system [105]. In the case of using endogenous fluorophores the efficiency of the technique strongly depends on the nature of the sample.

Advanced fluorescence techniques such as scanning near-field optical microscopy (SNOM) or waveguide evanescent field fluorescence (WEFF) microscopy have also been applied to supported monolayer studies, especially involving raft imaging [106,107]. Basically, the SNOM instrument consists of an optical probe whose apex contains a confined light excitation source. Scanning of the sample by the optical probe induces excitation of the fluorophores present in the sample [105,106]. Its main advantage over conventional fluorescence is that it allows high spatial resolution down to 50 nm [105]. In WEFF, laser light is coupled via an optical grating to a mono-mode waveguide. The beam propagating through the waveguide generates an evanescent field which is used to excite fluorescence in the sample. For nanometre thin lipid films all the fluorophores of the sample are excited as the penetration depth reaches 100 nm [108]. WEFF produces images with a much higher contrast than conventional fluorescence microscopy, lower photobleaching, and higher sensitivity [107]. In WEFF the wavelength of operation is fixed and very sensitive to the angle between the laser beam and the grating. SNOM and WEFF still carry the intrinsic disadvantages of fluorescence microscopy: chemical labels, scarcity of endogeneous fluorophores, photobleaching, etc.

Raman spectroscopy is a powerful quantitative technique for chemical imaging of biological specimens. It overcomes the limitation of fluorescence labelling and requires minimal sample preparation [109]. However, the weak spontaneous Raman signal from lipid monolayers and bilayers needs to be enhanced for effective detection. Techniques such as coherent anti-Stokes Raman scattering (CARS), tip enhanced Raman spectroscopy (TERS), and surface enhanced Raman spectroscopy (SERS) boost the Raman signal and have been successfully applied to supported lipid research. CARS allows clear detection of the lipids in the Raman spectral band corresponding to the C-H stretching vibrations (2800-3000 cm^{-1}) [109]. This establishes CARS as a suitable technique for fast lipid imaging. In contrast to traditional Raman spectroscopy, CARS only enhances one spectral band at a time and therefore information outside this spectral range is lost. Furthermore, CARS signal presents a high enhanced background masking subtle chemical information, especially problematic in the fingerprint region (from about 700 to 1800 cm^{-1}).

TERS and SERS spectra cover a wider spectral range than spectra acquired by CARS. TERS and SERS share the same fundamental physics principle: the Raman signal at the close proximity of rough metal surfaces is greatly enhanced as a consequence of the resonance of the surface plasmons of the metal. However, while SERS requires an external metallic nanostructure (substrate), TERS incorporates this metallic feature to the apex of an AFM tip. Therefore, TERS allows simultaneous characterisation of the sample morphologically and spectroscopically. To the author's knowledge, the first TERS study on supported lipid bilayers was reported in 2009 by Bohme *et al* [92]. The authors used a dried thin film of a mixture of palmitoyloleoylphosphatidyl-choline/dioleoylphosphatidylserine (POPC/DOPS) on mica. The acquired TERS spectra associated to the same location of the lipid surface and under the same experimental conditions seem to vary greatly. The authors associated the lack of reproducibility to the dynamical behaviour of the lipid agglomerate. As evidence of the bilayer formation and the phase separation of the heterogeneous mixture, height AFM images with conventional probes were reported (data not shown in the original paper). However, the image achieved with SERS-active tips has extremely low resolution. The authors associated low resolution to the effect of the silver coating of the AFM tip [92].

Another recent study on raft imaging with TERS was performed by Opilik *et al* [105]. They deposited thin arrangements of DPPC/DOPC on gold substrates and used a silver-coated tip. From the AFM image shown in the paper a uniform monolayer covering the whole substrate was not formed on hydrophilic gold. Bulk Raman spectra of both compounds were included, showing the spectral differences in the fingerprint region. However, TERS spectra from the regions of DOPC and DPPC within the thin lipid islands in the fingerprint region were not shown.

In the study carried out in this thesis simultaneous *in-situ* high topographic resolution of the sample and chemical specificity are needed to successfully characterise the lipid architectures. TERS is discarded due to its current early stages of development, leaving this field open for future work. Instead, a novel combined technique to study supported lipid arrangements is introduced, incorporating the well-established topographic high resolution of AFM and the high chemical specificity of SERS.

Early SERS studies on phospholipid monolayers created in an air-liquid interface commonly incorporated high electric fields to produce a voltage difference across the model membranes. A pioneering study by Mangeney *et al* [11] used a Langmuir-Blodgett (LB) trough to form a monolayer of a negatively charged phospholipid, tetramyristoyl cardiolipins (TMCL). Under the application of a voltage to the monolayer and using a subphase containing $AgNO_3$, silver deposits

were observed to grow concentrically under the phospholipid monolayer allowing SERS studies. However, a fluorescent dye (nonyl acridine orange) was added to the monolayer to demonstrate the high enhancement of the system and to mask the spectra from the pure phospholipid monolayer.

Guo *et al* [12] successfully acquired pure SERS spectra from DPPC monolayers without the addition of external labels. They studied the response of the lipids to a strong applied electric field. The ordering of the DPPC molecules on the electrode surface for different voltages was related to the ratio of intensities of specific SERS-active vibrational bands carrying structural information. However, no SERS spectra were detected in the absence of applied voltages. For the SERS experiments a green laser of 200 mW was used. The diameter of the laser beam on the sample was 0.1 mm and the acquisition time per spectrum was 7 s.

Another remarkable SERS study on phospholipid monolayers deposited on gold substrates was performed by Bernard *et al* in 2002 [110]. The substrates were made of gold colloidal monolayers deposited on silanised glass. No external voltage was applied in this experiment. SERS spectra of a probe molecule, trans-1,2-bis(4-pyridyl)ethylene (BPE), were studied in the presence and absence of a phospholipid monolayer of TMCL varying the pH. AFM studies on the substrates before and after the phospholipid monolayer deposition did not show any modification of the topography of the substrate. This result might be explained by the fact that glass roughness, especially when silanised, is higher than the phospholipid thickness. The presence of the phospholipid monolayer was found to modify the SERS spectra of BPE while varying the pH at the gold surface. However, SERS spectra of TMCL were not shown.

Further SERS investigations on mixtures of lipids and fatty acid on silver found that the peak at 1392 cm^{-1} of the lipids can be used as a biomarker to detect the presence of lipids in such mixtures. Spectra from amphiphilics were taken with different microprobes (silver coated microwires and a silicon-silver electrode) applying an external electric field. The amphiphiles did not form films [111].

Therefore, simultaneous optical and topographic characterisation of thin supported phospholipid films with a combined AFM-SERS system has, to the author's knowledge, not been performed yet. One of the aims of this thesis is to achieve such novel, simultaneous characterisation. The acquisition of SERS spectra from pure thin phospholipid films without applying external electric fields or dyes might be challenging, but it seems of great interest in the context of bio-nanotechnology and biomimetics. If successful, the simultaneous spatial correlation of the SERS spectra with AFM images might open a new line of research in thin lipid film characterisation.

Chapter 3

Experimental techniques: theoretical background

Chapter 3 introduces the theory behind the main experimental techniques used in this piece of work. Raman spectroscopy (RS) is the main technique and the thread linking the whole body of this thesis. Relevant theoretical aspects of RS are covered in detail. Raman scattering is explained by describing the interaction between light and matter using classical and semi-classical models. The description of the Raman scattering presented in this chapter not only elucidates the physics underpinning the experiments, it also demonstrates key relationships between intervening parameters, e.g. the dependence of the Raman intensity on the wavelength of the laser. Surface enhanced Raman spectroscopy (SERS), a variant of RS and atomic force microscopy (AFM) are also covered. The last part of this theoretical section introduces very briefly the techniques used for the synthesis of thin lipid films.

3.1 Raman spectroscopy

3.1.1 Theory of Raman scattering

Optical spectroscopy studies the interaction between light and matter. This interaction could be described in terms of absorption, emission or scattering processes. Raman spectroscopy focuses on the inelastic scattering of monochromatic radiation by atoms or molecules in a sample. Although the origin of Raman spectroscopy is previous to the laser revolution, lasers are the only excitation sources considered in this thesis. When a sample is irradiated with laser light of intensity I_0 the majority of the incident photons are elastically scattered, i.e. scattered without change in energy (Rayleigh scattering). In addition, a small fraction of

the incident photons ($\sim 10^{-5}$) are scattered inelastically experiencing frequency shifts. This is called the Raman effect [112]. If the frequency of the incident light is referred to as ν_0, the shifted frequency due to Raman scattering will be $\nu_f = \nu_0 \pm \nu_{molecular}$, where $\nu_{molecular}$ is an internal frequency associated to a vibrational or rotational mode of the molecule.

In terms of energy a molecule in an initial energy state $E_{0,i}$ is excited by incident photons of energy $h\nu_0$, where h is Planck's constant. By absorption of photons the system reaches a virtual excited state $E_{0,v}$. In general the incident photons do not have sufficient energy to induce electronic transitions in the molecule.

The system experiences relaxation via radiative emission until it reaches a stable final energy level, $E_{0,f}$ (see Figure 3.1). Note that Raman scattering is a two photon instantaneous process where the absorbed and emitted photons are intrinsically linked. If the final energy state of the molecule $E_{0,f}$ is higher than its initial state $E_{0,i}$ then the process is called Stokes Raman scattering. If otherwise $E_{0,f}$ is lower than $E_{0,i}$ the process receives the name of anti-Stokes Raman scattering.

If high energy photons are used the molecule can experience electronic transitions and the phenomenon is called the resonance Raman effect.

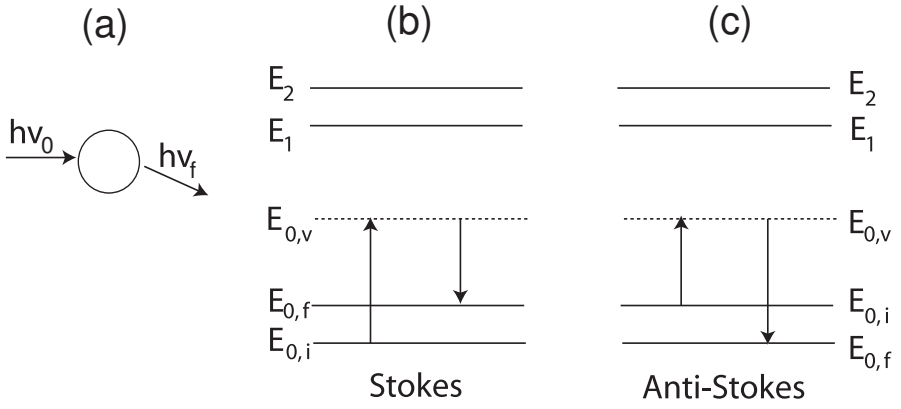

Figure 3.1: (a) Schematic of the incident and scattered light interacting with the molecule. (b-c) Jablonski diagrams for the Stokes and anti-Stokes Raman processes. $E_{0,i}$, $E_{0,v}$ and $E_{0,f}$ refer to the initial, virtual, and final energy states respectively of the fundamental electronic energy state. Subindices 0, 1, and 2 of the energy states refer to the fundamental, and first and second excited electronic energy states respectively. ν_0 and ν_f are the initial and final frequencies of the incident and scattered light respectively.

Figure 3.1 (a) represents how irradiating a molecule with a beam of photons of energy $h\nu_0$ results in scattered photons of shifted energy $h\nu_f$. Figure 3.1 (b) and (c) are Jablonski energy diagrams showing the excitation and relaxation of the molecule during Stokes and anti-Stokes Raman scattering [113]. Counting the number of Raman photons at different frequency shifts ($\Delta\nu = |\nu_f - \nu_0|$) a Raman spectrum is generated.

The Raman effect is caused by molecular vibrations in the irradiated sample and gives information about the composition and structure of the molecules. This molecular information is independent of the wavelength of the excitation source [114]. Molecular vibrations can be divided into two categories: deformational vibrations, where the bond angles change, e.g. bending, rocking, wagging or twisting, and stretching vibrations, where only the bond lengths change [112]. In order to understand qualitatively the process of Raman scattering the interaction between light and matter can be described using classical electromagnetism. However, if a quantitative study is desired leading to an accurate expression for the intensity of the Raman spectral lines it is necessary to treat the problem by using quantum-mechanics. In the semiclassical approach molecules are considered as quantum systems, while radiation is still treated classically.

Classical approach to spontaneous Raman scattering

Any molecule can be considered as the composition of two centres of charge, one corresponding to the electrons, negatively charged, and the other to the nuclei, positively charged. The spatial separation of both centres of charge gives rise to the polarisation of the molecule. Depending on the geometry of the molecule and its number of electrons and protons a molecule may have a net dipole moment in the absence of any applied electric field.

A laser beam propagating into a medium due to its electromagnetic-wave nature will have associated electric and magnetic orthogonal fluctuating classical fields. The effect of the electric field on any molecule constituting the medium will be the induction of a dipole moment $\boldsymbol{\mu_{ind}}$ in the molecule, due to the different response to the electric field of electrons and nuclei. If prior to application of the electric field the molecule was not polarised then the only dipole moment present after the laser irradiates the sample will be $\boldsymbol{\mu_{ind}}$. However, if the molecule was already polarised in the absence of any applied electric field, i.e. if it presents a permanent dipole moment $\boldsymbol{\mu_0}(t=0)$ then the resulting dipole after laser illumination will consist of both the permanent and induced dipoles:

$$\boldsymbol{\mu}(t) = \boldsymbol{\mu_0}(t) + \boldsymbol{\mu_{ind}}(t) \tag{3.1}$$

Under normal Raman scattering conditions, such as relatively weak laser fluxes, the relationship between the induced dipole and the applied electric field $\mathbf{E}$ can be expressed as [115]:

$$\boldsymbol{\mu_{ind}} = \tilde{\alpha}\mathbf{E} \tag{3.2}$$

The polarisability $\tilde{\alpha}$ is a property of each molecule depending on its molecular structure (geometry) and on the nature of the bonds. It describes the ease with which molecular orbits can be distorted by the presence of an external electric field [114]. Note that a particular molecular vibration can produce a change in the polarisability even if there is no change in the dipole moment of the molecule. The polarisability $\tilde{\alpha}$ is a second rank tensor of elements α_{jl} where the subindices j and l refer to the directions of the induced dipole moment and the incident electric field, respectively.

The dependence of the induced dipole moment on the Raman scattering frequencies, i.e. $w_f = w_0 \pm w_n$ (where w_0 and w_n are the frequencies of the laser and the molecular transition respectively) can be expressed in the form,

$$\boldsymbol{\mu_{ind}}(t, w_0 \pm w_n) \propto \sum_{n=1}^{Q} \left(\frac{\partial \alpha_{jl}}{\partial q_n}\right)_0 q_0 \mathbf{E_0} \left[cos\left((w_0 + w_n)t\right) + cos\left((w_0 - w_n)t\right)\right] \quad (3.3)$$

where q_n refers to the nuclear coordinates corresponding to the modes of vibration of the molecule, Q is the total number of normal vibrational modes of the molecule, and $\left(\frac{\partial \alpha_{jl}}{\partial q_n}\right)_0$ refers to the changes of the components of the polarisability tensor with the nuclear displacements. Note that for any Raman scattering to be observed $\left(\frac{\partial \alpha_{jl}}{\partial q_n}\right)_0 \neq 0$, i.e. any of the 9 components of the polarisability tensor can change with the nuclear displacements. The derivation of eq. (3.3) can be found elsewhere [115] and it is not the focus of this thesis.

Semiclassical description of spontaneous Raman scattering

In the semiclassical treatment proposed by Placzeck in 1934 [116] radiation is considered a classical electromagnetic wave while molecules are treated as quantum systems.

Consider that an oscillating electric field $\mathbf{E}$ is applied to a medium, being

$$\mathbf{E} = \mathbf{E_0} \cos wt \quad (3.4)$$

Note that the frequency of the laser is now named w and not w_0, as in the classical treatment for simplicity. Eq.(3.4) is valid if the linear dimensions of the atom or molecule are much smaller than the wavelength λ of the incident radiation, in order to consider the electric field uniform within the dimensions of the molecule [117]. An induced dipole moment will appear due to the interaction between the electric field and the molecules of this medium. From a quantum mechanical analysis this dipole moment is an observable operator. We are interested in calculating the

transition dipole moment [118], i.e.

$$\mathbf{M_{fm}} = \langle \Psi_f | \, \boldsymbol{\mu} | \Psi_m \rangle \tag{3.5}$$

with $\Psi_f(t)$ and $\Psi_m(t)$ being the eigenfunctions representing the final and initial states of the system, respectively. The intensity of the scattered radiation is proportional to $|\mathbf{M_{fm}}|^2$ [118]. $\Psi_f(t)$and $\Psi_m(t)$ are solutions of the time-dependent Schrödinger equation for the system,

$$i\hbar \frac{\partial \Psi_n}{\partial t} = H\Psi_n \tag{3.6}$$

where $\hbar$ is the reduced Planck constant, H is the Hamiltonian of the system, and the subindex n refers to a general eigenstate. Assume the oscillating electric field is not too strong [114], and it is not in resonance, but instead induces an oscillating dipole moment that re-radiates electromagnetic waves [118]. The Hamiltonian H of the system after the application of the laser can be considered as a perturbation of the initial Hamiltonian $H^{(0)}$ corresponding to the undisturbed system, i.e to the situation in which the laser is off. The wavefunction $\phi_n^{(0)}$ describing the state of the molecule in the undisturbed system satisfies the time-independent Schrödinger equation,

$$H^{(0)}\phi_n^{(0)} = E_n^{(0)}\phi_n^{(0)} \tag{3.7}$$

$$\Psi_n^{(0)} = \phi_n^{(0)} e^{-iw_n t} \tag{3.8}$$

where $w_n = \frac{E_n}{\hbar}$. (Note that this thesis uses the following notation: Ψ to refer to a time-dependent state and ϕ if the state is time-independent). The Hamiltonian H and wavefunction Ψ_n of the perturbed system can be expressed as [114, 118]

$$H = H^{(0)} + V = H^{(0)} - \boldsymbol{\mu}.\mathbf{E_0} cos wt \tag{3.9}$$

$$\Psi_n = \Psi_n^{(0)} + \Psi_n^{(1)} + ... \tag{3.10}$$

where $\Psi_n^{(1)}$ is the first-order correction of the wavefunction of the system. The expression for the oscillating transition dipole moment from a state $|m\rangle$ to the state $|f\rangle$ in first-order perturbation theory contributing to the Raman scattering will have two components, one associated to the scattering frequencies $(w_{mf} - w)$ and the other to the scattering frequencies of the form $(w_{mf} + w)$, where $w_{mf} = \frac{E_f - E_m}{\hbar}$ is the frequency associated to the transition between the states $|m\rangle$ and $|f\rangle$:

$$M_{fm}^{(1)}(t) = M^{(+)} e^{i(w_{fm}+w)t} + M^{(-)} e^{i(w_{fm}-w)t} \tag{3.11}$$

where

$$M^{\pm} \propto \sum_{k} \left(\frac{\boldsymbol{\mu_{fk}} \left(\boldsymbol{\mu_{km}} \mathbf{E_0} \right)}{w_{km} \pm w} + \frac{\boldsymbol{\mu_{km}} \left(\boldsymbol{\mu_{fk}} \mathbf{E_0} \right)}{w_{kf} \mp w} \right) \tag{3.12}$$

and $\boldsymbol{\mu_{ls}} = \left\langle \phi_l^{(0)} \middle| \boldsymbol{\mu} \middle| \phi_s^{(0)} \right\rangle$ such as $l = f, k$ and $s = k, m$.
The detailed derivation of (3.12) is included in refs. [117, 118].

The two terms in eq. (3.11) are associated to either the Stokes or anti-Stokes component of the Raman scattering. For Stokes Raman scattering w_{fm} is positive, i.e. $E_f > E_m$. On the contrary, for anti-Stokes Raman scattering w_{fm} is negative and $E_f < E_m$. Note that it is assumed that the energy of the incident photon is sufficient to induce the transition between the states $|m\rangle$ and $|f\rangle$. In order to quantify the intensity of the inelastically scattered radiation the correspondence principle is used following ref. [117]. Such principle states that atoms and molecules emit radiation as a set of oscillators. In the case of inelastic scattering these oscillators correspond to the two terms from eq. (3.11). The total radiation emitted per second by an oscillator of the form of the terms in eq. (3.11) with a natural frequency $(w_{mf} \pm w)$ over all solid angles is [117]:

$$\frac{dE^{\pm}}{dt} = \frac{4}{3c^3}(w_{mf} \pm w)^4 \mid M^{\pm} \mid^2 \tag{3.13}$$

where c is the speed of light in vacuum. The expressions calculated until now have neglected the population of the final state N_f and initial state N_m of the photoilluminated molecule. However, the absolute intensities of the scattered radiation depend on the number of atoms in the initial or final states of the molecule. If the subindices m and f correspond to the lower and excited energy states of the molecule respectively, the absolute intensity of the Stokes scattered radiation can be expressed as [117]:

$$I_s = N_m \frac{4}{3c^3}(w_{mf} - w)^4 \mid M^{-} \mid^2 \tag{3.14}$$

In analogy, the intensity of the anti-Stokes scattered radiation is:

$$I_a = N_f \frac{4}{3c^3}(w_{mf} + w)^4 \mid M^{+} \mid^2 \tag{3.15}$$

Therefore, for the transition between the same two energy levels the intensity of the Stokes lines are higher as the lower energy state of the molecule is more populated at normal conditions than the excited states. From eq. (3.14) the intensity of the Stokes line I_s for any particular vibrational transition between two states of the molecule (and by analogy for the anti-Stokes line) can be deduced. Note that $\mid M^{\pm} \mid^2$ can be expressed in terms of the polarisability tensor $\tilde{\alpha}$. Again, a detailed

calculation is not the focus of this thesis and can be seen in ref. [114], where I_s is expressed as:

$$I_s \propto N_m I_0 (w_{mf} - w)^4 \sum_{jl} \mid (\alpha_{jl})_{mf} \mid^2 \tag{3.16}$$

I_0 is the average of the Poynting vector $\mathbf{S}$ of the incident light mathematically defined as $\mathbf{S} = \frac{1}{\mu_0}\mathbf{E_0} \times \mathbf{B_0}$. $(w_{mf} - w)$ is the frequency of the scattered light, which depends on the laser frequency w and on the frequency w_{mf} of the molecular transition corresponding to a vibrational or rotational Raman process. α_{jl} are the components of the polarisability tensor and the subindices m and f refer to the initial and final states respectively. Expression (3.16) depends on the incident radiation and on the occupation of the energy states. It is convenient to introduce a new magnitude which is independent of these parameters. The Raman cross-section is defined as

$$\sigma_{Stokes} = \frac{I_{Stokes}}{I_0 N_m} \tag{3.17}$$

Expression (3.16) shows the dependence of the Raman intensities to the 4th power of the frequency of the incident laser light (and to the wavenumber or inverse of the laser wavelength, λ^{-1}). This dependence is also verified for the Raman cross-sections.

3.1.2 The Raman micro-spectroscopic system

Once the theory of Raman scattering has been covered, relevant background on the components integrating the Raman spectroscopic instrument is introduced. This theory is important for the instrumental development chapter (see Chapter 6) as well as for a better understanding of the experiments performed with the Raman micro-spectroscopic systems in Chapters 5-7. A Raman micro-spectrometer allows the collection of Raman spectra of microscopic samples with the help of a coupled optical microscope. A simplified instrument consists of an excitation source (a laser), a spectrograph (an interferometer or a dispersive instrument), detector, and an optical microscope.

Excitation laser

The introduction of lasers as excitation sources for Raman spectroscopy started in the early sixties, and the first instrument was reported by Porto and Wood [119]. The main advantages of lasers over conventional light sources, such as mercury lamps are the higher power density and spectral resolution [120]. Since Raman scattering cross-sections are very low, typically from 10^{-30} to 10^{-25}

$cm^2 molecule^{-1}$ [121], a high-intensity excitation source is desired. In order to choose a suitable source several parameters of the laser should be considered, e.g power and excitation wavelength.

- Laser power
  The intensity of the Raman signal is directly proportional to the power of the laser and thus higher laser powers might be advantageous. However, an excessive laser power might damage the sample under study. Special care must be taken with biological samples such as human tissue. In Raman micro-spectroscopy it is important to consider the laser power density at the sample, as the laser is focused on the sample by a microscope objective. While in point-scanning laser illumination mode all the beam is focused in a small spot of 500 nm to 1 μm of diameter in wide-field illumination the laser spot is spread over larger areas, resulting in a lower power density for the same laser power.

- Wavelength
  Near infrared (NIR) lasers present several advantages over visible ones:

  1. Reduced excitation of fluorescence, especially important for skin tissue samples. The use of visible lasers produces strong fluorescence emission from collagen I, which is a main component of dermis.
  2. They carry less energy than visible lasers. A higher wavelength λ implies less probability of damaging the sample.

  In contrast, the main advantages of visible lasers over NIR are:

  1. The intensity of the Raman signal is larger when the laser wavelength λ is smaller as the intensity of the Raman scattering is inversely proportional to λ^4.
  2. Technology more accessible for visible wavelengths (especially in terms of detectors and microscope objectives).

Optical microscope

In Raman micro-spectroscopy a microscope collects the signal with a high spatial resolution. Inverted microscopes are preferred for biological samples as they allow the specimen to be observed in aqueous solutions. In order to choose the right microscope objective some parameters have to be taken into consideration: field of view, magnification, working distance, and numerical aperture.
Magnification: Optical magnification is the ratio between the apparent size of

an object (or its size in the image plane) and its true size. High magnification objectives such as 50× or 60× are desired for observing micrometer samples.

Field of view: circular area seen with a particular objective. A higher magnification objective will imply a lower field of view and vice versa.

Working distance: distance between the objective front lens and the sample when the specimen is in focus. In most cases the working distance of an objective decreases as magnification increases.

Numerical aperture (NA): parameter used to describe the light gathering capability of the objective. Roughly, it imposes the limit of detail that the lens can resolve. It is denoted as:

$$NA = n \sin\theta \tag{3.18}$$

where n is the refractive index of the medium between the sample (or sample holder) and the objective front lens, and θ is the half of the angular aperture. The angular aperture is the maximum angle of the cone of light that the objective front lens can capture from the sample at its focal plane to form an image. As shown in eq. (3.18) the NA depends directly on the refractive index in which the light propagates. Consequently, if the gap between the objective and the sample is filled with a medium with a higher refractive index than air, such as water ($n = 1.33$), oil ($n = 1.51$) or glycerine ($n = 1.47$), the NA will increase. The NA of an objective

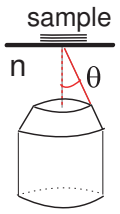

Figure 3.2: The numerical aperture of the microscope objective depends on the half of the angular aperture θ and the refractive index n of the medium between the sample and the objective lens.

is also dependent to a certain degree upon the amount of correction for optical aberrations, in particular spherical and chromatic. Highly corrected objectives tend to have much larger NAs for the respective magnification [122].

Resolution: In Raman spectroscopy resolution can refer to spatial or spectral resolution. Spatial resolution is the smallest distance between two points of the sample to be distinguished as separate entities. It includes transversal resolution in the XY-plane and axial resolution in Z or optical path direction, also known as effective height H_{eff} of the scattering volume. The parameters contributing to the transversal spatial resolution are the diameter of the laser spot and the microscope resolution. Three factors determine microscope resolution: light wavelength, acceptance angle (determined by the size of the lens, the larger the better, and the focal length, the shorter the better), and the optical refractive index of the media.

Using Abbe's criterion of resolution the transversal resolution of the microscope $R_{microscope}$ is

$$R_{microscope} = 0.61\frac{\lambda}{NA} \tag{3.19}$$

Considering λ the wavelength of the laser (e.g. 532 nm and 785 nm) for a NA of 0.75-1.2 the microscope resolution of the ideal system would be approximately 0.3 μm - 0.4 μm. These magnitudes are smaller than the approximately 500 nm of diameter of the laser spot. Spectral resolution is determined by the spectrograph and not by the microscope.

Spectrometer

The ideal spectrometer will allow maximum optical throughput and optimal spectral resolution. The throughput describes the capability of an optical system to transmit radiation. Throughput optimisation depends on the ability of F-number matching between the source and the spectrograph as well as on the efficiency of the optical elements. In real instruments maximum light collection has to reach a compromise with image fidelity. An increase in the NA implies that marginal rays with higher acceptance angle are collected, increasing spherical aberration. Chromatic aberration would also appear in the real instrument as the Raman light is polychromatic. Two types of spectrographs are considered in this thesis, a dispersive system of the Czerny-Turner type and a Michelson interferometer. Note that the terms spectrograph and spectrometer are sometimes used as synonyms, although strictly a spectrometer is the ensemble spectrograph-detector. Briefly, the principles of operation of the dispersive Czerny-Turner system and a basic Michelson interferometric model will be introduced.

- **Czerny-Turner dispersive spectrometer**.
  Dispersive spectrometers are optical systems designed to spectrally separate and detect an input beam of polychromatic light. Different mechanisms can be used to separate the incident photons depending on their wavelengths. A common method is to introduce a diffraction grating into the optical light path. Collimated photons of different wavelengths will exit the grating with different angles. This is the fundamental principle of a Czerny-Turner system. In the latter a lens at the entrance of the spectrometer focuses the incident beam into the plane of a slit. Also two concave mirrors in an off-axis configuration are needed, one to collimate the beam and direct it towards the grating, and the other to collect the spectrally separated photons and focus them on the detector of the spectrometer. For spectra acquisition, if the detector is a charged coupled device (CCD), each one of the horizontal

pixels of the CCD chip acts as a spectral channel. The angle of diffraction of the photons exiting the grating depends on their wavelengths, and therefore, photons with different wavelengths would reach different pixels of the CCD chip. Photons reaching a specific spectral channel for a certain acquisition time add up. Thus, the magnitudes measured to form a spectrum are the number of photons (or counts) per spectral channel. A representation of the Czerny-Turner dispersive spectrometer is shown in Figure 3.3.

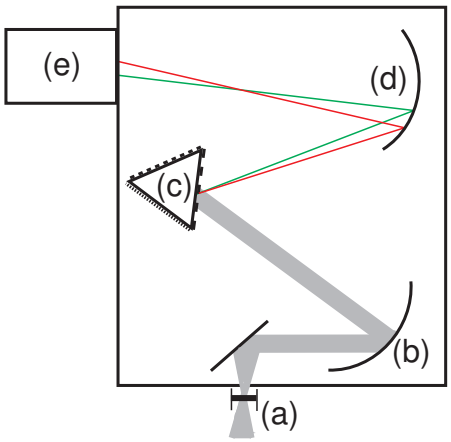

Figure 3.3: Simplified Czerny-Turner spectrometer. (a) Entrance slit. (b) Collimating mirror. (c) Diffraction grating (three different interchangeable gratings). (d) Focusing mirror. (e) Detector.

- **Michelson-interferometric spectrometer**

  A Michelson spectrometer is a device which measures optical spectra by calculating the Fourier transforms of the interference signals detected at the exit of a classical two-beam scanning Michelson interferometer. As for any other interferometer, Michelson's design allows phase measurements by encoding phase information into intensity variations.

  A schematic of the interferometer, first conceived by Michelson in 1891 [123], is shown in Figure 3.4. Optical path length differences between the light beams travelling along the two arms of the interferometer introduce a relative phase difference or retardation between the travelling waves. By mechanical translation of the movable mirror $M2$ along the optical axis (see Figure 3.4) an interference signal is generated. Mirror scanning can be done at a constant velocity (continuous scan-interferometry) or by sequential intermittent displacements of the mirror (step-scanning interferometry). For a detailed description of the physical phenomena occurring in the interferometer see pages 35-40 of ref. [124], or refs. [125] and [126]. For polychromatic

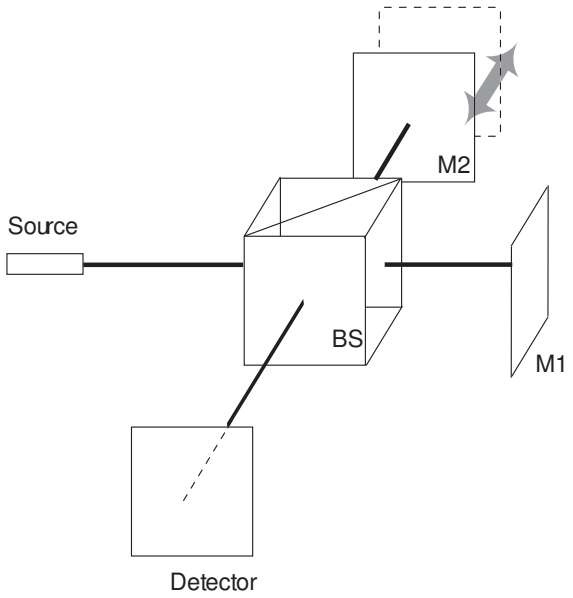

Figure 3.4: Simplified Michelson interferometer. A collimated beam of light generated by the source reaches the ideal beam-splitter labelled as BS (assumed to transmit and reflect 50% of the incoming radiation) and divided into two beams of equal intensity which follow perpendicular paths and are reflected by the orthogonal plane mirrors $M1$ and $M2$, respectively. While $M1$ is a fixed component $M2$ can be translated along the optical axis. The beams recombine at the beam-splitter and are projected onto the detector plane, where the interferogram is recorded. Note that the beam-splitter is a cube to avoid the need for a compensator plate.

light (such as the Raman signal), the irradiance of the interference term is

$$I\left(\Delta\right) \propto 2\int_0^\infty I\left(\sigma\right)\left(1+\cos\left(2\pi\sigma\Delta\right)\right)d\sigma \tag{3.20}$$

where Δ is the net optical difference between both arms, σ is the wavenumber, and I(σ) is the intensity for each frequency. Therefore,

$$\left(I(\Delta)-\frac{I(0)}{2}\right) \propto 2\int_0^\infty I(\sigma)cos(2\pi\sigma\Delta)d\sigma = 2\mathfrak{F}\left\{I(\sigma)\right\} \tag{3.21}$$

where $\mathfrak{F}\left\{I(\sigma)\right\}$ represents the Fourier transform operation. The detector in AC mode records the time-varying signal or interferogram, being the time coordinate related to the spatial position of the mirror. If the mirror is moving with a constant velocity v the relation between the sampling time and the mirror position x will be linear, $x = vt$. Therefore, the signal associated with $I(\Delta)$ is the magnitude measured. The spectrum can be

recovered by using the inverse Fourier transformation, as shown in eq. 3.22.

$$I(\sigma) \propto \mathfrak{F}^{-1}\left\{I(\Delta) - \frac{I(0)}{2}\right\} \tag{3.22}$$

The constants included in the definitions of the Fourier transform and its inverse follow the notation of ref. [124].

Advantages of FT-Raman spectrometer versus grating spectrometer

1. Fellgett or multiplex advantage.

   Interferometers use one pixel of the detector to record the information from the entire spectral range from a complete scan of the movable mirror. In grating instruments the diffracted light is spanned along one of the directions of the 2D detector chip, photons spatially distributed depending on their wavelengths. Therefore, each pixel of the chip only acquires information from a specific narrow spectral band. If the entire spectrum is to be recorded for a fixed optimal resolution the orientation of the grating can be sequentially tuned with the consequent increase in the acquisition time.

   The multiplex advantage of interferometers versus a grating system will imply a higher signal-to-noise ratio (SNR) in a factor equal to $\sqrt{N_f}$, where N_f is the number of spectral channels [124, 127]. The multiplex advantage assumes noise is independent of the intensity of the signal. This statement is normally satisfied for the IR region, where noise is mainly due to the detector thermal noise, but not in the visible, where the main contribution to noise comes from the photon or shot noise (see section 3.1.2). In these cases the interferometer SNR is not improved in comparison with the grating system by the fact of having contributions from all frequencies at once, as they also increase the noise.

2. Jacquinot or étendue advantage.

   In a lossless or ideal optical system the étendue or thoughput is constant from source to detector [128]. In Michelson's interferometer, the étendue can be expressed as [124],

   $$E_M = A_M \Omega_M \tag{3.23}$$

   where A_M is the effective area of the beam entering the interferometer in the plane perpendicular to the optical axis and Ω_M is the solid angle subtended by the source at the entrance of the interferometer. In terms

of the interferometric parameters,

$$E_M = 2\pi \frac{A_M}{R_M} \tag{3.24}$$

where R_M is the spectral resolution of the Michelson interferometer. In the grating system a lens focuses the input beam into the slit of the spectrometer. The effective source area is the slit area. In contrast, interferometers can be illuminated by large circular sources implying large light-acceptance solid angles and higher throughputs. The Jacquinot advantage is valid in the visible and infrared.

3. Connes advantage

   The use of an internal reference laser in the interferometer gives the system the ability to dynamically adjust the acquired data readings from scan to scan without the need for external calibration. This improves its accuracy and precision and eliminates artefacts coming from spectral shifts.

Disadvantages of FT-Raman spectrometer versus grating spectrometer

- The instrument throughput is limited by the transmittance of the elements forming the interferometer. Moreover, the Jacquinot advantage does not apply to non-ideal systems with big energy losses. Especially important is the optical transmittance of the beam-splitter, which by itself imposes a theoretical maximum of 50% throughput [129].
- Multiplex disadvantage: noise generated by a specific Raman or Rayleigh line is distributed over the whole spectrum. This problem can be overcome by adding filters [129].
- Using a laser as an internal reference for the system implies that potential inaccuracies in the laser path may lead to linear shifts in Raman spectral peaks [129].
- FT systems are vibration sensitive [129]. Therefore, the use of an environmental isolation platform is recommended, especially for optical and floor vibration isolation [130].

Detection system

The final element of the Raman micro-spectroscopic instrument is the photodetector. For accurate interpretation of the results measured by the detector it

is necessary to discriminate between the real Raman signal and the noise artificially introduced by this component. The main types of noise introduced by the photodetector are listed below.

- Thermal (Johnson's or dark noise): thermally-induced spontaneous electron generation and migration in the detector not associated with incident photons.

$$N_{thermal} = \sqrt{C\tau} \tag{3.25}$$

  where C is the rate of spontaneous electron creation per second and τ is the integration time. The product of C and τ is known as the dark current of the detector. Cooled detectors will have a lower dark current and thus lower thermal noise [131].

- Shot or photon noise: statistical noise arising from inherent uncertainty in counting the incoming photons [131].

$$N_{shot} = S^{\frac{1}{2}} \tag{3.26}$$

  where S is the incoming photon signal.

- Readout noise: noise generated by the on-chip amplifier. In the CCD, when measuring the voltage induced by the photoelectrons generated in the chip, random fluctuations appear. The higher the readout speed the greater the readout noise.

In this thesis the performace of a photodetector is studied in terms of several parameters such as responsivity, quantum efficiency, and signal-to-noise ratio.

- Responsivity: sensitivity of the detector to radiant energy. Mathematically, ratio of the detector output current (root square of the output intensity in amperes) to the light input (incident radiation power in W).

- Dark current: electrical output of a detector in the absence of input [132].

- Noise equivalent power (NEP): minimum input optical power (in W) to generate a photocurrent [133]. In this case, the output power is identical to the noise power, and the signal-to-noise ratio equals 1. Reciprocal magnitude to the NEP is the spectral detectivity D^*, which in contrast to NEP does not depend on the area of the detector.

$$D^* = \frac{A_d.B^{\frac{1}{2}}}{NEP} \tag{3.27}$$

where D^* is the spectral detectivity and has units of $(\text{cm})(\text{Hz})^{\frac{1}{2}}\text{W}^{-1}$, A_d the area of the photodetector in cm^2, B the bandwidth of the measuring system in Hz, and NEP the noise equivalent power in W.

- Quantum efficiency: ratio between the number of photoelectrons generated by the incident photons and the actual number of incoming photons. It is normally expressed as a percentage. It depends on the wavelength of the incident photons. It could be interpreted as the probability of an incident photon of a certain wavelength to produce a photoelectron in the sensor of the detector.

- Signal-to-noise ratio (SNR): ratio between the signal S and the total noise of the detector. Assuming that the main noise contributions come from the thermal, shot, and readout noises of the photodetector SNR can be expressed as

$$SNR = \frac{S}{\sqrt{{N_{thermal}}^2 + {N_{shot}}^2 + {N_{readout}}^2}} \tag{3.28}$$

Many detectors have been used in Raman spectroscopic instruments depending on the applications. High-sensitivity fast unidimensional detectors are the most common option for interferometric systems [130] while in dispersive instruments, 2D detectors such as charged coupled devices (CCDs) are usually preferred. In parallel to CCDs, CMOS sensors might be a suitable approach for specific applications. CCD and CMOS technologies are two different approaches to fast photon detection, both consisting on 2D arrays of photosensors overcoming photon-to-electron conversion by metal oxide semiconductor (MOS) technology. A photon striking the sensor would generate a photoelectron which is stored into a capacitor. Charge storage, transfer, and current-to-voltage conversion are controlled by inbuilt electronics in a different way in CCDs and CMOS cameras. While in a CMOS sensor each pixel has its own charge-to-voltage conversion circuit, in CCDs information from a row of pixels is simultaneously transferred through the device until it reaches the register, where each pixel is readout sequentially and converted to voltage. The latter readout architecture reaches a higher uniformity in signal conversion. CMOS sensors can be formed by pixels with a much smaller area, which facilitates digital integration, reduces power dissipation, and increases readout speed and performance responsivity [134]. In the past, CMOS technology was not compatible with single-photon detection in contrast to some models of ultrasensitive CCDs such as electron-multiplier CCDs (EMCCD). In the last few years, a new generation of electro-bombarded CMOS (EBCMOS) has been developed, reaching single photon-sensitivity [135]. Nevertheless, studies incorporating

EBCMOS to Raman spectroscopic instruments have not been published yet, to the author's knowledge.

3.2 Raman spectral imaging

Raman spectral imaging combines Raman spectroscopy with digital imaging technology in order to measure maps or images with spatially resolved molecular information. Therefore, by obtaining Raman spectra from different regions of a heterogeneous sample an image can be produced, revealing not only the spatial distribution of molecules within the sample but also structural information such as the degree of order, the strain or the polytypes present [136].

Since 1975, when the concept of Raman spectral imaging was first introduced by Delhaye and Dhamelincourt [137] there have been many studies aimed at producing Raman images of biological samples [138, 139]. Different Raman imaging methods include different types of sample illumination and detection [129]. Referring to sample illumination there are two common approaches: raster scanning and wide-field Raman spectroscopy.

Usually, both techniques rely on CCDs. One of the main disadvantages of the current Raman spectral imaging methods is their limitation to record information in two channels or two dimensions, as Raman spectral imaging involves three variables: two spatial dimensions (X and Y) related to the position (x_i, y_i) of any point within the sample plus an extra dimension related to the Raman shift (or alternatively the frequency of the inelastic scattered radiation) necessary to record the Raman spectra at each (x_i, y_i) point. This drawback can be overcome by fixing one degree of freedom in the system. For example, in wide-field Raman spectroscopy the two directions of the CCD sensor record the spatial dimensions X and Y of each position (x_i, y_i) but the frequency is fixed by an optical filter.

Apart from illumination sources and detectors, it is also important to consider the dimensions of the sample under study. Samples over 1 cm or below 200 nm would require techniques such as Raman macro-spectroscopy [140] or near-field [141], respectively, and their study is beyond the scope of this thesis.

The majority of studies reported in Raman mapping illuminate the sample by scanning a laser focused on its surface along one or two different spatial directions or otherwise by scanning the sample at a fixed laser position. Raman spectra or interferograms are collected, depending if the spectrometer follows a dispersive or interferometric approach. In the former Raman light is frequency dispersed by a grating spectrograph. Photons of different frequencies will emerge with different

angles, reaching different positions along one of the dimensions of the CCD sensor. For grating spectrographs the CCD will record the number of photons arriving (intensity) for each CCD pixel (corresponding to a specific frequency shift).

The dispersive spectrograph can be replaced by an interferometer using Fourier transform (FT) Raman spectroscopy. In order to cover the main Raman spectral imaging approaches, an introduction to point, line, and rapid line scanning as examples of raster scanning imaging, followed by an introduction to wide-field illumination are included in the next section.

3.2.1 Point scanning

In point scanning, also known as *point-by-point* scanning, a laser is initially focused on a point (x_0, y_0) of the sample surface by a microscope objective. The Raman signal is focused on the slit of a grating spectrograph or, alternatively, on the entrance of an interferometer. Therefore, for each point (x_0, y_0) of a sample a single spectrum or interferogram is acquired. Spectral imaging is achieved by scanning the laser (or alternatively scanning the sample with the laser fixed) sequentially along the two spatial dimensions X and Y of the sample surface.

One of the main limitations of point mapping is the long time required to collect the large number of spectra/interferograms to reproduce the whole area of the sample under study. If samples are not strong Raman scatterers, as it is the case for many biological samples such as tissues, acquisition times required per spectrum/interferogram might be of the order of 1-30 s depending on the tissue type or even as long as 120 s when measuring single cells [6]. Imaging tissue areas of 500 μm $\times$ 500 μm at step size of 5 μm with such integration times requires the total number of 10,000 Raman spectra which takes around 6 hours [142]. In order to reduce total mapping times alternative approaches to point scanning such as line scanning or wide-field illumination are more convenient [143]. Note that the total mapping time of a point mapping experiment is directly proportional to the dimensions of the sample, which can be expressed in terms of the number of pixels N_p of the image [136]. In addition to being a time-consuming process, point-by-point scanning presents further disadvantages such as a higher probability of sample photo-damage, as the whole laser beam is focused on a tight region of the sample.

Despite the described disadvantages, point scanning allows capture of the whole Raman spectrum and not a band of frequencies, which might be an advantage for specimens where the chemical information is spread over the entire spectrum [136] or consist of highly overlapped bands.

3.2.2 Line scanning

This technique is an extension of point scanning where the sample is illuminated line by line instead of point by point. It normally implies a dispersive spectrometer and a CCD. In Raman line mapping the laser beam used to raster the sample is expanded in one of the spatial dimensions, e.g. X, using cylindrical lenses or scanning mechanisms while the diameter of the laser spot in the other spatial dimension, Y, stays unaltered. The sample is scanned only in the Y direction ensuring that the slit of the dispersive spectrometer is parallel to X. A spectrum is collected at each position y_i. For each position y_i the CCD detector records the position x_i of the sample in one dimension, and in the other direction the Raman shift. The total mapping time of the experiment is therefore reduced in comparison with point scanning by a factor of $\frac{1}{\sqrt{N_p}}$, where N_p refers again to the number of image pixels [136]. This time improvement is only valid if for an acquisition time t similar to point measurement a comparable SNR in the Raman spectra can be achieved. This would require a $\sqrt{N_p}$ higher power laser or a factor to correct the point mapping times.

One disadvantage of line mapping resides in the fact that the laser intensity along the elliptical spot follows a Gaussian distribution. This leads to different values of SNR for spectra coming from different regions within the elliptical spot (larger laser intensity differences along the major axis of the elliptical spot between the edges and the centre) [6].

3.2.3 Rapid line scanning

In the last decade there have been improvements in line mapping in order to reduce the time of line scanning without losing spatial resolution. For example, Renishaw plc. (Gloucester, UK) has developed a system (StreamLine Plus) in which the elliptical laser line is scanned pixel by pixel along the X direction (parallel to the longer radius of the elliptical laser line) and after the former laser line edge has been located in every x_i -position within the whole line, the stage moves one step in the Y direction. Each spectrum corresponding to a x_i-position is calculated after the laser has been rastered all along X with each one of the different regions of its Gaussian intensity profile. Thus, the SNR variation due to laser intensity profile is eliminated.

CCD readout is performed constantly and occurs simultaneously to sample illumination, light collection, and movement of the microscope stage. Also opening and closing of the shutter detector takes place only once in these systems at the beginning and end of the experiment.

As the laser beam is spread along the X direction (as in conventional line mapping), at the same laser powers than point mapping a lower signal is collected. This trade-off can turn to an advantage in samples sensitive to photo-damage such as tissues [6,144]. The described system has been reported to require imaging times of 30 to 90 minutes for 2 mm oesophageal biopsies with acquisition times of 0.5 s per spectrum (low SNR spectra) and a step size of 25.3 μm [6]. If such measurements imply approximately the acquisition of 6400 spectra, the total acquisition time for an equivalent point mapping experiment may be estimated as approximately 2 h, considering a delay time due to the stage translation and CCD readout of 1.6 s per spectrum, and including a correction factor with the ratio of the step size and length of the laser line of the rapid line scan [6]. Reliable Raman spectral images were also generated with larger spectral datasets and higher SNRs [6].

3.2.4 Wide-field source illumination

A vast amount of work has also been done using wide-field or global illumination for Raman spectral imaging [136]. This technique uses an expanded beam to illuminate larger, or even the whole area of the sample. A specific Raman spectral band corresponding to a narrow range of frequencies from the total Raman signal is selected by an optical filter. The filtered light is recorded on the 2D detector, in which each dimension corresponds to one of the two spatial dimensions of the sample. The image recorded on the detector is directly related to the sample chemical image without the need for any further analysis or transformation of the acquired data. Despite the intuitive results obtained with this method, only a narrow part of the Raman signal is used each time, so contributions from different structural and chemical groups present in the sample can only be measured sequentially by changing the filters. In addition, this method implies a significant decrease in the already weak Raman signal, which can be translated as a reduction in the SNR ratio. Different filters have been used in different studies, both selecting a fixed or tunable band of wavelengths. Monochromators, dielectric filters, acousto-optics tuning filters or liquid-crystal tuning filters are common examples [136].

In wide-field imaging total mapping time is directly proportional to the number of frequencies or spectral channels N_f contributing to the signal. For instance, using half the number of spectral channels will decrease the imaging time by half, without reducing spatial resolution. Wide-field imaging is generally faster than point or line scanning as the acquisition time is not limited by the number of pixels N_p of the image as long as the number of spectral channels is low ($N_f < N_p$) [143]. Time comparisons between wide-field and the other imaging approaches

included in this thesis assume that the optics delivery and collection efficiencies are identical for each method, the time delay between acquisitions is sufficiently small to be neglected, power density at the sample is comparable between the different experimental configurations, and the image is squared [136] (otherwise, N_p would need to be redefined for each spatial coordinate of the sample image).

Reduced acquisition times of global sample illumination in, for example, single human cell mapping are discussed. Consider that the number of pixels N_p corresponding to the image of the cell is, for example, 150×150 (which may imply scanning over areas of 15 μm$\times$ 15μm with a step size of 0.1 μm for a high image fidelity). Assume that the cell is illuminated with laser light for 2 s at each relative position of the laser-sample scan. Hence, and without considering the time delay in the movement of the step motor mechanism, the point scanning experiment requires 12 h 30 min, the line scanning experiment 5 min, and the global field illumination experiment for 8 spectral channels requires 16 s. No correction factor to account for the differences in power density for the different configurations has been considered in the calculations following ref. [136] (for a discussion about such correction factors see [6]). An increase in the step size or a decrease in the number of pixels of the image reduces the time advantage of global illumination versus the raster techniques. Step sizes of 1 μm are common in experiments aiming to produce Raman images of single cells by point scanning [145, 146]. The total acquisition time depends on the size of the cell. Studies with point scanning have reported acquisition times of around 5 minutes for small single T-cells [145], approximately 10 minutes for medium size lung fibroblasts [146], and greater than 30 minutes for big white blood dendritic cells [145].

Additional parameters that can increase the total experimental time are, for example, the time needed for filter tuning [136]. Wide-field imaging is mainly used when all the molecular information needed to accurately elucidate the different components of the sample is concentrated in a low number of frequency bands and when the background signal and fluorescence emission are very low. It is also preferred when the number of image pixels N_p needed to produce accurate spectral images is large, as total experimental time for this technique is independent of N_p. However, when the chemical/structural information is spread along the whole Raman spectrum it is hard to discriminate between sample components by using this technique.

3.3 Surface enhanced Raman spectroscopy (SERS)

3.3.1 Definition

SERS is a powerful technique in which the optical properties of specific metals such as silver, gold or copper are used to largely amplify the Raman signal of molecules in close proximity to such metals, allowing even single molecule detection. As a first approach to the concepts involved in SERS the terms constituting its acronym are explained. *Surface* refers to the fact that the molecule of interest is adsorbed on a metal surface (or close by in the order of one or a few nanometres). *Enhanced* refers to the amplification of the Raman signal, which can take values up to 10^{10} times larger than for conventional Raman [147]. This enhancement is mainly attributed to plasmon resonances occurring at the surface of the metal, and it is called the electromagnetic enhancement. Surface plasmons are the collective oscillations of free electrons at the metal surface and are excited by the electric field of the incident laser radiation. At resonance the incident laser wavelength matches the wavelength of the local plasmonic electric field in the vicinity of the metal surface. In the quantum mechanical description, Raman spectroscopy is a two photon instantaneous process where the absorbed and emitted photons are intrinsically linked, therefore, all the absorbed photons are emitted "without any going missing" [147]. This absorption does not necessarily imply electronic transitions (this would be the case of resonance Raman -RR-). The "linking" of the absorbed and emitted photons means that an increase in the number of absorbed photons at the laser frequency would produce a greater amount of scattered (emitted) photons and, likewise, an increase in the efficiency or rate of emission of photons at the shifted Raman active frequencies would require more incident photons.

In summary, the Raman signal can be amplified by modifying both the emitted and absorbed photon rate. Quantitatively, the dependence of the Raman signal on the fourth power of the electric field means that an increase in the amplitude of the electric field produces a large amplification of the Raman signal. Finally, the SERS acronym includes the term *Raman spectroscopy* because only the Raman signal or inelastic scattering is measured. The main difference between Raman spectroscopy and SERS is that while the simplest possible Raman scattering process needs electromagnetic radiation and a sample molecule to occur, SERS requires an additional metallic nanostructure close (at a nanoscale level) to the molecule of interest.

3.3.2 Optical properties of metals, local electric field enhancement, and hot spots

Certain metals are particularly interesting because of their optical response to an applied electric field, which can be studied in terms of their dielectric function. Mathematically the dielectric function is a complex function of the form $\epsilon(\lambda) = \epsilon_R(\lambda) + i\epsilon_I(\lambda)$, where λ refers to wavelength. Its real part is the response of a dielectric (electric insulator) to polarisation by an external electric field, while its imaginary part refers to the energy absorption due to the external electric field. An ideal transparent material satisfies $\epsilon_I = 0$. For visible wavelengths the dielectric function of certain metals named "coinage" metals such as silver (Ag) or gold (Au) have in general a large negative real part and a small absorption. This is reflected in Figure 3.5 from ref. [147].

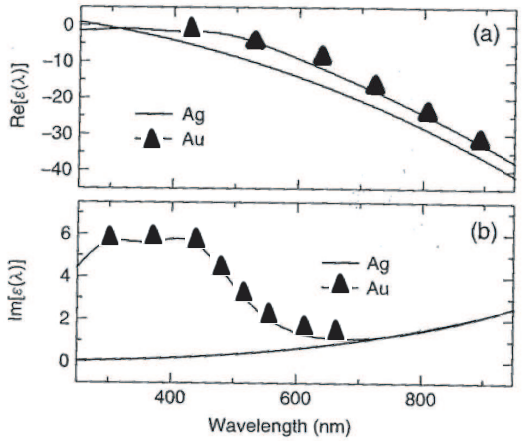

Figure 3.5: Real and imaginary parts of the dielectric function of Ag (solid line) and Au (line plus symbol). Adapted with permission from Wiley-VCH: ref. [147], © (2010).

A density of free electrons can be found at the surface of metals. In the presence of an applied external electric field, collective oscillations of this "plasma" of free electrons referred to as *surface plasmons* can be excited. Surface plasmons generate a local electric field depending on the geometry of the surface and the nature of the metal. A dimensionless factor which allows the quantification of the magnitude of this local plasmonic electric field with respect to the total electric field is here introduced. The local field intensity enhancement factor (LFIEF) is defined as

$$LFIEF = \frac{|E(r,\lambda)|^2}{|E_{ext}(r,\lambda)|^2} \tag{3.29}$$

where $|E(r,\lambda)|^2$is the intensity of the total electric field at a point A at (or close by) the metal surface, r is the distance from A to the origin of coordinates (at the

surface of the metal), $|E_{ext}(r,\lambda)|^2$ is the intensity of the applied electric field of the incident radiation at the same point A, and λ refers to wavelength. The spectral dependence of LFIEF for spherical nanoparticles of silver and gold is shown in Figure 3.6 [147].

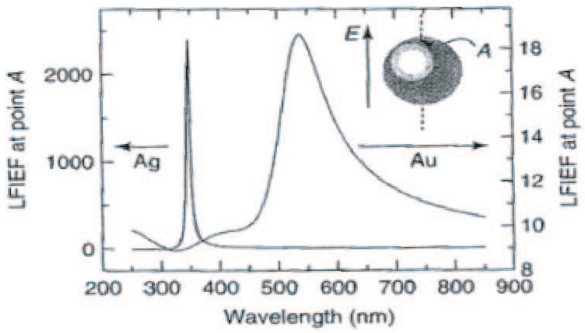

Figure 3.6: Local field intensity enhancement factor spectral dependence for a spherical metallic nanoparticle at the point A of its surface. The diameter a of the sphere is small compared to the wavelength, $a \approx$10 nm. Reprinted with permission from ref. [147] © (2010) Wiley-VCH .

If the electromagnetic radiation emitted by the illumination source is quasimonochromatic, as in the case of a laser, the situation of resonance occurs when the laser wavelength matches the maximum of the LFIEF. Note that the geometry of the metallic surface plays a key role in the solution of the local electric field. Figure 3.6 corresponds to the case of a spherical metal nanoparticle. If the surface under consideration is a planar metallic interface and the direction of propagation of the radiation is perpendicular to the surface, the solution of the local electric field at A would generate a LFIEF below one. This implies no enhancement but quenching. High amplitudes of the electric field would translate into even greater Raman signals due to the previously mentioned dependence of the Raman signal to the 4^{th} power of the amplitude of the electric field. In general, the enhancement only occurs for a rough surface, with features of nanometer dimensions. This electromagnetic enhancement depends on the geometry of the surface. The higher enhancement detected at sharp ends is attributed to the local concentration of electric fields. This effect is named the "lightning rod effect" [148].

The regions of higher enhancement are called *hot spots*. Hot spots do not have to be at the surface of a nanostructure, they can also be located in the gaps between nanostructures if the interestructural distances are of the order of nanometres. In the latter situation coupled plasmon resonance phenomena take place. Control of the field enhancement can be performed by tuning the laser wavelength or by optimising the design of the nano-featured substrates. For example, visible (green) lasers match generally better with the maximum of LFIEF of Ag substrates [149].

The discussion on SERS until now has considered exclusively the electromagnetic enhancement. Only the geometry and nature of the plasmonic substrate contribute to the electromagnetic enhancement. In the real experiment there is an interaction between the ad-molecule and the substrate. The adsorption can be physical or chemical, i.e. "physisorption" or "chemisorption" respectively. Physisorption is weak and it is dominated by Van der Waals forces. When the laser excites the chemisorbed molecules charge transfers can take place. Charge transfer is the excitation of electrons from the Fermi energy level of the metal to the lowest unoccupied molecular orbital energy level (LUMO) of the complex molecule-metal. If the photons from the laser excite the free electrons of the Fermi level with an energy corresponding to a transition between electronic levels of the new ad-complex, the charge transfer corresponds to a resonance Raman process.

3.3.3 Controversial aspects about SERS

Normally in SERS experiments the occurrence of resonance Raman (RR) phenomena is not desirable. When the energies of the absorbed photons are high enough for transitions between electronic levels to take place other processes more efficient for the visible than Raman scattering (e.g. fluorescence) also occur. This is the case in dye molecules such as rhodamine (RG6) or crystal violet. Their high cross-sections make them easier to be detected with Raman spectroscopy, and consequently, these molecules are common probes in SERS investigations. Nevertheless, care has to be taken on the regime in which the experiments with dye molecules are set-up, in terms of the spectral range and the distance between the plasmonic substrate and the molecule. For visible wavelengths, fluorescence is more efficient than Raman, so Raman spectra of fluorescent probes are in general masked by the fluorescence background. However, if the metal plasmonic substrate is in close proximity to the molecule in a maximum range of a few nanometres, fluorescence is quenched (e.g. the rate of non-radiative emission to radiative emission is highly increased) and SERS dominates. This allows SERS fingerprints of dyes to be distinguished from fluorescence emission. RR events remain a problem for the accurate calculation of conventional Raman cross-sections. These non-SERS cross-sections are needed in the normalisation of the enhancement factors used in SERS [150]. Also laser powers of the magnitude used in RR can lead to photodamage or photobleaching of the probe molecule: photodissociation, photoreactions and photodesorption [151]. Photobleaching implies the destruction or damage of the probe molecule due to exposure to high laser powers. To avoid irreversible alterations of the sample under study the perturbation to the system has to be minimal, to the cost of obtaining weak Raman signals. This might be a

problem when working with biological samples which are in general weak Raman scatterers. Note that larger perturbations can lead to structural changes in the probe [149].

Even at low laser powers, laser interaction with the adsorbate could lead to heating and damage of the samples, adsorbate transformations under the catalytic effect of metal nanoparticles and/or in the presence of oxygen and de-adsorbation of the molecule from the surface drastically decreasing its SERS signal. An example is the laser-induced deterioration of organic molecules in the presence of silver to produce carbonaceous species, especially in an oxygen atmosphere [149, 151]. These carbon products would have their own contribution to the spectra (the so-called "cathedral peaks") [151]. This questions the non-invasivity and innocuity of the SERS technique depending on the specific application. Therefore, fine substrate fabrication to produce higher LFIEFs rather than high laser powers should be used to maximise sensitivity. The ability of SERS to detect single molecules can also turn to a problem in terms of its vulnerability to sample/system contamination. This might contribute to the acquisition of erratic irreproducible SERS spectra of difficult interpretation. Phenomena such as "blinking", sudden sharp changes in the intensity of the Raman spectral peaks have recently been reported but their origin is not fully understood [152, 153].

In SERS, enhancement factors (EFs) of the order of up to 10^{14} have been reported. However, these results have been criticised and attributed to miscalculations of the Raman (non-SERS) cross-sections used for normalisation [154–157]. In the past, such high EFs generated the revision of the electromagnetic theory behind SERS, as these numbers could not be explained by the electromagnetic phenomenon alone. This lead to the idea of the existence of the chemical enhancement, independently contributing to the EF magnitude [147]. Although the chemical enhancement is qualitatively important (as the adsorption of the molecule on the metal surface may modify the intrinsic nature of the adsorbate), it does not have a large weight in the final EF values. Chemical enhancement can only contribute to the total EFs a maximum factor of the order of 10 [147]. Therefore, electromagnetic enhancement is the main mechanism in SERS calculations [154] and the only one considered in this thesis.

3.4 Atomic force microscopy (AFM)

3.4.1 Definition

The atomic force microscope (AFM) belongs to the family of scanning probe microscopes. AFM is a generalised technique for studying the morphology and mechanical properties of surfaces with high spatial resolution. AFM has been proven to successfully resolve atomic and submolecular features of various samples [98]. The basic principle of AFM consists of "sensing" surface features by measuring the forces between a sharp probe (ideally ended in a single atom) and the surface of the sample. Depending on the mode of operation, the physical principles can be described in a slightly different way. At the heart of the instrument is a cantilever, oscillating at a certain frequency ω either on or near resonant frequency ω_0 (dynamic AFM). The cantilever ends in a sharp tip which is vertically approached to the sample until the forces between the tip and the surface are detected. This thesis mainly includes results obtained by operating the AFM in amplitude modulation mode. The effect of the new forces in the system is to shift the resonance frequency to a new value ω_0' while the cantilever is still excited at the same frequency ω.

The mechanism for force detection includes a laser, a photodiode detector quadrant, and a 3D piezoelectric system. The laser is directed towards the back side of the cantilever (which is not facing the sample). The reflected signal is recorded on the photodiode quadrant. Depending on the angle of reflection the laser spot on the detection system will spatially cover a different region of each quadrant. Intensity changes are quantified and transformed into voltages that control a piezoelectric crystal. Mechanical changes in the piezoelectric dimensions enable the movement of the cantilever. In summary, the laser follows the deflection of the cantilever due to the tip-sample interaction forces, its position being tracked continuously and rectified with the piezoelectric system in order to keep the magnitude of the amplitude constant. Note that alternatively the sample can be scanned at a fixed tip position. This is the chosen mode in the experiments presented in this thesis in order to align the AFM tip with the external laser used to produce Raman scattering.

The forces sensed by the AFM also depend on the medium in which both, probe and sample are immersed. For biological samples liquid environments are of common use in order to mimic the physiological nature-like conditions. The control of parameters such as temperature, pH, and ionic concentrations are of extreme relevance in these media.

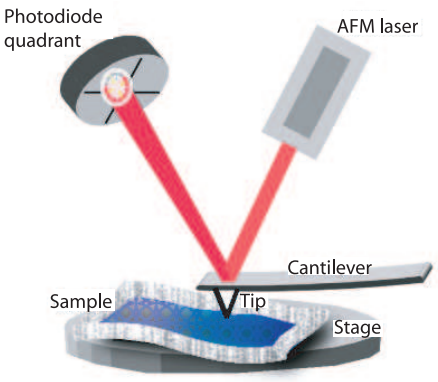

Figure 3.7: Basic components of the AFM instrument.

The nature of the forces being detected by the probe fall mainly into five categories: coulombic, double layer, van der Waals, capillary, and adhesive forces [158]. If coulombic forces are present in the system they tend to dominate over the other four categories. They appear as a result of the presence of a permanent density of charges of opposite or identical sign at the tip and at the surface [159]. If these interactions are to be suppressed, the introduction of an ionic medium which enables charge screening is convenient. Coulomb interactions between a negatively charged surface and, for example, a negatively charged silicon probe need to be screened to improve imaging. Addition of salts with bivalent cations to the medium is a possible solution. The interactions between the ionic charges present in the aqueous medium and the substrate surface charges are double layer forces.

Van der Waals forces are weaker than coulombic and capillary forces but play an important role when the others are not present. They appear between all molecules or atoms [159]. The main contribution to Van der Waals forces is caused by the electric interaction among instantaneous non-permanent oscillating dipoles (rigorously, multipoles) induced in the medium. From a macroscopic point of view the interactions are not among atoms or molecules but between surfaces. The spatial charge separations between the centres of the positive and negative density of charges appear both at the surface of the probe and the sample.

Capillary forces produce an adhesion effect on the tip-surface assembly. The relevance of capillary forces is higher for delicate samples such as biological specimens, in which case the sample can be moved during the measurement or in the worst case damaged [158]. Capillary forces can be eliminated by changing the medium for a low humidity environment (such as dry nitrogen or vacuum), a liquid medium [159] or by replacing contact mode in air for tapping mode [158]. When using AFM in water solutions there is also an additional contribution from the hydrophobic meniscus force. If the sample surface is formed by hydrophobic hydrocarbon tails (e.g. monolayer of phospholipids with their tails sticking out) after

the tip has come into contact with the sample, the hydrocarbon tails form a meniscus that produces strong adhesion forces [159]. Other types of adhesion forces are detected normally when the probe is penetrating the sample. This is the case when performing force spectroscopy measurements or if applying high forces to soft samples.

3.4.2 Operational modes

Contact versus tapping mode

The two main operational modes used in this work to obtain topographic images of the surface of a sample are contact and tapping mode. In contact mode the tip touches the surface of the sample while the scan is performed. In tapping mode the cantilever is dynamically oscillating and ongoing periodic cycles of instantaneous contact to non-contact regimes at each position of the XY scan. Contact mode is useful to characterise sharp features where large topographic differences are involved, as it allows better tracking of the surface. Using high forces in contact mode might induce irreversible damage or modification of the sample. Even in the low force regime contact mode applies lateral forces to the sample which can contribute to sample modifications or detachment from the substrate [158]. Contact mode performed in air is the ideal platform for capillary forces to rise, which is undesirable. Therefore, tapping mode seems more suitable for the characterisation of lipid films as it cancels the capillary force effect and allows higher forces to be applied without apparent alteration of the sample surface.

AFM imaging in air and liquids

AFM measurements were performed in both liquid and air environments. Liquid media were required to produce hydrated lipid bilayers. The tip and cantilever are normally made of silicon or silicon nitride because of the stiffness of these materials, resistance, suitability for micro-fabrication, and market availability [158]. The lever geometry is also important. V-shaped cantilevers minimise torsional motions of the cantilever while scanning the surface of the sample and is the preferred shape when the main target is imaging. However, some studies on rectangular cantilevers show that their performance is also outstanding in terms of torsion-free characteristics [158]. The sharpness of the tip apex is given by its radius of curvature. The imaged features would be the convolution of the tip and the sample topography.

Force spectroscopy.

In force spectroscopy the vertical movement of the tip (in the Z direction) allows the approach and/or separation of the tip towards/from the sample. This enables the measurement of the interaction between tip and sample (force F) to be recorded as a function of their relative distance D.

To describe the main interactions acting on the system different approximations can be made depending on the mechanical properties of the sample. Consider in first place a regime in which the sample is a non-deformable material (and therefore non-breakable) and there is no loss in the mass of the tip (due to de-attachment of any molecule from the tip). This is the case represented in Figure 3.8 (a). Figure 3.8 (b) corresponds to a deformable material experiencing tip indentation on the sample and breakage when the tip and the sample are in contact. In this system the tip indentation is of the order of the cantilever deflection. The sample is referred to as a "soft material" (e.g. cells or lipids) [160]. In this regime when the tip penetrates the sample the $F - D$ curve presents jumps which break its linear behaviour. These jumps or "break-throughs" are explained in multilamellar lipid stackings by the indentation of the tip breaking the superposed individual bilayers.

The third regime shown in Figure 3.8 (c) corresponds to situations in which the tip jumps out of contact in several steps, likely due to change in the mass of the tip as molecules detach from the tip while the tip is retracted.

Figure 3.8 (b) corresponds to a deformable material neglecting the effect of adhesion forces. In this system the tip indentation is of the order of the cantilever deflection. The sample is referred to as a "soft material" (e.g. cells or lipids) [160]. In this regime when the tip penetrates the sample the $F-D$ curve presents jumps which break its linear behaviour. These jumps or "break-throughs" are explained in multilamellar lipid stackings by the indentation of the tip breaking the superposed individual bilayers. The third regime shown in Figure 3.8 (c) corresponds to situations in which adhesion forces are not neglected. The effect of adhesion forces would contribute to the tip jumping out of contact in several steps.

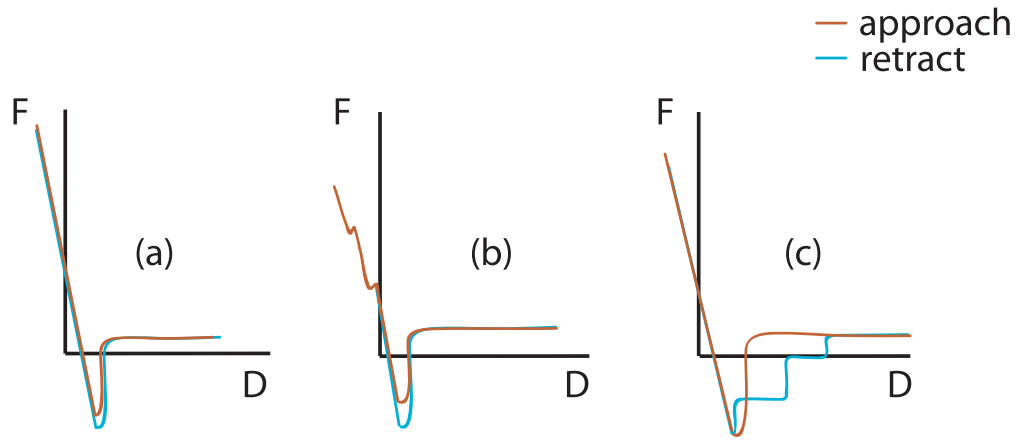

Figure 3.8: Representation of ideal force spectroscopy curves for (a) non-derformable material and tip with constant mass, (b) deformable (breakable) material and tip with constant mass, and (c) deformable (breakable) material and tip with variable mass due to detachment of molecules from the surface of the tip, F and D correspond to the force and tip-sample distance, respectively.

3.5 Supported lipid layer synthesis methods

3.5.1 Langmuir-Blodgett trough

The Langmuir-Blodgett (LB) deposition technique allows lamellar lipid formation on a solid substrate by transferring a monolayer formed at an air-liquid interface to the substrate. It enables accurate control of the thickness and molecular organisation of the deposited material. It is possible to transfer a controlled number of layers of the same or different kind of lipid/lipid mixture on almost any kind of solid substrate [71]. A major disadvantage of LB is its limitation on the maximum number of bilayers and monolayers of a multilamellar lipid architecture that can be successfully transferred to the substrate. Other disadvantages that might be considered for future studies is that LB does not allow adding proteins into the lipid bilayer because proteins in the air-water interface are exposed to air and can denature [161]. In this thesis, small amounts (e.g. 20-60 μl) of amphiphiles dissolved in a volatile solvent such as chloroform are deposited on the water-air interface. Once the solvent evaporates, the pressure on the molecules is increased by compression. Compression is performed by mechanically reducing the dimensions of the trough and therefore the surface area in which the molecules are spread. By measuring the pressure-area curve (i.e. the P-A *isotherm*) the conditions for formation of a monolayer can be found. Vertical dipping of a substrate on the stabilised monolayer enables transfer of the monolayer to the desired support. When using the Langmuir-Blodgett technique for lipid monolayer deposition either highly hydrophilic or highly hydrophobic substrates are desired. If hydrophobic, the substrate is dipped vertically through the monolayer and the transfer is driven by the hydrophobic interactions between the alkyl chains and

the surface. When hydrophilic, the substrate is withdrawn in upstroke from the subphase through the monolayer and the transfer is produced via hydrophilic interactions between the polar headgroups and the substrate surface. For supported lipid layers to form the electrostatic interaction between the lipid polar heads and the substrate must be more favourable than the interaction between the polar heads and the water. The pH of the subphase and the presence of ions in it can alter the charge distribution of lipids and substrate surfaces, and their interaction [85]. The deposition ratio (DR) is the ratio of the area of film deposited to the change in area at the air/water interface corresponding to the deposition. Perfect deposition will imply DR=1. Low withdrawal speeds facilitate transfer resulting in high DRs [84]. The experiments shown in this thesis correspond to centrosymmetric or Y-type deposition, i.e. deposition of the monolayer on the substrate takes place during either withdrawal and immersion of the substrate.

3.5.2 Lipid vesicle fusion

Liposomes are any kind of lipid bilayer surrounding an aqueous space. They can be classified depending on the number of layers forming their onion-like structure in multilamellar vesicles and unilamellar vesicles (ULV). They can also be classified by size into large or small vesicles, the threshold diameter being approximately 100 nm [162]. The vesicle fusion technique consists of formation of single lipid bilayers on solid substrates by fusion of small ULVs using the surface of a solid substrate as platform. Therefore, the first step of vesicle fusion is the preparation of liposomes. Vesicles are typically prepared by sonication, extrusion, freeze-thawing, or a combination of these, and spreading on the substrate takes place by simply exposing the substrate to the vesicle suspension. The bilayer structure can be equilibrated before transfer to the support and the procedure allows membrane proteins to be incorporated in the membrane. A limitation of vesicle fusion is that the success of the spreading process may depend critically on factors such as the membrane composition, substrate material, concentration of salts, pH, temperature, vesicle size, washing procedure, and more [99]. In addition the maximum number of bilayers that can be stacked by this method is limited, as for the LB technique [81].

3.5.3 Spin coating

Thin layers of lipids self-assemble on a planar substrate by centrifugation of optimal amounts of lipid in a volatile solvent solution. The thickness of the layer is controlled by the speed of rotation and lipid concentration. Spin coating is a

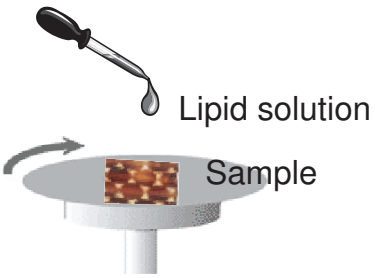

Figure 3.9: Spin coater.

straightforward method for deposition of thin films that allows a uniform coverage [10,99]. One of the key parameters in spin coating is the ability of the solvent to wet the substrate, for which hydrophilicity match of substrate and solvent is required. Hydrophobic substrates such as sapphire, glass, or those covered with metal oxides tend to need a hydrophobic solvent, e.g. chloroform. Hydrophilic substrates such as freshly cleaved mica or piranha cleaned sapphire are expected to work better for hydrophilic solvents, e.g. 2-propanol [163]. In addition, the solvent needs to allow the lipids to dissolve in it. DPPC, cationic DPPC, and AA dissolve well in isopropanol and chloroform as reported in ref. [81]. Note that also the rate of evaporation of the solvent may affect the uniformity of the coverage. For example, solvents with fast evaporation rates such as chloroform may lead to a non-uniform coverage of the substrate.

Chapter 4

Experimental techniques: instruments

This chapter includes a detailed description of the two main instruments used for acqusition of the data in this thesis: the Raman micro-spectroscopic instrument for skin cancer diagnosis and the combined AFM-Raman micro-spectroscopic instrument for measuring lipid layers. Raman spectra from relevant standard bulk compounds such as pure collagen or DNA powder are included. These Raman spectral data allow direct comparison of the Raman and SERS spectra of skin and thin lipid layers obtained in the experimental chapters 5-7 with Raman spectra of pure substances. The analysis of the Raman-active vibrational modes of such spectra and their correspondent spectral peak assignment is included in this chapter as a reference for posterior interpretation of the experimental results.

4.1 Description of the instruments

4.1.1 Raman micro-spectrometer for skin tissue spectral imaging

For spectral imaging of skin tissue samples a Raman micro-spectrometer using an inverted optical microscope and a near-infrared laser was developed (see Figure 4.1) [164]. The inverted microscope (IX71, Olympus, Japan) was equipped with an automated XYZ translation stage (H117, Prior Ltd., UK), a deep-depletion back-illuminated CCD (DU401A-BR-DD, Andor Ltd., UK) and spectrograph (SR-303i, Andor Ltd.), and a 785-nm continuous wave GaAs diode laser (XTRA, Toptica Photonics, Germany). The laser power was set to 50 mW at the

sample to avoid sample damage and ensure repeatable measurements. The objective lens of the microscope had a numerical aperture of 0.75 and a magnification of 50×. A microscopic camera (2-1C Infinity, Lumenera, Canada) was used to record images of the tissue sections.

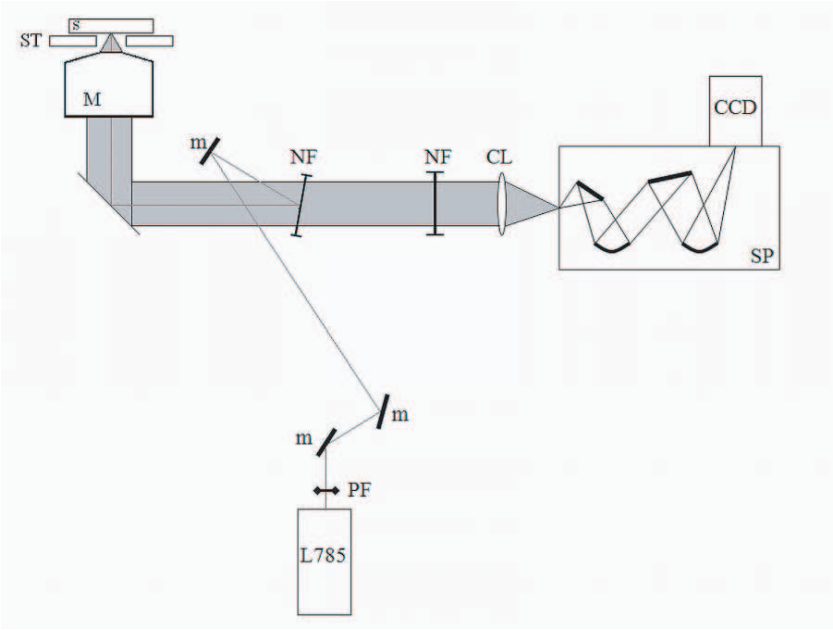

Figure 4.1: Schematic of the Raman micro-spectrometer. L785- laser; PF- plasmaline filter; m-mirror; M-microscope; ST-stage; s-tissue sample; NF- notch filter; CL- collecting lens; SP- Czerny-Turner Spectrograph; CCD- detector. Courtesy of Dr. Zoladek.

4.1.2 Wide-Field Fourier transform Raman spectroscopic imaging instrument

A schematic of the instrument is included in Figure 4.2. A continuous wavelength Nd:YAG (neodymium-doped yttrium aluminium garnet) laser (JPM-X-3, Laser Vision, USA), frequency doubled to emit light of 532 nm-wavelength, was used to irradiate the sample which was placed on a microscope stage (Prior Scientific, UK). The inverted microscope (Diaphot 300, Nikon Corp., Japan) was equipped with a 50× microscope objective of 0.75 numerical aperture (UIS2, Olympus). A microscope digital camera (DCM35, Nikon Corp.) was attached to the microscope. A 45 degree dichroic beamsplitter (RazorEdge, Semrock) was placed on the cube of the microscope, in the optical path. The microscope was coupled to a Michelson interferometer and a low-noise, cooled CCD (DV420-OE, Andor Ltd.). The CCD was connected to a personal computer by a graphics card.

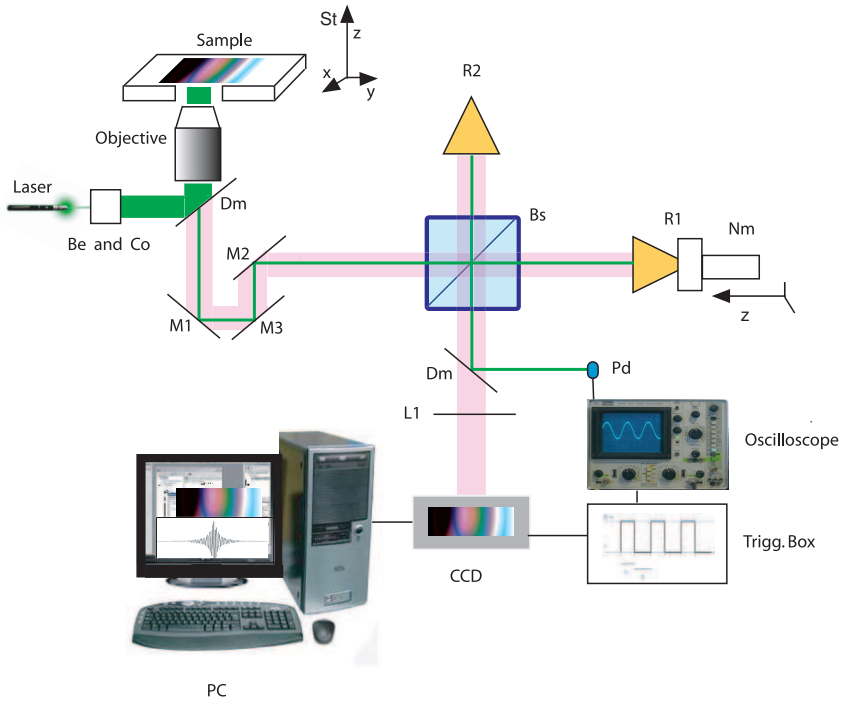

Figure 4.2: Wide-field Fourier-transform (WF-FT) Raman set-up. Abbreviations: Beam expander and collimator (Be and Co), dichroic mirror (Dm), mirrors (M1, M2, M3), lenses(L1, L2), retroreflectors (R1, R2), step-motor (Nm), stage (St), photodiode (Pd), beamsplitter (Bs), triggering box (Trigg. Box), and charged coupled device (CCD).

The beam of light coming from the laser was expanded and collimated in order to illuminate a wide area of the sample in the so-called wide-field sample illumination regime. The diameter of the laser beam on the sample was ≈50 μm.

Interaction between the monochromatic light and the molecules of the sample resulted in elastically (Rayleigh) and inelastically (Raman) scattered light. This combined signal was collected by the microscope objective, the Rayleigh light being blocked by a dichroic beamsplitter. In practice, a weak beam of 532 nm wavelength passed through and travelled along with the Raman light. The collimated beam was reflected in an internal mirror of the microscope (M1), which directed the beam towards the exit port of the microscope. The beam entered the interferometer by reflection in mirrors M2 and M3. These mirrors allowed the collimated beam to be aligned along the optical axis of the interferometer at the correct height and angle.

The Michelson interferometer described in Figure 4.2 used a 50:50 non-polarizing N-BK7 cube beamsplitter (J49-682 Techspec, Edmund Optics, USA). As explained in Chapter 3 in a classical Michelson interferometer two beams of equal intensity named B_1 and B_2 exit the beamsplitter. In this system each one of these beams followed one of the arms of the interferometer, being reflected in either the fixed or moving corner cube retroreflectors (UBBR2.5-1I, Newport, USA). The moving

corner cube retroreflector (labelled $R1$ in Figure 4.2) was attached to a step-motor of 10 nm of spatial resolution and minimum speed of 5000 nms^{-1}(Nanomotion II, Melles Griot, USA).

After exiting the beamsplitter for a second time, B_1 and B_2 passed through a 45 degree dichroic beamsplitter for visible light labelled Dm in Figure 4.2. This component let the Raman signal pass through reflecting the remaining laser light. The Raman light was focused by lens L_1 on a CCD sensor acquiring images for each position of the movable retroreflector R_1. The CCD sensor consisted of 1024×512 26 μm-pixels. Each one of these pixels recorded the total number of Raman photons that reached the surface of the CCD chip for a certain acquisition time at a fixed position of the retrorreflector $R1$. The values of the Raman photon counts, in addition to the position of $R1$, and the spatial coordinates of the pixel within the CCD sensor was the information needed to create Raman spectral images of the sample.

The Rayleigh light reflected by the dichroic beamsplitter was focused by lens L_2 on a silicon pin photodiode (Pd)(S5973-02, Hamamatsu Photonics, Japan). The signal detected on the Pd was the result of the interference between the laser light carried by beams B_1 and B_2. Due to the monochromatic nature of the two interfering beams the signal recorded in the Pd was sinusoidal. This sinusoidal signal was amplified and converted to a TTL pulse by a customised electronic box. This signal was monitored on an oscilloscope, and data was recorded on a SD memory card for later processing with MATLAB software. The TTL signal was used to externally trigger the CCD.

4.1.3 Integrated SERS-AFM system for lipid characterisation

An integrated AFM-Raman microscope has been developed for characterisation of nanomaterials [165]. The system consists of a Raman micro-spectroscopic instrument coupled to a commercial AFM (Nanowizard, JPK Instruments, Germany) with a piezoelectric XY-stage fitted to the inverted Raman spectroscopic microscope. Figure 4.3 is a schematic of the instrument. For the AFM measurements in air, silicon probes of 70 (50-90) kHz resonant frequency and 2 (0.5-4.4) Nm^{-1} spring constant were used (AC240TS, Asylum Research, UK). For the AFM in liquid mode silicon nitride cantilevers were preferred, gold coated, with a spring constant of 0.12 (0.06-0.24) Nm^{-1}, and a resonant frequency of 23 (16-28) kHz (NPG, Veeco, USA). AFM data were processed with several software packages

(commercial JPK image analyser processor and open source softwares WSxM 5.0 [166] and Gwyddion [167]).

The Raman micro-spectroscopic instrument consists of a continuous wave laser of 532 nm wavelength and maximum power 20 mW (MSL532, Laser 2000, UK). The laser was directed through 100 μm diameter optical fibres (Ocean Optics, USA) towards the inverted microscope (IX71, Olympus), crossing a dichroic 45 degree beamsplitter (Razor Edge, Semrock Inc., USA) which is optimised for transmission of light of 532 nm wavelength with a negligible reduction in transmitted intensity. The beam arrives at the microscope and is focused onto the sample by a water-immersion 1.2 NA 60× objective (UPLSAPO, Olympus) producing a maximum laser spot at full laser power of 500 nm in diameter at the focal plane of the illuminated sample. The scattered light is collected in transmission mode and sent back to the beamsplitter, which directs half of the beam intensity to a photodiode detector and the other half towards the spectrometer.

The dichroic beamsplitter-photodiode system was added to improve the lateral alignment between the Raman laser and the AFM tip. The alignment was carried out using the tip-assisted optics (TAO) module by scanning the tip through the laser spot and then locking it at the position of maximum scattering intensity (see Figure 4.4). The second beam existing the beamsplitter was directed via fibre optics towards the entrance of the spectrometer. A notch filter (Semrock Inc.) was placed in front of the spectrometer to filter the Rayleigh signal. The Czerny-Turner Raman spectrometer (SR-303i, Andor Ltd.) used incorporates a back-illuminated CCD (DV-model, Andor Ltd.). Raman spectra recorded with commercial software (Solis, Andor Ltd.) were pre-processed in MATLAB (MathWorks, USA) following the procedure described in section 4.3.1, optimising the number of points in the smoothing algorithm.

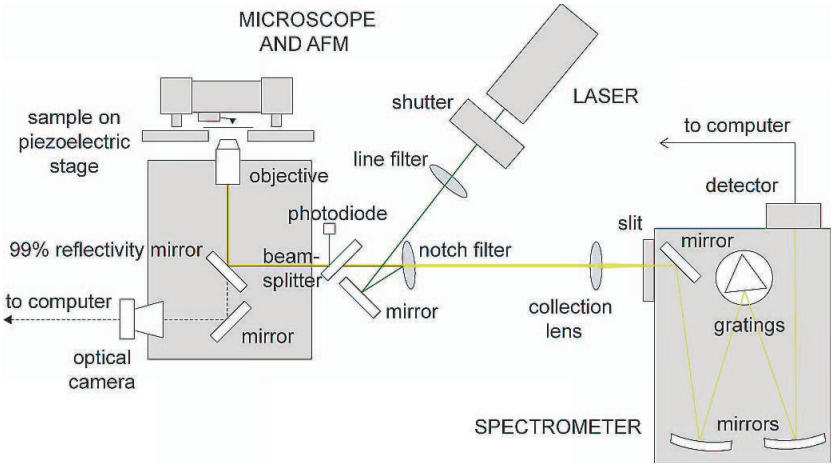

Figure 4.3: The combined AFM-Raman micro-sprectroscopic instrument. Courtesy of Dr. Sweetenham.

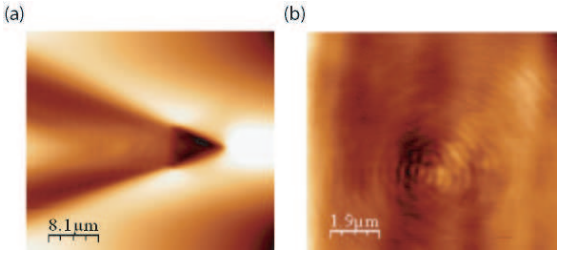

Figure 4.4: Measured intensity of the laser light reflected on the AFM tip and detected by the photodiode for an XY laser scan at a fixed focal plane. (a) The microscope is focused far from the plane where the tip is located. The shadow corresponds to the region closer to the tip, according to the tip geometry. (b) The microscope is focused on the tip. Interference fringes are detected at this plane.

4.2 Instrument design

From the three Raman micro-spectroscopic instruments described in this thesis only the wide-field Fourier transform instrument was designed and built by the author of this thesis. Therefore, only the steps in the design and implementation of this instrument are included.

A photograph of the interferometer is shown in Figure 4.5.

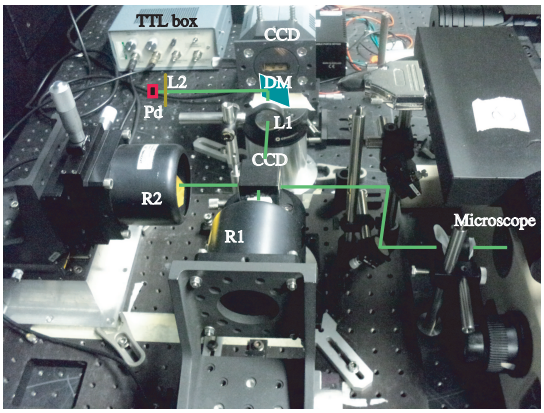

Figure 4.5: Interferometer. Abbreviations: Dichroic mirror (DM), lenses(L1, L2), retroreflectors (R1, R2), photodiode (Pd), triggering box (TTL box), and charge coupled device (CCD).

In the following sections a discussion of the optimal components for the implementation of the instrument is presented.

4.2.1 Optical components

A Nd:YAG visible laser with <5 mW and 532 nm excitation wavelength (JPM-X-3, Laser Vision) was used. For the initial work including alignment and testing of the operational principle of the system a visible laser was chosen, as the Raman signal is higher for smaller wavelengths and therefore easier to detect. Using a visible

laser implies that in the interferometer the Jacquinot advantage was present but not the multiplex advantage. In future prototypes designed for skin imaging NIR lasers might be preferred.

Dichroic beamsplitters are non-absorbing optical filters which reflect light from a specific spectral region while allowing optimal transmission at different wavelengths. 45 degree oriented dichroic beamsplitters reflect light perpendicularly to the incident light. In Raman spectroscopic systems dichroic beamsplitters are used to reject the strong Rayleigh component of the scattered light. Although an ideal dichroic beamsplitter will completely separate the Raman and Rayleigh components in practice a small amount of elastically scattered light is transmitted along with the Raman signal. A 45 degree ultrasteep dichroic beamsplitter with 538.9-824.8 nm passband and < 186 cm^{-1} transition width (RazorEdge, Semrok) was chosen for the instrument.

In addition, a 25 mm N-BK7 cube beamsplitter (Techspec, Edmund Optics) optimised for the spectral range of 430-670 nm was used. The coating guarantees reflection and transmission of $50 \pm 5\%$. While plate beamsplitters require the introduction of a compensation plate of the same material as the beamsplitter to ensure symmetry between both arms of the interferometer, cube beamsplitters do not.

Broadband hollow retroreflectors (UBBR2.5-1I, Newport, Irvine, USA) of parallelism 1 arc sec, 63.5 mm diameter aperture, and total reflectivity $R > 73\%$ for the spectral range of 400-650 nm-wavelength were used. In corner cube retroreflectors the reflected beam is parallel to the incident beam regardless of the angle of incidence. The retroreflectors were optimised for the NIR (in NIR, $R > 94\%$, coated for 650 to 12000 nm operation). Due to its high cost this piece of equipment was optimised for the final NIR instrument although visible retroreflectors would have been desirable for the first prototype described in this thesis.

4.2.2 Step-motor: rapid-scanning versus step-scanning

Step scanning allows longer exposure times for recording each interferogram as the movable mirror can be stopped and left at each position as long as needed. This is a key aspect when dealing with weak Raman signals. For skin tissues Raman spectral acquisition times might be as long as 1 s. However, introduction of accelerations that allow the mirror to move and stop intermittently add mechanical and electronic background noise to the interferogram. Rapid scanning reduces this noise as well as lowers the acquisition time, but faster mirror velocities imply

shorter exposure times to collect the Raman signal. In addition, a fast driven mirror requires a detector with faster frame rates normally of higher cost.

4.2.3 Laser reference signal detection and TTL converter box

1. Internal calibration: reference laser.
   Both Raman and 532 nm-wavelength laser signals pass through the interferometer. The laser component allowed internal calibration of the spectral axis. When a source of monochromatic wavelength is used and the mirror is moved with constant velocity v, the frequency of the interference signal f_{int} can be expressed as

$$f_{int} = \frac{2v}{\lambda} \tag{4.1}$$

   As the laser wavelength was 532 nm and the interval of mirror velocities was 5000 (nm)s^{-1}-1 (mm)s^{-1}, f_{int} was estimated to belong to the range of frequencies 18.7-3.8 kHz. If v is larger than 1(mm)s^{-1}, the process is called rapid-scan interferometry [168]. Thus, the working regime used in this thesis is below rapid-scan interferometry.

   As lasers are quasi-monochromatic sources the shape of the laser interferogram recorded was sinusoidal. The period of the signal depends on the step-motor velocity v and goes from 0.3 ms to 53.5 ms. A threshold voltage can be used to convert this signal into a TTL signal or square wave. If the detected voltage is larger than a certain value close to the maximum of the signal, a 5 V voltage will be generated. Otherwise, the output voltage of 0 V will be produced. Each time that a maximum of signal (5V) was detected by the CCD, a frame was recorded by the device. Time retardation between consecutive frames was the time delay between two maxima in the TTL signal. The period of the TTL signal was the same as that of the original sine signal. For longer periods a slower detector could be used in terms of frames per second. However longer periods imply slower step-motor velocities and an increase in the acquisition time.

2. TTL conversion circuit
   The TTL conversion circuit was built by the electronics workshop of The School of Physics and Astronomy of The University of Nottingham. A detailed description is included in Appendix II.

4.2.4 Detectors

The interferometer output beam carries both the Raman contribution and a remaining laser signal. As the Raman signal intensity is much smaller than the laser intensity both components need to be separated for the Raman beam to be detectable. A dichroic beamsplitter was introduced in the optical path (LPD01-532RS-25×36×2.0, Semrok) at the interferometer exit. The Raman signal passed through, while the laser component was reflected towards the photodetector. Both signals were focused on the focal plane of their respective detectors by focal-length optimised convergent lenses. A Si PIN photodiode with a photosensitivity of 0.4 AW^{-1} for the desired wavelength, an active area diameter of 0.4 mm, and NEP of $1.5 \times 10^{-15}\mathrm{WHz}^{-\frac{1}{2}}$ was used to detect the laser signal reflected by the dichroic beamsplitter.

A cooled CCD with a maximum of 2-3 frames per second (fps) was also used. The CCD had a quantum efficiency of $\approx 45\%$ at 532 nm, and a dark current of 0.002 electrons per pixel per second at maximum cooling. In this experiment a high responsivity and low dark current were required. The calculation of the three main sources of noise (thermal, shot, and readout) are included.

The register well depth for the CCD is 10^6 electrons per pixel. Assuming an electron signal of 10^6 electrons per pixel for 1 second of exposure time, from eq.(3.26) (see Chapter 3) the shot noise would be 10^3 electrons. This is the maximum shot noise provided by the CCD.

In the instrument described in this chapter the total noise of the CCD was mainly dominated by the shot noise contribution when using a laser and a halogen light source. In contrast, for Raman signals shot noise may not be the dominant source of noise. From eq.(3.25) for 1 s exposure time the thermal noise is 4.10^{-2} electrons per pixel. For much longer exposure times and operation at higher temperatures the dark noise might increase considerably.

Finally, the maximum readout noise for the DV420-OE CCD is 10 electrons. In conclusion, in the DV420-OE CCD the dominant noise contribution is the shot noise when the current of photons detected at the CCD is high enough. Otherwise, it will depend on factors such as temperature or exposure time.

The optimal CCD camera for this prototype needs to have a fast frame rate. In the design the camera was triggered by the laser reference signal. For a fine control of the instrument the camera should be able to produce a frame each time it is triggered by a maximum of the TTL signal. Therefore, it needs to respond to frequencies in the range of 18.7 Hz-3.8 kHz. This means

that with the current step-motor-driven mirror a camera that records at least 18.7 fps is needed for a mirror with a constant velocity of 5000 nm(s^{-1}). The available CCD was not fast enough as it reached a maximum of 3 fps at full read-out.

Two approaches can be taken to overcome the mentioned problem. In first place, a slower step-motor can be used coupled to the current CCD camera. This will increase acquisition time and consequently contradict one of the main objectives of the prototype design, which was to speed-up the process. A second option is to use a faster detector. Fourier transform Raman systems with unidimensional high-sensitivity detectors have been widely developed [130]. However, these detectors do not allow 2D imaging.

The main trade-off of common CCDs such as the one reported in this study when compared with fast point-like detectors such as photomultiplier tubes (PMT) is the higher time-response of 2D systems. In general, a faster response would have to be a compromise over sensitivity or vice versa. Ultrafast CCDs (around thousands of fps) coupled to intensifiers that allow single photon detection are commercially available.

For the future system in the NIR the problem of etaloning is likely to appear. Etaloning is an intrinsic problem of thin back illuminated CCDs which becomes of great importance in the NIR. Etaloning could represent up to the 20% of the detected radiation, masking the Raman signal. Reflections between the parallel front and back surfaces of these CCDs cause them to act as "etalons". This behavior leads to unwanted interference fringes.

4.3 Characterisation of the instruments

4.3.1 Raman micro-spectroscopic instruments

This section includes the characterisation of the Raman micro-spectroscopic instruments in terms of their spatial and spectral resolution. Considerations concerning Raman spectral data analysis are also discussed.

Resolution

The vertical resolution H_{eff} of the Raman micro-spectroscopic instrument combined with the AFM was determined with a silicon wafer and a 60× water immersion 1.2 NA objective [165]. The variation in the intensity of the Raman spectral peak of silicon at 520 cm^{-1} was recorded as a function of the

transversal plane at which the microscope objective was focused. The experimental results were represented as a scatter plot which followed a Gaussian distribution. The measured H_{eff} was the full width at half maximum of the Gaussian fit. From Figure 4.6 the calculated value of H_{eff} was 18.50 μm. The H_{eff} of the Raman micro-spectroscopic instrument for skin research was estimated by Zoladek [164] by substituting the silicon wafer with other samples. The estimated values were 50.35 μm and 7.42 μm for oil and polystyrene beads respectively. Note that experimental values were higher than the theoretical Z-resolution, as $H_{eff} = \frac{2\lambda n}{NA^2}$. For a laser wavelength of 785 nm and considering the refractive indexes of oil, polystyrene, and silicon to be 1.47, 1.59, and 3.42 respectively, the estimated theoretical H_{eff} were 2.8, 3.1, and 2.5 μm respectively.

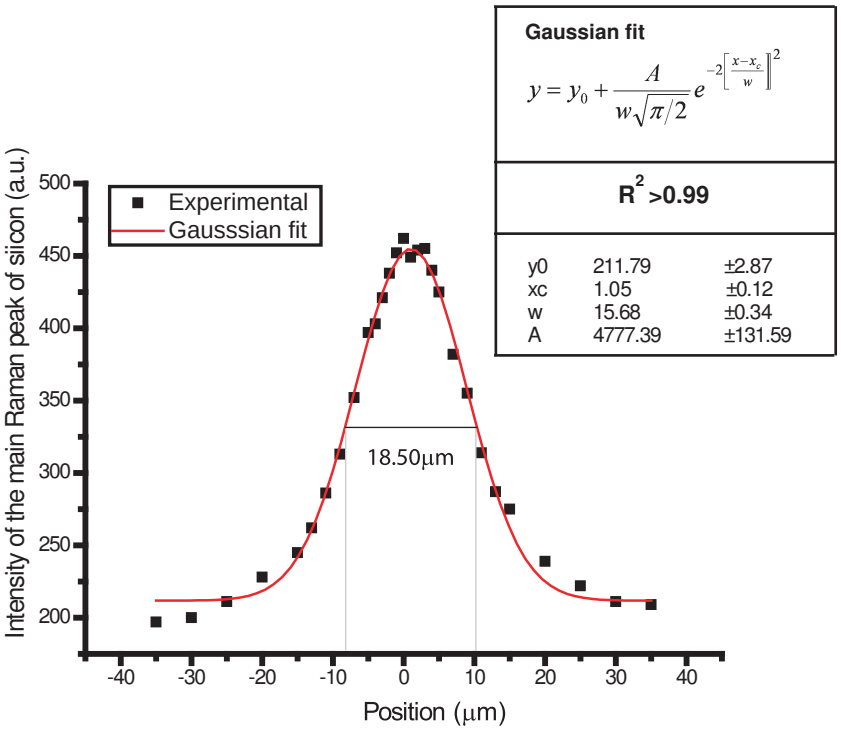

Figure 4.6: Calculation of the effective height H_{eff} of the scattering volume: H_{eff} is the width at half maximum of the Gaussian fit of the experimental pairs formed by the intensity of the Raman spectral peak of silicon at 520 cm^{-1} and the transversal plane at which the laser is focused. Position zero corresponds to the focal plane at which the spectral peak intensity is maximum.

Raman spectral data analysis

- **Calibration and instrumental spectral error**

  The wavenumber axes of the Raman micro-spectroscopic instruments were calibrated using Raman standard samples (American Society for Testing and Materials -ASTM-) such as naphthalene or

Raman spectral bands of 4-acetamidophenol-Tylenol- (cm^{-1})			
(i) ASTM standard	**(ii) Order 1**	**(iii) Order 2**	**(iv) Order 3**
710.8	720	711	711
797.2	800	797	797
834.5	836	834	834
857.9	856	857	858
968.7	962	968	970
1105.5	1094	1104	1105
1168.5	1159	1169	1169
1236.8	1227	1237	1237
1278.5	1270	1278	1279
1323.9	1317	1324	1324
1371.5	1366	1372	1371
1561.5	1570	1561	1562
1648.5	1666	1648	1649

Table 4.1: Comparison between the main peaks of Tylenol established by ASTM standards (i), and the spectral values obtained with the Raman micro-spectroscopic instrument for skin investigations with data fitting to (ii) linear, (iii) quadratic, and (iv) cubic polynomials.

4-acetamidophenol -Tylenol- (Sigma, UK). All data recorded by the CCD were acquired as photon counts versus pixels and the horizontal coordinate was transformed to Raman shift (cm^{-1}). The transformation from pixels to spectral shift was performed by a polynomial fit using MATLAB software (MathWorks). Figure 4.7 and Table 4.1 show the effect of the order of the polynomial fit in the spectral calibration of the Raman sprectum of Tylenol acquired with the Raman micro-spectroscopic system designed for skin oncological investigations. Calibrating the spectral axis with a polynomial of order 1, 2, and 3 gave a mean error of 2, 0.9, and 0.2 cm^{-1} respectively.

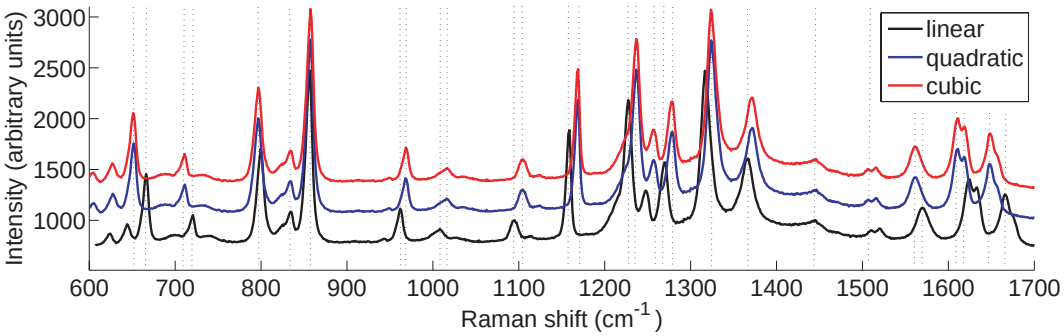

Figure 4.7: Raman spectra of Tylenol in which spectral calibration has been done by fitting the spectral data to polynomial of different orders.

In analogy, the spectral calibration of the Raman micro-spectroscopic instrument of the combined AFM-SERS system was performed. A polynomial fit of order 3 was used for obtaining all the Raman spectra presented in this thesis. Table 4.2 shows in column (i) the values of the

Raman spectral bands of 4-acetamidophenol(Tylenol) (cm^{-1})	
(i) ASTM standard	**(ii) Measured by the AFM-SERS system**
797.2	796.9
834.5	835.0
857.9	857.9
968.7	969.1
1105.5	1104.0
1168.5	1169.0
1236.8	1238.0
1278.5	1279.0
1323.9	1325.0
1371.5	1372.0
1561.5	1561.0
1648.5	1649.0

Table 4.2: Instrumental spectral error calculation for the AFM-SERS system: comparison of (i) ASTM standard for Raman spectral peak assignment of Tylenol powder and (ii) the values measured with the AFM-SERS system for a 1800 line grating.

main Raman spectral peaks of Tylenol in the fingerprint region corresponding to the ASTM standards [169] in comparison to the values experimentally measured with the AFM-Raman micro-spectroscopic instrument (column (ii) of Table 4.2). Maximum and mean wavenumber accuracy was found to be ± 1.5 and ± 0.2 cm^{-1} respectively.

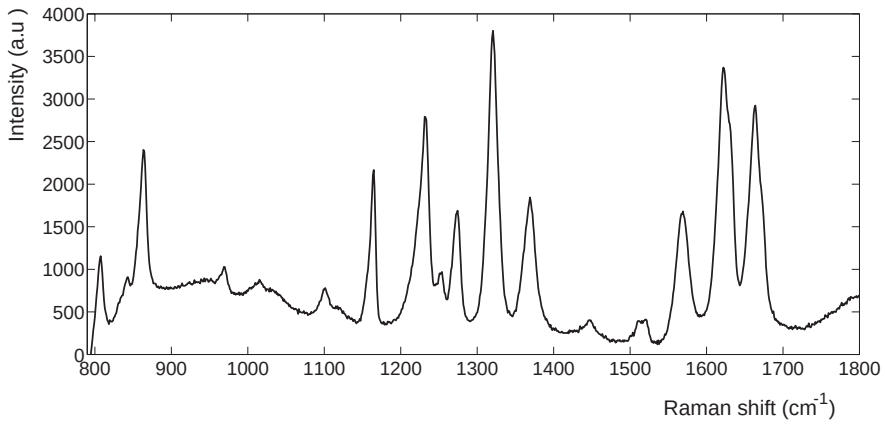

Figure 4.8: Raman spectrum of Tylenol corresponding to column (ii) of Table 4.2

- **Spectral data pre-processing**

  Standard pre-processing of the recorded spectra involved cosmic ray removal, subtraction of the contribution of the microscope objective, baseline correction, normalisation to zero mean and unity standard deviation, and smoothing using the Savitzky-Golay algorithm (5-11 points, 2^{nd} order polynomial) [170]. Cosmic rays are charged particles from space which randomly bombard the CCD sensor. They are detected as

high energy spikes at a certain frequency and must be removed from the acquired data. A semi-automatic program was written with MATLAB software to detect the cosmic rays in the measured spectra. The program selected the peaks of each spectrum with intensities I_{CR} separated from the mean intensity $\bar{I}$ in more than 3 times the standard deviation σ (i.e. $I_{CR} > \bar{I} + 3\sigma$). A plot was generated displaying which peak was going to be removed and asked for authorisation from the end user. This supervised step minimised the risk for removing meaningful spectral bands. The intensities of the cosmic rays were substituted by the mean intensities of the two edges of the deleted peaks.

Baseline correction was performed by subtraction of a sixth order polynomial. For biological samples polynomials of orders 5 and 6 are commonly used [57, 171, 172]. In this thesis only small spectral differences were found between both baseline corrections as seen in Figure 4.9, which shows three examples of SERS spectra of p-ATP on a SERS-active substrate corrected using polynomials of 5^{th} and 6^{th} order. For consistency exclusively polynomials of order 6 are used throughout this thesis for the background correction of Raman and SERS spectra.

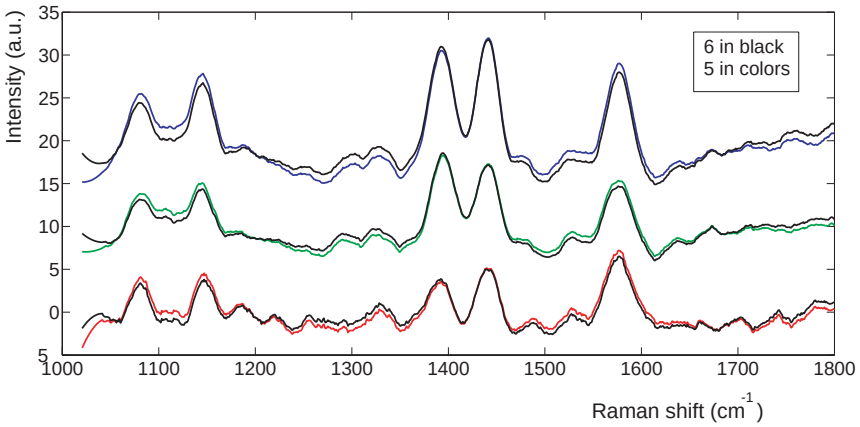

Figure 4.9: Preprocessing of Raman spectra: effect of baseline subtraction of a polynomial of order 5^{th} and 6^{th} on three spectra of p-ATp on a SERS-active substrate.

4.3.2 Atomic force microscope

AFM imaging in air and liquids

AFM images in air were obtained using rectangular silicon cantilevers with pyramidal silicon tips of 9±2 nm radius of curvature. Triangular (also referred to as V-shaped) silicon nitride cantilevers with pyramidal tips were used for the liquid measurements. The nominal radius of curvature of the liquid tips was 30 nm (the maximum radius of curvature was 90 nm). The liquid cantilevers were gold coated to improve reflection. For thermal stability in liquid, samples were pre-heated to around 55°C prior to any measurement and the system was left to stabilise for at least 10 minutes. This helped to reduce the thermal drift during scanning, related to the inhomogeneous expansion of the experimental components due to temperature gradients. The thermal drift resulted in difficulties in the acquisition of the AFM images, as the cantilever tended to come away from the substrate surface every few scanned lines, especially for slow scans.

Calibration

In order to quantitatively interpret the AFM results the maximum error in vertical and horizontal measurements needs to be determined. Due to the requirement of nanometre accuracy in the height measurements (as a lipid monolayer is approximately 3 nm thick) conventional grids with features of the order of hundreds of nanometres should not be used for vertical (Z axis) calibration. A more accurate approach is possible by measuring the roughness of an atomically flat sample, such as an atomic layer of mica freshly cleaved with a razor blade. Experimentally, in this dissertation a surface is considered "flat" if the detected roughness is less than 1 nm. Roughness is defined in this thesis as the vertical height variation in the topographic images of a surface. From Figure 4.10 it can be seen that height differences on the order of hundreds of picometres were detected and that in the vertical direction the AFM has sub-nanometre resolution. Quantitatively, the maximum experimental error in Z estimated from Figure 4.10 is 0.9 nm. For the experiments presented in this thesis calibration in XY of the order of ≈ 100 nm is sufficient. In order to test the lateral spatial resolution of the AFM, samples of closely packed polystyrene beads of 384±20 nm and 1000±50 nm diameter were deposited on atomically flat mica supports which were then imaged in air. Figures 4.11(a) and 4.11(b) show that the error in the

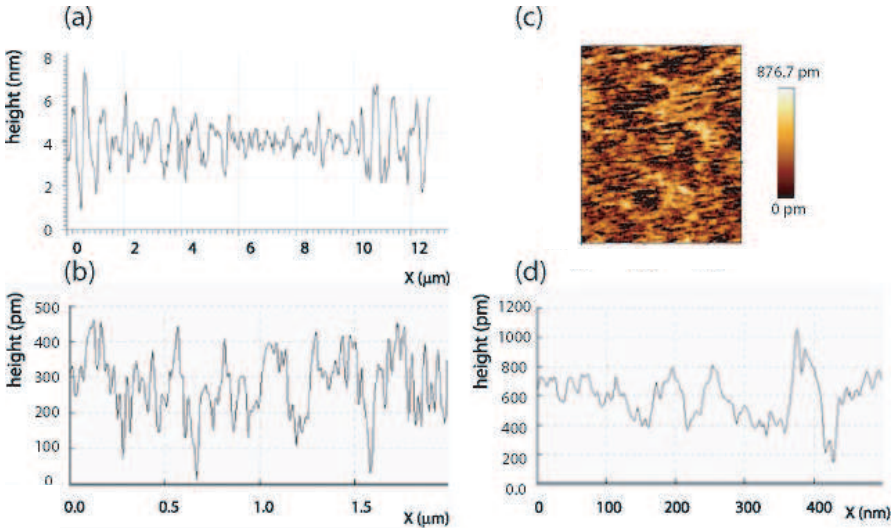

Figure 4.10: (a) Roughness of mica cleaved with masking tape in both sides and (b) roughness of mica razor cleaved. (c) AFM image and (d) roughness of a sapphire substrate.

AFM estimation for the diameter of the individual beads is better than the required 100 nm.

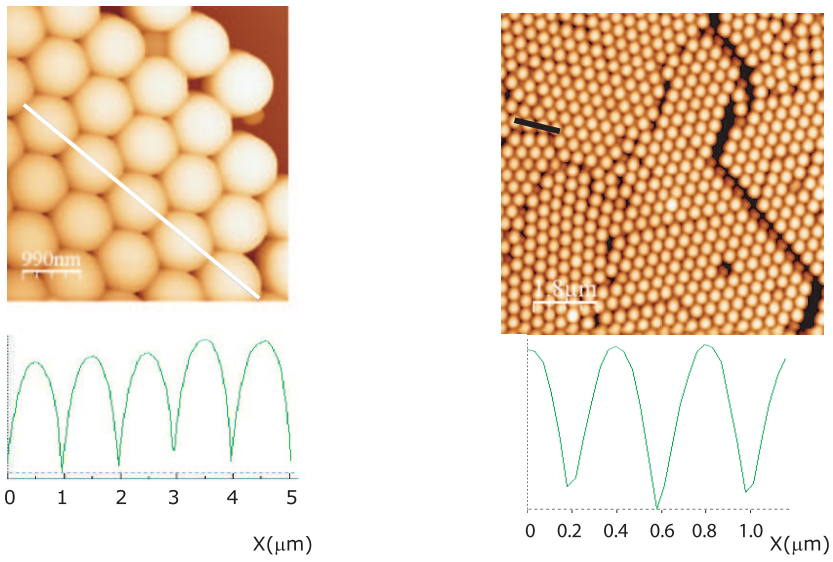

(a) 1μm PB (b) 400nmPB

Figure 4.11: AFM XY calibration

The resonant frequency of the cantilever was found by tuning the cantilever prior to any experiment. Figures 4.12(a) and 4.12(b) show typical cantilever tuning curves for the silicon probes in air and silicon nitride tips in liquid, respectively.

The spring constant was calculated by the thermal noise method with new tips and reproducing the experimental conditions (see Figure 4.3.2). The thermal noise method measures the thermal fluctuations in the deflection

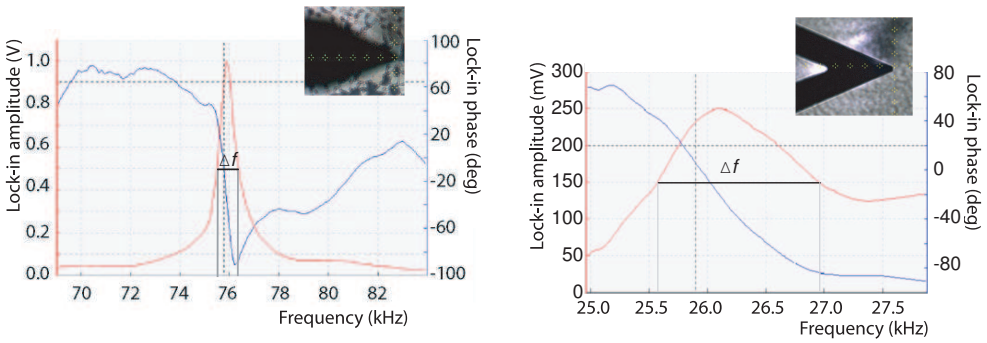

(a) Air (b) Liquid

Figure 4.12: Cantilever resonance curves for air and liquid tips. Δf is the width of the resonance curve at half maximum.

of the cantilever. The AFM software (JPK) returns automatically the resonance curve and the values of the spring constant k_c calculated by the thermal noise method. For the liquid and air tips k_c was estimated to be 0.21 Nm^{-1} and 1.93 Nm^{-1}, respectively. These values belong to the wide interval provided by the manufacturer (0.06-0.24 Nm^{-1} and 0.5-4.4 Nm^{-1} for the liquid and air tips, respectively).

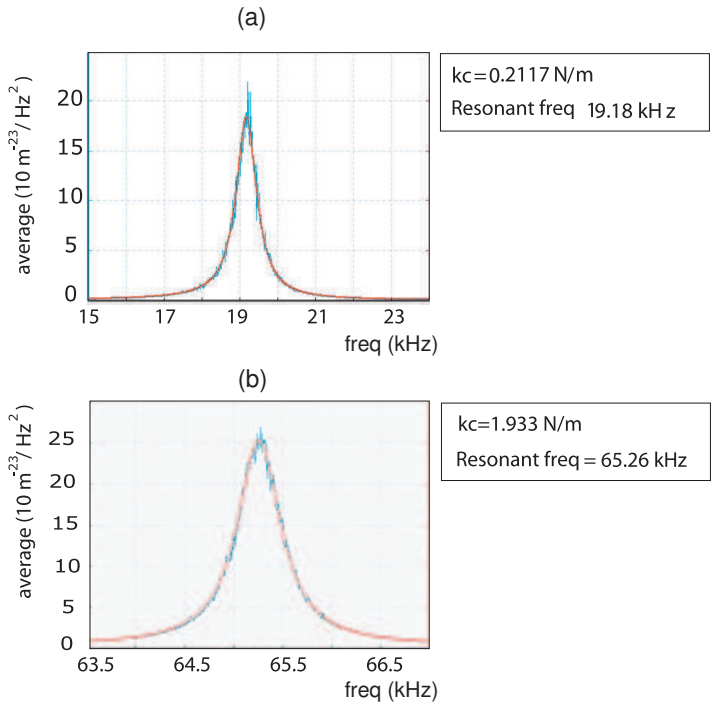

Figure 4.13: Spring constant calculation for the AFM tips in liquid (a) and air (b) by the thermal noise method.

Tip effects

One of the major experimental difficulties encountered during acquisition of AFM images of supported lipid films was the contamination of the probe by molecules belonging to the sample itself. This problem is common when characterising lipid membranes and has been previously reported [173]. The extra molecules attached to the tip can produce artefacts in the AFM images such as multiple tip effects (see Figure 4.14). In practice, when unexpected tip effects were detected while measuring lipid multilayers the corresponding cantilever resonance curves were studied. If the curve did not present a clear Lorentzian shape (in air) an abrupt movement was repeatedly performed on the lever with high target amplitudes at a distance far from the sample surface. In some cases this was sufficient to detach the lipid material from the tip.

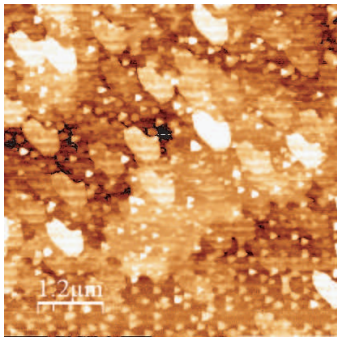

Figure 4.14: Multiple tip effect due to the adhesion of lipid molecules to the AFM tip.

4.4 Peak assignment of the Raman spectra of amphiphiles and skin components

4.4.1 Raman spectral peak assignment of skin components.

Table 4.3 presents the vibrational assignment for the main peaks observed in a typical Raman spectrum of dermis. Several papers have been used for the spectral peak assignment [2, 5, 174–177] but particularly the study compiled by Movashaghi *et al.* which includes an extensive database of Raman molecular fingerprints of biological tissues [176]. The 788 cm^{-1} Raman spectral peak corresponds to the PO_2 stretching in DNA and RNA, and it has been reported as a biomarker for quantifying nucleic acids present in a

Dermis	
Raman band(cm^{-1})	**Assignment**
788	PO_2 symmetric stretching of DNA and RNA
850	Valine, proline and polysaccharides stretching vibrations
950	Valine, proline and polysaccharides stretching vibrations
1003	Ring breathing of phenylalanine
1093	PO_2^- symmetric stretching of nucleic acids
1268	Amide III (collagen vibrations); and CH vibrations of lipids
1312	CH_3CH_2 twisting, CH_3 and CH_2 twisting, wagging and bending mode of collagen/lipids
1450	Lipids, proteins (CH_2 deformation)
1661	Amide I (peptide bonds in proteins)

Table 4.3: Assignment of the experimentally measured Raman spectral peaks of dermis [5, 174, 176, 177].

sample [176]. Raman spectral peaks at 850 cm^{-1} and 950 cm^{-1} are assigned to single bond stretching vibrations of amino acids forming proteins, in particular proline and valine, and polysaccharides. One of the most intense Raman spectral peaks, at 1003 cm^{-1}, corresponds to the ring breathing of phenylalanine. The PO_2^- symmetric stretching vibration from DNA generates a Raman spectral peak at 1093 cm^{-1}. The Amide III spectral region (1200-1350 cm^{-1}) also contains characteristic wide Raman spectral peaks with maxima at 1268 and 1312 cm^{-1}. The Raman spectral peak at 1268 cm^{-1} corresponds to molecular vibrations of collagen and the CH group in lipids. The Raman spectral peak at 1312 cm^{-1} has been assigned to CH_3CH_2 twisting mode, and CH_3 and CH_2 twisting, wagging, and bending modes of collagen and lipids. Finally, the Raman spectral peak at 1450 cm^{-1} corresponds to CH_2 bending modes of methyl groups in proteins such as collagen, CH deformation modes in lipids, and CH_2CH_3 deformation modes in collagen. The Amide I Raman spectral band was measured at 1637-1693 cm^{-1}, with a maximum at 1661 cm^{-1}. This Raman spectral band originates from the vibrations of peptide bonds in proteins and give information about their secondary structure [2]. Figure 4.15 shows a typical dermis spectrum in comparison to the Raman spectra of common powder components present in skin: collagen type I, DNA, RNA, albumin from human serum, glycogen, and cholesterol (all purched from Sigma-Aldrich and used without further treatment).

4.4.2 Raman spectral peak assignment of amphiphiles.

Figure 4.16 shows the Raman spectra of bulk powder arachidic acid (AA) (Sigma-Aldrich, UK), 11-*cis* eicosenoic acid (Sigma-Aldrich), neu-

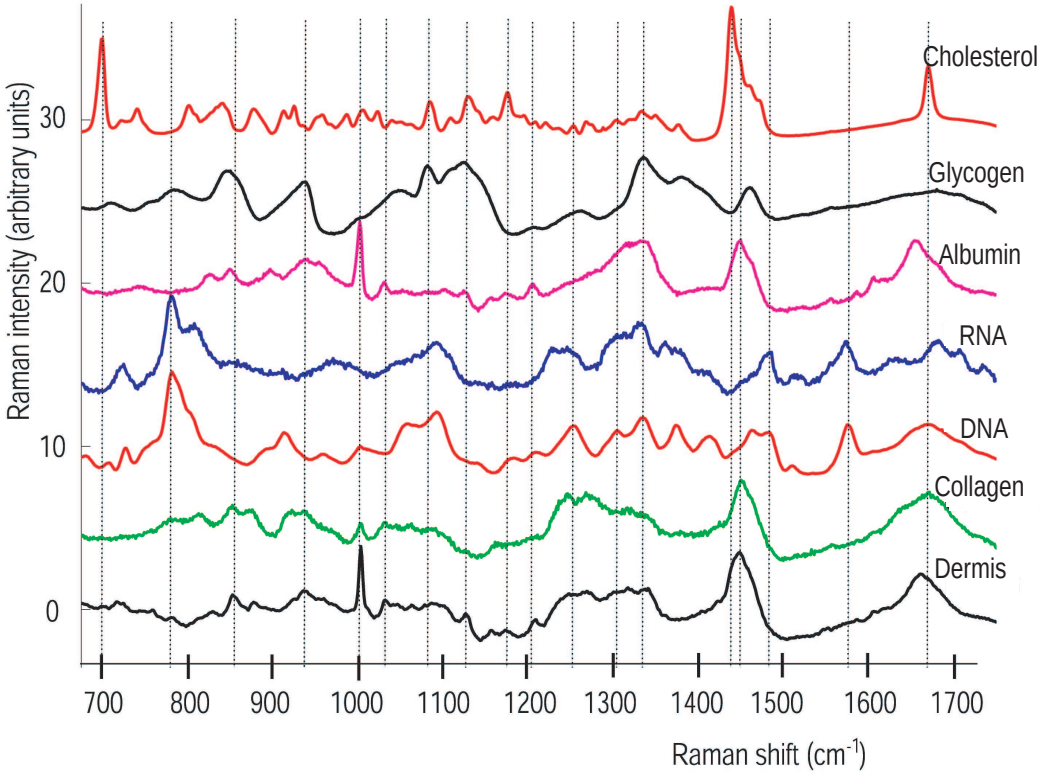

Figure 4.15: Raman spectra of dermis and powder of collagen type I, DNA, RNA, albumin from human serum, glycogen, and cholesterol.

tral 1,2-dihexadecanoyl-*sn*-glycero-3-phosphocholine (DPPC) (Avanti Polar Lipids, USA), and charged $1,2-$dihexadecanoyl$-sn-$glycero-3$-$ethylphosphocholine (cationic-DPPC or EPC), (Avanti Polar Lipids). Spectra have been acquired in two spectral regions: the fingerprint region ($800-1800$ cm^{-1}) and the CH stretching region ($2800-3100$ cm^{-1}). As the amphiphiles under study present hydrocarbon chains it is relevant to comment on the spectral band of the fingerprint region at $1000-1150$ cm^{-1} corresponding to the CC stretching modes. In Figure 4.16 spectrum (a) is introduced in order to clarify the assignment of the spectral peaks in (b). $11-$*cis* eicosenoic AA is an unsaturated version of AA; therefore, extra peaks associated with the carbon double bond vibrational modes are expected. The clearest example is the appearance of a peak at 1655 cm^{-1}, or an extra shoulder at 1266 cm^{-1}. Furthermore, due to its *cis* configuration the Raman peaks associated to the *trans* configuration of AA disappear, at 1420 and 1462 cm^{-1}. A detailed peak assignment of AA and DPPC is included in Tables 4.4-4.5, respectively.

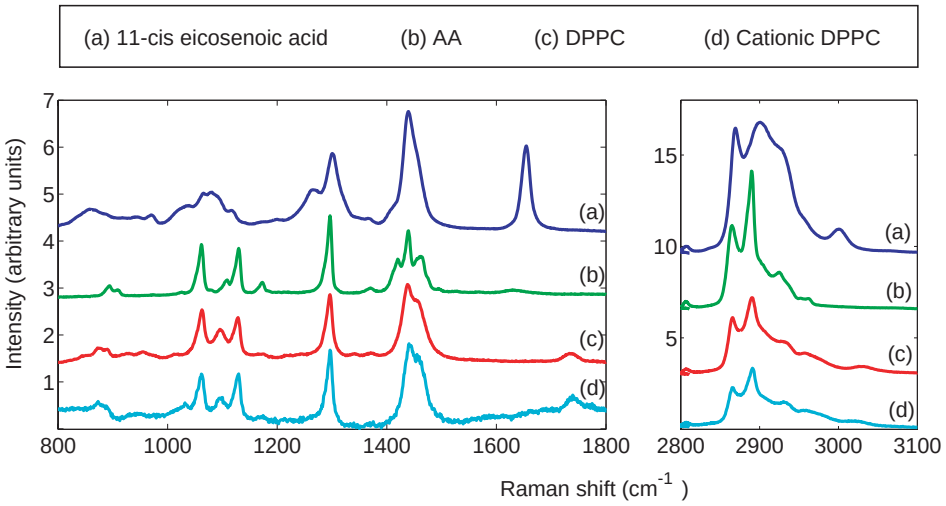

Figure 4.16: Raman spectra of (a) 11-*cis* eicosenoic acid, (b) arachidic acid, (c) neutral DPPC, and (d) cationic-DPPC .

Arachidic Acid (AA)	
Raman band (cm^{-1})	**Assignment**
909	CC stretching
1062	CC *trans* stretching
1130	CC *trans* stretching
1296	CH_2twisting deformation
1420	CH_2 scissoring and CH symmetric bending
1440	CH_2 scissoring and CH symmetric bending
1462	CH_2 scissoring and CH symmetric bending
2865	CH stretching
2890	CH stretching

Table 4.4: Assignment of the Raman spectral peaks of arachidic acid experimentally measured.

Typical Raman spectrum of arachidic acid (AA)

Vibrational mode assignment to the main Raman spectral peaks of AA −see Figure 4.16 (b)− is included in Table 4.4 [165]. Raman peaks at 1062 and 1130 cm^{-1} can be assigned to CC *trans* stretching (note there are not present in the spectrum (a) of Figure 4.16). The Raman band at 1296 cm^{-1} denotes CH_2 twisting deformations. Peaks in the Raman spectrum at 1420, 1440, and 1462 cm^{-1} correspond to CH_2 scissoring and symmetric bending of the CH bonds in the ester methyl group. The weak peak at 909 cm^{-1} can be assigned to CC stretching [178].

DPPC	
Raman spectral peak (cm^{-1})	**Assignment**
1063	CC stretching
1096	CC stretching
1129	CC stretching
1296	CH twisting deformations
1438	CH scissoring deformations
2866	CH stretching
2891	CH stretching

Table 4.5: Assignment of the Raman spectral peaks of DPPC experimentally measured.

Typical Raman spectrum of phospholipids: DPPC and cationic DPPC

Cationic DPPC differs from neutral DPPC in that it incorporates an extra ethyl group (CH_2) to its chemical structure. Figure 4.16 (c-d) shows that cationic and neutral DPPC were found to present the same active Raman spectral peaks with the same spectral shifts (considering the spectral error) with the exception of the Raman spectral peak corresponding to the CH scissoring deformations. This Raman spectral peak was measured at 1438 cm^{-1} for DPPC and slightly shifted for cationic DPPC, at 1442 cm^{-1}. The assignments of the main Raman spectral peaks of DPPC detected are included in Table 4.5 [165]. In the fingerprint region peaks at 1063, 1096, and 1129 cm^{-1} correspond to CC stretching modes. The 1296 cm^{-1} spectral peak is related to CH twisting deformations. Finally, in the CH stretching region, two Raman spectral peaks were detected at 2866 and 2891 cm^{-1}.

Chapter 5

Raman micro-spectroscopy for automated detection and imaging of basal cell carcinoma

This chapter studies the potential of Raman micro-spectroscopy (RMS) as an optical tool in the automated diagnosis and imaging of basal cell carcinoma (BCC). Firstly, a database including Raman spectra from the tumorous and non-tumourous regions of skin tissue sections was created. Selected Raman bands responsible for the largest spectral differences between BCC and normal skin regions and linear discriminant analysis (LDA) were used to build a multivariate supervised classification model. The model was based on 329 Raman spectra measured on skin tissue obtained from 20 patients. BCC was discriminated from healthy tissue with 90±9% sensitivity and 85±9% specificity in a 70%−30% split cross-validation algorithm. This multivariate model was then applied on tissue sections from new patients to image tumour regions. The RMS images showed excellent visual agreement with the gold standard of histopathology sections, BCC being detected in all positive sections. This study demonstrates that RMS may be used as an automated objective method for tumour evaluation for samples from Mohs micrographic surgery (MMS). To conclude the chapter the main limitations of this dispersive approach are discussed. The need for further alternative studies such as those presented in Chapter 6 is justified.

5.1 Materials and Raman spectral data

5.1.1 Skin tissue samples

Skin tissue sections were obtained from the Nottingham University Hospitals NHS Trust. Consent was obtained from the patients and ethical approval was granted from the Nottingham Research Ethics Committee. Tissue sections were cut from blocks removed during Mohs micrographic surgery (MMS) and standard basal cell carcinoma (BCC) excision into 20 μm sections for Raman micro-spectroscopy (RMS) investigations. After the RMS measurements the analysed sections were stained using conventional haematoxylin and eosin (H &E) staining. Diagnosis of the H&E stained samples was given by a consultant histopathologist.

5.1.2 Spectral data acquisition

First, an adjacent H&E stained skin section was placed on the microscope and the regions of interest (BCC, epidermis or dermis) were identified. The corresponding unstained skin section, which had been deposited on a MgF_2 window, was placed on the microscope and the position of each measured region was recorded. After RMS measurements, the tissue section was returned to the pathology laboratory, H&E stained, and then placed on the Raman microscope for retrospective acquisition of images to be used for diagnosis by a consultant histopathologist. Once identified, the measured regions were classified into three groups: BCC, epidermis, and dermis. The precision of retrospective location was determined to be better than 5 μm based on two marks engraved on each slide.

In order to account for tissue heterogeneity, each Raman spectrum in the model was the average of 100 spectra measured at 5 μm intervals over a 50 μm$\times$50 μm region. The integration time for each position was 1 s. A total of 329 measurements from 20 patients were recorded: 127 BCCs (nodular and morphoeic), 92 epidermis, and 110 dermis.

5.2 Methods

5.2.1 Spectral data analysis and creation of the 2-step LDA-based classification model

Spectral data pre-processing was performed as specified in Chapter 4. The classification model was built using the spectral band area of several selected Raman peaks which showed the highest contrast in the computed difference average spectra for each class. The peak areas were calculated after a local linear baseline was subtracted in the regions of interest. This approach allows direct control over the selection of spectral features which could be assigned to specific tissue biochemicals. A small number of features were selected by directly optimising their discriminatory power. This is a very intuitive procedure for dimensionality reduction especially suitable for small datasets. However, knowledge of which are the key bands which enclose the most relevant information is required. This might imply that spectral bands which can play a key role in discrimination but whose visual analysis is not straightforward are foreseen.

Nevertheless, this visual supervised selection suppress the introduction of mathematical artefacts without biological meaning, in contrast to unsupervised methods for dimensional reduction such as the frequently used principal component analysis (PCA) [5, 6]. PCA relies on the calculation of the covariance matrix of the dataset. In this thesis typical datasets correspond to hundreds of spectra with 1024 spectral channels (maximum allowed by the spectrometer). The covariance matrix takes into account the grade of correlation among the variables. Consider that this covariance matrix represents a linear transformation that can be expressed in terms of its eigenvectors and eigenvalues. The eigenvectors would be the directions in which the matrix acts as a scaling transformation (the eigenvalues being the scalar factors). In this case, the eigenvectors of the covariance matrix would represent the directions showing the maximum information about the correlation among data. The higher the value of their associated eigenvalue, the more weight the eigenvector has in the whole transformation. Therefore, transformations in the directions with the smallest eigenvalues retain less information about the correlation among the original variables. To reduce the dataset dimensions, a new transformation matrix is created which does not include the eigenvectors associated to smallest eigenvalues. Although PCA is a widely spread method for dimensionality reduction it requires large datasets to ensure that extra artefacts only detected by computer comparison are not

being artificially selected. These artefacts could rise from interpatient and intersample variability. As has been reported in statistical studies automated methods may not be optimal as a feature selection approach when the ultimate goal is classification because class-related information would not be directly taken into account by such methods [179].

Once the dataset is dimensionally reduced the next step is to implement a mathematical classification algorithm for the class separation. The final goal of the classifier is to allow automated diagnosis of a measured tissue region as BCC, epidermis or dermis. The three-class classifier was implemented as a composition of two consecutive 2-class classifiers. In a first step, dermis is separated from the other classes (i.e. BCC and epidermis) by linear discriminant analysis (LDA). Linear discriminant analysis is a statistical classification method which establishes a decision region among the given classes. For a detailed mathematical explanation of LDA see Appendix I. LDA returns an eigenvector with the direction of maximum class separation. Once this first eigenvector is known, a new LDA is performed. In this second step, BCC and epidermis are now separated. The classification process can be flexibly tuned to a desirable regime by controlling either specificity or sensitivity while optimising the other measure. The terms "sensitivity" and "specificity" are widely used to assess the performance of a model. In our study, sensitivity refers to how precise the technique is in detecting true BCC, while the specificity shows how accurately it identifies healthy tissue.

To emulate a realistic scenario of BCC detection, a highly sensitive regime (90% or higher) was targeted. In order to assess the performance of the model, different statistical approaches could have been taken. First, the whole dataset could have been used for training the model and to estimate the error. However, this simple method will underestimate the real error as well as create a model that overfits the data. It is more convenient to split the dataset in at least two independent subsets, one for training the model (*training set*) and the other to test it (*validation set*). This is called the "holdout method". It has two main disadvantages. It requires a large dataset, as in small datasets it might not be "affordable" to keep aside some of the data and not to use them to train the model. In addition, some of the fundamental characteristics of the data may be neglected in the model if by chance an unbalanced split is performed [180, 181]. These drawbacks can be overcome by cross-validation (CV). CV is a resampling method where the partition between *training set* and *validation set* is repeated. The selection of subsets as training or validation sets is a dynamic process, in principle more accu-

rate than the holdout method but also more time consuming as it requires more calculations. Typical examples of CV are k-fold CV and leave-one-out cross-validation (LOOCV). In k-fold CV, the dataset is divided into k subsets. *k-1* of these subsets are used as training set and the remaining subset for testing. The process is performed k times, every time using a different subset as validation set [181]. At this step, the model can be optimised and the parameters adjusted and re-tested for maximum performance. LOOCV is a particular case of k-fold CV in which k is the total number of samples. Therefore, the model is trained with *k-1* samples and tested only with the remaining value, and the process repeated until all the samples have been individually tested. The choice of the number of folds depends on the size of the dataset [181]. In all the reported cases the prediction error is calculated as the average error on the validation examples [180]. Finally, after the model is completely trained and validated, it is also common practice to use an independent dataset called the *test set* to assess the performance of the fully-trained classifier. This last dataset in this project is formed by skin tissue samples of unknown class. Once the validation process is finished the parameters of the model should no longer be adjusted.

As CV estimation might depend on the splitting ratio, CV estimates where obtained with three different settings, namely 70−30%, 80−20% and LOOCV schemes.

The 2-step model used in this thesis is tested by sampling 92 times the spectral data in a 70−30% setting. First the spectral dataset of known classes (epidermis, dermis, and BCC) is linearly ordered in 3 groups. Every partition is performed for each one of these groups, i.e. for each partition, 70% of the BCC spectra are used for training the model and 30% of the BCC spectra for testing it. In a similar way, 70% of the epidermis and dermis spectra are used for training the model and the rest for the test. For each partition one value for the sensitivity and one value for the specificity of the model are produced. The number of partitions performed was 92, which corresponds to the spectra of the class with a lower number of spectra (epidermis). After the model was tested with all the partitions, the mean and standard deviation of all the sensitivity and specificity values were calculated. The final error of the sensitivity and specificity of the model was estimated as the corresponding standard deviation. In analogy, the final estimated value for the sensitivity and specificity of the model was the mean of the set containing all the means of each particular partition.

5.2.2 Spectral imaging of BCC with the 2-step LDA-based classification model

After the 2-step LDA model was built and validated the ability of RMS to detect and image BCC was tested on a set of 6 skin sections obtained from 3 new patients. No samples from these patients were included into the 2-step LDA-based classification model as these samples corresponded to the test set. Raman spectra from a selected region were acquired at 5 μm intervals with 2 s integration time. Each spectrum was pre-processed as specified in Chapter 4. Raman spectra of MgF_2 substrate were detected using a threshold filter in the 1370−1500 cm^{-1} spectral range and eliminated from the classification model.

Spectra were binned over 10 or 15 μm to account for tissue heterogeneity, i.e. each new spectra was the average of the 4 or 9 adjacent spectra to ensure that the acquired spectral data were representative of the tissue class. Thus, spatial resolution of biochemical images achieved was 10 or 15 μm, respectively. The 2-step LDA model was then applied to predict the class of each spectrum as BCC, epidermis or dermis. An image was constructed based on the 2-step LDA classification model. An alternative method combining unsupervised k-means clustering followed by LDA discrimination was also proposed (k-means−LDA). k-means clustering is a prototype method for pattern recognition. It is highly unstructured and the nature of the differences among clusters obtained by this method are generally of difficult interpretation. It has been referred by Hastie *et al* as "an effective black box prediction engine for real data problems" [181]. Prototype methods are based on a set of class-labelled points in the feature space, i.e. each one of these points has associated a different class label. These points do not necessarily directly correspond to the transformation of one experimental measurement, as they can be, for example, averages of several measurements. In prototype methods, clustering is performed by transforming the experimental data to the "feature space"(in contrast to the space of the raw measurements) and measuring the distance to each one of these labelled points. The unclassified data will be assigned the class of their closest labelled point [181]. k-means clustering divides the dataset into an *a priori* fixed number of clusters and calculates their centroids. In this case the centroids are the labelled points in the feature space previously mentioned. Centroid calculation is done by assigning initial centroid values and then iteratively recalculating these values to minimise the total within cluster variance.

The aim of using k-means clustering in this study was to observe any loss in spectral images caused by data compression methods as well as to speed-up the diagnoses. k-means clustering was used to find patterns in the Raman spectra and group these spectra into clusters, providing qualitative false-colour images. The centroids of each class are the average Raman spectra of all the members of the corresponding cluster [5]. The LDA classification algorithm was then applied on the centroid spectra to assign a class to each one of these spectral clusters providing thus an automated objective diagnosis. Note that k-means clustering was not part of the classifier training phase. The final classifier was only used after "blindly" separating the dataset into clusters using the idea of the "black box prediction engine" suggested by Hastie [181].

5.3 Results and discussion

5.3.1 Spectral database

Mean Raman spectra of the 329 measured tissue specimens (127 BCCs, 92 epidermis and 110 dermis) from 20 patients used to construct the multivariate classification model are presented in Figure 5.1 a). This figure shows that there are spectral differences between BCC and epidermis or dermis, in agreement with previous reported works on skin cancer [2, 5, 64]. The differences between dermis and BCC are mainly due to the presence of collagen I in dermis and not in BCC, as infered from the computed spectrum difference shown in Figure 5.1 b). In addition, the main differences between BCC and epidermis can be explained by the higher amount of DNA in the tumour tissue (see Figure 5.1 c). The higher amount of DNA is caused by the smaller amount of cytoplasm and higher density of cells present in the tumour. Figure 5.2 is a typical H&E image showing regions of 50 μm by 50 μm diagnosed as BCC, epidermis, and dermis from where the Raman spectra were acquired to create the classification model. Regions with higher DNA were found to be darker, e.g. cancerous areas. On the contrary, regions with higher collagen content showed a paler colour, e.g. dermis.

5.3.2 The 2-step LDA-based classification model

Based on the comparison among the mean Raman spectra of the three classes shown in Figure 5.1, six Raman bands have been chosen as "fingerprints" to

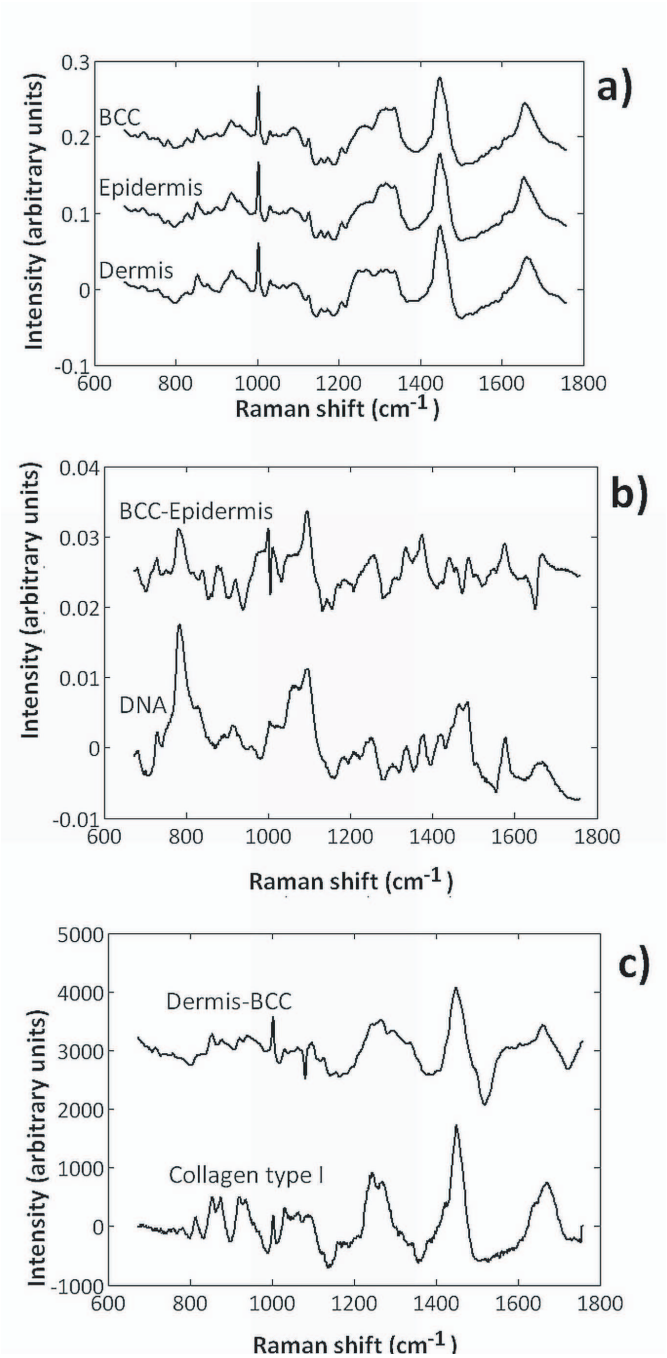

Figure 5.1: a) Mean Raman spectra of 329 tissue specimens, 127 BCCs, 92 epidermis and 110 dermis, from 20 patients used to construct the model. Spectra have been shifted vertically for clarity. Comparison between the Raman spectra of computed differences Dermis minus BCC and BCC minus epidermis are shown in b) and c) along with Raman spectra of purified collagen type I and DNA (Sigma, UK).

discriminate between healthy skin and tumour regions. Selection criterion was to maximise differences among classes, thus the following band area ratios were chosen:

$$r_1 = \frac{I_{788cm^{-1}}}{I_{1003cm^{-1}}}, r_2 = \frac{I_{850cm^{-1}}}{I_{1003cm^{-1}}}, r_3 = \frac{I_{950cm^{-1}}}{I_{1003cm^{-1}}}, r_4 = \frac{I_{1093cm^{-1}}}{I_{1003cm^{-1}}}, r_5 = \frac{I_{1312cm^{-1}}}{I_{1268cm^{-1}}}$$

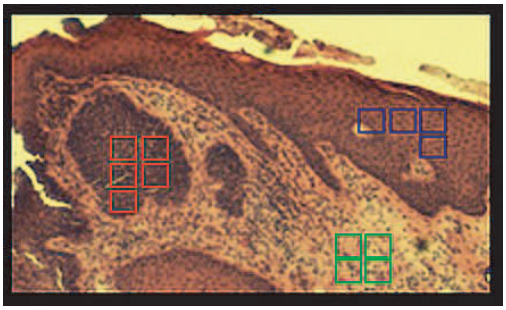

Figure 5.2: *H&E* image of a typical skin tissue section showing measured regions of 50μm by 50μm, being represented as empty squares. Colour code: blue for epidermis, red for BCC, green for dermis.

These Raman bands can be assigned to specific vibrations in DNA and collagen type I as specified in detail in Chapter 4. The intensity of the Raman spectral peak at 1003 cm^{-1} was selected as the denominator of the ratio because it showed only small neglectable differences between classes. For building an automated detection and imaging method the 2-step LDA-based method described in section 5.2.1 was implemented, with the ratios of the peak intensities, i.e. r_1, r_2, r_3, r_4 and r_5 as input parameters.

The model showed that RMS was able to discriminate nodular and morphoeic BCC from healthy tissue with 90±9 % sensitivity and 85±9% specificity in a 70%-30% split cross-validation technique with 92 different partitions. The reported estimates are the means and standard deviations of sensitivity and specificity over randomly chosen partitions. The values obtained for 5−fold CV were 89±11% sensitivity in BCC discrimination and 84±10% specificity, and 94% and 84% for sensitivity and specificity, respectively for LOOCV.

A typical result for CV is shown in Figure 5.3, where all 329 spectra from the spectral database have been classified into 3 groups: red for BCC, blue for epidermis and green for dermis. 70% of the data were used for training the model and are represented as empty circles in Figure 5.3. The other 30% were used for validation of the model, and their symbol in Figure 5.3 is a cross. The two consecutive LDAs are labelled as LDA1 and LDA2, respectively. The blue line (Boundary 1) and the dash red line represent the 95% target sensitivity discrimination lines of LDA1 and LDA2 respectively. The LDA score plot in Figure 5.3 shows that there is a significant clustering of the spectra into three groups corresponding to BCC, epidermis, and dermis.

Misclassification occurs mostly between BCC and epidermis, where clusters overlap over the 95% sensitivity boundary. Such overlap is expected consi-

dering the higher similarity between the mean spectra of BCC and epidermis (see Figure 5.1).

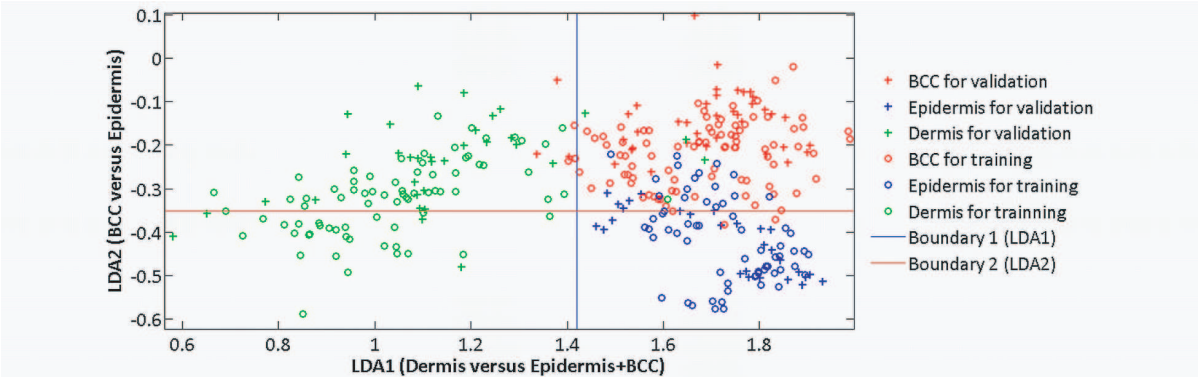

Figure 5.3: Classification of 329 Raman spectra from BCC, epidermis and dermis samples into 3 groups by two consecutives linear discriminant analysis (LDA). The blue line (Boundary 1) and the dash red line (Boundary 2) represent the 95% target sensitivity discrimination lines of the LDA1 and LDA2 respectively. 70% of the data were used for training the model and are represented in the figure as empty circles. The other 30% were used for validation of the model, and their symbol in the figure is the cross. Colour code: red for BCC, blue for epidermis, and green for dermis.

Mean Raman spectra of dermis and BCC in Figure 5.1 show large differences in some of the selected peaks used in the model, such as those for r_5, i.e. the main peaks attributed to collagen. Thus, it could be expected few dermis spectra to be misclassified as BCC and *vice versa*. However, Figure 5.3 shows that there are several dermis spectra located in the middle of the BCC cluster. Inspection of these spectra showed that they were more similar to the BCC mean spectrum of Figure 5.1 than to the mean Raman spectra of the dermis presented in the same Figure 5.1. Comparison with the *H&E* images indicated that these spectra corresponded to inflamed dermis regions, which had a higher amount of cell nuclei than normal dermis. The variability in Raman spectra of dermis depending on its distance to the tumour has already been reported [5].

5.3.3 Raman spectral imaging with the 2-step LDA classifier

The 2-step LDA model was applied to create 2-D biochemical images of tissue sections using two different procedures. In the k-means method, at least 11 classes were required to ensure discrimination between BCC and epidermis. As k-means clustering is an unsupervised method, the presence of any skin irrelevant element or alteration in the sample was detected and classified first as a new class, prior to BCC and epidermis discrimination. After

splitting the spectra into 11 clusters, the Raman band ratios of the centroid spectra corresponding to each cluster were introduced as input in the 2-step LDA model. Therefore, each cluster corresponding to a colour in the pseudo-colour image was classified as BCC, epidermis or dermis. The second method consisted in applying directly the 2-step LDA model to the individual Raman spectra measured at each location of the analysed tissue region to classify each unknown spectrum as BCC, epidermis or dermis. The schemes of both procedures are presented in Figure 5.4. Pseudo-colour images using

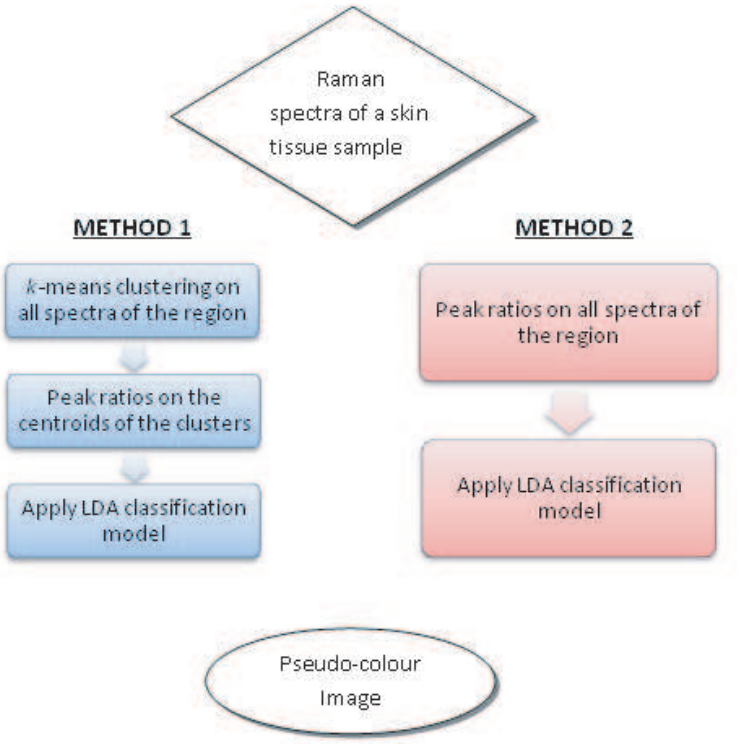

Figure 5.4: Schematic diagram of the two different supervised procedures using the 2-step LDA classification method followed to build 2-D biochemical images of skin tissue sections.

both classification methods are presented in Figures 5.6, 5.5, and 5.7. These figures contain the automated RMS diagnosis and are presented for comparison with the gold standard histopathology images. Typical RMS images of skin sections containing nodular BCC are shown in Figure 5.5. Figure 5.5 a-c) highlights the ability of the RMS models to image tumour regions in a tissue section containing only BCC and dermis. Both dermis and tumour are accurately located within the tissue and are correctly classified. Only a few regions of inflamed dermis are being misclassified as epidermis. The reason of this misclassification is likely to be the lower amount of DNA at those locations. In Figure 5.5 d-f), RMS was used to detect nodular BCC in a typical section containing all three regions included in the model:

BCC, epidermis, and dermis. The correlation of the spectral images with the $H\&E$ image was excellent. Dermis were correctly identified despite the presence of a large number of cells. The k-means-LDA model had a better accuracy in classification of epidermis and less misclassification of BCC as epidermis. Excellent agreement with $H\&E$ staining images was also obtai-

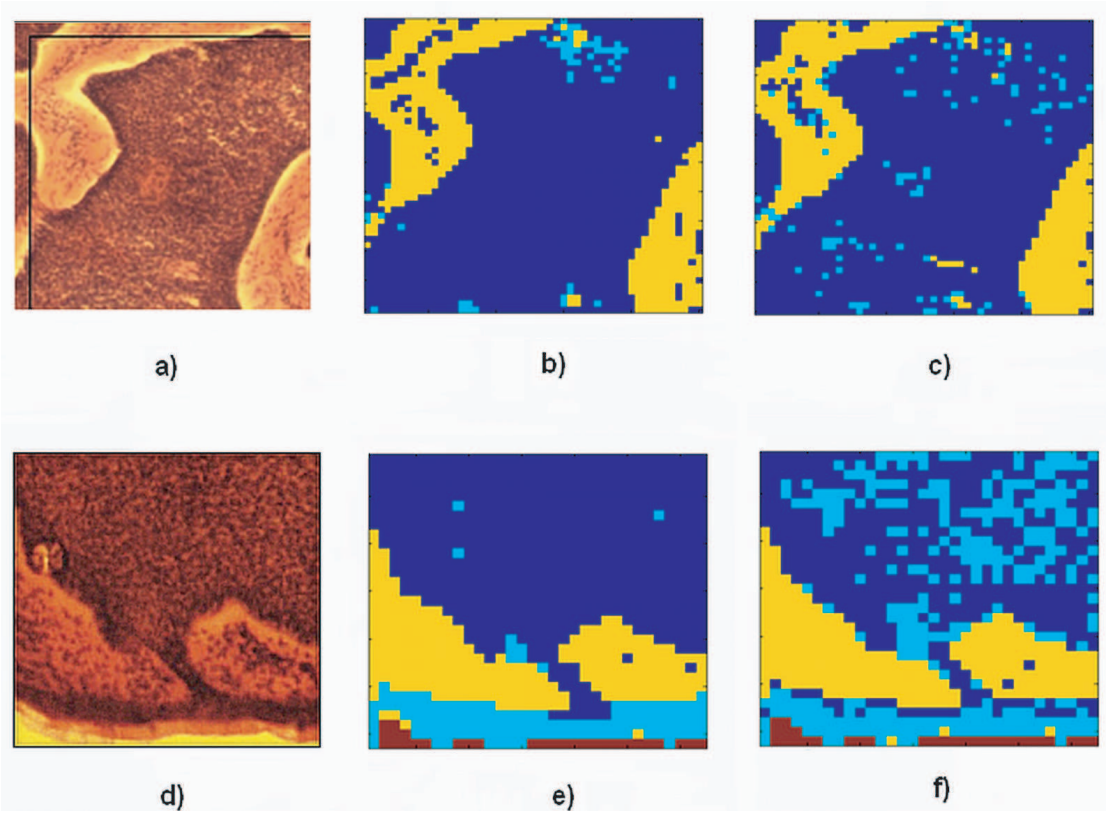

Figure 5.5: Raman spectral imaging of nodular BCC in skin sections. Comparison between pseudo-colour Raman images b), c) and e), f) produced with the two supervised methods and corresponding $H\&E$ images a) and d). Colour codes: yellow = dermis, light blue = epidermis and dark blue = BCC. Images b) and e) were produced by the k-means-LDA method while c) and f) are produced by direct 2-step LDA model. Tissue size: 500 μm by 500 μm.

ned with morphoeic BCC (Figure 5.6), where BCC regions as small as 30-40 μm were detected. In these cases, the k-means-LDA method showed higher number of epidermis misclassification as BCC than direct application of 2-step LDA model to each individual spectrum. However, from a clinical point of view it is crucial that both classification methods were able to detect with high accuracy the presence of nodular and morphoeic BCC within the tissue sections, as well as the dermis regions.

Due to the overlap of BCC and epidermis clusters shown in Figure 5.3 some of the epidermis spectra were misclassified as BCC. This misclassification of epidermis as BCC has a less clinical significance, because if a region at the edge of the tissue is predicted as BCC but shows no BCC regions within the

dermis, it is likely to be misclassified epidermis. Also, areas located deep into the sample been predicted as epidermis are more likely to be BCCs or very highly inflamed dermis rather than epidermis, unless they belong to hair follicles.

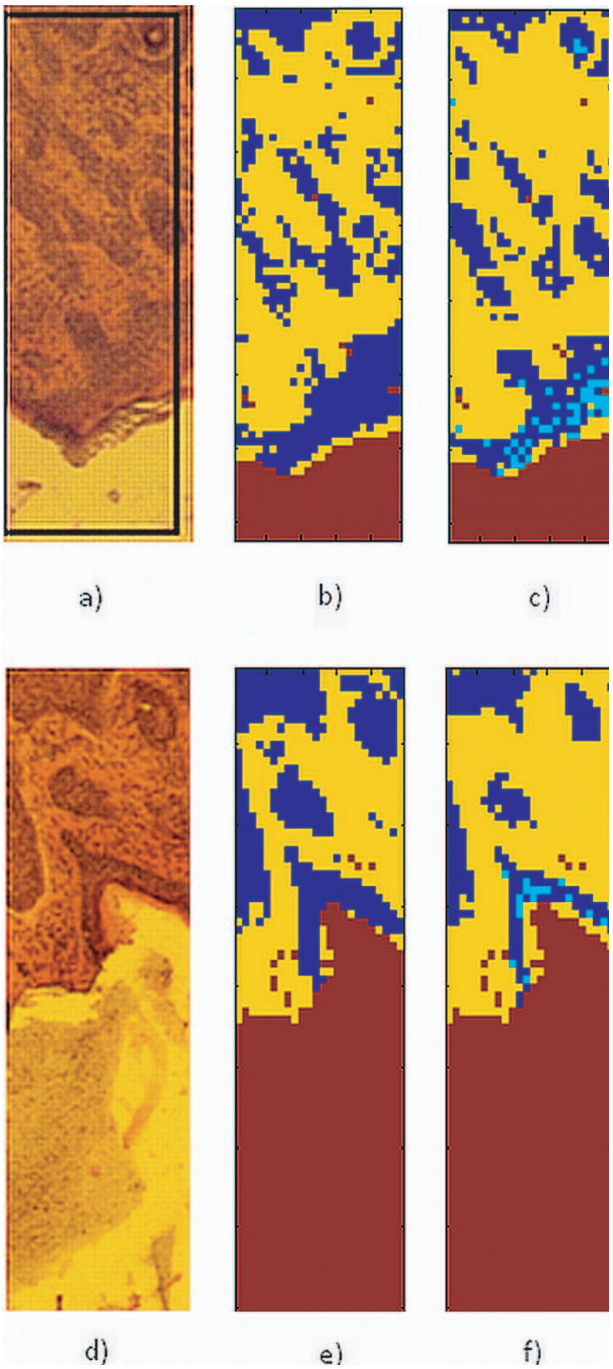

Figure 5.6: Raman spectral imaging of morphoeic BCC in skin sections. Comparison between pseudo-colour Raman images b), c) and e), f) produced with the two supervised methods and corresponding hispathology e *H&E*images a) and d). Colour codes: substrate = brown, yellow = dermis, light blue = epidermis and dark blue = BCC. Images b) and e) were producd by the *k*-means-LDA method while c) and f) are produced by direct 2-step LDA model. Tissue size: a) 240 μm$\times$ 720 μm; d) 240 μm$\times$ 840 μm.

Finally, the technique was applied to skin tissue sections excised during MMS and declared clear of BCC by histopathology (Figure 5.7). Both methods were able to detect dermis with high accuracy and no BCC regions were predicted within the dermis. Some epidermis regions were misclassified as BCC, particularly by the k-means-LDA method, due to the higher spectral similarities between BCC and epidermis.

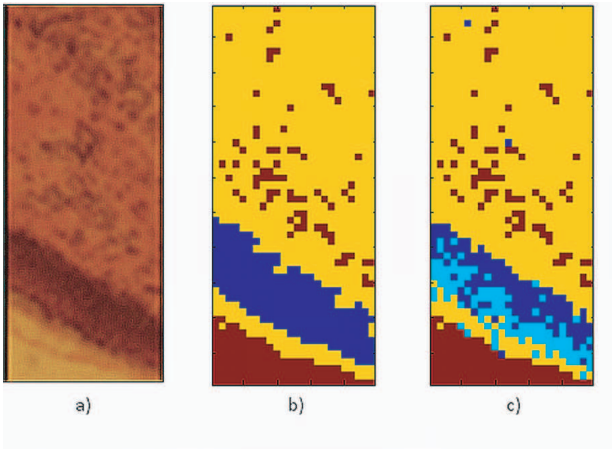

Figure 5.7: Raman spectral imaging of a skin section clear of BCC. Comparison between pseudo-colour Raman images b), c) produced with the two supervised methods and corresponding hispathology $H\&E$ images a). Colour codes: substrate = brown, yellow = dermis, light blue = epidermis and dark blue = BCC. Image b) was produced by the k-means-LDA method and c) was produced by direct 2-step LDA model. Tissue size: 240 μm$\times$ 540 μm.

Despite the current low specificity of the RMS method here presented, this technique may have clinical applicability at its current stage of development. The RMS method may be used to image all tissue layers removed during MMS. Only the sections whose automated diagnosis is "clear of BCC" or where BCC is detected at the edge of a large epidermis section in the Raman spectral images would be evaluated by the surgeon using frozen sections to check that no BCC was missed. As the prediction accuracy and specificity of the RMS method would increase by inclusion of a larger number of tissue specimens, RMS may be used as an automated imaging method for BCC, eliminating the need for frozen section preparation and histopathological observation. In addition, the provision of automated objective diagnosis may also reduce inter-observer variations during the histopathology evaluation of skin sections. These potential changes in surgery practice may lead to an improvement in MMS efficiency, allowing more BCC patients to benefit from the best treatment available.

5.3.4 Spectral imaging of BCC with other classification methods

This section compares the performance of several classification methods on Raman spectral imaging with the 2-step LDA method previously developed in this chapter, when compared to the $H\&E$ diagnoses.

Several common methods for dimension reduction and classification were applied to the Raman spectral data acquired from two skin tissue samples. All of these methods start by drastically reducing the dimension of the raw spectral data followed by classification in the space of reduced dimension, which is known as the feature space. The methods were applied to the same set of skin tissue samples. The classification was performed with the function *classify* of MATLAB changing the different classification algorithms. In order to train the model 329 mean spectra from 20 patients were used (including 127 BCCs, 92 epidermis, and 110 dermis).

Figures 5.8 and 5.9 are images produced by conventional Raman spectral imaging methods and correspond to MMS tissue sections of known histopatholgical diagnosis (see Figure 5.5 (a, d)) and which will be analysed with the 2-step LDA-based diagnostic method, (see Figure 5.5 (b-c, e-f)). One of the skin tissue samples contains only dermis and BCC (Figure 5.8) whereas the other tissue section presents also epidermis (Figure 5.9).

For dimensionality reduction PCA was used as an alternative method to spectral band selection. The images were obtained by selecting the 6, 12, and 20 initial PCs of the hyperspectral dataset thus reducing the dimensions of the dataset from 1024. Taking a larger amount of PCs, e.g. 100, increased the noise in the image without revealing any extra information. The final classification was then based on: multiclass linear discriminant analysis (LDA) for 3 classes, diagonal linear discriminant analysis (DLDA), quadratic discriminant analysis (QDA), and a type of QDA labelled in MATLAB as "Mahalanobis distance classification", which does not correspond to the standard Mahalanobis classifier as described in, for example, ref. [181] but whose assumptions are explained in detail in the following paragraphs.

Any dataset can be represented by points in the feature space which are scattered across regions corresponding to the different classes. The regions divide the feature space and their boundaries are the decision boundaries of the classifier. These boundaries are linear for the so-called "linear classification methods" including LDA and its special case DLDA. An example of a non-linear classification method is QDA which, as it can be inferred from

its name, has a quadratic decision boundary. LDA, DLDA, and QDA are derived by assuming that the features within each class follow a Gaussian distribution. In the case of LDA it is also assumed that all of the classes have a common covariance matrix. The covariance matrix accounts for the pair-wise correlations between the features. The diagonal terms of the covariance matrix are related to the variances of the respective features. If the covariance matrix is diagonal the variables/features are uncorrelated. DLDA is a special case of LDA with the extra assumption that the covariance matrix is diagonal [181].

In contrast to LDA and DLDA in QDA a different covariant matrix is associated to each class. The standard "Mahalanobis classifier" as described in ref. [181] assumes all the class covariance matrices to be equal; thus, it is a version of LDA. The difference between LDA and the standard "Mahalanobis classifier" [181] is that the former sets the decision boundaries to minimise the posterior probability of classification error, taking into account the proportions of the classes in the training set while the latter assumes *a priori* that the classes are equally probable. This classification method measures the Mahalanobis distance (MD) from each point in the dataset to the centroids (mean features) of the classes and assigns to the unclassified point the class of the centroid for which the MD is smallest. The MD between two vectors is computed as the Eucledian distance between them after they have been de-correlated and normalised to unit variance.

However, the classifier used in the computation performed in this thesis and labelled as "MATLAB Mahalanobis classification" assigns to each class its appropriate class covariace matrix without the assumption of these matrices to be equal, similar to QDA. The main difference with QDA is that the "MATLAB Mahalanobis classification" assumes that all the classes are *a priori* equally probable.

Figure 5.8 shows the images produced by selecting the first 6, 12, and 20 PCs of a spectral dataset and classifying them by 3-class LDA. The effect of spectral averaging is also studied. Images without spectral averaging (a-c), and with an average of 4 spectra per pixel (d-f) are presented. The best results are for 6 PCs, either with or without averaging (a) and (d), as they succeed in predicting only 2 classes, in contrast to the 2-step LDA-based classification method. However, when all the classes are present the 2-step LDA-based classification method is more accurate as shown in Figure 5.9.

In Figure 5.9 all the images of each pixel corresponds to the average of 9 spectra. Images with 6, 12 and 20 PCs and linear, diagonal linear, quadratic,

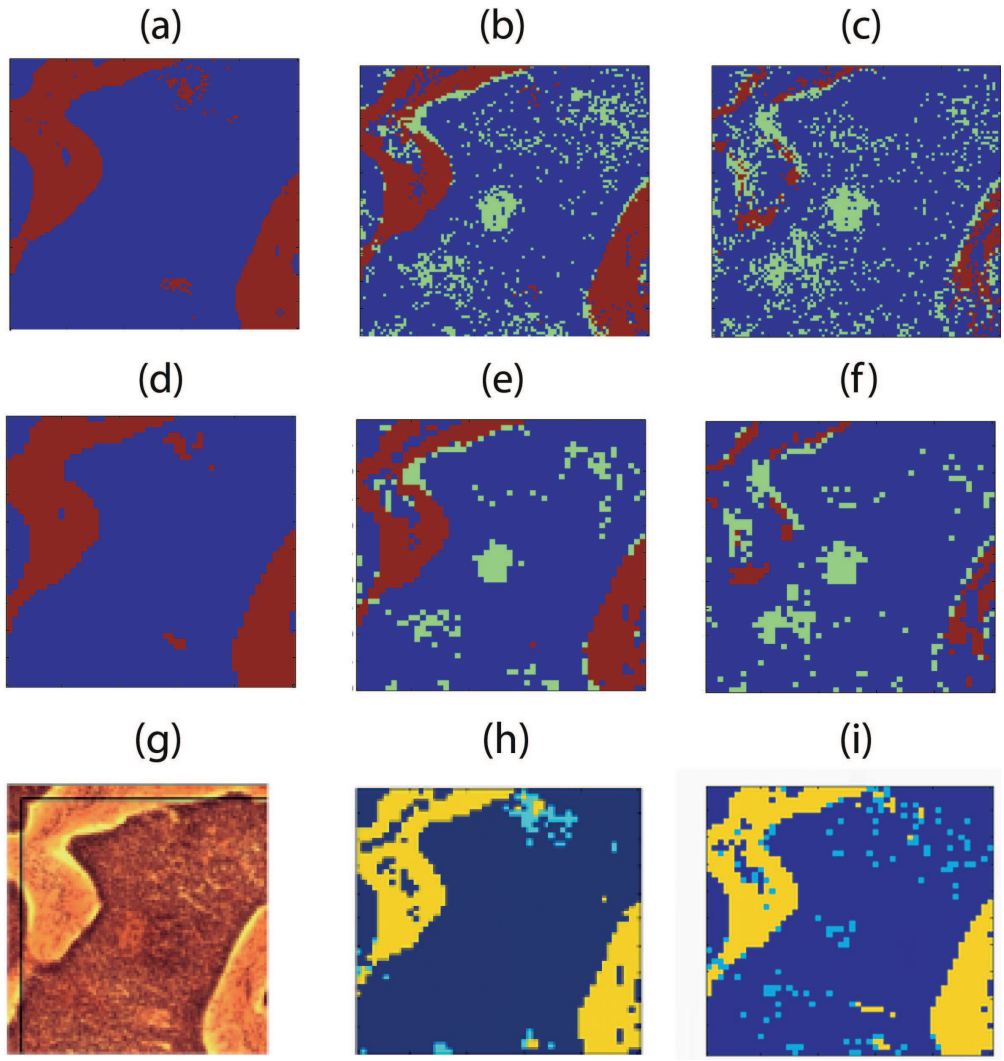

Figure 5.8: Comparison between Raman spectral images produced with unsupervised methods (a-f), the diagnosed histopathological image (g), and the Raman spectral images produced with the supervised 2-step LDA model (h-i). a) 6 PCs, (b) 12, and (c) 20 PCs from spectra with no averaging, classification with linear analysis, (d) 6 PCs, (e) 12 and (f) 20 PCs from image where each pixel is the average of 4 spectra, with linear analysis.
Colour code for (a-f): blue for BCC, green for epidermis, and dark red for dermis. Colour code for (g): dark brown for BCC, lighter brown for dermis. No epidermis present in the sample. Colour code for (h-i): dark blue for BCC, light blue for epidermis, and yellow for dermis.

and Mahalanobis analysis are presented. The images are less accurate than those produced with the 2-step LDA-based model. The best results were found for (i) quadratic and (l) "MATLAB Malahanobis classification" for 20 PCs, where it was found to be a high BCC detection (the model is more sensitive to the presence of cancer), without misclassifying a large amount of epidermis spectra.

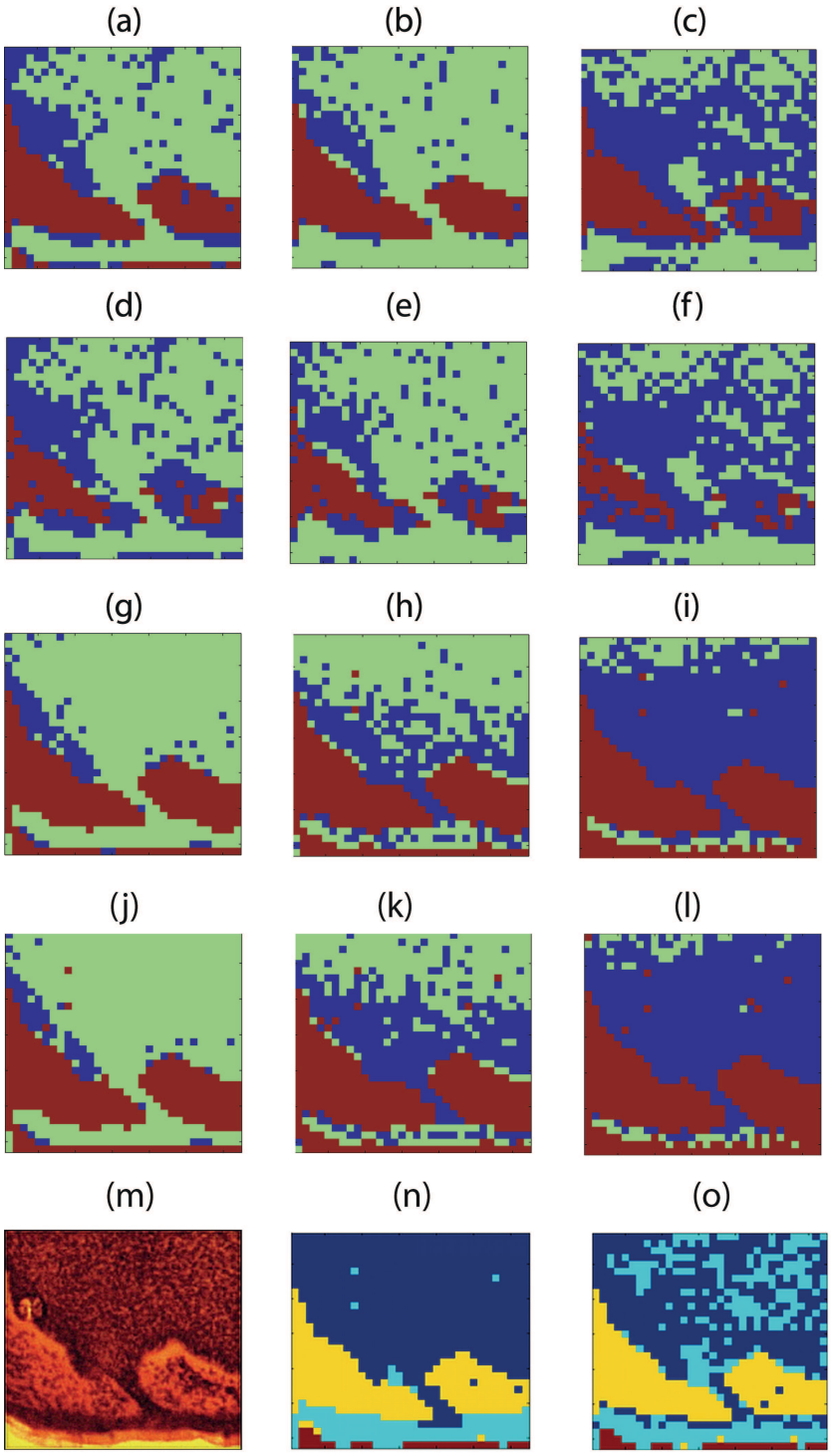

Figure 5.9: Comparison between Raman spectral images produced with unsupervised methods (a-l), the diagnosed histopathological image (m), and the Raman spectral images produced with the supervised 2-step LDA model (n-o).(a) 6 PCs, (b) 12 PCs, and (c) 20 PCs using for classification linear analysis. (d) 6 PCs, (e) 12 PCs, and (f) 20 PCs using for classification diagonal linear analysis. (g) 6 PCs, (h) 12 PCs, and (i) 20 PCS using for classification quadratic analysis. (j) 6 PCs, (k) 12 PCs, and (l) 20 PCs, using for classification the "MATLAB Malahanobis analysis". 100 PCs gave worse results in terms of diagnostic accuracy (not shown).
Colour code for (a-l): blue for BCC, green for epidermis, and dark red for dermis. Colour code for (g): dark brown for BCC, lighter brown for dermis. Epidermis is also dark brown and it is an horizontal line at the bottom of the image. Colour code for (n-o): dark blue for BCC, light blue for epidermis, and yellow for dermis.

5.4 Summary

In this study it is shown that RMS using supervised classification models can be used for detection and imaging of BCC in skin tissue sections excised during MMS. This technique may represent a feasible alternative towards the development of automated tumour imaging during surgery.

The 2-step LDA-model was developed using 329 Raman spectra from 20 patients, including 127 BCCs, 92 epidermis, and 110 dermis. Selected Raman bands corresponding to nucleic acids and collagen type I were computed and used as input into the multivariate model. BCC was discriminated from healthy tissue with 90±9% sensitivity and 85±9% specificity in a 70%-30% split cross-validation algorithm.

The model was utilised to build 2D biochemical images of unknown skin tissue samples excised during MMS. The images were obtained using two supervised methods. The first method applied k-means clustering to the whole spectral database, and then ratios of selected Raman bands for each centroid were computed and introduced into the 2-step LDA-based classification model. The second method directly applied the 2-step LDA model to compute the peak ratios of the whole spectral database. Both analysis methods provided quantitative images by applying a classification model on new tissue samples. The pseudo-colour images revealed the presence/absence of tumour without intervention of histopathologists and determined accurately its location within the sample.

The performance of the 2-step LDA-based classification methods was compared with other common methods, using principal component analysis for dimensional reduction in combination with different classification algorithms: 3-class LDA, quadratic discriminant analysis, a special case of quadratic discriminant analysis named in this thesis as " MATLAB mahalanobis analysis", and diagonal linear analysis. Images with different number of principal components (PCs) were tested: 6, 12, and 20. Larger numbers of PCs were found to produce lower agreement (results not shown). These alternative methods were applied to two samples of nodular BCC already analysed by the 2-step LDA-based classification method, from which the $H\&E$ diagnosis was known. First, an image of nodular BCC presenting only dermis and cancer was studied, fixing the classification algorithm to 3-class LDA, and varying the number of PCs used for dimensional reduction. The best diagnosis in terms of visual agreement with the $H\&E$ evaluated section was given by choosing only the first 6 PCs, either with our without spectral avera-

ging. This image did not falsely predict the presence of epidermis in the tissue section in contrast to the 2-step LDA-based model. However, the 2-step LDA-based classification methods were found superior when the three classes of skin components were present in the tissue sections, for nodular BCC. Images with 6, 12, and 20 PCs were produced varying the classification algorithm (3 class-LDA, diagonal linear, quadratic, and "MATLAB mahalanobis analysis"). The diagnostic images were found less accurate than those produced by the 2-step LDA-based supervised technique. The best results from the alternative study in terms of visual agreement to the *H&E* diagnosis were found for quadratic and "MATLAB mahalanobis analysis" with 20 PCs, where BCC detection was high although lower than that achieved by the 2-step LDA-classification method.

This study demonstrated the ability of RMS for automated diagnosis of nodular and morphoeic BCC; therefore, the first hypothesis of this thesis is verified: *Automated spectral imaging of BCC using RS in combination with mathematical models can be introduced as an alternative to histopathological evaluation of MMS-excised tissue sections.* Further studies are required to establish the ability of this technique to detect more types of BCC.

It is also important to consider that the samples used in this study are samples with straightforward diagnosis, i.e. there was no subjectivity in the diagnosis for a trained histopathologist. This was done in order to assess correctly the performance of RMS, as the histopathological diagnosis was taken as the true diagnosis and compared with the automated diagnosis. In this case the technique does not present any real advantage.

The real potential of this technique lies in the automated diagnosis of samples with difficult diagnosis. Further studies in this direction in order to create a model which allows the distinction of BCC from other skin structures which are morphologically similar to BCC, such as hair follicles or inflammation is of great scientific interest. In addition, the potential of RMS to image BCC regions in tissue blocks has still to be demonstrated.

In conclusion, Chapter 5 demonstrates that it is possible to detect and image BCC using RMS. However, there is a weak point in this approach in terms of practical application in a medical theatre: the time required for data acquisition is too long (hours).

Chapter 6

BCC-hair follicle discrimination by RMS and instrumental development for spectral imaging

This chapter reports two independent studies which attempt to overcome the major two limitations found in the automated diagnosis of basal cell carcinoma (BCC) when the dispersive Raman spectrometer was used.

In first place, a study on automated diagnosis of challenging samples was performed focusing on the discrimination of BCC from hair follicles. Raman spectra corresponding to the epidermal regions of hair follicles were found to resemble more the spectra of healthy epidermis rather than BCC spectra. Comparison between Raman spectral images and the gold standard haematoxylin and eosin (H&E) histopathological slides showed good agreement when comparing the boundaries of the defined tissues by eye with the image boundaries provided by the prediction model. However, a large amount of Raman spectra from the outermost layer of the hair follicle were misclassified as BCC. These misclassified spectra were assigned to the basal cells of hair follicles with higher nucleic acid concentration. This preliminary study showed the ability of RMS to distinguish between BCC and other tissue structures associated with healthy skin which can be confused with BCC due to their similar morphology.

In second place, a Raman spectral imaging prototype designed for shorter acquisition times for imaging and diagnosis of BCC was implemented.

The system combined wide field illumination, Fourier interferometry, and CCD detectors. Although the prototype was not completed due to technical limitations and low cost-effectiveness, the necessary technology and components for its completion are discussed in detail.

6.1 Discrimination between BCC and hair follicles by RMS

6.1.1 Motivation, introduction, and methodology

Histopathological evaluation of the tissues by qualified personnel is a subjective technique and one of the main drawbacks of Mohs micrographic surgery (MMS) as discussed in Chapter 2. The most common staining procedure for the histopathological biopsies is haematoxylin and eosin ($H\&E$). In $H\&E$ treated samples, some skin structures such as inflammation, hair follicles or benign tumours might be confused with certain BCC subtypes due to their apparent morphological similarity and colour after staining [38].

In the study presented in Chapter 5 the focus was on samples with easy diagnosis. This was due to the fact that to build the model it was needed to know with 100% certainty the class of the sample measured. Otherwise the values of sensitivity and specificity of the model would be underestimated. But the real potential of the automated diagnosis with RMS relies on the classification of difficult samples in which a morphological evaluation may be misleading.

In this preliminary study the ability of RMS to discriminate between hair follicles and BCC in skin tissue sections excised during MMS was investigated. Imaging and diagnosis of skin sections was automatically generated using the 2-step spectral linear discriminant analysis (LDA) model described in Chapter 5. Although this model did not include hair follicle as a class, hair follicles are primary invaginations of the epidermis. Understanding this biochemical similitude, the performance of the 3 group classifier in discriminating epidermis from BCC is tested. Depending on the morphology and position of such epidermis spectra within the tissue, this spectra would be interpreted as hair follicle or outer epidermal layer. Therefore, with *a posteriori* interpretation of the spectral class returned by the 3 group classifier, images containing 5 classes were produced. Such classes are: hair, hair follicle, epidermal layer, BCC, and dermis.

In *H&E*-stained skin samples hair follicles adopt the same dark blue colour as the external epithelial layer, inflammation, and BCC. In samples with BCC, epidermis surrounding hair follicles might be confused with malignant tissue especially if the *H&E* stained slides are a tangential cut of the hair follicle showing the base of the follicle. In these specific cases epidermis forming the hair follicle appears in the hair cross-section as a solid circular BCC-like shape (and not in a hollow ring form). Examples of *H&E* skin tissue specimens with straightforward and difficult diagnosis are shown in Figure 6.1.

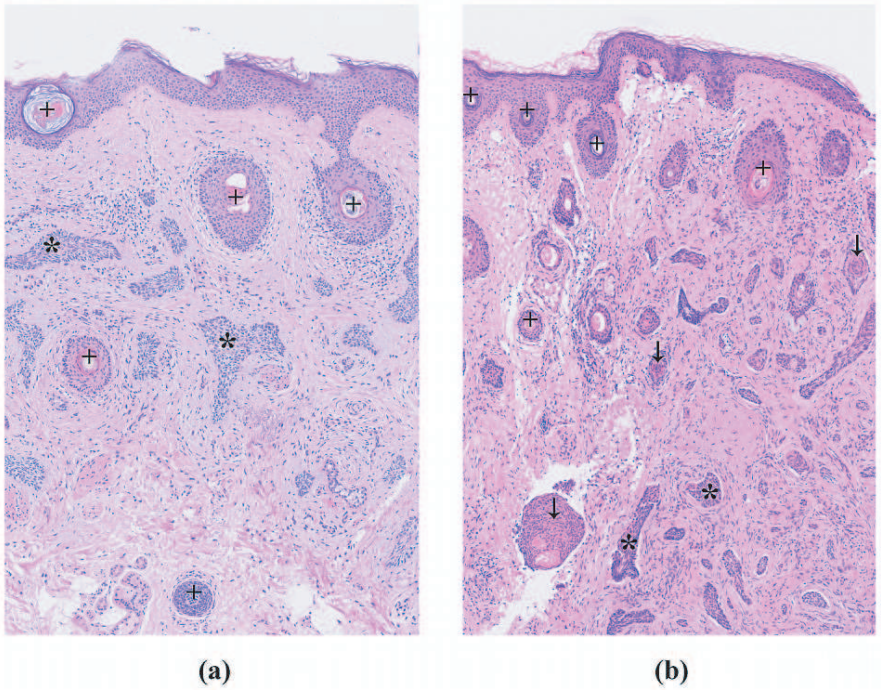

Figure 6.1: *H&E* images of two MMS sections of skin tissue where hair follicle-BCC diagnosis is (a) straightforward to the trained histopathologist, and (b) difficult to discriminate. Symbol code: crosses (+) over easy-to-diagnose hair follicles, asterisks (*) over clear BCC regions and arrows (↓) pointing regions where diagnosis is difficult and not clear.

The same experimental set-up, skin sample preparation, data acquisition and analysis as described in Chapter 5 were used in this study. The 2-step LDA model described in Chapter 5 was tested on new skin tissue sections presenting hair follicles and BCC, as well as epidermis and dermis.

6.1.2 Results and discussion

Figure 6.2 shows the *H&E* image of a typical skin section excised during MMS which contained BCC, epidermis, dermis, and hair follicle. The left image of Figure 6.2 is a *H&E* image of the MMS-excised sample with

the labels included after histopalogical evaluation. Although $H\&E$ images tend to be in blue and pink colour as in Figure 6.1, the results presented in Figure 6.2 showed DNA in dark brown and dermis in pale orange due to the camera calibration. In the right hand side of Figure 6.2 the mean

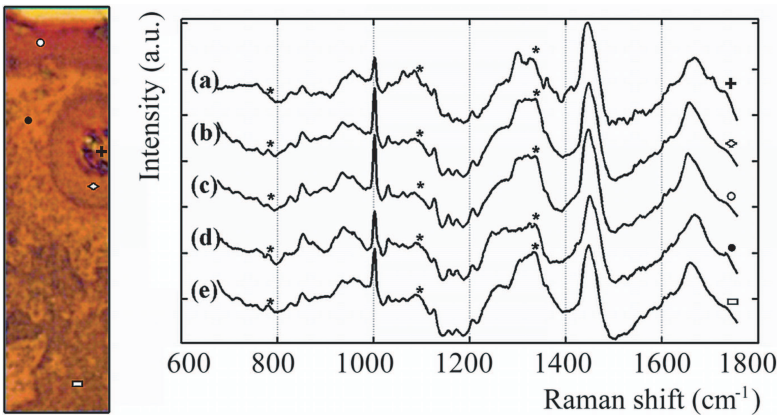

Figure 6.2: Right: Raman spectra of different regions within a skin tissue section. The labels correspond to: (a) hair, (b) hair follicle, (c) epidermis, (d) dermis, and (e) BCC. Asterisks correspond to main DNA peaks and collagen peak. Left: $H\&E$ image of the skin tissue section from where the Raman spectra where taken. Symbol code: empty circle for epidermis (○); filled circle for dermis (●); rhombus for hair follicle (◇); rectangle for BCC (□).

Raman spectra of the regions corresponding to each feature are presented. Asterisks have been introduced to highlight the Raman bands at 788 cm^{-1}, 1093 cm^{-1}, and 1350 cm^{-1} assigned to the main peaks in DNA and collagen type I (see Chapter 4).

In agreement with the previous RMS study Figure 6.2 confirms that BCC has a higher amount of DNA compared to the other tissue regions associated to the higher cell density in cancerous regions. The Raman spectrum of dermis was similar to the spectrum of collagen type I and showed lower contribution from DNA than epidermis and BCC (there are fewer cells in dermis). Furthermore, these results agree with the study done by Barry *et al* [175] where the Raman bands of *stratum corneum* were reported. The *stratum corneum* is the outermost epidermal layer and it is composed mainly by keratin. Hair is also mainly formed by keratin and therefore the Raman spectra of hair and *stratum corneum* are expected to be similar.

The hair spectra were found to have a strong Raman spectral peak at 1447 cm^{-1} assigned to the CH_2 deformation (protein vibration), a medium-strong Raman spectral peak around 1667 cm^{-1} assigned to the in-plane peptide carbonyl stretching vibration (C=O stretch) of the amide I band, a medium Raman spectral peak at 1003 cm^{-1} associated to the aromatic ring CC stretching mode of phenylalanine, a strong-medium peak at 1300 cm^{-1} assigned

to the deformation mode of the CH_2, and two medium broad peaks at 1324 and 1330 cm^{-1} that might be due to the CH_3CH_2 wagging mode in purine bases of DNA and to phospholipids or DNA [65, 176].

Less intense Raman spectral peaks were measured at 829 cm^{-1}, 852 cm^{-1}, 956 cm^{-1}, 1032 cm^{-1}, 1061 cm^{-1}, 1085 cm^{-1}, 1126 cm^{-1}, 1155 cm^{-1}, 1173 cm^{-1}, and 1206 cm^{-1} which may be due to aliphatic and aromatic deformation of CCH, CH_2 rocking, CH_3 rocking or olefinic deformation of CCH, skeletal vibrations of CC, COH deformation, again CC vibrations and CH_2 deformation, respectively [65, 175]. A weak broad Raman spectral peak was found at 890 cm^{-1} probably associated to CH_2 rocking. Finally a shoulder was detected at 1360 cm^{-1} which might be due to tryptophan [175, 176].

To identify the differences between epidermis, BCC, and hair follicles the computed difference spectra of BCC minus hair follicles, and BCC minus epidermis are presented in Figure 6.3 and compared to the Raman spectrum of purified DNA. Asterisks highlight the main DNA peaks which can also be observed in the difference spectrum. Figure 6.2 shows that the Raman spectrum of hair follicle has a higher similarity to epidermis than to BCC. This agreed with the results shown in Figure 6.2(a-b), in which the similarity between the Raman spectrum of hair follicle and the measured spectrum of the epidermal layer was clear, in consistency with their anatomical nature (see Chapter 2).

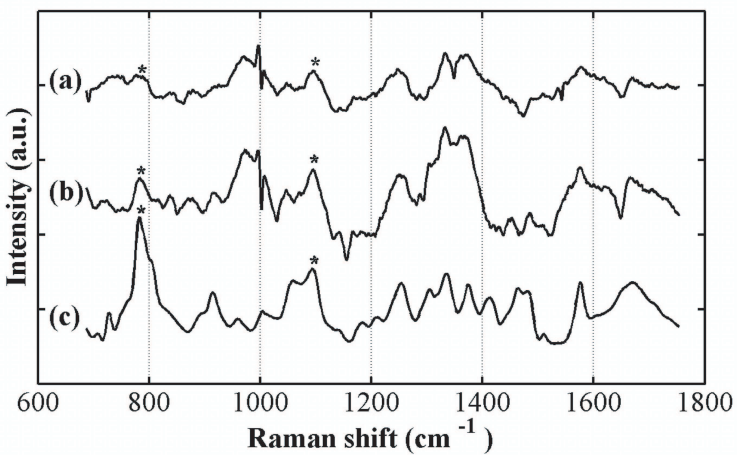

Figure 6.3: Raman spectra of (a) difference between BCC and hair follicle spectra, (b) difference between BCC and epidermis spectra and (c) DNA. Asterisks correspond to main DNA peaks.

Figure 6.4 shows the comparison between the Raman spectral image and the $H\&E$ image of the same tissue section. The spatial resolution of the Raman spectral image is 10 μm. Figure 6.4 shows a good agreement between the Raman spectral image and the gold-standard histopathological

diagnosis showing good classification of BCC, epidermis, dermis, hair, and hair follicles. The majority of the hair follicle and epidermis spectra were classified as "epidermis".

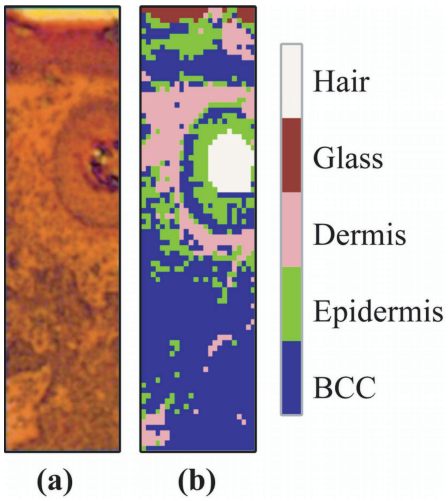

Figure 6.4: (a) *H&E* image of the skin tissue section from Figure 6.2.; (b) Raman spectral image.

Although the presence of BCC in the sample was correctly predicted several false positives were found mainly for regions of epidermis and hair follicles with higher DNA concentration. These regions were mainly found at the edges of the hair bulb which correspond to the basal layer. As BCC arises from this layer, it is likely to resemble basal cells not only morphologically but also from a chemical point of view, as these cells have less cytoplasm and an increased nucleus-to-cytoplasm ratio than the rest of the cells in the hair follicle.

Dermis was also correctly predicted. However, cases presenting inflammation were several times misclassified due to their higher concentration of cells.

6.1.3 Conclusions and future work

This section showed a preliminary study of RMS using supervised classification models for producing images discriminating BCC from hair follicles in skin tissue sections excised during MMS which may present a clinical challenge to histopathologists. The introduction of RMS as an optical diagnostic tool to enhance chemical information from MMS samples is especially interesting in these cases where morphological information is not sufficient to discriminate between normal skin structures and malignant lesions.

The previously developed 2-step LDA-model based on supervised Raman spectral peak selection (BCC discrimination with 90±9% sensitivity and

85± 9% specificity) was used in this study to create Raman spectral images taking into consideration the *a priori* knowledge that cells forming hair follicles biochemically resemble epidermal cells. The classes included in these Raman spectral images were BCC, dermis, epidermis, hair, and hair follicles. The Raman spectra of hair follicles had a higher amount of nucleic acids than the external epithelial layer spectra. Raman spectral images showed high visual agreement with $H\&E$ diagnosed images by visual comparison of the boundaries of the $H\&E$ diagnosed tissues with the image boundaries provided by the prediction model.

Further studies are required to include Raman spectra from a large number of skin samples with hair follicle, as well as other structures found in healthy skin but often misdiagnosed as BCC. The Raman spectra of such skin structures must be included as separated classes in the classification models to make the process automated. Future work in building a larger model database with more classes and which can produce images of larger areas is needed. Such new models are more likely to increase the accuracy rate for BCC diagnosis.

6.2 Wide-field Fourier transform Raman spectral imaging

The development of a new fast Raman spectral imaging system combining wide-field Fourier-transform (WF-FT) Raman and two dimensional detectors − e.g. a CCD −, might be the solution to long-time data acquisition. The new approach presented in this section combined RMS with interferometry and digital technology in order to visualise the chemical composition and molecular structure of the skin samples. This approach would integrate the main advantages of RMS such as diffraction limited spatial resolution at the sub-micrometre scale, minimal sample preparation, and chemical specificity [146] with the high acquisition speed of wide-field sample illumination (the whole sample is illuminated at once with an expanded laser beam). An advantage of using Fourier transform spectroscopy with 2D imaging detectors (CCDs or CMOS detectors) is that information was recorded from three different channels. Each pixel from the 2D detector had an associated interferogram that after a Fourier transformation returned two spatial coordinates and an extra coordinate related to the phase difference between the two beams interfering in the detector. This hyperdimensional data recording allowed reconstruction of Raman images of the sample under observation. A Raman spectrum was produced for each pixel on the 2D detector which had a one-to-one spatial correspondence with the skin tissue sample.

The idea of the described system was recently patented by Koo [8] but to the knowledge of the author of this thesis it has not been experimentally demonstrated. If feasible, this instrument might be the solution to overcome long acquisition times in Raman spectral imaging. The aim of the current study was to build cost-effectively such an instrument and test its operational principle. Its application to skin cancer imaging was far beyond the aims of this thesis, although it was the starting motivation of this piece of work.

6.2.1 Results and discussion

Interferograms were recorded onto a secure digital (SD) card via the oscilloscope. The sampling frequencies used were always higher than the Nyquist frequency to ensure true reproducibility of the signal.

Laser interferogram with Si photodiode

The laser beam propagating through free-space was focused on a glass slide on the microscope stage. The signal was detected by the Si PIN photodiode. The signal had sinusoidal shape (see Figure 6.5) as expected for interferograms of a monochromatic source. The intensity of the signal along the whole scan (25 mm) varied significantly likely due to slight interferometric errors in alignment. The power spectrum was obtained by Fourier transformation.

The maximum of the power spectrum of the laser was recorded at 533.3 nm (for the 532 nm-wavelength laser). The base of the peak had a width of 17.8

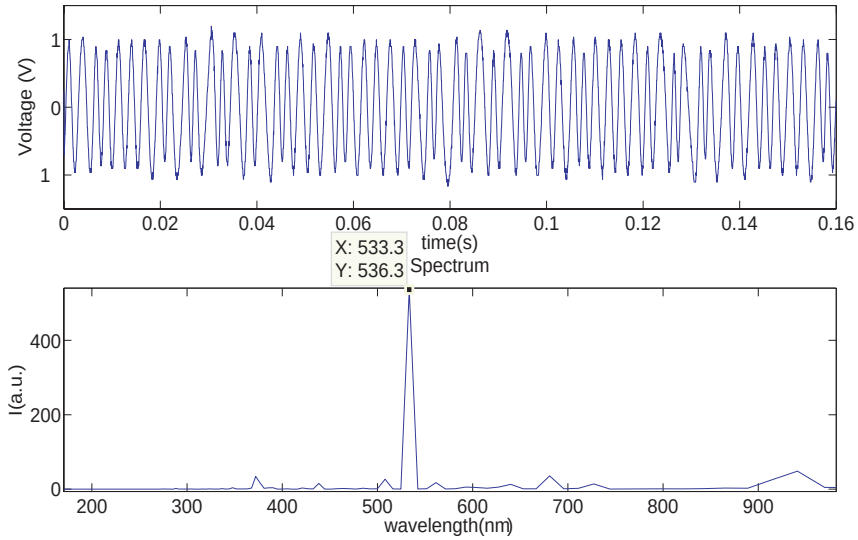

Figure 6.5: Laser interferogram on photodiode after amplification. Mirror velocity $v = 0.1\text{mms}^{-1}$ and sampling period of 4.10^{-5}s.

nm. The measured resolution corresponds to the width of the peak at half maximum, which was approximately 10 nm. Due to the limitation on the oscilloscope data storage the recorded interferogram had a temporal length of 0.16 s which limited its resolution.

In order to study the dependence of the spectral resolution on the temporal length of the interferogram, temporal lengths of 1.6 s were acquired. Results are shown in Figure 6.6. The sinusoidal dependence of the signal from Figure 6.6 is difficult to assess visually due to the high frequency of the signal. The maximum of the spectrum appears at 530.7 nm. The base of the peak reduced to a width of 3.5 nm. Therefore, the measured resolution was approximately 2 nm. The resolution improved by a factor of 10 with respect to that estimated for Figure 6.5.

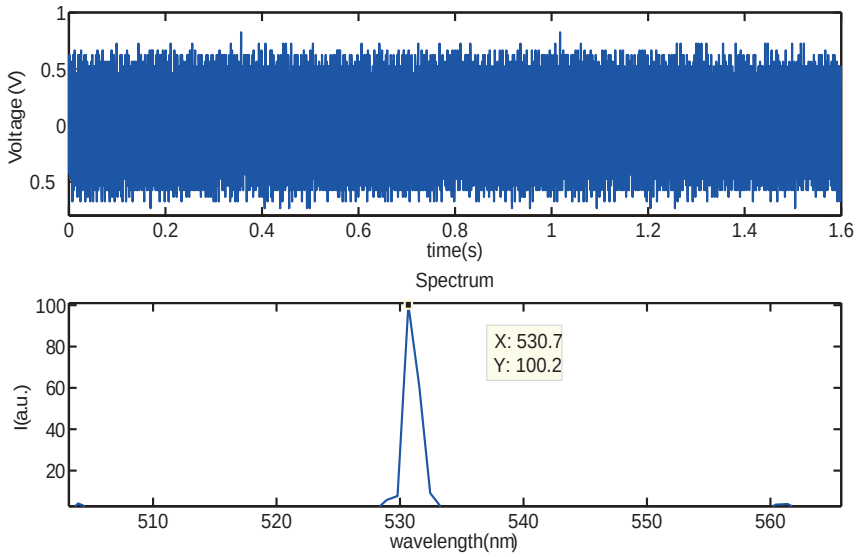

Figure 6.6: Laser interferogram on photodiode increasing the temporal length interval. Mirror velocity v=0.1mm/s and sampling period of 4.10^{-5} s.

Interferogram of laser with Si photodiode

For the laser interferogram the maximum laser intensity was detected changing the glass coverslip by a mirror in order to reduce beam energy losses. In this case the voltage from peak-to-peak V_{pp} of the signal was around 100 mV and the noise of 20-60 mV. This implies a SNR of 3.5-14.0 dB. With such high levels of SNR for the laser interferogram with a mirror, the Raman signal from a sample was expected to be completely buried by the noise. Before measuring the Raman signal from any sample noise levels needed to be reduced. First, noise due to imperfect instrumentation must be minimised. This includes the noise introduced by the operational amplifier used in the current-to-voltage converter. Second, the interferometer should be placed in an isolation platform to reduce undesired vibrations. Third, the photodiode could be substituted by a detector with a smaller shot-noise, e.g. a high sensitivity CCD. Fourth, beam loss could be minimised by using fibre optics or shortening the distances travelled by the beam of light through air.

White light interferogram with Si photodiode

Interferograms of white light were measured on the Si PIN photodiode. The temporal coherence of the 532 nm laser was very large. In order to de-

termine the point of zero path difference (ZPD) between the arms of the interferometer a source with a broad spectrum was used. A halogen light source (HL-2000-CAL, Mikropack, Ocean Optics, USA) with spectral output in the range of 300-1000 nm and maximum power for wavelengths of 900-1000 nm was chosen. A broad green filter of 494-618 nm (AP-820901, Chengdu shi Ji Zhongke Instrument Co., China) was introduced into the optical path in order to help in ZPD identification. Light was coupled to the microscope port via an optical fibre of 100 μm-diameter (P100-2-VIS/NIR, Ocean Optics). A pinhole of 50 μm-diameter was introduced to ensure the spatial coherence of the source. A typical example of the results obtained is shown in Figure 6.7.

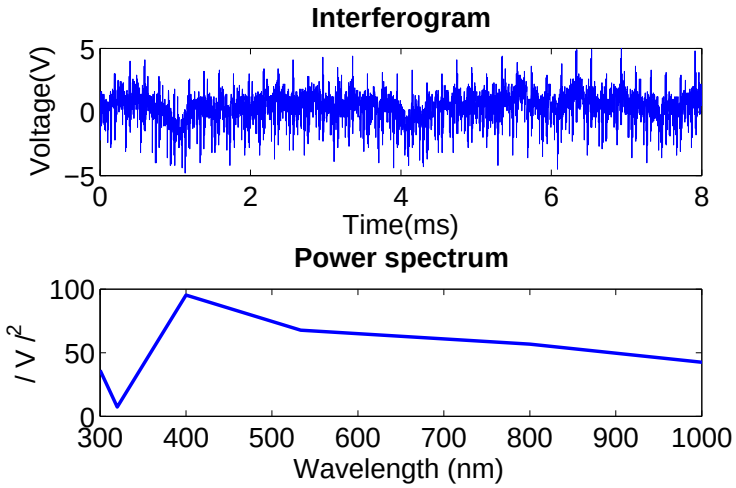

Figure 6.7: Interferogram of fibre-coupled halogen light after amplification, introducing a 50 μm pinhole in the system and recorded using the Si PIN photodiode detector. Sampling time of 4.10^{-5} s and driving velocity of the mirror $v = 0.1\text{mms}^{-1}$.

These spectra do not represent clearly the 494-618 nm spectral band of the white light. The signal was buried under the noise. One solution to improve the SNR might be to use a more powerful laser with a maximum power of around 100-300 mW. As previously mentioned, another possibility is to mount the interferometer on an isolation platform. It may be also a problem of the detector. The maximum power density reached by the halogen lamp was 100 μWcm^{-2} for a wavelength of 1000 nm. The area of the emitting source is the area of the cross-section of the optical fibre which connects the lamp with the focal plane of the microscope objective, which was 1.57×10^{-4} cm^2. Assuming no power losses in the system the photodiode would detect a maximum power of 14.14 nW. As the photosensitivity of the diode is of 0.44 AW^{-1}, the maximum intensity that could be detected is of approximately 6.22 nA. The minimum dark current in the photodetector

was 0.1 nA. Therefore, the photodiode was replaced by a detector of higher photosensitivity such as the CCD model previously described.

Laser interferogram with CCD

The instrument described in the previous section was modified by replacing the halogen light by laser light. A CCD was used for data acquisition. Laser light was guided by a 100 μm-diameter optical fibre connected to the stage of the inverted microscope. The signal was collected by a 50× objective. In the microscope the signal was attenuated by the 532 nm dichroic beam-splitter considerably reducing its intensity. A filter was added to avoid CCD saturation.

In order to test the ability of the CCD in acquiring a 2D set of spectra to produce meaningful images, hyper-dimensional cubes recording information from the 2 spatial coordinates and the spectral one were created with MATLAB-based software. As a first approach, a very small number of images were taken with the CCD, for example 30 frames. In a step-scanning approach the mirror was moved in steps of 50 nm. The main aim of this experiment was to recover an image showing the spatial distribution of the laser spot. The final image was created from the spectra associated to each one of the pixels of the CCD. The measured intensities of each CCD pixel at different positions of the mobile mirror gave one interferogram per pixel. These interferograms were Fourier transformed to obtain their correspondent one-to-one spectra. Note that due to the low amount of frames recorded in this first manual approach, low spectral resolutions were obtained. For recovering an accurate spectrum the process would need to be automated, the number of frames increased in 2 or more orders of magnitude, the step size reduced, and the number of images per step at least duplicated. The velocity at which the nanomover drove the mirror was 5000 nm(s^{-1}).

Once all the spectra were calculated (one per pixel of the CCD), they were dimensionally reduced. In other words, from the 1024 spectral channels characterising each spectra only certain spectral bands were kept to build the 2D images. In the case of the laser spectra a univariate approach was performed. Only the intensity of the spectral band with maximum at 532 nm-wavelength was used. The information enclosed in this band was sufficient to build a 2D image whose points relate one-to-one to the spatial coordinates X and Y of the sample. In addition, the colour distribution of the image represented the intensity of the 532 nm-wavelength spectral band of the sample. The image showed the position of the laser spot within the

whole mirror surface. Note that the laser spectrum was only recovered at certain positions (pixels) of the CCD chip.

Figures 6.8 and 6.9 show the recovered spectra for two different positions of the CCD chip. Figure 6.8 corresponds to the laser spectrum and Figure 6.9 is the spectrum from the background signal. In future experiments with the Raman signal different spectra from different locations within the sample will allow the reconstruction of chemical images (Raman maps) of the sample specimen.

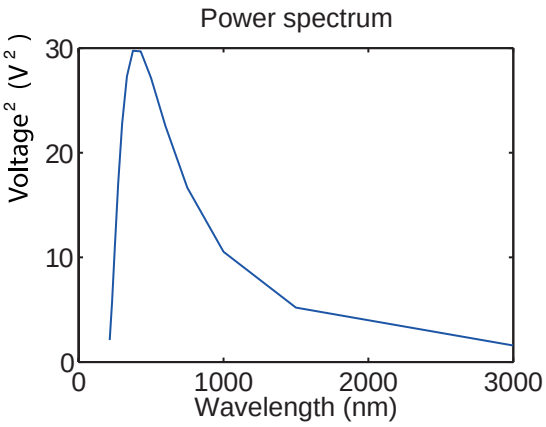

Figure 6.8: Spectrum of the laser.

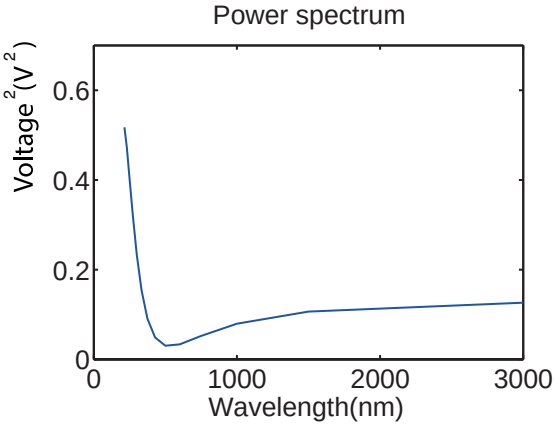

Figure 6.9: Background spectrum.

As it is clear from Figure 6.8 the spectral resolution of this result is not sufficient. The system has to be automated to record hundreds of frames if the aim is to recover accurate spectra. However, within this project it is only possible to show the working principle of the future design.

Figure 6.10 is one of the 30 pictures directly recorded on the CCD chip, for a fibre-coupled laser placed on the objective focal plane at each one of the 30 positions of the mobile mirror. Each one of those 30 frames was used to build up a total of 2.5856×10^4 interferograms. The hyper-spectral cubes were subsequently Fourier transformed using the fast discrete Fourier transformation function of MATLAB, obtaining one spectrum per pixel of the 2D chip. Figure 6.11 shows the final 2D intensity image obtained. It was built by selecting the spectral band corresponding to the laser wavelength for all the spectra within a selected CCD area of 101×256 pixels. Note that the images in Figures 6.10 and 6.11 did not present a circular laser spot, as expected. This is due to an artificial optical effect called blooming. Blooming is produced by overflow of the excess of photo-generated electrons from one pixel to the adjacent pixels of the CCD chip. It occurs when the

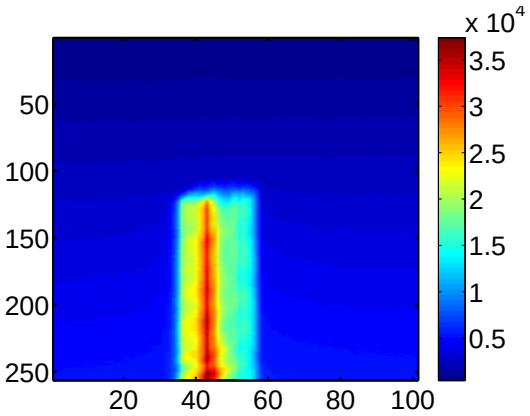

Figure 6.10: Number of photons reaching a region of the CCD when illuminating the Raman imaging system with a fibre-coupled laser. Axis correspond to pixel number of the CCD.

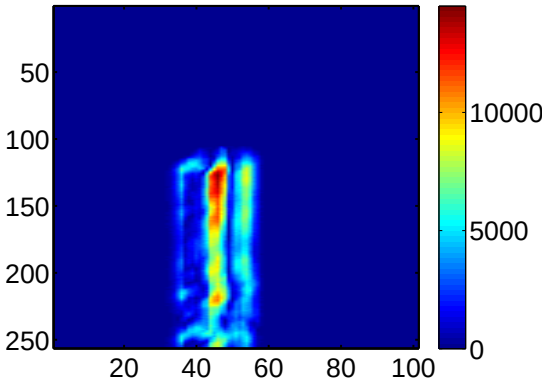

Figure 6.11: Image showing the intensity of the peak at 532 nm from the spectrum recovered by Fourier transformation of the interferograms measured by the Raman imaging system. Axis correspond to pixel number of the CCD.

maximum charge transfer capacity of the CCD is reached. A reduction in the exposure time considerably reduces the blooming effect, as less light arrives at the photo-sensors and consequently, charge-transfer saturation is not reached. Figure 6.12 shows the effect of varying the CCD shutter time.

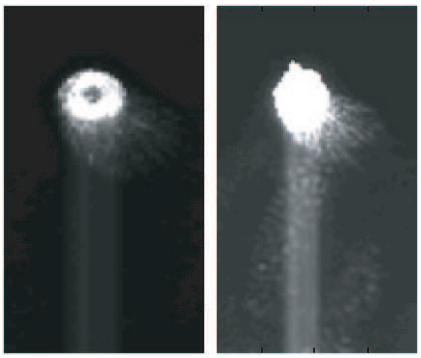

Figure 6.12: Image of the laser light through a 150 μm-diameter pinhole recorded by the CCD at different shutter times: **(a)** 5 s **(b)** 10 s.

In these images, the blooming or streaking effect is present, i.e. a bright column appeared which is a CCD artefact.

White light interferogram with CCD

White light has a shorter temporal coherence length than laser light. Acquisition of white light interferograms is much more difficult experimentally as it can only be achieved in a range of 1 μm around the ZPD point. In order to facilitate the process a green filter was introduced into the optical

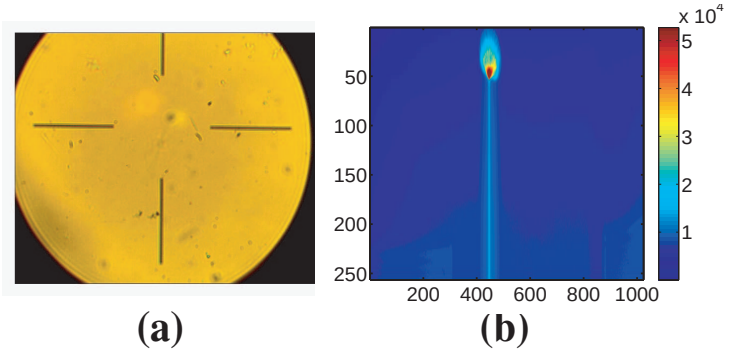

Figure 6.13: **(a)** Image with the 50× objective of the exit of the 100 μm-diameter optical fibre coupled to a halogen light and 150 μm pinhole and **(b)** image detected on the CCD chip. The axial coordinates correspond to pixel number. No filter was introduced.

path. Note that due to the broad spectral bandwidth of the filter used, the temporal coherence length would only be slightly increased, and this is why it was important to use the oscilloscope in triggering mode to find the ZPD point. A step-scanning experiment was performed moving the mirror 16 times with a step-size of 50 nm around the estimated ZPD point. The base velocity of the mirror was 5000 nm(s^{-1}). Results are shown in Figure 6.14 from which is clear that the filter considerably reduced the throughput of the instrument. Resolution should be improved by increasing the number of data points recorded by system automation. Light between 300-700 nm was detected with the CCD. Light in the range of 494-618 nm was expected as the spectral bandwidth was limited by the passband of the filter.

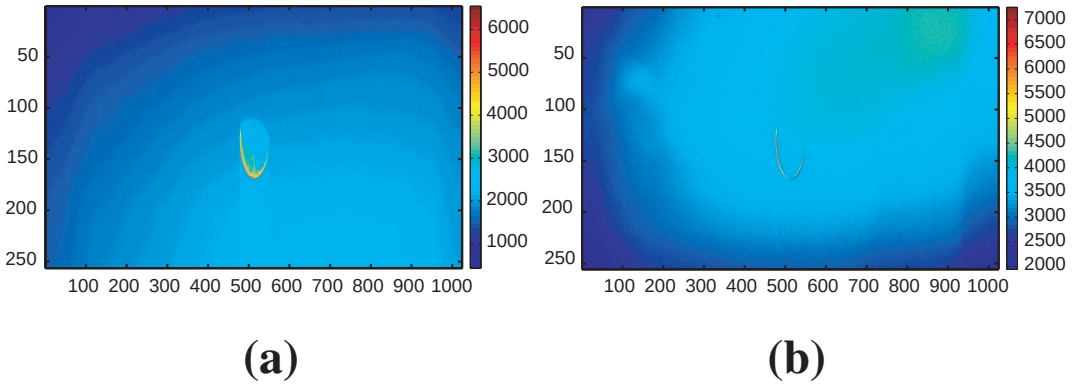

Figure 6.14: Intensity image of the light detected in the CCD illuminating the system with a halogen fibre-coupled source, introducing a 150 μm-diameter pinhole and a green filter in the optical path. **(a)** Directly detected by the chip for one position of the mirror. **(b)** Image produced by selecting a spectral band around 500−600 nm-wavelength in the Fourier-transformed spectra related to each CCD pixel. Axes correspond to pixel number of the CCD.

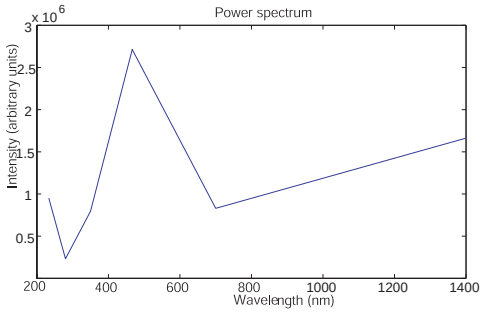

Figure 6.15: Spectrum of the halogen light with wide green filter obtained for one position of the CCD chip, sampling for 16 positions of the mirror.

6.2.2 Conclusions and future work

Conclusions

The aim of the study presented in the second part of Chapter 6 was to evaluate the feasibility of a cost-effective Raman imaging prototype, as a first step to a fast alternative to current techniques, which could be applied for wide-field Fourier transform Raman imaging. However, the instrument did not have sufficient sensitivity or spectral resolution to enable the detection of Raman signals even for a strong Raman scatterer such as a polystyrene. The most likely sources of error are:

- Interferometer misalignment, which is of extreme importance when working with polychromatic light.
- High levels of noise. In theory, the resolution is mainly limited by the quantum or shot noise of the detector. However, the device performance may be affected by other types of noise such as thermal, mechanical or electronic. The performance of interferometric systems is known to be highly dependent on noise levels. These levels of noise can mask the weak Raman signal, making it completely indistinguishable from the background.
- Velocity mismatching of two of the components used in the system: the nanomover for mirror driving and the CCD camera. A slower nanomover or a faster CCD would be required to reach the desired spectral resolution (10 cm^{-1}).

Potential solutions for these problems

A customised system built with high-accuracy commercial components might be the solution to the practical trade-offs of the current prototype. However,

the system would not be cost-effective, which was one of the main motivations of this study. For such an instrument which should be optimal for tissue imaging the following equipment might be considered:

- A powerful NIR laser (current model is a visible laser of a maximum power <5 mW).
- A new inverted microscope and suitable objective with high numerical aperture to effectively collect the weak Raman signal.
- A commercial interferometer with step-scanning and mirror alignment control over entire scan.
- A fast photon-sensitive detector (slower if the interferometer allows step-scanning).
- A vibration isolated optical bench.

Future work

The optimal commercial equipment to build the first wide field Fourier transform Raman imaging system would need to reach a compromise between budget and performance. After an exhaustive search and direct contact with the leading manufacturers the following three options for building a feasible instrument are suggested:

(a) Laser illumination: powerful Ti-sapphire CW laser working in the NIR (700-1000 nm) (3900S, Newport-Spectra Physics).

Interferometer: Customised Nicolet 8700 FT-IR (Thermo Fisher Scientific) spectrometer, with a quartz beam splitter and step-scanning mirror driving.

Detector: Photon-sensitive fast (but not ultrafast) CCD. The current CCD (DV420-OE, Andor) might be fast enough when combined with step-scaning.

(b) Laser illumination: Ti-sapphire laser, as defined in 1.

Interferometer: Perkin Elmer 100NIR spectrometer customised (without source, detector or sample positioned in one of the arms of the interferometer). It requires 1,300 fps at minimum mirror scan velocity (1 mms^{-1}).

Detector: Focuscope SV200i is a CMOS sensor fibre coupled to a GenIII image intensifier, allowing single photon sensitive. It can reach up to 2,000 fps without need of pixel binning (area of 512×512 pixels^2). It has a good response at wavelengths around 785 nm.

(c) Laser illumination: Ti-sapphire laser, as defined in 1.

Interferometer: MIR8025 (Newport). It comes with 3 possible mirror driving velocities. The slowest corresponds to 3.15 mms^{-1}, which implies the need for a CCD able to record at least 16,051 fps. The maximum mirror displacement is 12.7 mm, and the maximum resolution achievable is of 0.4 cm^{-1}.

Detector: FASTCAM SA1.1 or FASTCAM SA5. These ultrafast cameras record up to 675,000 fps and 1,000,000 fps, respectively. However, they are not single photon-sensitive, so they might require to be coupled with an intensifier. A GaAs multiple micro-channel plate (MCP) stage intensifier such as the model C10880-03 (Hamamatsu Photonics) will allow an increase in sensitivity detection of 6 orders of magnitude, achieving single photon detection. A GaAs photocathode was chosen because it has a higher sensitivity, which implies a higher QE. Further research might be done to find the optimal photocathode material.

6.3 Summary

This chapter is a continuation of the study presented in Chapter 5 in which two important issues related to the previous work in skin cancer are covered.

On the one hand, samples of difficult diagnosis including hair follicles were investigated. On the other hand, the problem of the long acquisition times required to produce the Raman spectral images was addressed, and the instrumental development of a new Raman spectral imaging prototype which could tackle this major drawback, reported.

The chapter tests the third and fourth hypotheses of this thesis:

- 3^{rd}*) Discrimination between hair follicle and BCC can be accurately obtained with the RS automated method and applied to MMS-excised tissue sections of difficult, ambiguous diagnosis.*
- 4^{th}*) A fast Raman spectral imaging instrument combining wide-field Fourier transform Raman spectroscopy and charged coupled devices (CCD) can be cost-effectively built and designed for its future application to skin oncological research.*

In this small feasibility study, hair follicle was identified from BCC and epidermis as hypothesised. The distribution of predicted layers may enable identification, alternatively a 5 group classifier could be developed in the future.

Although the fourth hypothesis of this thesis was rejected, the reported study opens new avenues of investigation in the field of Raman imaging instrumental design. It underlines practical problems encountered when building the instrument and proposes several feasible approaches to create a non cost-effective prototype with customised commercial equipment.

In the next chapter a different application of Raman spectroscopy in biology is covered: the investigation of thin supported lipid films, where once again the performance of this versatile technique was tested.

Chapter 7

Characterisation of supported lipid layers by simultaneous AFM and SERS

In this chapter an integrated instrument combining atomic force microscopy (AFM) and surface enhanced Raman spectroscopy (SERS) was used for simultaneous chemical and mechanical characterisation of supported lipid layers (SLLs). Different materials such as sapphire and mica, and several surface modification treatments were investigated for manufacturing of optically transparent SERS substrates. These substrates were produced by nanosphere lithography (NSL) and optimised for spectroscopic investigations of the SLLs. The optimal SERS substrate maximises the SERS signal while allowing AFM characterisation of the lipid layer(s) on its surface with nanoscale accuracy.

In this study different amphiphilic molecules were used: first, fatty acids (arachidic acid −AA−) and then, phospholipids (DPPC). SLL deposition was carried out by different techniques: Langmuir-Blodgett (LB) trough, vesicle fusion, and spin coating. The performance of these deposition methods is discussed in detail.

AFM topographic characterisation of supported lipid monolayers and hydrated bilayers fabricated with the LB method and vesicle fusion was demonstrated. However, simultaneous SERS measurements did not allow the detection of thin lipid films deposited with the latter techniques. In contrast, cationic DPPC and AA multilamellar arrangements of 15-25 nm thickness produced by spin coating on silver/sapphire SERS-active substrates were

successfully and simultaneously characterised by the AFM-SERS system.

These results show the ability of this "dual" technique as a non-invasive label-free method for characterisation of thin supported lipid layers. The current study is a step forward towards chemical and topographic imaging of more complex thin lipid architectures including lipid mixtures, which may be used as models for cell membranes or other applications.

7.1 The design of SERS-active substrates

The main experimental aim discussed in this chapter is the design and fabrication of a SERS substrate that is optimised for maximum enhancement of the Raman signal of supported lipid films. As a first approach, homogeneous lipid membranes would be investigated. Imaging lipid rafts needs a high topographic accuracy in order to detect height differences of only 1-2 nm corresponding to these phase-separated domains, as well as a technique able to identify the lipids and measure the thickness of the membrane. The choice of the substrate must enable detection of nanometre height differences for its future use with lipid mixtures. The ideal substrate needs to satisfy the following requirements:

(a) Flatness and uniformity: atomically flat substrates would allow detection of nanometre height differences between phase-separated domains of the films. Substrates with roughness higher than 4 nm are not suitable for topographic characterisation of the lipid monolayers or bilayers, which are approximately 2-4 and 4-8 nm of height respectively. Multilayer arrangements of 3 or more monolayer stackings might allow greater flexibility in the roughness of the substrate. However, in any case atomically flat surfaces are ideal. Polished single crystal sapphire and freshly cleaved mica are preferred to glass, quartz, and MgF_2 [165].

(b) SERS enhancement must be of around 10^5 and consistent over large areas. For maximising the surface plasmon resonance effect the substrate should present sharp metallic nanosized features. If the adsorbate to be characterised is a uniform lipid bilayer whose dimensions are greater than those of the nanostructures then, it is desirable that the nanostructures are arranged in a way that they promote a uniform enhancement. NSL is the technique chosen to produce the metallic nanopatterns due to its cost-effectiveness and for being a well established

technique for SERS substrate preparation [182]. The optimal size of the spheres for this study is 400 nm as shown by Sweetenham [91] which allows a high and uniform enhancement of the signal. Separations in the metallic nanostructures of around 400 nm between the 25 nm-height sharp metallic features compromise the need for a high density of metallic nanostructures to achieve maximum Raman enhancement and at the same time minimise the effect on the homogeneity of the membrane. Note that 400 nm diameter spheres imply interstructural distances of the order of hundreds of nanometres and consequently, coupled surface plasmon resonance effects are not present. Silver is preferred to gold due to a higher Raman enhancement factor associated to a greater coupling of the surface plasmon resonances with the 532 nm laser [165, 183]. However, silver quickly oxidises while gold remains oxide-free. Oxidation could introduce chemical impurities into the lipid layer. This may reduce the experimental reproducibility and introduce other unexpected phenomena altering the uniformity in the adsorption of the membrane on the surface of the substrate. This drawback connects with the next requirement.

(c) The substrate needs to enable lipids to be adsorbed on its surface. The affinity of lipids to form a uniform bilayer chemically and electrostatically stable need to be considered. Absence of organic contaminants and oxides might be crucial. Different substrate treatments prior to lipid deposition were studied. High radii of curvature of sharp protuberances or undesirable wetting properties of the material may affect lipid deposition on the substrates.

(d) The basis material (or "*matrix*") of the SERS-active substrate − i.e. the planar solid support on which the metal structures are formed− needs to be hydrophilic (or turned hydrophilic) prior to the nanosphere lithography process. This requirement facilitates polystyrene bead deposition (see nanosphere lithography protocol).

(e) Optical transparency to visible light is needed because the Raman signal generated by the excitation of a 532 nm visible light laser is collected in transmission mode with an inverted Raman microscope. The inverted configuration is more suitable for AFM measurements, especially in liquid environment.

(f) The Raman spectrum of the substrate alone must not cover the Raman signal of the lipid bilayer. Substrates with low background (low self-

fluorescence) and few number (if any) of peaks in the spectral bands of interest for lipid identification are needed.

(g) The substrate has to be thinner than 0.28 mm for compatibility with the working distance of the 60× water immersion 1.2 NA objective of the Raman microscope. Mica can be peeled into thin layers, and sapphire of the required thickness is also available.

7.2 Substrate fabrication step 1. The planar solid support

Mica and sapphire were investigated as planar solid supports or "*matrix*" materials of the SERS-active substrate with the AFM-Raman micro-spectroscopic instrument. The Raman spectra of mica and sapphire are shown in Figure 7.1. Spectra were acquired for 5 s at 20 mW laser power. Note that the measurements are taken over a quartz window. The quartz holder has been designed to keep the SERS samples in TRIS buffer solutions. The introduction of an extra interface in the measurements and an increase in the Raman background are the pay-off in order to better reproduce a natural environment with controlled pH. Figure 7.1 is discussed in detail for each substrate in the following section. A vertical translation was applied to the spectra for easiness in comparison.

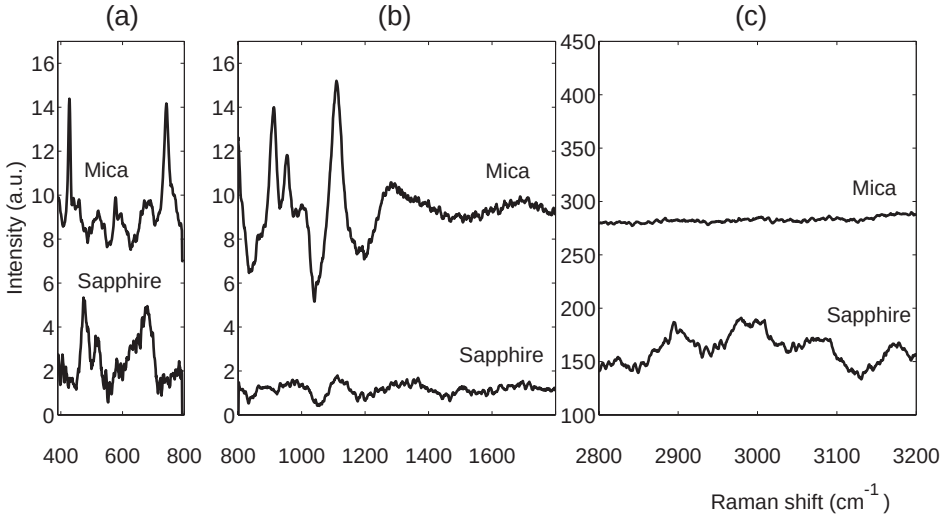

Figure 7.1: Raman spectra of mica and sapphire in (a) the lower spectral region, (b) the fingerprint region, and (c) the CH stretching mode region.

7.2.1 Mica substrate

Muscovite mica sheets of 0.15 mm of thickness (G250-3, Agar, UK) were freshly cleaved with a sterile surgical razor blade allowing large atomically flat 11×11 mm^2 areas, satisfying requirements 1 and 7 (see section 7.1). This method provided superior results than cleavage with a masking tape where chemical contamination and smaller flat areas were achieved. Results of an AFM line profile of the topography of razor cleaved mica versus that cleaved with tape are presented in Figure 4.10. Good cleavage was found critical for the success of the experiment. Cleaved mica is hydrophilic and optically semi-transparent to visible light, satisfying criteria 4 and 5. It does not need to be cleaned from organic contamination as long as the cleavage is done immediately prior to the measurements.

In previous SERS studies [165] mica was considered unsuitable as the "matrix" of the SERS substrates due to its high density of peaks in the lower part of the "fingerprint" spectral region. For example, the lipid Raman spectral peak centred at 795 cm^{-1} (see Chapter 4) is likely to be masked by the Raman spectral contribution of the substrate. However, results displayed in Figure 7.1 show that mica does not present sharp strong Raman peaks for Raman shifts higher than 1300 cm^{-1}. This study investigates the performance of mica as a SERS substrate in higher parts of the Raman spectrum (1300 cm^{-1}-1800 cm^{-1} and 2800-3000 cm^{-1}) where there are other Raman spectral bands characteristic of the lipids such as the 1438 cm^{-1} spectral peak, the 2800-2900 cm^{-1} spectral peaks corresponding to the CH stretching or the 1655 cm^{-1} Raman spectral peak appearing only in unsaturated amphiphiles (see Chapter 4, section 4.4.2).

7.2.2 Sapphire substrate

All chemicals for substrate preparation were of analytical grade (Sigma-Aldrich, UK) and used without further purification. Two-side polished 0.26 mm thick sapphire wafers (requirement 7 of section 7.1) of 2 inches of diameter with C-plane crystallisation (Pi-Kem, UK) were cut to 11×11 mm^2 areas with a diamond tip pen and piranha cleaned for 1 h (solution of 3:1 sulfuric acid $-$ H_2S0_4 $-$ and hydrogen peroxide $-$ H_2O_2 $-$) for removal of organic contaminants and turning the surface of the substrate hydrophilic (requirements 3 and 4 of section 7.1). As seen in Figure 4.10 (d) the roughness of the substrate is found to be of a maximum of 1 nm.

7.3 Substrate fabrication step 2. Nanosphere lithography.

7.3.1 Nanosphere lithography protocol

All chemicals were of analytical grade (Sigma-Aldrich) and used with no further purification. For the NSL protocol ref. [182] was followed. 2 μl of 1:1 solution of ethanol and 384 ± 20 nm diameter polystyrene latex beads (PLB) (Varian, USA) were spread on hydrophilic silicon wafers (111) (PI-KEM) of dimensions $3{\times}2$ cm^2 letting the solvent evaporate. The silicon wafers were previously cleaned by immersion and ultrasonic bath in L-acetyl lactate, acetone, and isopropanol. The wafers were turned hydrophilic by treatment with piranha solution (3:1 H_2SO_4 and H_2O_2) for 1 h, followed by 24 h soaking in 10% sodium dodecyl sulphate solution (SDS) in deoinised water (Millipore, Milli-Q resistivity, 18:1 MΩcm). Slow vertical dipping of the silicon wafers into a water bath allows the transfer of the self-assembled closed-packed polystyrene bead (PB) aggregates into the water-air interface. 2 μl of 2% SDS solution in deoinised water was added to the water bath to change its surface tension enhancing the packing of the nanospheres into larger aggregates. The deposition on the freshly razored mica and the hydrophilic sapphire substrates was done by vertical dipping and withdrawal of the substrate into the water bath. For deposition of only one monolayer of closely packed spheres on the surface of the sapphire and mica substrates several quality control samples were made. PB deposition on control samples of hydrophilic glass (previously piranha cleaned for 1 h) were observed using a microscope (see Figure 7.2).

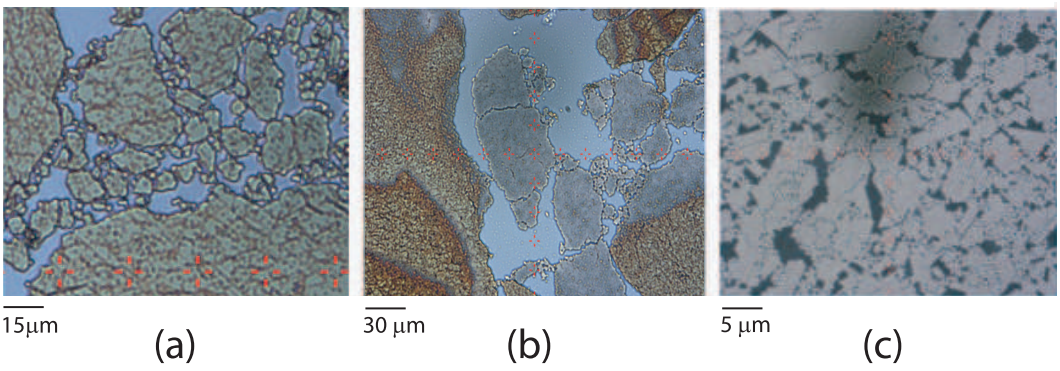

Figure 7.2: Closed packed polystyrene latex beads (PLB) on control samples of hydrophilic glass (a-b) and sapphire (c). Monolayers show a clearer light grey colour while multilayers present a brownish colour. (a) and (c) correspond to a PLB monolayer while (b) presents areas of monolayer and multilayers.

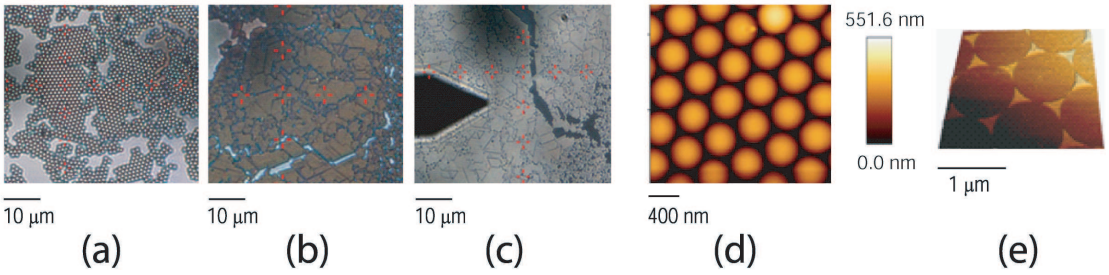

Figure 7.3: Nanosphere lithography process. (a) Optical image of a monolayer of closely packed 400 nm polystyrene latex beads (PLB). (b) Silver layer on PLB sample. (c) After PB removal. (d) AFM image of a PB monolayer. (e) 3D representation of an AFM height image of the substrate after PLB removal.

One of the main problems of using NSL to produce SERS substrates is the low surface coverage of the self-assembled closed-packed PB arrays. High hydrophilicity of the surface of the substrate is a key element for successful deposition of large areas of closed packed sphere aggregates. The increase in the time of the piranha etching to 1 h (as in ref. [184]) was found to facilitate the latex bead deposition in the sapphire and glass substrates. Success in deposition on mica substrates was highly dependent on a successful cleavage. It was also observed that a decrease in the amount of PB solution spread on the silicon wafers from those quantities previously reported by other studies [165, 182] from 4 to 2 μl produced larger areas of monolayers of closely packed spheres.

An automatic thermal evaporator (Edwards, USA) was used for deposition of 25 ± 1 nm of silver over the layer of latex spheres in vacuum at a pressure of $2-4\times10^{-7}$ mbar and deposition rate of $0.3-0.5$ nms^{-1}. Finally, the PBs were removed by different solvents depending on the nature of the substrate. Glass and mica were immersed for 10-15 min in dichloromethane (CH_2Cl_2), washed in an ethanol flow to remove the detached PBs, and dried under a N_2 stream. CH_2Cl_2 was preferred to tetrahydrofuran (THF) as it was found to produce larger areas of periodic patterns.

The samples were not immersed in an ultrasonic bath in order to avoid silver detachment from the substrate. If the mica surface was not atomically flat the detachment of the silver was much more likely to occur. This phenomenon has been reported in the literature [185]. Suggested solutions to silver detachment are to evaporate an intermediate material such as chromium or titanium to increase the adhesion of silver to mica. This is a common procedure also to attach gold to glass [186, 187]. It has been reported in NSL studies that for mica the deposition of chromium as an intermediate layer does not improve the adhesion of the metal to the substrate surface [188].

Sapphire substrates were found to respond better to treatment with THF than to CH_2Cl_2 or toluene. The samples were immersed in an ultrasonic bath for 20 s in ethanol to dissolve and remove completely the polystyrene spheres.

In order to minimise the oxidation of the silver, the sphere lift-off by solvents was carried out on the day prior to the lipid deposition day.

7.3.2 AFM characterisation on control substrates prior to lipid deposition

The SERS substrates were characterised before deposition of the lipids to ensure that the silver structures did not detach during removal of the PB spheres. Figure 7.4 is a 3D representation of a height image of a sapphire/Ag SERS-active substrate where the silver pyramids detached due to an excessive solvent exposure. The higher (white/yellow) regions of the image correspond to the remaining silver while the dark periodic arrangements correspond to the areas where the metallic nanostructures were previously attached. Figures 7.5 and 7.6 show typical AFM height images of mica/Ag

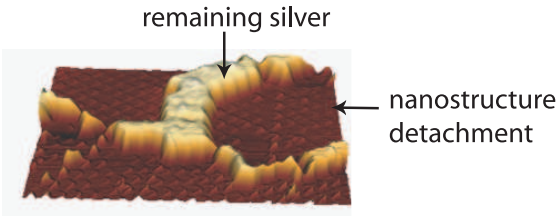

Figure 7.4: 3D AFM height image of a mica/Ag substrate where the silver metal nanostructures have detached.

and sapphire/Ag substrates produced by NSL. The effect of plasma cleaning the substrate after NSL was studied. Plasma cleaning is a common procedure for the removal of organic contaminants and increase of the hydrophilicity of surfaces such as gold. However, it has been reported that oxygen plasma cleaning can turn the surface structure of sapphire amorphous [189]. Furthermore, oxygen plasma might accelerate the oxidation of silver. Argon plasma was chosen for the plasma cleaning experiments. Samples were exposed to high energy plasma for 5 min at 150°C. An AFM height image before and after treatment with the plasma is displayed in Figure 7.7. The figure shows that plasma cleaning the SERS-active substrates after silver deposition increased the surface roughness and irreversibly modified the metallic

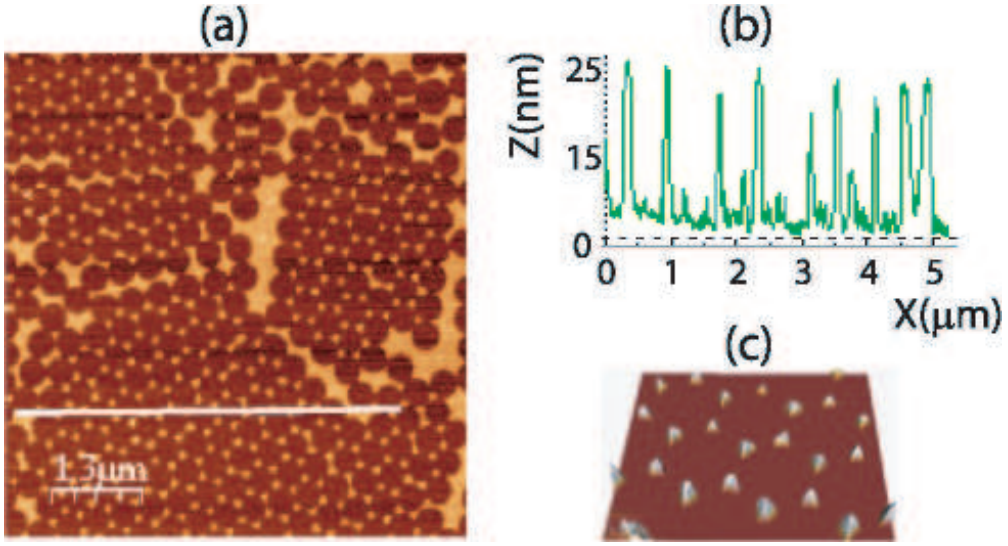

Figure 7.5: Mica/Ag SERS substrates after NSL (a) AFM height image and (b) line profile of a typical mica/Ag SERS-active substrate produced by NSL. (c) 3D AFM height image showing the atomic flatness of the mica "matrix".

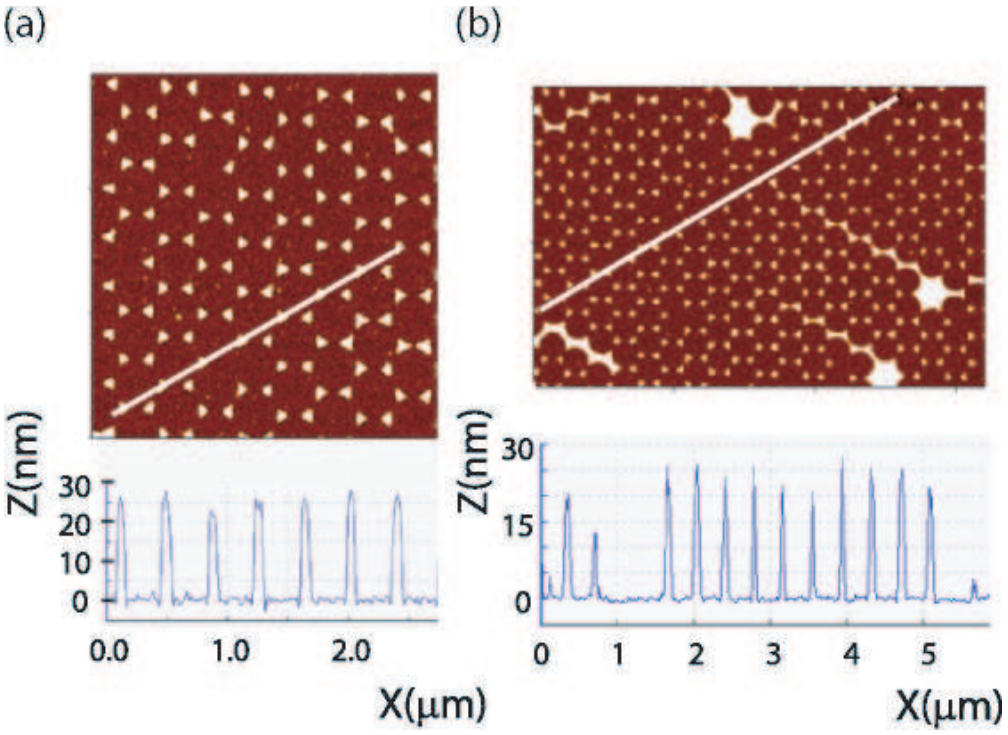

Figure 7.6: Sapphire/Ag SERS substrates after NSL. (a) and (b) are typical examples of sapphire/Ag AFM height images and their line profiles.

nanostructure periodic patterns. Therefore, plasma cleaning treatment was not applied in the NSL protocol.

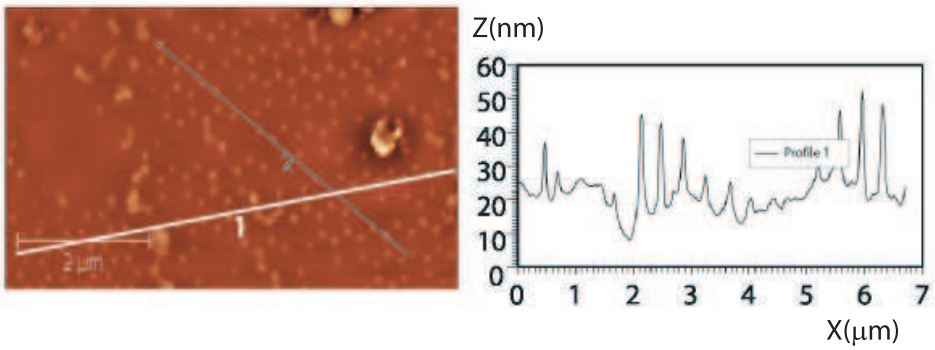

Figure 7.7: Effect of plasma cleaning on a sapphire/Ag SERS-active substrate.

Figure 7.8 shows two AFM images of NSL substrates made of Ag/glass for comparison with typical examples of NSL substrates of mica/Ag and sapphire/Ag. Roughness of the glass matrix in the SERS-active substrates was found to be 5 nm or higher. This made glass substrates not suitable for AFM studies on lipid bilayers where height resolution of 1-2 nm is required (see requirement 1 of section 7.1).

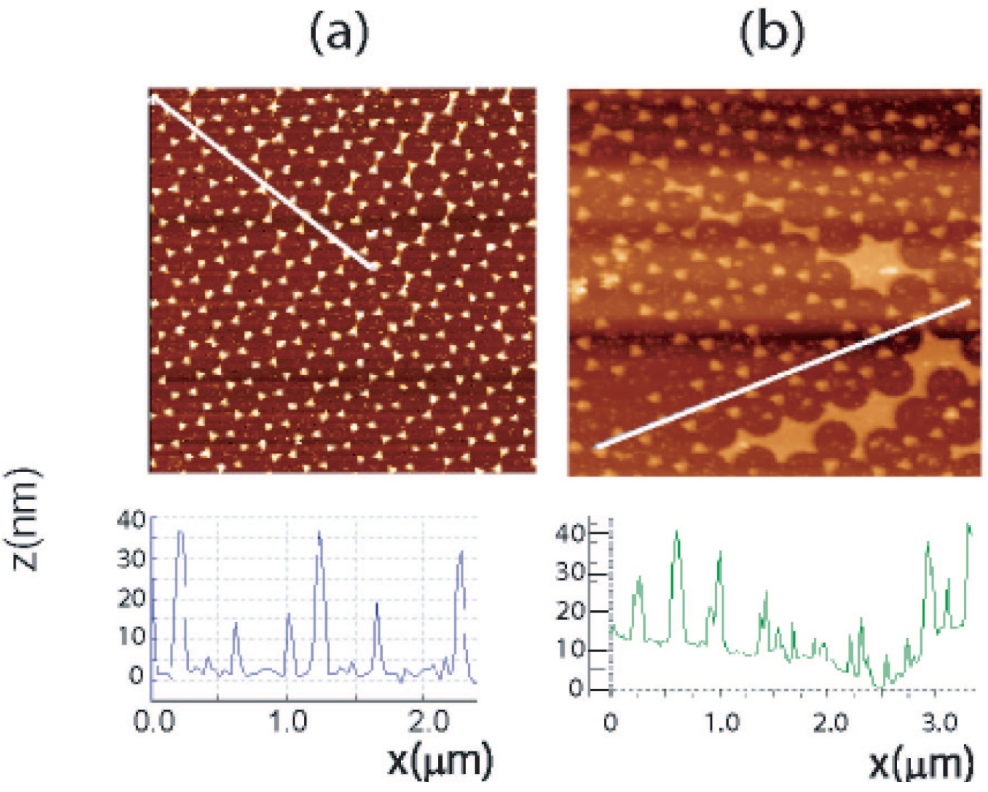

Figure 7.8: Typical AFM height images and their line profiles of glass/Ag SERS substrates fabricated with NSL. Note that the roughness of the glass surface is of at least 5 nm.

7.4 Enhancement factor calculations

Many efforts have been made to merge the different definitions of the SERS enhancement factor (EF) into one generalised parameter that allows direct comparison between different experimental set-ups [154, 156]. Due to the generalised confusion in this matter it is important to justify the choice for the EF definition and its applicability to the experiments carried out in this thesis.

First of all, a small probe molecule that does not present a resonant Raman effect but has a high Raman scattering cross-section for the specific laser wavelength is desirable. In addition, it is preferred that the absorption spectrum of the probe molecule does not shift when adsorbed on the metal. Resonance Raman scattering (RRS) takes place when the absorption spectrum of the analyte overlaps with the laser excitation wavelength. RRS implies that the virtual state described in Chapter 3 (see subsection 3.1) is in resonance with a real electronic state of the molecule and therefore, the scattering efficiency of the molecule is enhanced by several orders of magnitude [154]. This enhancement is not due to the localised surface plasmon effect and should be somehow removed from the true SERS EF calculations. However, in SERS experiments it is common to use analytes presenting RRS for visible wavelengths, e.g. rhodamine or crystal violet, as their Raman signals are much more intense and hence easier to detect [154]. When using probes in RRS or close-to-resonance conditions as reference for the EF calculations care has to be taken as a shift in the absorption spectrum may appear after the analyte is adsorbed onto the substrate. This effect may cause a slight decoupling between the virtual and electronic states. It might affect the value of the scattering cross-sections leading to a miscalculation in the EF [190].

Para-aminothiophenol (p-ATP) was the probe molecule chosen for the experiments. p-ATP does not experience resonant Raman effect for visible lasers as it was demonstrated by recording the transmission spectrum of p-ATP in methanol in the visible spectral range with a commercial UV-vis spectrometer (SpectraSuite, Ocean optics) and a tungsten halogen source. Results shown in Figure 7.9 correspond to 100 averaged spectra acquired for 3 ms. The molecule is non-resonant for light of 532 nm-wavelength, with a transmission higher than 90%. In the recorded data the maximum absorption corresponds to wavelengths close to 400 nm, i.e. higher absorption was detected towards the UV region.

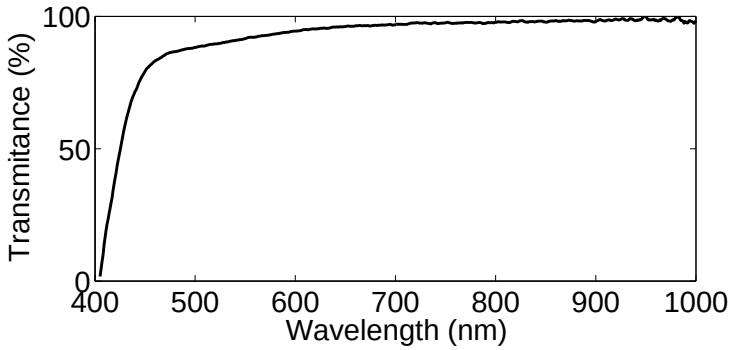

Figure 7.9: Transmission spectrum of p-ATP in methanol.

p-ATP has been widely used as a probe in SERS [149, 191, 192]. p-ATP strongly interacts with noble metals such as silver or gold via its thiol group (SH) and was irreversibly adsorbed on the surface of these noble metals. It has been reported that on silver the molecule is oriented with the Z axis normal to the surface in the so called "standing-up" orientation (see Figure 7.10) [193].

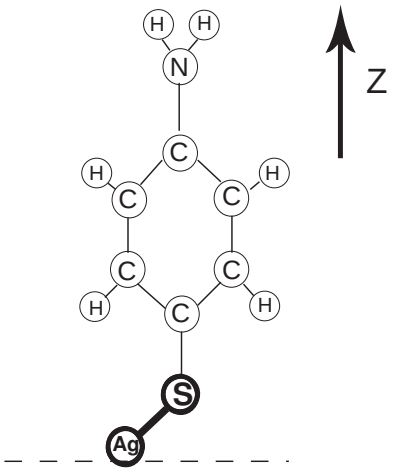

Figure 7.10: Representation of the bonding between the S atom of the p-ATP and a Ag atom of the metal nanostructure.

Despite the wide use of p-ATP as probe molecule for SERS experiments it has recently been published that p-ATP can turn into 4,4-dimercaptoazobenzene (DMAB) on a roughened silver surface in the presence of oxygen even at low laser powers [149, 194]. Huang *et al.* [149] reported a general misinterpretation of the origin of the peaks contributing to the SERS spectra of p-ATP adsorbed on a silver electrode after laser irradiation. This laser-induced oxidation was detected in the measurements performed in this thesis as shown in Figures 7.12 and 7.13. In these figures, SERS spectral peaks assigned to the DMAB contribution as well as p-ATP contribution were detected.

The six strongest SERS spectral peaks were measured for the sapphire/Ag substrates at 1076 cm^{-1}, 1141 cm^{-1}, 1188 cm^{-1}, 1389 cm^{-1}, 1435 cm^{-1}, and 1576 cm^{-1} and for the mica/Ag substrates at 1077 cm^{-1}, 1141 cm^{-1}, 1188 cm^{-1}, 1392 cm^{-1}, 1435 cm^{-1}, and 1580 cm^{-1}. Results agree with previous SERS measurements of a p-ATP monolayer adsorbed on a silver electrode [149,193]. Osawa *et al* [193] reported 5 strong and strong-medium Raman spectral peaks at 1077 cm^{-1}, 1142 cm^{-1}, 1391 cm^{-1}, 1440 cm^{-1}, and 1573 cm^{-1}. The Raman spectral band of medium-to-strong intensity detected in the results of this thesis at 1188 cm^{-1} is reported in the study of Osawa *et al* as a Raman spectral band of weak intensity at 1190 cm^{-1}, [193]. Osawa and co-workers attributed all the Raman spectral peaks measured in the cited study to the adsorbed p-ATP monolayer [193]. However, following the latter work of Huang *et al* [149] in this thesis only two of the six strongest Raman spectral peaks detected were assigned to untransformed p-ATP (the Raman spectral peaks at 1076/1077 cm^{-1}, and at 1188 cm^{-1}). The rest of the Raman spectral peaks measured were mainly attributed to the DMAB contribution [149].

In the EF calculations fine selection of the spectral bands was performed. Bands assigned to untransformed p-ATP and not to DMAB were chosen. The Raman spectral peak detected at 1077 cm^{-1} and at 1076 cm^{-1} for mica/Ag and sapphire/Ag substrates respectively, and reported at 1077 cm^{-1} and 1075 cm^{-1} by refs. [149, 193] was selected as characteristic from the untransformed p-ATP (see Figures 7.12 and 7.13). This Raman spectral peak is assigned to the SC stretching [195].

Secondly, a definition of the SERS EF that suited the experimental conditions was required. As a first intuitive approach the enhancement factor is the amplification of the Raman signal obtained with the SERS set-up under the same experimental conditions as used for the Raman measurements (laser power and wavelength, exposure time, instrument, settings, etc.). This signal amplification can be measured in terms of intensity [154]. This intuitive idea leads to the so-called analytical enhancement factor (AEF). AEF is defined as [156]:

$$AEF = \frac{I_{SERS}/c_{SERS}}{I_{RS}/c_{RS}} \tag{7.1}$$

where I_{SERS} and I_{RS} are the integrated intensities of specific bands in the SERS and Raman spectra respectively, and c_{SERS} and c_{RS} are the concentrations of the analyte used for the SERS and the Raman spectroscopic experiments, respectively. Note that AEF only makes sense if the experimental conditions are exactly the same. In the experiments reported in this

thesis a monolayer of p-ATP was deposited on the SERS substrates following ref. [191]. SERS substrates were immersed in a 10^{-4} M solution of p-ATP for 2 h and then rinsed in methanol to ensure adsorption of only a monolayer of the probe molecule [193]. In absence of the SERS substrate, solutions of such concentrations of p-ATP do not produce sufficient Raman signal to be detected by the Raman micro-spectroscopic instrument. Thus, for the Raman spectroscopic experiment a concentration of 1 M of p-ATP in methanol was used. A drop of 20 μl of this solution was deposited on bare sapphire, mica, and glass and Raman spectra were measured under the same conditions as used for the SERS experiments. Spectral data acquisition was performed at laser power of 64 μW and 500 s acquisition time with a 60× 1.2-NA water immersion objective (USAPO, Nikon).

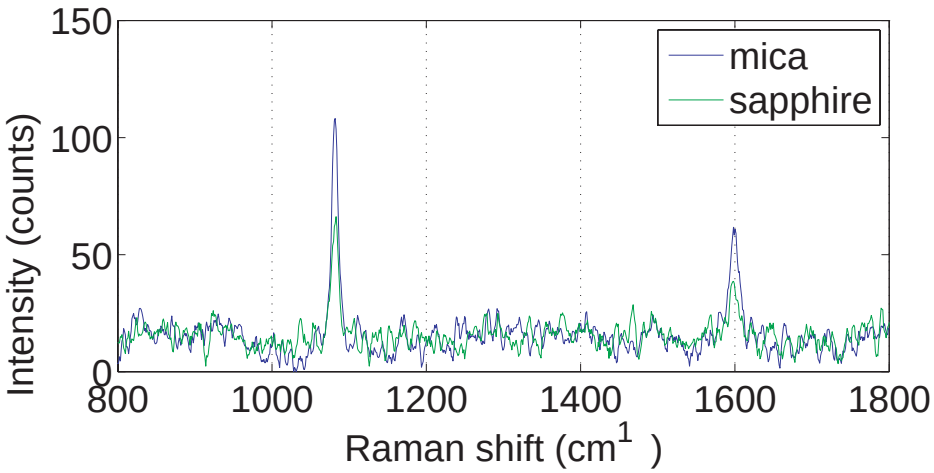

Figure 7.11: Raman of bare mica and sapphire substrates with 20 μl of p-ATP in methanol 1 M.

7.5 Mica/Ag SERS-active substrates after p-ATP deposition

Once the deposition of p-ATP was performed on the mica/Ag NSL-fabricated substrates a simultaneous SERS and AFM study was performed. Results are shown in Figure 7.12. The SERS signal (b) was collected from selected points which are represented in the figure by an asterisk and an empty circle. The experiments were repeated for at least two samples and the results shown in Figure 7.12 correspond to a single example. Figure 7.12 (a) shows the height AFM image and line profile of the mica/Ag substrates. Raw SERS spectra clearly present the characteristic spectral peaks from p-

ATP/DMAB as previously discussed. The Raman spectra were acquired for 500 s at laser power of 64 μW.

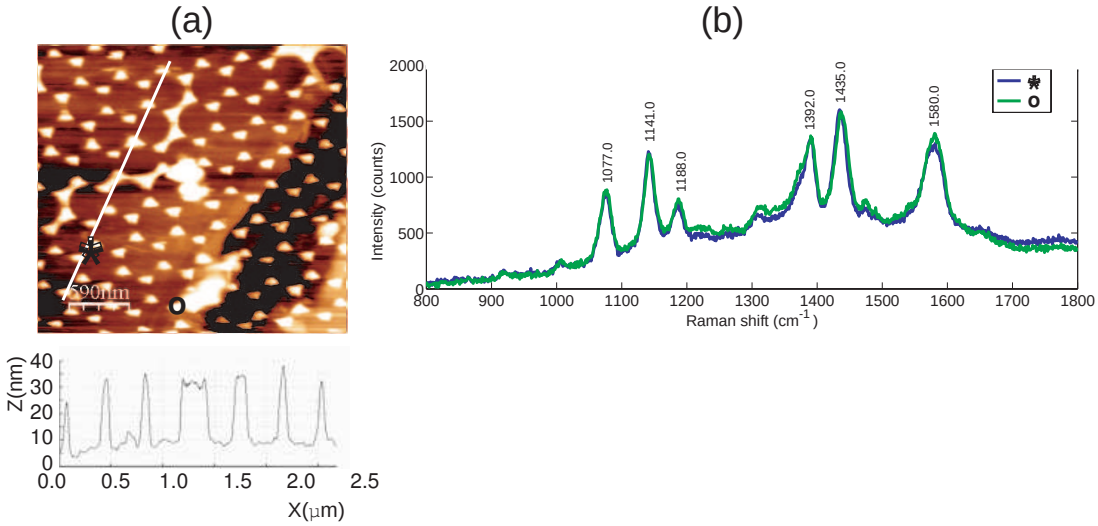

Figure 7.12: (a) AFM height image and line profile, and (b) selected SERS spectra from the locations labelled in (a)of mica/Ag SERS substrates with a monolayer of p-ATP in methanol. (Raw data)

7.6 Sapphire/Ag SERS-active substrates after p-ATP deposition

Figure 7.13 (c) shows a typical raw SERS spectrum of a monolayer of p-ATP on sapphire/Ag SERS-active substrates. Spectral acquisition time was 500 s at a laser power of 68 μW. The spatial position corresponding to the SERS measurement is labelled with an asterisk in Figure 7.13. The experiments were repeated for at least two samples and the results shown in Figure 7.13 correspond to a single example. Figure 7.13 (a) is the optical image of the sample with the 60× objective. Figure 7.13 (b) shows the AFM image and line profile of a typical sapphire/Ag SERS-active substrate with a monolayer of p-ATP.

A rough estimation of AEF by eq. 7.1 gave a value of the order of 10^4 and 10^6 for mica/Ag and sapphire/Ag SERS substrates, respectively. These numbers are between the interval of values expected for the NSL-fabricated SERS substrates previously reported [165]. These values of AEF are average values of the whole area illuminated by the laser spot for several periodic regions of the substrate. If the signal enhancement measurements had been only performed in the hot spots then higher AEFs would be expected [154].

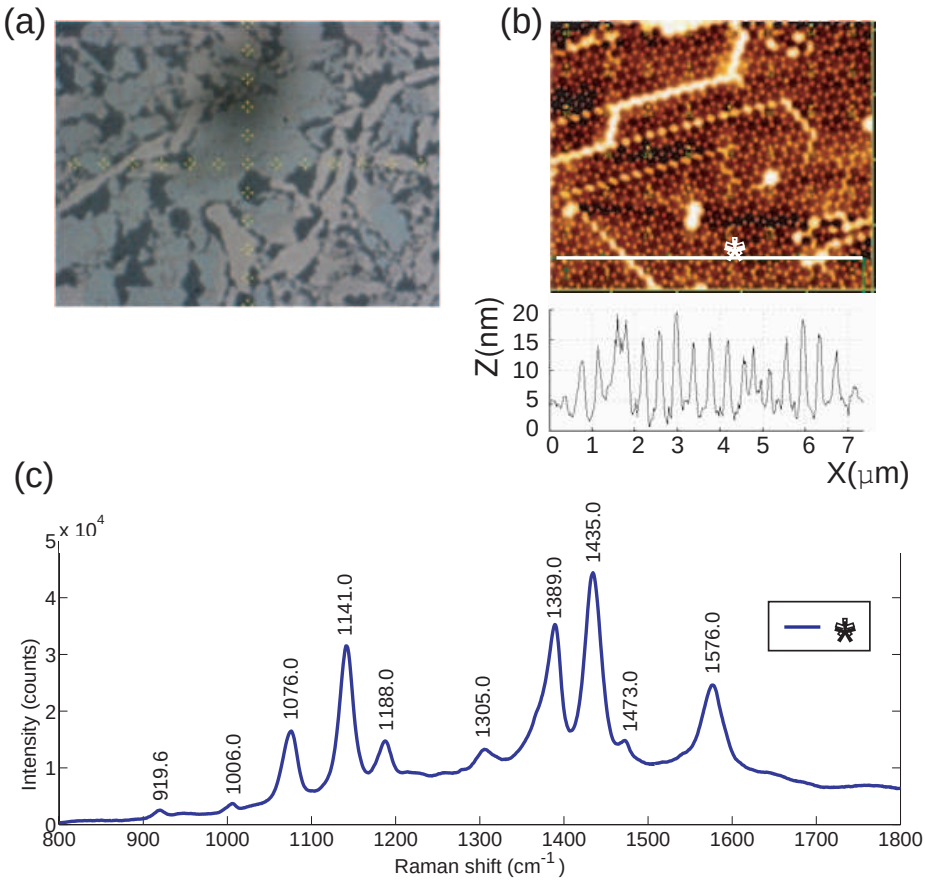

Figure 7.13: (a) Optical image, (b) height image and its line profile, and (c) typical raw SERS spectrum (from the position labelled by an asterisk) of a monolayer of p-ATP adsorbed on a sapphire/Ag SERS-active substrate.

However, the region illuminated by the laser covers not only hot spots but also regions where the electromagnetic enhancement of the local electric field is lower.

Results show that a higher enhancement of the Raman signal was achieved by using sapphire as the "matrix" planar support of the SERS substrates. These results give a first intuitive idea of the order of magnitude of the enhancement. However, AEF is directly dependent on the SERS probe concentration and does not consider that only the adsorbed molecules contribute to the SERS signal, as SERS is strongly distance-dependent [156]. The number of molecules contributing to the SERS signal depends on the deposition technique (Langmuir-Blodgett trough, vesicle fusion or spin coating) and the real coverage of the substrate [154]. Therefore, a more rigorous approach for EF calculations is needed. Following a detailed study carried out by Le Ru *et al* [156] the SERS substrate enhancement factor SSEF is defined as

$$SSEF = \frac{I_{SERS}/\mu_M \mu_S A_M}{I_{RS}/c_{RS} H_{eff}} \tag{7.2}$$

I_{SERS} and I_{RS} are the intensity of the chosen spectral bands from the SERS and Raman spectra of p-ATP as described in AEF. c_{RS} is the concentration of the solution used for the Raman measurement. For a concentration of 1 M of p-ATP in methanol, and a density and molecular weight of p-ATP of 1.18 g(cm^{-3}) and 125.19 g(mol^{-1}), respectively c_{RS} is 5.66 (molecule)nm^{-3} .

$\mu_{\mathbf{M}}[m^{-2}]$ is the surface density of an individual nanostructure producing the enhancement. Analysing the problem in 2D the primitive unit cell of the substrate is a parallelogram containing 2 metallic nanostructures. However, for simplicity a regular hexagon of diagonal equal to the diameter D of the beads (D=2R) and containing 6 metallic nanostructures is used as unit cell of the lattice.

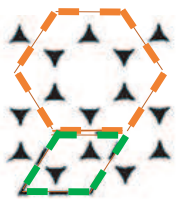

Figure 7.14: Unit cell of the SERS substrate

The density of metallic nanostructures is the ratio between the number of metallic nanostructures per unit cell and the area of a hexagonal unit cell,

$$\mu_m = \frac{4/\sqrt{(3)}}{D^2} \tag{7.3}$$

For 384 nm diameter beads and a hexagonal unit cell containing 6 metallic nanostructures μ_M is 1.57×10^{-6} nm^{-2}.

μ_S is the surface density of molecules on the metal. It has been reported that a p-ATP molecule within a closed-packed monolayer occupies an area of 2.2 nm^2 [165, 196]. Then, μ_S is estimated to be 4.55×10^{-1} nm^{-2}.

I_{RS} is the intensity of the Raman spectra from a solution of bare p-ATP on methanol at concentration c_{RS} (note that the concentrations would be much higher than 10^{-4} M to be detected with conventional Raman spectroscopy at equivalent laser powers than in SERS, i.e a c_{RS} of 1 M was used). Approximately 250 μl of solution were deposited on the centre of a Teflon ring on pure mica and pure sapphire. For consistency, the same spectral bands as used in I_{SERS} calculations were selected.

H_{eff} is the effective height of the scattering volume of the Raman micro-spectroscopic instrument. A value of 18.5 μm was estimated for the Raman micro-spectrometer as shown in Chapter 4 of this thesis. This result is consistent with the value calculated for the same Raman micro-spectroscopic instrument reported in a previous study [165].

A_M is the exposed surface area of the metallic nanostructures. Previous reports have approximated the surface of similar metallic nanostructures fabricated by NSL by truncated tetrahedrons [165, 183, 197]. However, such a model implies that the untruncated geometrical figure is formed by four identical equilateral triangles. In order not to make this assumption in this thesis the metallic nanostructures are modelled by truncated triangular pyramids. For each nanostructure the surface exposed to laser illumination is approximately the surface area of a truncated triangular pyramid without its bottom triangular base. A detailed geometrical calculation is included in the appendix 2 of this thesis. The estimated value for the total area A_M is approximately 2.18×10^4 nm^2 while considering a truncated tetrahedron was reported to be 9.07×10^3 nm^2 [165]. Although of approximately the same order of magnitude the calculations done in this thesis estimate a value of A_M 2.4 times larger. Eq. (7.2) shows that a higher A_M implies a lower value of SSEF. For describing the same substrate pattern, a model that provides lower values of SSEF guarantees higher fidelity in the final calculation of

SSEF which would be at least of the order of the estimated value. A 2D computational study of the substrates with finite element analysis showed that the highest electric field enhancement arises from the vertices or sharp features of the nanostructures [91]. A good coverage of these so-called "hot spots" is desired. Incomplete coverage of these regions with the molecule under study may lead to insufficient SERS sensitivity.

Substituting all the variables of eq. (7.2) by their respective estimated values the SERS substrate enhancement factor SSEF of the NSL substrates described in this thesis is

$$SSEF = \frac{I_{SERS}}{I_{Raman}} 1.12 \times 10^6 \tag{7.4}$$

SSEF was estimated to be of the order of 10^6 for the mica/Ag and 10^8 for sapphire/Ag SERS-active substrates, respectively. These values are of 2 orders of magnitude higher than those predicted by the AEF calculations. The results obtained showed higher enhancement for the sapphire/Ag substrates and predicted a larger enhancenment of the sapphire/Ag and mica/Ag substrates on other adsorbates than previously reported studies on glass/Ag SERS-active substrates also produced with 384 nm diameter spheres and NSL [91]. The EF for these glass substrates was estimated to be 10^5 [91,165]. Note that in the latter studies a different geometric model was used to calculate A_M, as well as a slightly different experimental set-up.

EFs of 10^{14}-10^{15} reported in bibliography are in general consequence of non-careful normalisation [155]. On the contrary, SSEFs of the order of 10^6-10^8 are reasonable results [156] and sufficient to allow SERS detection of thin supported lipid films.

7.7 Deposition of amphiphiles on the SERS-active substrate

Sapphire was shown to be the most suitable material as "matrix" substrate in terms of low contribution to the Raman spectrum, flatness, and enhancement factor. However, the affinity of a lipid layer to form on the top of the sapphire/Ag substrates has to be evaluated. In this study sapphire samples with a C(0001) crystal orientation were used and presented a negatively charged surface [198–200].

Electrostatic interactions with the negatively charged carboxilate groups of the AA in water are therefore mainly repulsive (see Chapter 2). Treatment of the sapphire surface with piranha solution adds extra OH groups to its surface, increasing its hydrophilicity and thus its affinity to amphiphilic deposition. AA binding to the sapphire surface is produced via the interaction of the carboxilate groups with two oxygen atoms from the OH groups on the sapphire surface. Silver rapidly oxidises in air or water and this oxide layer is negatively charged. Thus, the dissociated carboxilate groups of the AA will experience electrostatic repulsion from the regions covered with silver. This was a problem when depositing uniform layers of amphiphilic molecules over the SERS substrate.

For SERS measurements, proximity of the order of nanometres between the metal and the lipid layer is necessary for enhancement of the Raman signal to occur. An interesting approach to overcome this electrostatic repulsion would be to use positively charged lipids. An alternative approach might be to provide charge to the lipid layer through adsorption of ions (bivalent cations) added to the aqueous medium. The cations will be surrounded by water molecules and linked to the lipid head groups by H bonds, in the so-called "screening" process. This would reduce repulsion between the negatively charged head group and the negatively charged substrate surface. When the adsorbate is a neutral phospholipid instead of a fatty acid, repulsion forces arise from the interaction between the negatively charged substrate and the real negatively-charged impurity-induced head group of the lipid (in this thesis the head group refers to phosphatildylcholine PC-). As sapphire, mica is negatively charged in water.

Three different methods were used to deposit the lipid bilayers on the mica/Ag and sapphire/Ag substrates: vesicle fusion, Langmuir-Blodgett (LB), and spin coating. The following section describes the characterisation of lipid membranes deposited by these methods.

7.7.1 The vesicle fusion technique

In order to have the most natural model for cell membranes, an aqueous environment with controlled pH is required. Supported lipid bilayers (SLB) created by self-fusion of extruded liposomes adsorbed on a solid substrate is a common method that satisfies this requirement. The extrusion technique allows size-control of the liposomes in solution. Fusion of homogeneous unilamellar vesicles enables single bilayer deposition. The buffer used was TRIS

solution with pH 7.4. Control over the pH and the ionic strength of the aqueous medium is important not only to better reproduce physiological conditions but also to overcome electrostatic interactions between the tip and the charged sample in the AFM measurements. Such interactions may increase the instrumental error in the measured height [9]. However, the effect of the buffer on the sample needs to be discussed as for example it has been reported that ripple phase formation in lipids is enhanced by the presence of TRIS [201].

As a first approach to SLB deposition onto the SERS-active substrates, formation of a single bilayer of phospholipids (DPPC) in a common planar solid substrate such as mica was studied.

First, all equipment was cleaned thoroughly with a variety of solvents. Around 250 μl of the 50 (mg)ml^{-1} lipid solution in 5:1 chloroform-methanol were placed in a small round-bottomed flask and dried under a stream of nitrogen until a thin lipid film was formed. The dried lipid film was rehydrated with at least 1 ml of TRIS to give a milky solution known as "lipid cake". At this stage the dried lipid film had turned into a stack of fluid bilayers. The lipid cake was frozen in liquid nitrogen and thawed several times. This allowed the bilayers to detach from the flask and self-close to form large multilamellar vesicles. Finally, the suspension was extruded 11 times through a 19 mm diameter polycarbonate filter with 100 nm diameter pores (Avanti Polar Lipids) to produce a monodisperse, unilamellar suspension of 100 nm diameter lipid vesicles. 50 μl of the lipid vesicle suspension were diluted in 50 μl of water. This solution was deposited on a 1 cm^2 piece of freshly-cleaved mica previously treated with 500 μl of 10 mM magnesium chloride ($MgCl_2$) to encourage fusion of the lipid vesicles into a bilayer by reducing the electric repulsion between the bilayer and the substrate by ion screening. The sample was left for around 3 h. In this time the vesicles spontaneously adsorbed onto the hydrophilic surface of the mica, breaking and spreading across the substrate. After the 3 h the sample was washed with water several times to remove any vesicles that remained unfused. This resulted in a unilamellar supported lipid bilayer formed between two layers of water, which was kept hydrated to guarantee stability of the bilayer.

Figures 7.15 and 7.16 show that a large bilayer can be formed and imaged by liquid AFM in tapping mode. The measured height of the bilayer was 4.5-6 nm. This value agrees well with previous studies [158]. The size of the holes in the bilayer was controlled by pre-heating the sample at 55°C, which was over the main phase transition temperature of DPPC (at 41-43°C

started the transition from the gel phase to ordered liquid). For cationic DPPC this temperature was 37°C) [101]. Leaving the sample to cool down to room temperature (20-25°C) produced larger holes but more scarce as had been previously reported [173].

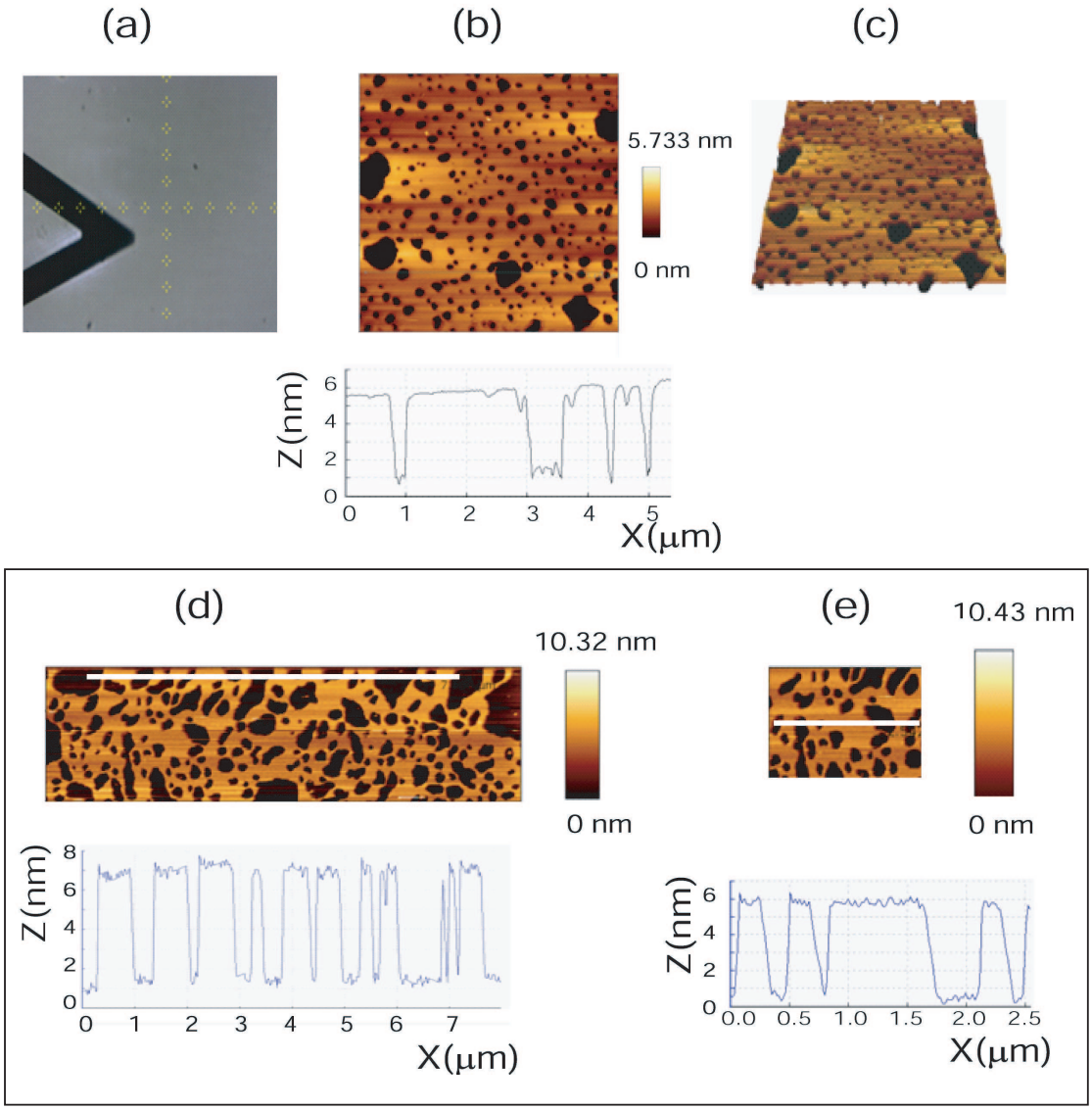

Figure 7.15: AFM height images and line profiles (b,d-e), and 3D height image (c) of a uniform bilayer of DPPC on mica formed by vesicle fusion.(a) Optical image of the bilayer, which is transparent optically.

Figure 7.17 shows two typical force spectroscopy curves of DPPC bilayers in a concentration of 10 mM of TRIS buffer on the mica substrate. In these experiments a silicon nitride tip was used. These tips are hydrophobic and slightly negatively charged for a pH of 7.4 [101]. As can be seen in Figure 7.17 when approaching towards the lipid bilayer the tip experienced repulsion. The distance at which the tip first interacted with the bilayer was approximately 10-12 nm from the mica surface for both examples.

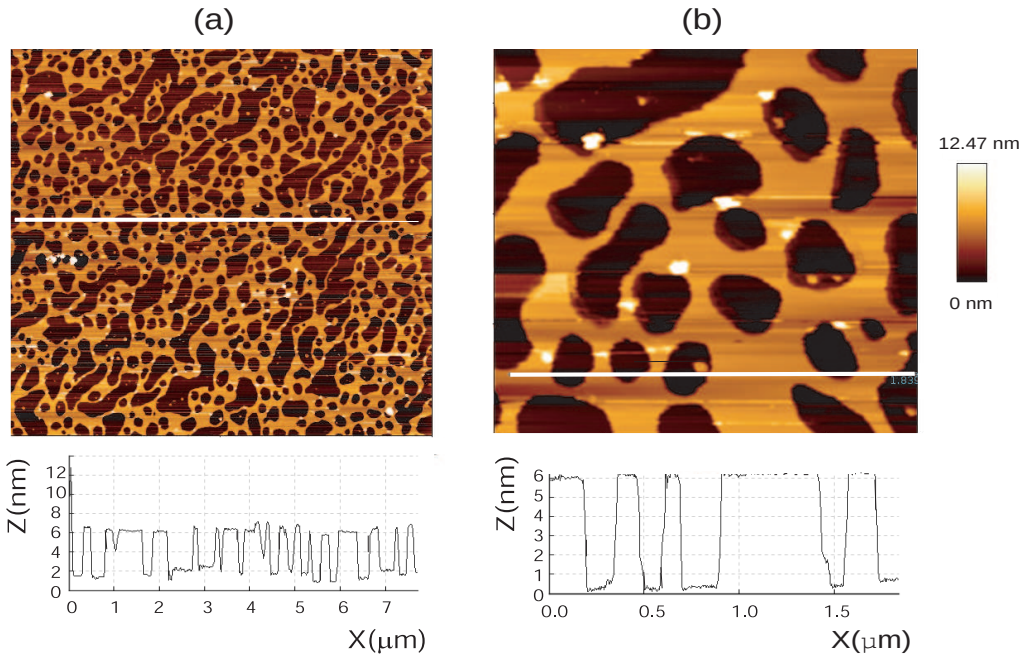

Figure 7.16: (a-b) AFM height images and line profiles of a uniform bilayer of DPPC formed on mica by vesicle fusion.

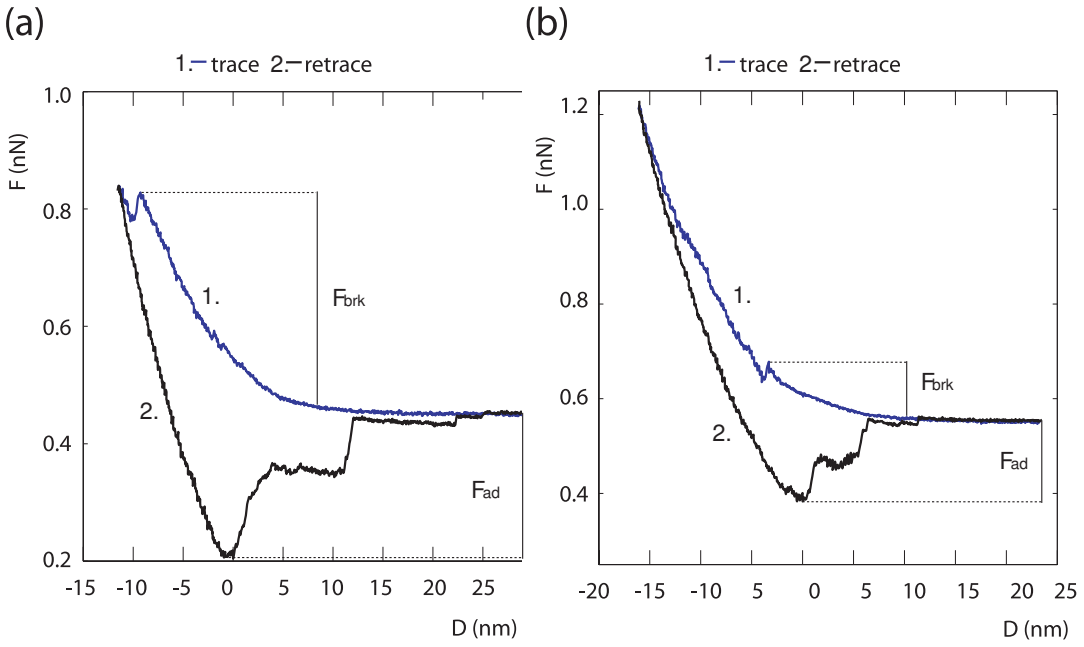

Figure 7.17: Force spectroscopy curves of two typical hydrated DPPC lipid bilayer. F and D correspond to the force and tip-sample distance, respectively, and F_{adh} and F_{brk} refer to the adhesion and breakthrough forces on the bilayer.

As the force on the bilayer was increased the bilayer experienced compression. At loading forces of 0.37 ± 0.02 nN and 0.11 ± 0.02 nN in Figure 7.17 (a) and (b) respectively the tip suddenly jumped into the sample, penetrating the lipid bilayer. This loading force can be associated to the breakthrough force of the lipid bilayer [202]. The jump-in distance measured was approximately 2-3 nm for the two graphs. The measured values were expected to be related with the predicted/measured thickness of the lipid bilayer [202]. However, they were approximately half. This might imply that for the loading forces used in the experiments only the first top lipid layer was penetrated. The change in force experienced by the system from the situation of maximum compression of the bilayer until the bilayer breakage was of the order of 10^{-2} nN. At normal conditions (below the main phase transition temperature) the lipid bilayer was in gel or solid phase and thus it presented higher mechanical stability than in the liquid order phase [101]. It is likely for the breakthrough forces to be higher in the experiments described in this thesis than in the case of a more fluid bilayer. In the retrace the minimum of the curve corresponded to the point of maximum adhesion P_{ma} between tip and sample. The value of the force at P_{ma} was the maximum adhesion force or detachment force. This force was 0.45 ± 0.02 nN and 0.16 ± 0.02 nN for (a) and (b) respectively. From P_{ma} the tip returned to zero deflection (for long-range distances) in three steps presumably associated to the sequential desorption of lipids from the tip [9]. The first step implied the highest change in force. Changes in force of 0.35 ± 0.03 nN and 0.07 ± 0.03 nN were experienced during intervals of 12 nm and 5 nm for (a) and (b), respectively. In the second step the change in the force measured was 0.09 ± 0.03 nN for (a) and 0.08 ± 0.03 nN for (b). These variations occurred for a space of around 4-10 nm. The forces between the tip and the surface were similar for both systems during the progressive detachment of small amounts of lipids from the tip. Finally, a small step occurred presumably due to last detachment of lipids from the tip. This implied change in forces of around 0.02 nN for both systems. At a distance of approximately 20 nm from the contact the forces resulting from the tip-sample interaction could be neglected.

For every experiment a membrane was formed on mica substrates as proof of the success in lipid preparation. Then, the same solution was spread on previously characterised SERS-active substrates following the same protocol as for the mica control samples and on the same day. Simultaneous measurements with the AFM in liquid mode and the Raman micro-spectroscopic system were performed after lipid deposition. Typical examples are shown in Figures 7.18 and 7.19. Figure 7.18 shows the height and line profile of a

bilayer of DPPC in TRIS buffer on a mica/Ag SERS-active substrate performed with liquid intermittent AFM.

Several aspects need to be considered regarding the line profile of Figure 7.18. Since the enhancement of the Raman signal decays strongly with the distance between the adsorbate and the rough metallic surface, the highest enhancement is likely to come from the regions of the membrane in direct contact with the metal. One of the questions that the experiment aimed to answer was in which regions of the metallic nanostructures the bilayer would form. It is important to discuss if the uniformity and dynamic properties of the bilayer were affected by the substrate or if on the contrary, a uniform bilayer covered smoothly the entire patterned areas of the substrate without breaking into patches. In the line profile -Figure 7.18- the measured height of the metallic nanostructures was approximately 30 nm. The deposited silver layer with the automated evaporator was 25±1 nm in agreement with the maximum measured height with the AFM in air on the control substrates (with no lipids). The AFM calibration allowed an accuracy in the Z-axis of 1 nm as explained in Chapter 4 of this thesis. Therefore, the immersion of the substrate in the DPPC solution altered the measured height of the metallic nanostructures. This result might imply successful deposition of a 5 nm bilayer over the whole metallic nanostructures including their top. This would be a positive result as implies the lipid coverage of the hot spots of the metallic nanostructures. However, it might also be a false increase in height caused by the repulsion between the tip and the sample. If the latter case describes the real situation also an increase in the measured height of the bilayer may be expected. The values of the bilayer height measured from Figure 7.18 ranged from 5 to 7 nm. Previous measurements of the height of the bilayer on the ionic medium on a planar mica substrate were 4.5-6.0 nm. An important result inferred from these experiments is that around the base of the silver nanostructures the bilayer were found to break. This rupture might have an electrostatic or a mechanical origin. The former may imply that there was not sufficient electrical affinity between the lipids and the silver. Repulsion between the negatively charged substrate and the lipids might still be dominant even in the presence of an ionic medium. In case of a mechanical origin of the lipid bilayer breakage it might have been caused by stress acting on the bilayer. Either way, the uniformity of the bilayer was found to be altered by the presence of the metallic nanostructures losing its resemblance with the natural systems they modelled. If the bilayer was not adsorbed on the silver nanostructures then, due to the restriction

of the plasmon resonance effect to short-distance ranges this method was unsuitable for performing SERS experiments.

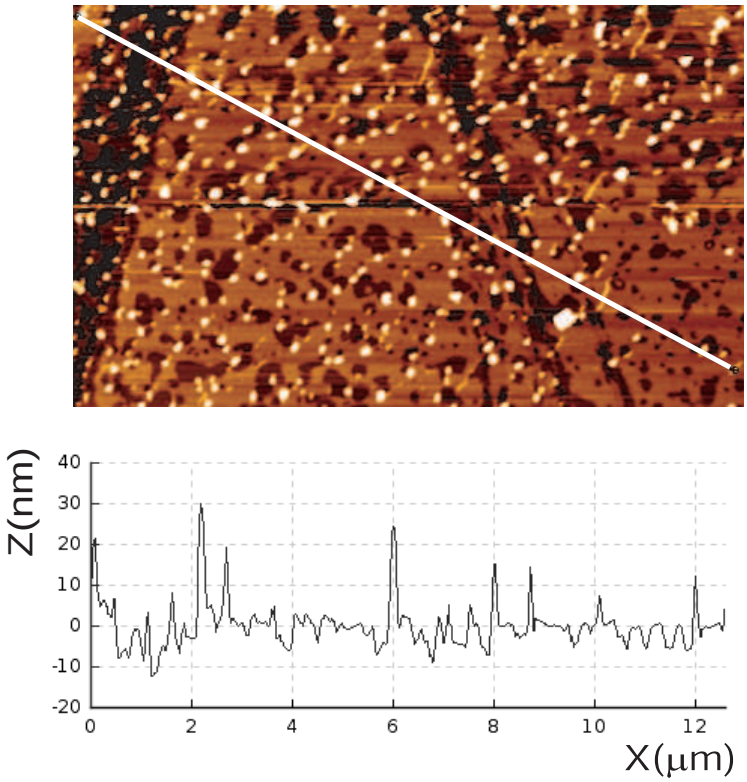

Figure 7.18: Height and line profile of liquid intermittent AFM image of DPPC in TRIS buffer on a mica/silver SERS-active substrate.

In addition, in the experiments the silver nanostructures often moved and detached with a loss in the periodic arrangement of the nanostructures. A loss in periodicity does not affect the SERS enhancement factor of an individual metallic nanostructure as the hot spots are located within each individual nanostructure and there are not coupled plasmon resonance effects within the interstructural gaps. However, this effect would introduce spatial substrate heterogeneity which could lead to a misinterpretation of the quantitative Raman spectroscopic results. Fluctuations in the Raman intensity distribution due to irregular substrates might be wrongly attributed to heterogeneities in the adsorbate. In general, the arrangement of the metallic nanostructures forming periodic patterns in the SERS substrates was modified after vesicle fusion was performed. The distribution of the nanostructures only remained unaltered when the lipid deposition was partial, i.e. if patches of lipids and not a uniform bilayer were formed as shown in Figure 7.19.

The vesicle fusion protocol used for formation of the supported bilayer on mica included the addition of magnesium chloride prior to the deposition

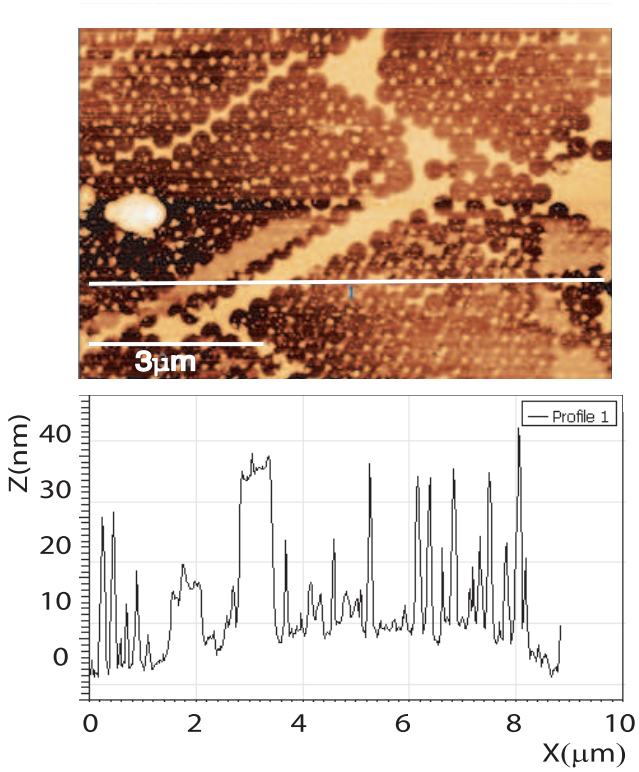

Figure 7.19: Height and line profile of liquid intermittent AFM image of DPPC in TRIS buffer on a SERS-active substrate. Only small areas of lipids are deposited.

of the vesicle solution for charge screening. This introduction reduced the electrostatic potential and thus, the repulsion between the solid substrate and the lipids decreased. However, the effect of this salt on the silver nanostructures needs to be discussed.

Three SERS-active substrates were immersed in solution of magnesium chloride, magnesium sulphate, and TRIS buffer in deionised water respectively at a concentration of 10 mM for 24 h. AFM and optical follow-up were performed as shown in Figure 7.20. While the substrate in magnesium chloride solution presented no silver nanostructures left after 24 h and a whiter colour, the other two substrates were unaltered. This suggested that chemical reaction between the silver and the chloride anions had taken place in the first sample. Therefore, the lipid deposition protocol was modified and $MgSO_4$ was used instead of $MgCl_2$ to avoid silver-Cl^- interaction.

The ability of a bilayer to form on a uniform silver layer in the ionic medium (TRIS plus $MgSO_4$ in its ionic form) was studied as shown in Figure 7.21. 25 nm of silver were deposited with a vacuum evaporator (Edwards) on a large freshly cleaved mica planar substrate exactly under the same experimental conditions as followed in the NSL protocol.

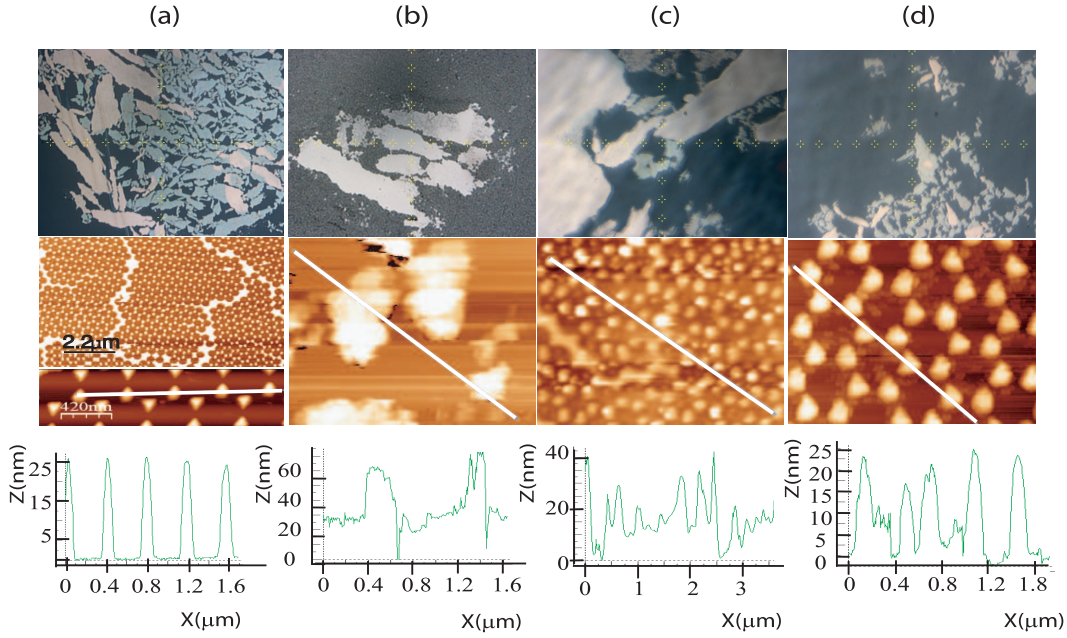

Figure 7.20: Effect of the ionic solutions used in the vesicle fusion experiments on the SERS-active substrates. The figures show the optical images, AFM height images and lines profiles of (a) an untreated control sample and samples after 24 h immersion in (b) $MgCl_2$, (c) $MgSO_4$ and (d) TRIS buffer.

The silver layer was treated with $MgSO_4$ solution and drops of the DPPC liposome solution prepared as previously reported in this chapter were deposited covering nearly the whole surface of the treated silver (but avoiding the contact with edges). Then, the sample was washed with TRIS buffer several times to ensure only one bilayer (if any) was adsorbed on the surface. Results are shown in Figure 7.21. The uniform lipid bilayer was not formed on bare silver by self-fusion of liposomes in the medium containing TRIS buffer and $MgSO_4$. The uniform bilayer was not formed likely due to Coulombic repulsion between the negatively charged silver (covered by a negatively charged oxide layer) and the locally negative head groups of the lipids. Ions in the medium partially shielded these Coulombic repulsions; however, in the experiment the use of drops of $MgSO_4$ at a concentration of 10 mM did not reduce sufficiently the potential between the lipid layer and the silver surface. An alternative approach to reduce repulsion and allow lipid adsorption on silver was the introduction of positively charged lipids.

In parallel to AFM characterisation, the bilayers of DPPC deposited by vesicle fusion on the SERS-active substrates were studied by SERS. However, no SERS signal from the lipids was distinguished from the background. This lack of SERS sensitivity might be attributed to an unsuccessful lipid bilayer formation on the top of the silver nanostructures.

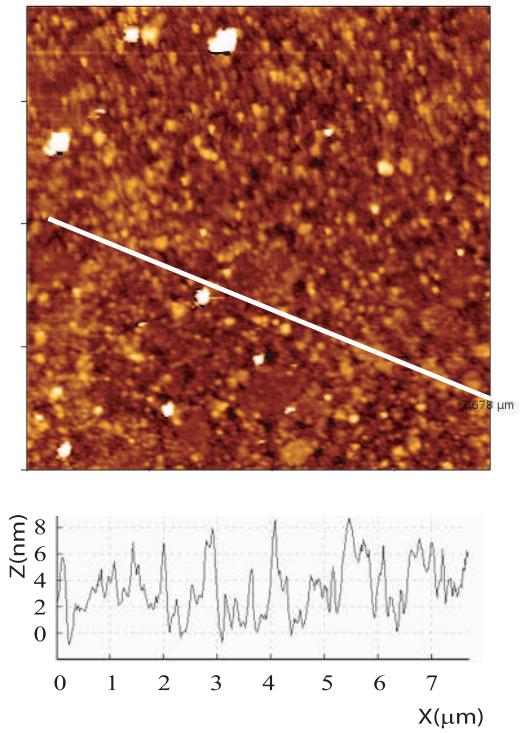

Figure 7.21: Unsuccessful formation of a uniform DPPC bilayer on flat silver-coated mica

Simultaneous AFM studies on the samples revealed the difficulties in obtaining uniform bilayers on the SERS substrates as well as frequent detachment of the silver nanostructures in the hydrated scenario which might had been related to the electrostatic interactions undergoing in the system. In order to prove that the Coulombic repulsion was a generalised problem when dealing with thin lipid arrangements on the SERS substrates other methods were used for depositing the lipids on the substrates. To simplify the electrostatic problem experiments with non-hydrated lipid layers of cationic lipids were performed.

7.7.2 The Langmuir-Blodgett technique

In all Langmuir-Blodgett (LB) deposition experiments a subphase of ultrapure water (Millipore, Milli-Q, and NANOpure, Barnstead; resistivity,18:1 MΩcm) was used. Cationic solutions were discarded to avoid the problems described in the previous section. Experiments with neutral fatty acids (first), neutral phospholipids (second), and charged phospholipids (third) were performed.

The first set of experiments with fatty acids and LB technique aimed to study if a uniform monolayer of AA could be deposited on planar solid substrates of the "matrix" material, i.e plain sapphire and mica. 20-60 μl of

1 (mg)ml^{-1} solution of AA in chloroform were deposited in the LB trough. The solution was left for 20 min for the solvent to evaporate and the system to stabilise. Experiments were performed at room temperature (approximately 20°C). Barriers were closed at a rate of 20 cm^2(min^{-1}) while the surface pressure- surface area (Π-A) isotherm curve was recorded. Figure 7.22 shows a typical AA isotherm for 60 μl of AA deposited on the air-water interface where three phases were clearly distinguished. When the area per molecule of AA was greater than 20.3 Å^{2}molecule^{-1} the AA molecules presented a gaseous behaviour as the molecules were too separated to effectively interact with each other. As the barriers closed the surface pressure increased gently as the AA molecules were entering the liquid disordered or liquid-expanded phase. At a surface pressure Π around 15 (mN)m^{-1} and an area per molecule around 16.0 Å^{2}molecule^{-1} the transition to the liquid ordered phase (also called the liquid-condensed phase) took place. The final state was the monolayer which occurred at a pressure around 70-75 mN m^{-1} when the surface area per molecule was 15.1-15.6 Å^{2}molecule^{-1} in agreement with previous studies [203, 204]. The monolayer was left for 20 min at constant pressure for stability before withdrawing the substrate at a constant speed of 3-5 mm min^{-1}.

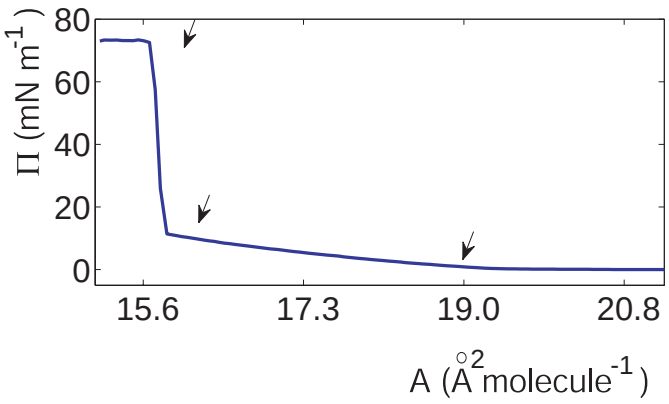

Figure 7.22: Arachidic acid (AA) isotherm in pure water.

Once the monolayer was deposited on the substrate simultaneous AFM and SERS measurements were performed. Several aspects need to be considered related to the LB deposition. Firstly, the heights of the amphiphilic monolayers estimated from LB experiments corresponded to average heights of the deposited layers. In these experiments, maximum spread or coverage of the substrates was aimed. Progressive deposition of amphiphilic layers on the substrates was found to decrease surface uniformity.

Once the deposition was successfully performed on a control planar substrate experiments were repeated for sapphire/Ag SERS-active substrates in the

same conditions. Figure 7.23 shows typical AFM images of the sapphire/Ag SERS-active substrates after AA deposition by LB. The topographic AFM images indicate a thickness of the amphiphilic layer of around 10 nm and a transfer ratio below unity. In Figure 7.23 amphiphiles were found forming patches as it is clearly appreciated in the larger area scanned with the AFM and shown in Figure 7.23 (b). This result implies that the fatty acids covered only partially the substrate, which was an important limitation of the LB technique in this study. Simultaneous SERS spectra recorded from the sample did not distinguish any SERS contribution from the amphiphiles over the background signal.

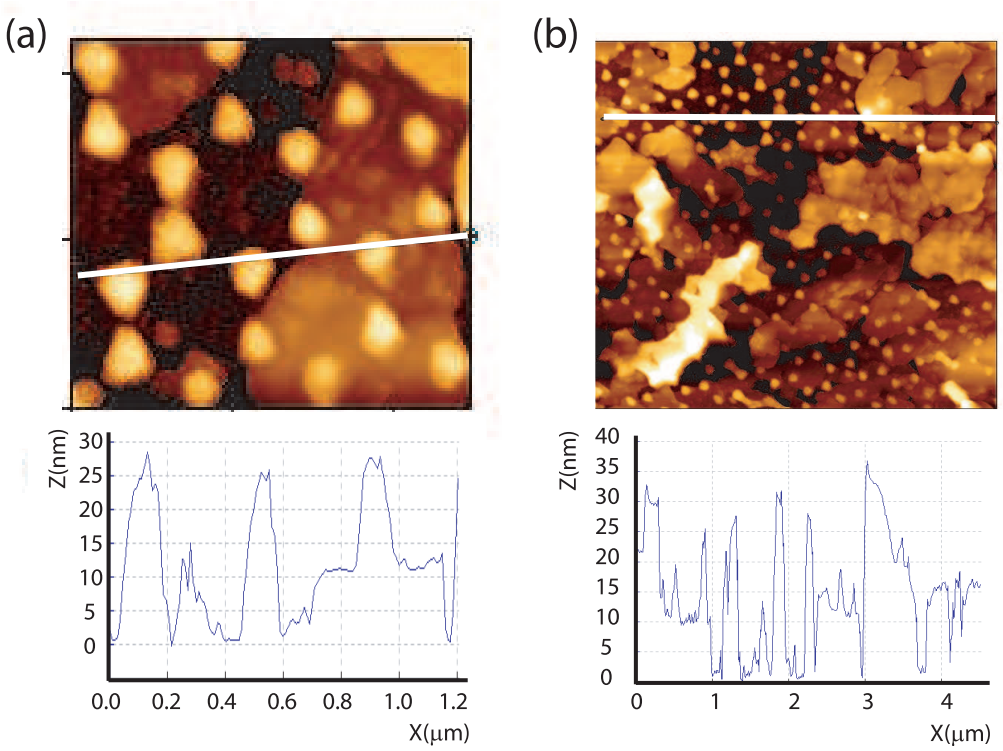

Figure 7.23: AFM topographic images of a thin layer of AA deposited on sapphire/Ag SERS-active substrates by Langmuir-Blodgett.

In the second set of experiments with LB neutral DPPC was used. 20 μl of 2 (mg)ml^{-1} solution of DPPC in chloroform-methanol (5:1) were deposited in the trough. The solution was prepared in a two-step process from re-suspension in the solvents of the lipid residue from a 50 (mg)ml^{-1} solution of DPPC in chloroform-methanol (5:1) dried with N_2 in a round-bottom flask. The same procedure as for the samples with AA was followed. A typical pressure-area isotherm is shown in Figure 7.24. Again, four phases can be distinguished: "gaseous", liquid-disordered, liquid-ordered and collapsed solid monolayer. Transitions between phases took place at surface pressures Π of 3, 34, and 67 (mN) m^{-1}. Note that in Figure 7.24 there is a small kink

at 49 mNm^{-1} which should not be misinterpreted as the collapsing point and it was marked with a red cross. This kink was attributed to the rectangular dimensions of the LB trough as reported in ref. [205].

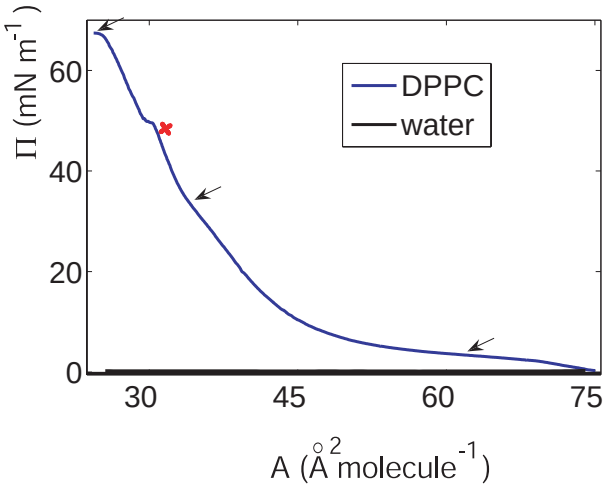

Figure 7.24: *Isotherm of DPPC*

Once the monolayer was formed deposition on bare sapphire and mica substrates were performed. An example is shown in Figure 7.25.

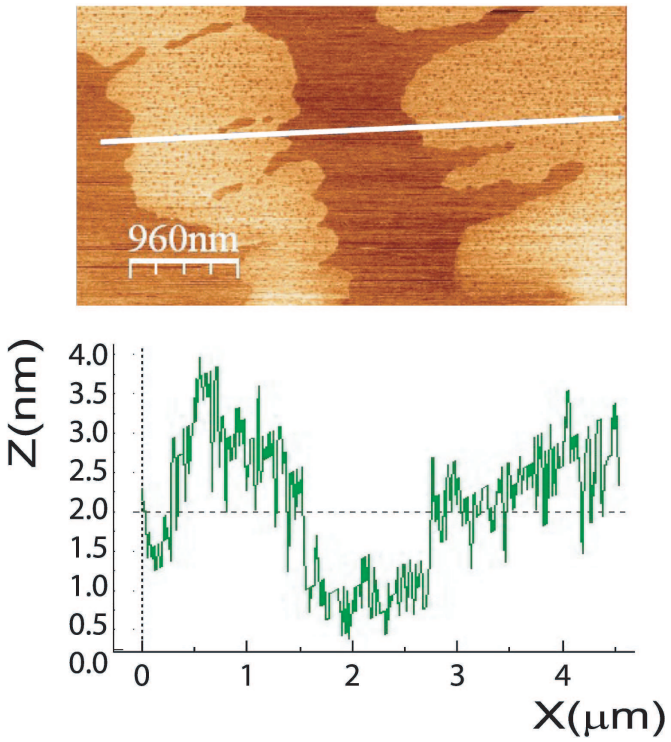

Figure 7.25: *Neutral DPPC monolayer deposited on freshly razor cleaved mica by Langmuir-Blodgett technique.*

Figures 7.26 and 7.27 show AFM topographic images of DPPC monolayers deposited on sapphire/Ag substrates by LB. Figure 7.26 corresponds to NSL

substrates fabricated with 1 μm diameter spheres. The experiment was successful as a uniform lipid layer was formed on the SERS substrate as can be inferred from measuring with the AFM the height of the membrane holes. Typically, the thickness of the measured DPPC monolayer was found to be 3-5 nm. Monolayer uniformity increased when the distance among the nanostructures was larger. However, this reduced the surface density of nanostructures illuminated by the laser and the number of hot spots per measurement presumably reducing the average enhancement of the signal. Accurate laser-tip alignment was performed allowing high spatial resolution and focusing of the laser in the location where lipid monolayer patches were deposited. NSL substrates using polystyrene latex beads of 400 nm spheres were preferred to those fabricated using spheres of 1000 nm of diameter because the former produced higher enhancement of the signal while enabling uniform spatial enhancement of the Raman signal. On the contrary, the enhancement of the substrates produced with spheres of 1 μm of diameter varied considerably depending on the spatial position of the measurement within the sample. These findings agreed with the results reported by Sweetenham for glass substrates [165]. A uniform enhancement of the substrate would be required to produce SERS maps of the lipid bilayers with quantitative spatial information.

Figures 7.27 (b-c) correspond to substrates fabricated with 1000 nm diameter spheres where a uniform lipid layer was successfully formed. Lower densities of metallic features in the substrate were found to be directly related to a higher homogeneity in the deposited amphiphilic layer. Figure 7.27 (c) show a uniform lipid monolayer formed on a region with a lower density of metallic nanostructures.

Figures 7.27 (a) and (d-e) are images corresponding to SERS substrates fabricated with 400 nm diameter spheres showing low transfer ratios. (e) corresponds to a sample in which the "matrix" substrate was reused (after annealing, and solvent and piranha cleaning the sapphire). The low deposition of the lipid monolayer on the reused substrate limited the substrates to a unique use. This might be an important disadvantage in the use of sapphire as SERS substrates due to their high price and limited availability.

If the problem of lack of SERS sensitivity can be solved with an uniform coverage of the substrate the deposition of thicker amphiphilic arrangements might be a successful approach. Figure 7.28 explores this possibility by comparing simultaneous AFM and Raman measurements on the same sap-

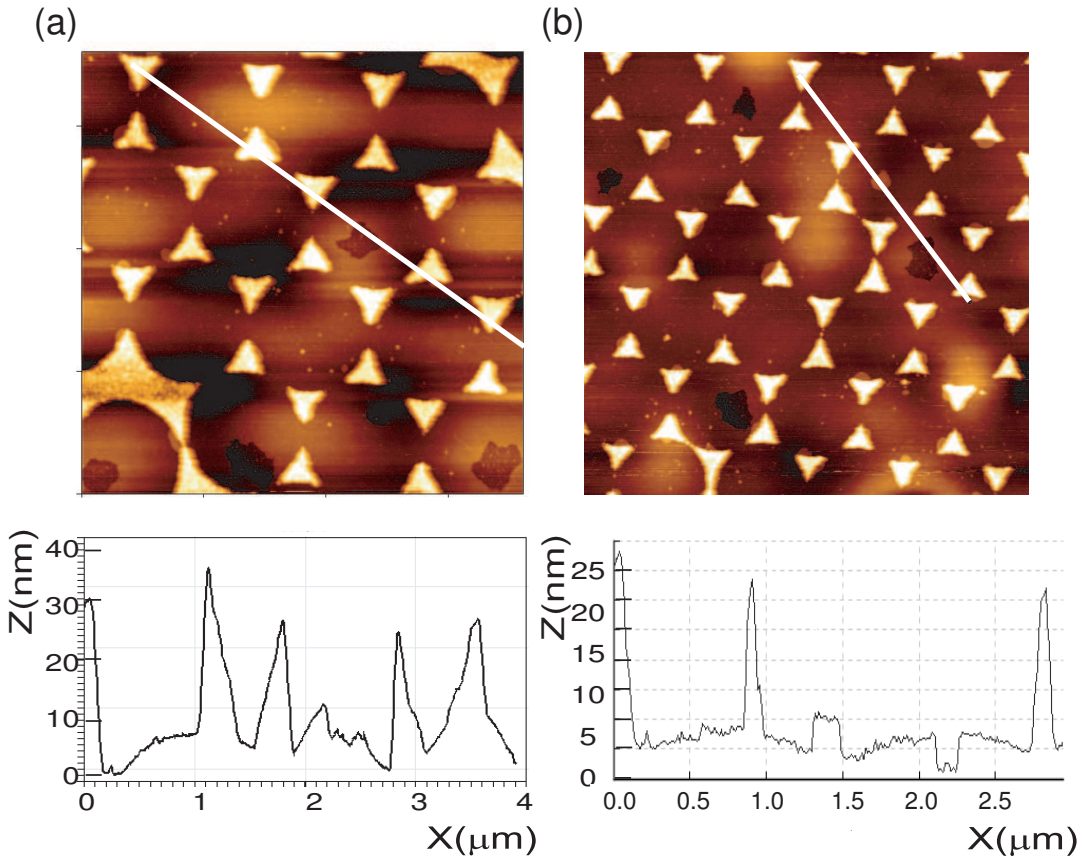

Figure 7.26: AFM height image of a monolayer of DPPC on sapphire/Ag substrates deposited by the Langmuir-Blodgett technique.

phire/Ag SERS-active substrate after the deposition of one and three layers of zwitterionic DPPC was performed.

Although deposition transfer ratios were clearly below unity as shown by the AFM images, a difference in the SERS spectra of the mono and multilayers was detected for a exposure time of 500 s and a laser power up to 1 mW. The signal to noise ratio of the spectra was very low and the results were considered inconclusive.

Only partial transfer of neutral DPPC was achieved on the SERS-active substrates by the LB trough technique even for multilamellar arrangements. As cationic lipids were expected to have more electrostatic affinity to deposit on a negatively charged substrate, neutral DPPC was replaced by cationic DPPC. An AFM and SERS follow-up was performed by depositing and measuring consecutive monolayers of cationic DPPC on control samples (bare freshly razor cleaved mica and bare sapphire) to establish the maximum number of layers that could be successfully deposited on the same sample.

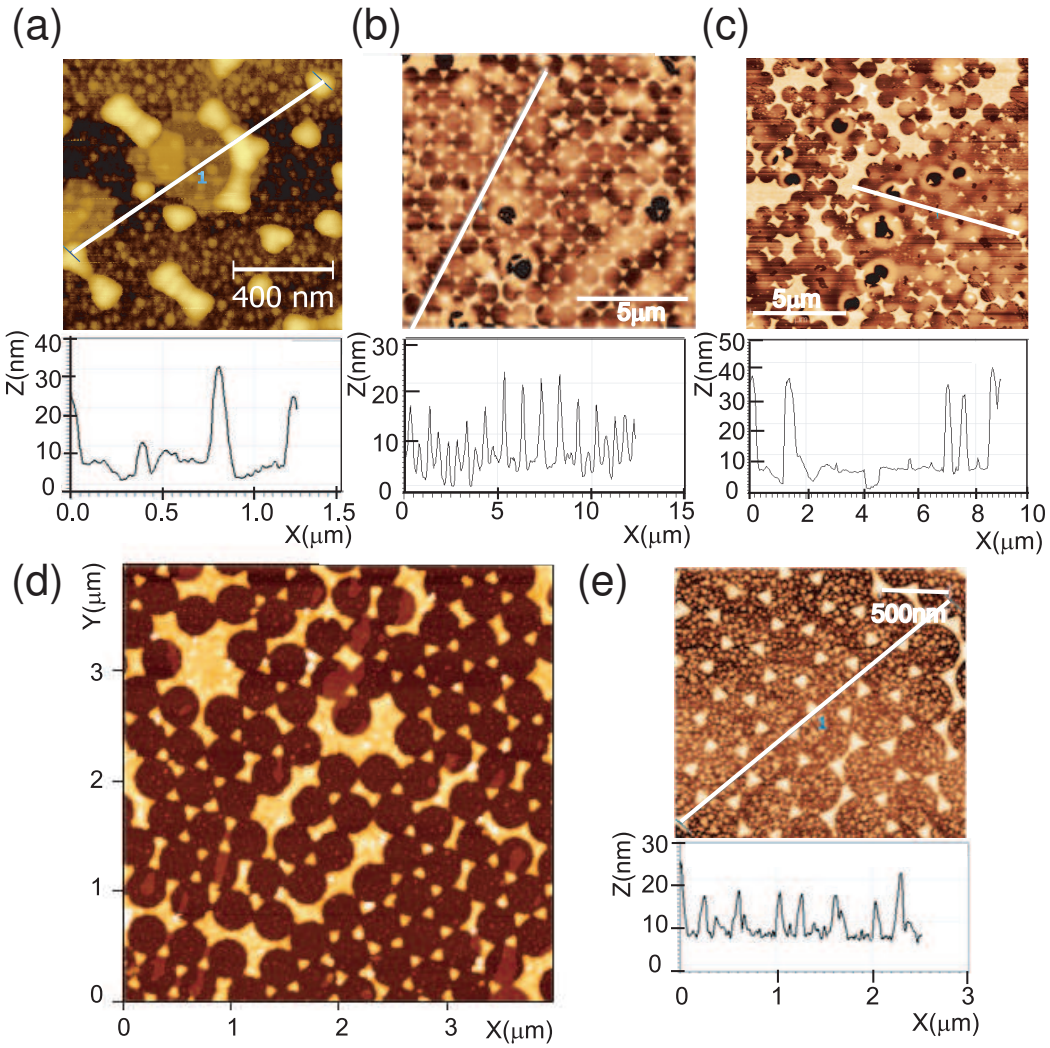

Figure 7.27: AFM height image of a monolayer of DPPC on sapphire/Ag substrates. (b-c) Larger interstrusctural distances (1 μm-diameter spheres). (a,d,e) Examples of deposition transfer ratio lower than unity with 400 nm-diameter spheres, (e) corresponds to a sample where the sapphire was reused.

The experiment aimed also to determine the minimum thickness of the lipid layer needed to produce a detectable Raman signal.

AFM images presented in Figure 7.29 (a-b) show that a neutral DPPC monolayer of 3-5 nm and 4-5 nm was formed on mica and sapphire, respectively. The monolayer was more easily transferred to mica. Much larger areas were covered on freshly razor cleaved mica than on solvent-cleaned sapphire. This might imply that, unless the introduction of silver improves the transfer ratio of the amphiphile on the substrate, the LB trough method might not be ideal for the preparation of supported lipid layers on SERS-active substrates with a sapphire "matrix".

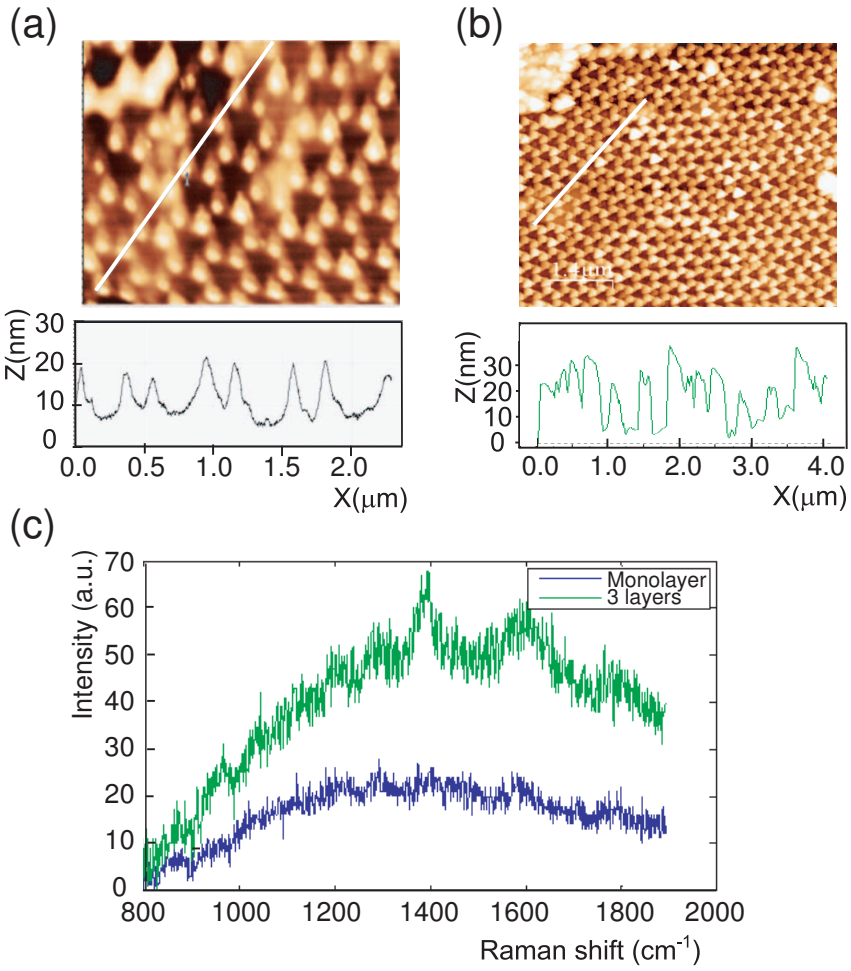

Figure 7.28: (a-b) AFM height images of 3 layers of DPPC deposited by Langmuir-Blodgett on sapphire/Ag substrates and their line profiles. (c) SERS spectra of the DPPC monolayer versus the 3 layer arrangement. SNR is low; therefore, results are inconclusive.

Figure 7.29 (c) corresponds to 5 layers of the lipid deposited on mica. In the associated line profile different topographic features at 5, 10, 20, and 25 nm can be seen. These features are likely to correspond to the monolayer, bilayer, 4th, and 5th layer, respectively. However, the highest heights may belong to impurities. The estimation for the height of the monolayer inferred from this experiment was 3-5 nm. In (d) and (e) the deposition process was repeated in order to achieve a stacking of 9 layers of lipids. However, the results indicated a maximum height for the stacking of lipid layers of 5 and 7 nm for mica and sapphire, respectively. Therefore, less than 9 layers were deposited, which implied a limitation in the number of layers that could be transferred to the "matrix" substrate by the LB method. Parallel Raman micro-spectroscopic measurements were taken from the samples with no success in lipid detection.

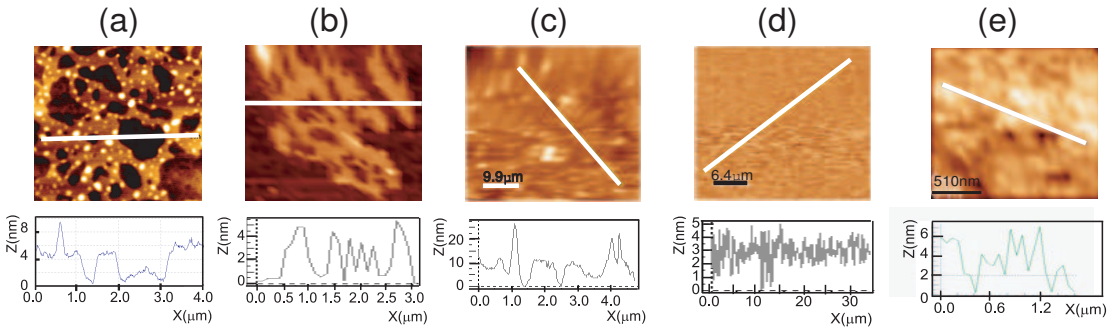

Figure 7.29: Layers of the same Langmuir-Blodgett preparation of cationic DPPC. (a) Monolayer on mica, (b) monolayer on sapphire, (c) 5 layers on mica, (d) 9 layers on mica, and (e) 9 layers on sapphire.

From the latest experiment it can be concluded that a cationic DPPC monolayer was successfully transferred to bare mica but not sufficient coverage was detected for the sapphire substrates. Raman micro-spectroscopic measurements of the lipid layers on mica and sapphire were not sensitive enough to distinguish between the lipid contribution and the bare background. In the case of the sapphire samples this result might be explained by the limited adsorption of the lipids as well as the low Raman scattering cross sections of lipids. For mica, thicker lipid films (up to 5 monolayers) were spectroscopically measured but no Raman signal from the lipids was detected. A lipid stacking thicker than 5 monolayers was not successfully transferred to the substrates.

7.7.3 Spin coating

The lack in sensitivity for detecting SERS signals from monolayers and small number of layers of lipids and fatty acids deposited on the SERS-active substrates by vesicle fusion and Langmuir-Blodgett led to the search for a new method of lipid film deposition. In order to know the minimum amount of amphiphiles (in terms of film thickness and number of layers) needed for SERS detection with the reported micro-spectroscopic instrument several experiments were performed. The deposition method must enable control of the thickness of thin uniform amphiphilic films in a reproducible and accurate manner. It had been reported in literature that vesicle fusion and Langmuir-Blodgett trough techniques do not allow the deposition of more than 3 piled lipid bilayers mainly due to repulsion forces between the bilayers [81, 85]. This repulsion is even more enhanced when using cationic DPPC [85].

In order to simplify the electrostatic problem hydrated bilayers were substituted by monolayer piles. A maximum of 5 monolayers were successfully deposited on planar substrates but attempts to deposit a larger amount of monolayers with LB showed negative results. Therefore, an alternative approach to thin lipid deposition on the SERS-active substrates with spin coating was chosen.

Optimisation of the speed and lipid concentration for the spin coater was performed on bare mica substrates as these parameters can change slightly from one system to another.
Figure 7.30 shows a thick lipid layer of about 100 nm obtained by spin coating 5 (mg)ml^{-1} of cationic DPPC in 2-propanol at 3000 rpm for 50 s on a freshly cleaved mica substrate. The lipid solution was heated at 55°C prior to spin coating for the lipids to be in their liquid disordered phase, which increased the uniformity on the formation of the lipid film.

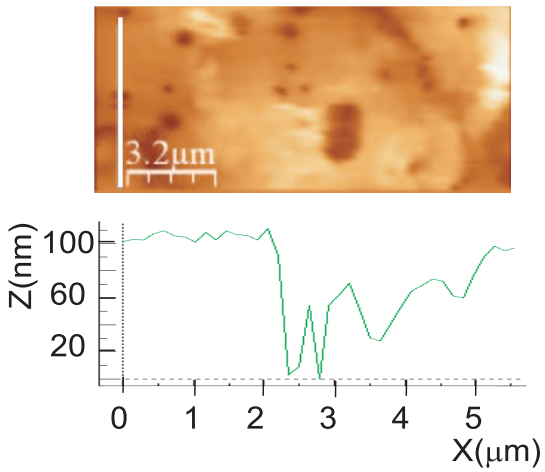

Figure 7.30: AFM height image and line profile of cationic DPPC multilayer arrangement on mica.

The amount of lipid solution deposited on the sample did not affect the results, as long as the drop did wet the whole substrate during the centrifugation process. An excess of solution would exit the sample not affecting the thickness of the deposited layer. However, this might introduce contamination from the external support of the spin coater to the sample. In order to avoid contamination volumes of 20-40 μl of solution were used.

Once the thickness of the layer was controlled via experiments on mica the same parameters were applied to a sapphire/Ag SERS-active substrate. The sample was left in a vacuum desiccator for 21 h to evaporate remaining traces of the solvents. Simultaneous AFM and SERS experiments were performed. Results are shown in Figures 7.31 and 7.32. The lipid average thickness

measured was in agreement with the control experiments on mica. The silver nanostructures were covered by the lipid layer. Holes and regions of lipids covering the nanostructures were also detected, which might affect the uniformity of the lipid signal. Nevertheless, as the diameter of the laser spot responsible of sample illumination was large (500 nm) an average signal was collected.

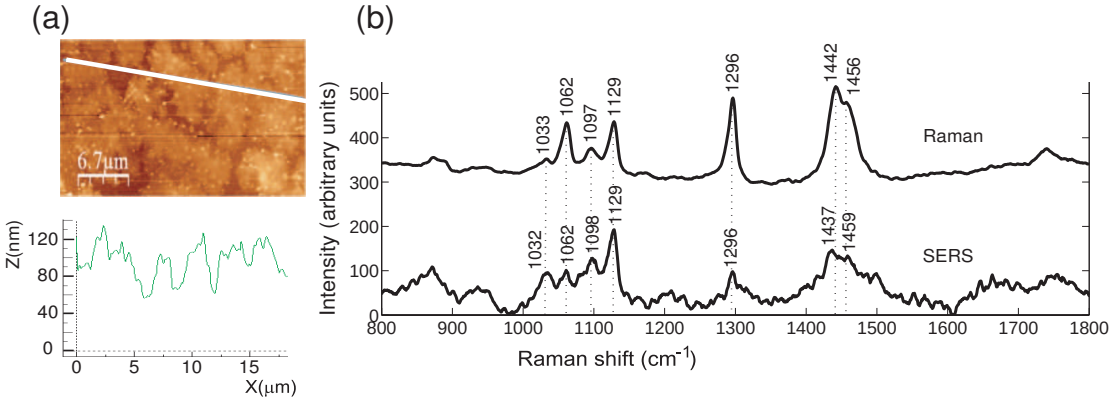

Figure 7.31: (a) AFM height image and line profile of cationic DPPC spin coated on a sapphire/Ag SERS-active substrate and its simultaneous SERS signal is shown in (b). At the top the lipid signal of cationic DPPC powder (Raman) and at the bottom the signal (SERS) from the spin coated layer at 1-2 mW of laser power.

The interchange of isopropanol and chloroform as solvent of the cationic DPPC was found not to affect the thickness of the lipid layer formed. Isopropanol was preferred for its lower evaporation rate which enabled a more uniform deposition. In Figure 7.31 (b) the SERS signal of the lipids was acquired with a laser power of 1 mW and 500 s of exposure time. A typical SERS spectrum is compared with the Raman signal from a bulk powdered cationic DPPC sample. As can be seen four major peaks of the Raman spectra corresponding to the lipid spectral bands at 1442 cm^{-1}(CH scissoring), 1296 cm^{-1}(CH twisting), 1129 cm^{-1}(CC stretching), and 1097 cm^{-1}(CC stretching) were detected for the SERS spectra at 1437cm^{-1}, 1296 cm^{-1}, and 1129 cm^{-1}. For a full Raman peak assignment to the correspondent Raman vibrational modes see Chapter 4.

A lipid thickness of 100 nm was sufficient for the system to detect the presence of lipids. As reported in previous studies lipid concentration was found to be the parameter with the greatest impact in the thickness of the deposited film [99]. Reducing the lipid concentration to 1.25 (mg)ml^{-1} thinner lipid layers of approximately 25 nm were fabricated. Simultaneous AFM and SERS measurements were performed on a sapphire/Ag substrate by deposition of 20 μl of cationic DPPC in 2-propanol and spin coated at 3000 rpm for 50 s. Regions of the desired thickness were found by the AFM measure-

ments as shown in Figure 7.32 (a-b) and 7.33 (a). The simultaneous SERS measurements seen in Figure 7.32 (c) and 7.33 (b) were recorded at a laser power of 56 μW at the sample for 500 s of exposure time. The spectrum of bulk powdered cationic DPPC normalised to enable comparison with the raw SERS spectra is included as a reference. Figure 7.33 (b) shows the five major characteristic peaks of the lipid Raman fingerprint which are labelled in the figure for easiness in the interpretation. Raman spectral peaks at 1062 cm^{-1}, 1097 cm^{-1}, 1129 cm^{-1}, 1296 cm^{-1}, and 1442 cm^{-1} (for a full assignment of the these bands to the vibrational Raman modes see Chapter 4) were measured for the SERS spectra at 1063 cm^{-1}, 1100 cm^{-1}, 1131 cm^{-1}, 1302 cm^{-1}, and 1440 cm^{-1}. Therefore, the combined AFM-SERS system enables spectroscopic/topographic lipid detection of cationic DPPC multilamellar arrangements of an approximate thickness of 25 nm on sapphire/Ag SERS-active substrates.

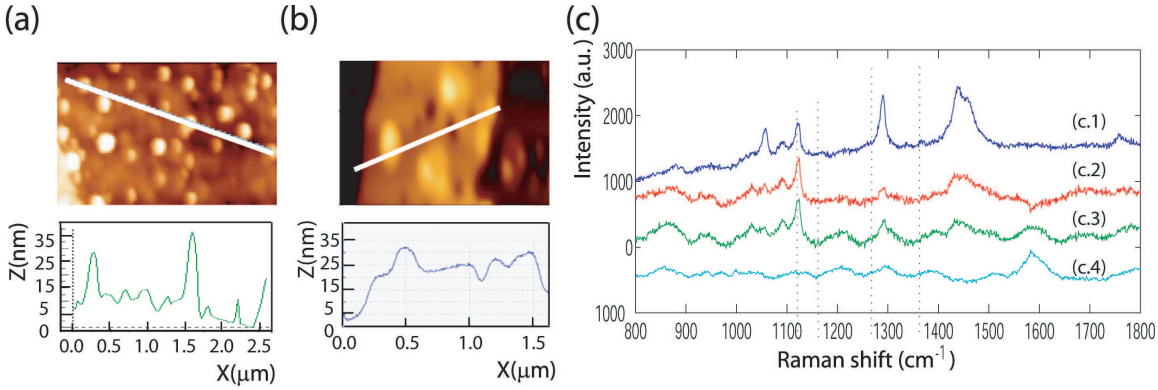

Figure 7.32: (a-b) AFM and line profile of a thin layer of cationic DPPC spin coated on a sapphire/Ag 400 nm SERS substrate. (c) Simultaneous SERS spectra of sample (b), where (c.1) is the Raman spectrum of bulk cationic DPPC, (c.2) and (c.3) are the SERS spectra of the thin layer without and with background contribution, respectively and (c.4) is the background of the SERS substrate alone.

In Figure 7.33 a region of 15 nm of lipids was detected by AFM and then measured by SERS. The same major five peaks than in Figure 7.32 characteristics of the Raman spectrum of cationic DPPC were detected.

The most enhanced were the peaks at 1129 cm^{-1}, 1296 cm^{-1}, and 1442 cm^{-1}. Also a weak but reproducible Raman spectral peak appeared at 1097 cm^{-1}. The Raman spectral peak at 1062 cm^{-1} was very weak and could barely be detected over the background. Note that the AFM images showed a multilamellar structure with heterogeneous thickness which can be attributed to the different number of layers, ranging from less than 5 nm (monolayer) to 15 nm.

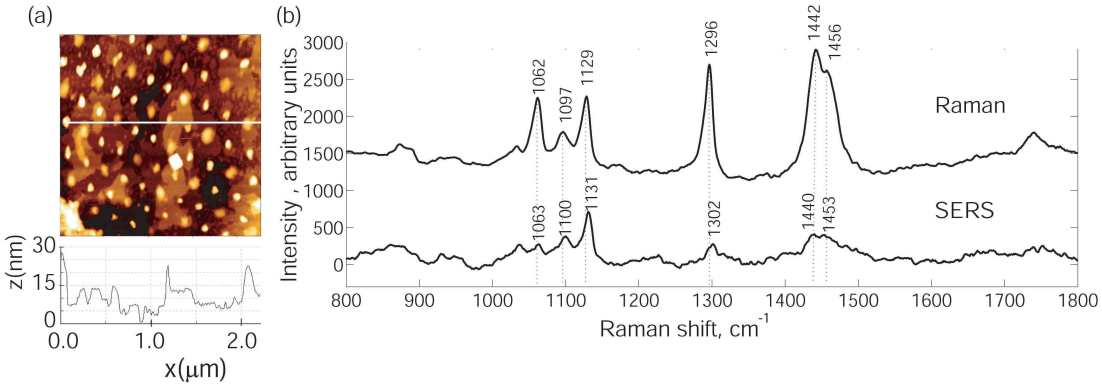

Figure 7.33: Simultaneous AFM/SERS characterisation of 3 monolayers of cationic DPPC on a sapphire/Ag substrate. (a) AFM image and line profile showing a thickness of the lipid multilayer structure of 5 (monolayer) to 15 nm (3 layers). (b) Raman spectra of bulk cationic DPPC powder and SERS spectra of the multilamellar lipid structure on sapphire/Ag substrates without the substrate contribution. SERS spectra were recorded with a 532 nm laser, power 56 μW at sample, for 500 s.

Figure 7.34 is a AFM height image corresponding to the same sample of Figure 7.33. Note that in Figures 7.33 and 7.34 the nanostructures are clearly present; however, the images may show tip effect likely due to the easiness of the lipids to attach to the AFM tip as reported by previous studies of AFM in lipids [173].

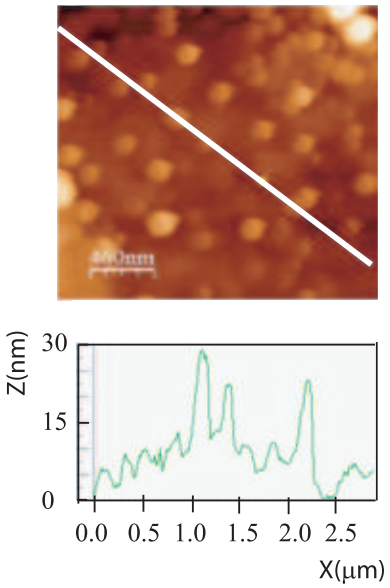

Figure 7.34: AFM height image corresponding to the same sample of Figure 7.33 with tip effects.

Figure 7.35 corresponds to a simultaneous AFM-SERS study on multilamellar arrangements of AA deposited on sapphire/Ag SERS-active substrates by spin coating with the same conditions and parameters as used for the experiments with cationic DPPC of Figures 7.31 to 7.34. The line profile

of Figure 7.35 (a) shows that 3 monolayers of AA were deposited on the substrate. Simultaneous SERS measurements (b) were performed at a laser power of 56 μW at sample with acquisition times of 500 s and results are displayed in Figure 7.35 (b). Raman spectra of AA powder was included in the figure for comparison with the enhanced spectral bands. The SERS spectra were background corrected as described in Chapter 4. The main difference between the Raman and the SERS spectra of AA was the appearance of an extra spectral peak in the SERS measurements at 1396 cm^{-1}. This peak corresponds to symmetric CH_2 deformations and has been used previously to detect the presence of fatty acids in mixtures of fatty acids and lipids adsorbed on silver electrodes by SERS [111]. Peaks in the Raman spectrum at 1418, 1438, and 1460 cm^{-1} (CH_2 scissoring and CH symmetric bending) can be associated to the mentioned SERS shifted spectral peak at 1396 cm^{-1} and to the weak SERS spectral peak at 1437 cm^{-1}. Vibrational modes at 1060, 1107 and 1128 cm^{-1} in the Raman spectrum of AA (CC *trans* stretching) relate to SERS spectral peaks at 1062, 1108 and 1129 cm^{-1}. The Raman spectral peak at 1295 cm^{-1} occurs at 1298 cm^{-1} in the SERS spectrum (CH_2 twisting deformations). An additional peak was detected in the SERS spectrum of AA at 925 cm^{-1} (CC stretching). For a detailed Raman peak assignment of AA see Chapter 4.

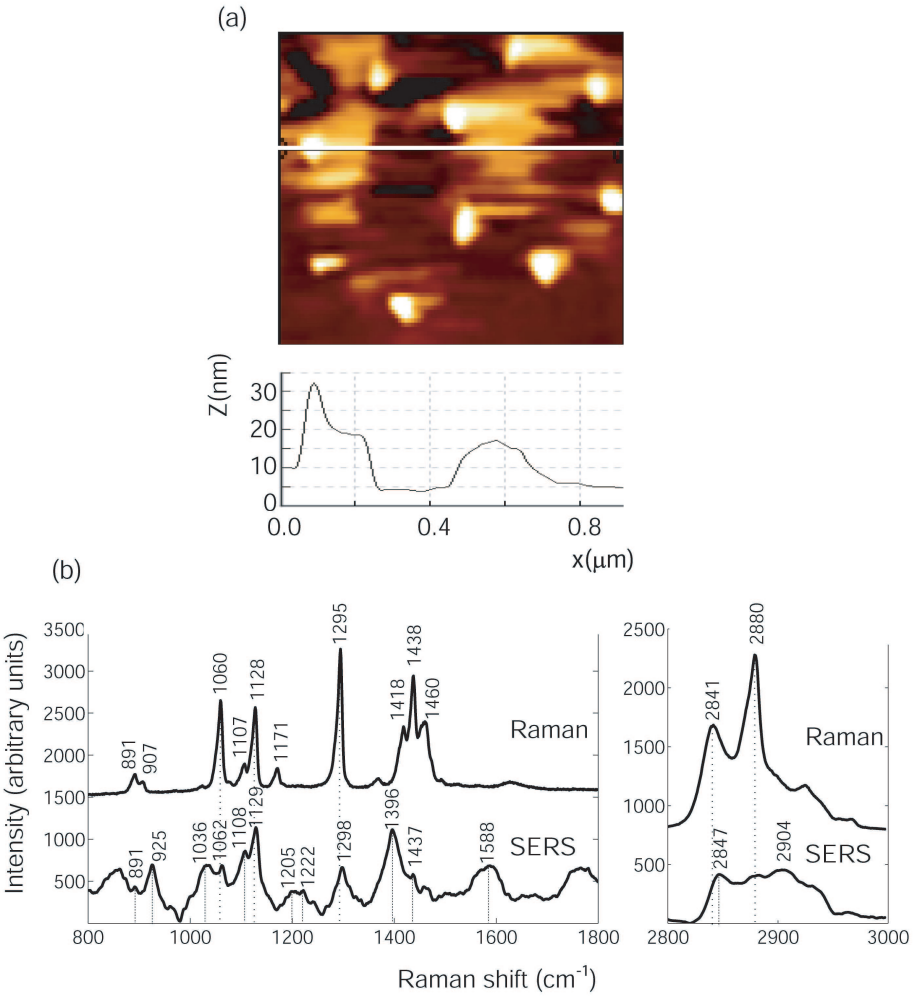

Figure 7.35: Simultaneous AFM/SERS characterisation of arachidic acid(AA) layers on a sapphire/Ag substrate. (a) height and line profile of a thin AA film deposited by spin coating. (b) Raman spectra of AA powder versus the SERS spectra of the multilamelar AA structure background corrected (power 56 μW at sample, 500 s).

7.8 Summary

The study presented in Chapter 7 tests the fourth hypothesis of this thesis: *if it is possible to achieve a "dual" characterisation of thin supported lipid films by simultaneous AFM and SERS measurements.*

Thin supported lipid films have a wide range of applications, from models of the cell membrane to selective biosensors. Thus, a "dual" characterisation of these thin lipid films is of great scientific interest, where *"dual"* refers to *"spectroscopic"* and *"topographic"* characterisation. The spectroscopic measurements performed with SERS provided the chemical information from the thin lipid films, whereas the morphological information from the lipids was measured with the AFM.

The aim of this study was to simultaneously record AFM images and SERS spectra of supported lipid monolayers and multilamellar lipid architectures. In order to achieve this aim three stages were covered:

(a) Fabrication of substrates (to support the lipid layers) optimised for both the SERS and AFM measurements.

(b) Synthesis of thin lipid films on the substrates using three methods: vesicle fusion, Langmuir-Blodgett, and spin coating.

(c) AFM and SERS simultaneous measurements were performed on the thin supported lipid films.

Nanosphere lithography was used to produce silver nanostructures in a periodic arrangement on solid planar substrates. Sapphire/Ag and mica/Ag substrates were fabricated. Sapphire and mica were proven to have a roughness of less than 1 nm as required for the AFM measurements on thin supported lipid films. Sapphire was preferred to mica due to SERS considerations. When tested with a small non-resonant analyte (p-ATP) sapphire/Ag substrates produced higher SERS enhancement factors (of the order of 10^8) and less Raman spectral peaks masking the SERS "fingerprint" of the lipids.

Uniform hydrated phospholipid bilayers were successfully produced by vesicle fusion in control planar substrates (bare mica) and characterised with the AFM. Height images and force spectroscopy curves ensured the presence of the bilayer. Formation of a uniform lipid bilayer on the SERS-active substrates was not successful. The coverage of the silver nanostructures was largely below the unity likely due to the electrostatic repulsive forces intervening in the system. Even in ionic solutions uniform bilayers did not

adsorb on the silver. No SERS signal from the lipids was detected over the background. To improve the coverage arrangements of multilamellar lipid architectures were considered. However, vesicle fusion (as well as the Langmuir-Blodgett (LB) technique) only allowed a limited amount of bilayers to pile up introducing a limitation in the maximum thickness of the thin lipid film which could be synthesised with this technique. The need for a new method allowing a more accurate control on the number of monolayers piled up to form the lipid architecture appeared.

The LB technique was also used to produce thin lipid films. For operational easiness, non-hydrated bilayers were fabricated. LB lipid films formed by 1-3 monolayer stackings of cationic DPPC on mica/Ag and sapphire/Ag SERS-active substrates were successfully characterised with the AFM but none of the SERS spectra measured could be attributed to the lipid contribution.

Spin coating was explored as an alternative to vesicle fusion and the LB technique to accurately deposit a small but upper limit-free number of piled monolayers of cationic DPPC and other amphiphiles on SERS active substrates. AFM was sucessfully performed allowing the detection of the different sequential monolayer levels. SERS spectra of multilamellar arrangements of cationic DPPC and AA on sapphire/Ag SERS substrates of ≈15-20 nm thickness were successfully detected with the Raman micro-spectroscopic instrument. The main spectral peaks from the SERS spectra were related to the Raman spectral peaks of the pure lipids/fatty acids.

In conclusion, thin supported films of phospholipids and fatty acids deposited by spin coating were detected by SERS, and their topography simultaneously characterised by the AFM. To the author's knowledge this is the first study in which a "dual" characterisation on such systems is successfully performed with AFM and SERS without introducing strong Raman scatterers within the lipid films or external voltages. New approaches in the estimation of the enhancement factor of the SERS-active substrates were reported in this thesis and might lead to future discussions. The study described in Chapter 7 showed the potential of the combined AFM/SERS technique towards the optical (spectroscopic) and topographic characterisation of a single phospholipid bilayer.

The strict requirements satisfied by the SERS-active substrates fabricated for this investigation enable their generalisation to broader studies with more complex systems including lipid mixtures, which could mimic more accurately cell rafts. Still open questions are the level of specificity of the AFM-SERS system, i.e whether the Raman micro-spectroscopic instru-

ment is sufficiently sensitive to distinguish between different lipid classes coexisting in those rafts. If this is the case then the acquired SERS spectra could be used for chemical imaging of lipid mixtures. These images would be complemented with their simultaneous topography via AFM images. Furthermore, this study can be used as a solid basis for tip-enhanced Raman spectroscopy investigations on thin supported phospholipids.

Bibliography

[1] E. Sackmann. Supported membranes: Scientific and practical applications. *Science*, 171:44–48, 1996.

[2] M. Gniadecka, H.C. Wulf, O.F. Nielsen, D.H. Christensen, and J. Hercogova. Distinctive molecular abnormalities in benign and malignant skin lesions: Studies by Raman spectroscopy. *Photochem Photobiol*, 66:418–423, 1997.

[3] C. Murali Krishna, N.B. Prathima, R. Malini, B.M. Vadhiraja, R. A. Bhatt, D. J. Fernandes, P. Kushtagi, M.S. Vidyasagar, and V.B. Kartha. Raman spectroscopy studies for diagnosis of cancers in human uterine cervix. *Vib Spectrosc*, 41:136–141, 2006.

[4] M. Keller, E.M Kanter, and A. Mahadevan-Jansen. Raman spectroscopy for cancer diagnosis. *Spectrosc*, 21(11):33, 2006.

[5] A. Nijssen, T.C.B. Schut, F. Heule, P.J. Caspers, D.P. Hayes, M.H. Neumann, and G.J. Puppels. Discriminating basal cell carcinoma from its surrounding tissue by Raman spectroscopy. *J Invest Dermatol*, 119:64–69, 2002.

[6] J. Hutchings, C. Kendall, B. Smith, N. Shepherd, H. Barr, and N. Stone. The potential for histological screening using a combination of rapid Raman mapping and principal component analysis. *Biophoton*, 2(1-2):91–103, 2009.

[7] M. Gniadecka, P. Alshede Philipsen, S. Sigurdsson, S. Wessel, O.F. Nielsen, D.H. Christensen, J. Hercogova, K. Rossen, H.K. Thomsen, R. Gniadecki, L.K. Hansen, and H.C. Wulf. Melanoma diagnosis by Raman spectroscopy and neural networks: Structure alterations in proteins and lipids in intact cancer tissue. *J Invest Dermatol*, 122:443–449, 2004.

[8] T. W. Koo. Method and instrument for collecting Fourier transform (FT) Raman spectra for imaging applications, April 2009.

[9] D. Muller. Electrostatically balanced subnanometer imaging of biological specimens by AFM. *Biophys J*, 76:1101, 1999.

[10] L. Krapf, M. Dezia, W. Reichsteina, J Köhlera, and S. Oellericha. AFM characterization of spin-coated multilayered dry lipid films prepared from aqueous vesicle suspensions. *Colloid Surface B*, 82:25–32, 2011.

[11] C. Mangeney, V. Dupres, Y. Roche, N. Felidj, G. Levi, J. Aubard, and S. Bernard. Surface enhanced Raman scattering of a lipid Langmuir monolayer at the airwater interface. *Biopolymers*, 74:136–140, 2004.

[12] F.C. Guo, Y.C. Chou, and W.G. Wu. The surface enhanced Raman spectroscopic study of the ordering of lipid molecules deposited on the silver electrode. *Chinese J Phys*, 28:173, 1990.

[13] L.H. Gu and P. A. Coulombe. Keratin function in skin epithelia: a broadening palette with surprising shades. *Curr Opin Cell Biol*, 19:13–23, 2007.

[14] P.A. Riley. Molecules in focus: melanin. *Int. J Biochem Cell Biolog*, 29:1235–1239, 1997.

[15] S.M. Maricich, S.A. Wellnitz, A. M. Nelson, D.R. Lesniak, G.J. Gerling, E.A. Lumpkin, and H.Y. Zoghbi. Merkel cells are essential for light-touch responses. *Science*, 324:1580–1582, 2009.

[16] D.J. Gawkrodger. *Dermatology: an illustrated colour text*. Churchill Livingston, Elsevier Science, 2003.

[17] W.M. Becker, L.J. Kleinsmith, J. Hardin, and G.P. Bertoni. *The World of the Cell*. Pearson International, 2009.

[18] M. Mogensen and G.B.E. Jemec. Diagnosis of non-melanoma skin cancer/keratinocyte carcinoma: A review of diagnostic accuracy of non-melanoma skin cancer diagnostic tests and technologies. *Dermatol Surg*, 33:1158–1174, 2007.

[19] L. Brochez, E. Verhaeghe, E. Grosshans, E. Haneke, G. Pirard, D. Ruiter, and J.-M. Naeyaert. Inter-observer variation in the histopathological diagnosis of clinically suspicious pigmented skin lesions. *J Pathol*, 196:459–466, 2002.

[20] R.L. Souhami and J. Tobias. *Cancer and its management*. Blackwell Science Inc., 1995.

[21] Cancer Research UK . "http://info.cancerresearchuk.org/cancerstats/types/skin/", 2009.

[22] American Cancer Society. Cancer facts & figures 2008. "http://www.cancer.org/downloads/STT/2008CAFFfinalsecured.pdf", 2008.

[23] American Cancer Society. What are basal and squamous cell skin cancers? "http://www.cancer.org/cancer/skincancer-basalandsquamouscell/index".

[24] G. Saldanha, A. Fletcher, and D.N. Slater. Basal cell carcinoma: a dermatopathological and molecular biological update. *B J Dermatol*, 148:195–202, 2003.

[25] K.L. Agnew, B.A. Gilchrest, and C.B. Bunker. *Skin Cancer*. Health Press, 2005.

[26] T.W. McGovern. Mohs surgery: The informed view. *Arch Dermatol*, 135:1255–1259, 1999.

[27] N. Smeets, G. Krekels, J. Ostertag, B. Essers, C. Dirksen, F. Nieman, and H. Neumann. Surgical excision Mohs micrographic surgery for basal cell carcinoma of the face: randomised controlled trial. *The Lancet*, 364(9447):1766– 1772, 2004.

[28] N.R. Telfer, G.B. Colver, and W. Bowers. Guidelines for the management of basal cell carcinoma. *Br J Dermatol*, 141(3):415 –423, 1999.

[29] I. Leibovitch, S.C. Huilgol, D. Selva, S. Richards, and R. Paver. Basal cell carcinoma treated with Mohs surgery in Australia i. experience over 10 years. *J Am Acad Dermatol*, 53:445–451, 2005.

[30] R. Rowe, R. Carroll, and C. Day. Long-term recurrence rates in previously untreated (primary) basal cell carcinoma: Implications for patient follow-up. *J Dermatol Surg Oncol*, 15(3):315–328, 1989.

[31] T.L. Bialy, J. Whalen, E. Veledar, D. Lafreniere, J. Spiro, T. Chartier, and S.C. Chen. Mohs micrographic surgery vs traditional surgical excision: A cost comparison analysis. *Arch Dermatol*, 140:736–742, 2004.

[32] B.A.B. Essers, C.D. Dirksen, F.H.M. Nieman, N.W.J. Smeets, G.A.M. Krekels, M.H. Prins, and H.A.M. Neumann. Cost-effectiveness of Mohs micrographic surgery vs surgical excision for basal cell carcinoma of the face. *Arch Dermatol*, 142:187– 194, 2006.

[33] F. Bath-Hextall, J. Bong, W. Perkins, and H. Williams. Interventions for basal cell carcinoma of the skin: systematic review. *BMJ*, 329:705–709, 2004.

[34] National Institute for health snd clinical excellence. Improving outcomes for people with skin tumours including melanoma. "http://www.nice.org.uk/guidance/CSGSTIM", February 2006.

[35] A.B. Fleischer, S.R. Feldman, J.O. Barlow, B. Zheng, H.B. Hahn, T.Y. Chuang, K.S. Draft, L.E. Golitz, E. Wu, A.S. Katz, J.C. Maize, T. Knapp, and B. Leshin. The specialty of the treating physician affects the likelihood of tumor-free resection margins for basal cell carcinoma: Results from a multi-institutional retrospective study. *J Am Acad Dermatol*, 44:224–229, 2001.

[36] A. Hernández-Martín, D. Arias-Palomo, E. Barahona, C. Hidalgo, C. Muñoz, and I. García-Higuera. Analysis of surgical treatment for nonmelanoma skin cancer performed by dermatologists in a public hospital: Clinical-pathological correlation, use of hospital resources, and waiting list time from diagnosis. *Actas Dermo-Sifiliográficas (English Edition)*, 98:694–701, 2007.

[37] M.J. Trotter and A.K. Bruecks. Interpretation of skin biopsies by general pathologists: diagnostic discrepancy rate measured by blinded review. *Arch Pathol Lab Med*, 127:1489–1492, 2003.

[38] H.A. Horiba and M.B. Morgan. *Mohs Micrographic Surgery*. W.B. Saunders, 1991.

[39] A. Stevens and J.S. Lowe. *Human histology*. Mosby, 2nd edition, 1997.

[40] A.N. Yaroslavsky, V. Neel, and R.R. Anderson. Demarcation of nonmelanoma skin cancer margins in thick excisions using multispectral polarized light imaging. *J Invest Dermatol*, 121:259–266, 2003.

[41] O. Arnon, A.J. Mamelak, and L.H. Goldberg. *Mohs Surgery and Histopathology: Beyond the Fundamentals*. Cambridge University Press, 2009.

[42] T.R. Humphreys, A. Nemeth, S. McCrevey, S.C. Baer, and L.H. Goldberg. A pilot study comparing toluidine blue and hematoxylin and eosin staining of basal cell and squamous cell carcinoma during Mohs surgery. *Dermatol Surg*, 22:693–697, 1996.

[43] M.M. Todd, J.W. Lee, and V.J. Marks. Rapid toluidine blue stain for Mohs micrographic surgery. *Dermatol Surg*, 31:244–5, 2005.

[44] L. Brancaleon, A.J. Durkin, J.H. Tu, G. Menaker, J. D. Fallon, and N. Kollias. In vivo fluorescence spectroscopy of non-melanoma skin cancer. *Photochem Photobiol*, 73:178–183, 2001.

[45] B. Stenquist, M.B. Ericson, L . Molne, A. Rosen, O. Larko, and A.M. Wennberg. Bispectral fluorescence imaging of aggressive basal cell carcinoma combined with histopathological mapping: a preliminary study indicating a possible adjunct to Mohs micrographic surgery. *Br J Dermatol*, 154:305–309, 2006.

[46] R. Na, I.M. Stender, and H.C. Wulf. Can autofluorescence demarcate basal cell carcinoma from normal skin? a comparison with protoporphyrin IX fluorescence. *Acta Derm Venereol*, 81(4):246–249, 2001.

[47] L. M. McIntosh, M. Jackson, H. H. Mantsch, M. F. Stranc, D. Pilavdzic, and A.N. Crowson. Infrared spectra of basal cell carcinomas are distinct from non-tumor-bearing skin components. *J Invest Dermatol*, 112:951–956, 1999.

[48] R. Cicchi, D. Massi, S. Sestini, P. Carli, V. De Giorgi, T. Lotti, and F. S. Pavone. Multidimensional non-linear laser imaging of basal cell carcinoma. *Opt Exp*, 15:10136–10148, 2007.

[49] J. Paoli, M. Smedh, A.M. Wennberg, and M.B. Ericson. Multiphoton laser scanning microscopy on non-melanoma skin cancer: Morphologic features for future non-invasive diagnostics. *J Invest Dermatol*, 128:1248–1255, 2008.

[50] S.J. Lin, S.H. Jee, C.J. Kuo, R.J. Wu, W.C. Lin, J.S. Chen, Y.H. Liao, C.J. Hsu, T.F. Tsai, Y.F. Chen, and C.Y. Dong. Discrimination of basal cell carcinoma from normal dermal stroma by quantitative multiphoton imaging. *Opt Lett*, 31:2756–2758, 2006.

[51] N. Vogler, T. Meyer, D. Akimov, I. Latka, C. Krafft, N. Bendsoe, K. Svanberg, B. Dietzek, and J. Popp. Multimodal imaging to study the morphochemistry of basal cell carcinoma. *J Biophotonics*, 3:728–736, 2010.

[52] T. Gambichler, A. Orlikov, R. Vasa, G. Moussa, K. Hoffmann, M. Stücker, P. Altmeyer, and F.G. Bechara. In vivo optical coherence tomography of basal cell carcinoma. *J Dermatol Sci*, 45:167–173, 2007.

[53] M. Mogensen, T. M. Joergensen, B.M. Nürnberg, H.A. Morsy, J.B. Thomsen, L. Thrane, and G.B.E. Jemec. Assessment of optical coherence tomography imaging in the diagnosis of non-melanoma skin cancer and benign lesions versus normal skin: Observer-blinded evaluation by dermatologists and pathologists. *Dermatol Surg*, 35:965–972, 2009.

[54] D. Huang, E.A. Swanson, C.P. Lin, J. S. Schuman, W.G. Stinson, W. Chang, M. R. Hee, T. Flotte, K. Gregory, C.A. Puliafito, and J.G.

Fujimoto. Optical coherence tomography. *Science*, 254:1179–1181, 1991.

[55] R. Manoharan, Y. Wang, and M.S. Feld. Histochemical analysis of biological tissues using Raman spectroscopy. *Spectrochim Acta Part A*, 52:215–249, 1996.

[56] K.K. Kumar, A. Anand, M.V.P. Chowdary, K. Thakur, J. Kurien, C.M. Krishna, and S. Mathew. Discrimination of normal and malignant stomach mucosal tissues by Raman spectroscopy: a pilot study. *Vib Spectrosc*, 44:382–387, 2007.

[57] T.R. Hata, T.A. Scholz, I.V. Ermakov, R.W. McClane, F. Khachik, W. Gellermann, and L.K. Pershing. Non-invasive Raman spectroscopic detection of carotenoids in human skin. *J Invest Dermatol*, 115(3):441–448, 2000.

[58] C.A. Lieber, S.K. Majumder, D.J. Ellis, D.D. Billheimer, and A. Mahadevan-Jansen. In vivo non-melanoma skin cancer diagnosis using Raman microspectroscopy. *Laser Surg Med*, 40:461–467, 2008.

[59] M. Gniadecka, H.C. Wulf, N.N. Mortensen, O.F. Nielsen, and D.H Christensen. Diagnosis of basal cell carcinoma by Raman spectroscopy. *J Raman Spectrosc*, 28:125–130, 1997.

[60] A. S. Haka, K. E. Shafer-Peltier, M. Fitzmaurice, J. Crowe, R. R. Dasari, and M. S. Feld. Diagnosing breast cancer by using Raman spectroscopy. *Proc Natl Acad Sci USA*, 102:12371–12376, 2005.

[61] C. Kendall, N. Shepherd, B. Warren, K. Geboes, H. Barr, and N. Stone. Raman spectroscopy a potential tool for the objective identification and classification of neoplasia in Barretts oesophagus. *J Pathol*, 200:602–609, 2003.

[62] Z. Huang, A. McWilliams, H. Lui, D. I. McLean, S. Lam, and H. Zeng. Near-infrared Raman spectroscopy for optical diagnosis of lung cancer. *Int J Cancer*, 107:1047–1052, 2003.

[63] P. Crow, N. Stone, C. A. Kendall, J. S. Uff, J. A. M. Farmer, H. Barr, and M. P. J. Wright. The use of Raman spectroscopy to identify and grade prostatic adenocarcinoma in vitro. *Br J Cancer*, 89:106–108, 2003.

[64] H.G.M. Edwards, A.C. Williams, and B.W. Barry. Potential applications of FT-Raman spectroscopy for dermatological diagnostics. *J Mol Strut*, 347:379–388, 1995.

[65] W. Akhtar, H. G. M. Edwards, D.W. Farwella, and M. M. Nutbrownb. Fourier-transform Raman spectroscopic study of human hair. *Spectrochim Acta A*, 53:1021–1031, 1997.

[66] P. J. Caspers, G.W. Lucassen, and G.J. Puppels. Combined in vivo confocal Raman spectroscopy and confocal microscopy of human skin. *Biophys J*, 85:572–580, 2003.

[67] C. Krafft, D. Codrich, G. Pelizzo, and V. Sergo. Raman mapping and ftir imaging of lung tissue: congenital cystic adenomatoid malformation. *The Analyst*, 133:361–371, 2008.

[68] G. Shetty, C. Kendall, N. Shepherd, N. Stone, and H. Barr. Raman spectroscopy: elucidation of biochemical changes in carcinogenesis of oesophagus. *Br J Cancer*, 94:1460–1464, 2006.

[69] M. J. Romeo and M. Diem. Infrared spectral imaging of lymph nodes: Strategies for analysis and artifact reduction. *Vib Spectrosc*, 38:115–119, 2005.

[70] C.L. Evans and X. S. Xie. Coherent anti-stokes raman scattering microscopy: Chemical imaging for biology and medicine. *Anal Chem*, 1:883–909, 2008.

[71] A.P. Girard-Egrot and L.J. Blum. *Langmuir-Blodgett technique for synthesis of biomimetic lipid membranes in 'Nanobiotechecnology of biomimetic membranes'*. Springer, 2007.

[72] B. Alberts, A. Johnson, J. Lewis, M. Raff, K. Roberts, and P. Walter. *Molecular Biology of the Cell*. Garland Science, 2002.

[73] D.A. Hammer and D.A. Lauffenburger. A dynamical model for receptor-mediated cell adhesion to surfaces. *Biophys J*, 52:475–487, 1987.

[74] R.J. Pelham and Y.L. Wang. Cell locomotion and focal adhesions are regulated by substrate flexibility. *Proc Natl Acad Sci USA*, 94:13661–13665, 1997.

[75] K. Simons and D. Toomre. Lipid rafts and signal transduction. *Nature*, 1:31–41, 2000.

[76] H. M. McConnell, J. C. Owicki, J. W. Parce, D. L. Miller, G. T. Baxter, H. G. Wada, and S. Pitchford. The cytosensor microphysiometer: Biological applications of silicon technology. *Science*, 257:1906–1912, 1992.

[77] F. Harris, K. Brandenburg, U. Seydel, and D. Phoenix. Investigation into the mechanisms used by the c-terminal anchors of escherichia coli penicillin-binding proteins 4,5,6, and 6b for membrane interactions. *Eur J Biochem*, 269:5821–5829, 2002.

[78] C.D. Heyes and M.A. El-Sayed. The role of the native lipids and lattice structure in bacteriaorhodopsin protein conformation and stability as studied by temperature-dependent Fourier transform-infrared spectroscopy. *J Biol Chem*, 77:29439–29443, 2002.

[79] K. Ishihara. Bioinspired phospholipid polymer biomaterials for making high performance artificial organs. *Sci Technol Adv Mat*, 1:131–138, 2000.

[80] K. Ishihara and M. Takai. Bioinspired interface for nanobiodevices based on phospholipid polymer chemistry. *J R Soc Interface*, 6:S279–S291, 2009.

[81] U. Mennicke and T. Salditt. Preparation of solid-supported lipid bilayers by spin-coating. *Langmuir*, 18:8172–8177, 2002.

[82] L. Perino-Gallice, G. Fragneto, U. Mennicke, T. Salditt, and F. Rieutord. Dewetting of solid-supported multilamellar lipid layers. *Eur Phys J E*, 8:275–282, 2002.

[83] P. Koole, A.J. Dammersa, G. Van Ginkela, and Y.K. Levine. Low-motion ESR of cholestane spin labels in planar multibilayers of diacyldigalactosyldiglycerides. *Biochim Biophys Acta*, 777:297–305, 1984.

[84] A. Ulman. *An introduction to ultrathin organic films: from Langmuir-Blodgett to self-assembly*. Academic Press, 1991.

[85] G. Oncins Marco. *Nanomechanics of organic layers and biomembranes*. PhD thesis, School of Chemistry, Universitat de Barcelona, 2007.

[86] Y. K. Levine and M. H. F. Wilkins. Structure of oriented lipid bilayers. *Nature*, 230:69–72, 1971.

[87] S.J. Johnson, T.M. Bayerl, D.C. McDermott, G.W. Adam, A.R. Rennie, R.K. Thomas, and E. Sackmann. Structure of an adsorbed dimyristoylphosphatidylcholine bilayer measured with specular reflection of neutrons. *Biophys J*, 59:289–294, 1991.

[88] J. Majewski, J. Y. Wong, C. K. Park, M. Seitz, J. N. Israelachvili, and G. S. Smith. Structural studies of polymer-cushioned lipid bilayers. *Biophys J*, 75:2363–2367, 1998.

[89] R. Henderson. The potential and limitations of neutrons, electrons and X-rays for atomic resolution microscopy of unstained biological molecules. *Q Rev Biophys*, 28:171–193, 1995.

[90] E. Meyer, L. Howald, R. M. Overney, H. Heinzelmann, J. Frommer, H.-J. Gntherodt, T. Wagner, H. Schier, and S. Roth. Molecular-resolution images of Langmuir-Blodgett films using atomic force microscopy. *Nature*, 349:398 – –400, 1991.

[91] C.S. Sweetenham and I. Notingher. Combined atomic force microscopy-Raman mapping of electric field enhancement and surface-enhanced Raman scattering hot-spots for nanosphere lithography substrates. *J Nanophotonics*, 5:059504, 2011.

[92] R. Böhme, M. Richter, D. Cialla, P. Rösch, V. Deckert, and J. Popp. Towards a specific characterisation of components on a cell surface − combined TERS-investigations of lipids and human cells. *J Raman Spectrosc*, 40:1452–1457, 2009.

[93] T. Isono, T. Ikeda, and T. Ogino. Evolution of supported planar lipid bilayers on step-controlled sapphire surfaces. *Langmuir*, 26:9607–9611, 2010.

[94] D. Millo, A. Bonifacio, M.R. Moncelli, V. Sergo, C. Gooijer, and G. Van der Zwan. Characterization of hybrid bilayer membranes on silver electrodes as biocompatible SERS substrates to study membrane-protein interactions. *Colloid Surface B*, 81:212–216, 2010.

[95] P.K. Ang, M. Jaiswal, C. Lim, Haley, Y. X. Lim, Y. Wang, J. Sankaran, A. Li, C.T. Lim, T. Wohland, O. Barbaros, and K.P. Loh. A bioelectronic platform using a graphene lipid bilayer interface. *ACS Nano*, 4:7387–7394, 2010.

[96] A.L. Plant, M. Brighamburke, E.C. Petrella, and D.J. Oshannessy. Phospholipid/alkanethiol bilayers for cell-surface receptor studies by surface plasmon resonance. *Anal Biochem*, 226:342–348, 1995.

[97] J. Radler, M. Radmacher, and H. E. Gaub. Velocity-dependent forces in atomic force microscopy imaging of lipid films. *Langmuir*, 10:3111–3115, 1994.

[98] F. J. Giessibl, S. Hembacher, H. Bielefeldt, and J. Mannhart. Subatomic features on the silicon (111)-(77) surface observed by atomic force microscopy. *Science*, 289:422–425, 2000.

[99] A.C. Simonsen and L.A. Bagatolli. Structure of spin-coated lipid films and domain formation in supported membranes formed by hydration. *Langmuir*, 20:9720–9728, 2004.

[100] U. Bernchou, J.H. Ipsen, and A.C. Simonsen. Growth of solid domains in model membranes: quantitative image analysis reveals a strong correlation between domain shape and spatial position. *J Phys Chem B*, 113:7170–7177, 2009.

[101] S. Garcia-Manyes, G. Oncins, and F. Sanz. Effect of ion-binding and chemical phospholipid structure on the nanomechanics of lipid bilayers studied by force spectroscopy. *Biophys J*, 89:1812–1826, 2005.

[102] S.M. Rigby-Singleton, M.C. Davies, H. Harris, P. OShea, and S. Allen. Visualizing the solubilization of supported lipid bilayers by an amphiphilic peptide. *Langmuir*, 22:6273–6279, 2006.

[103] M.M. Lipp, K.Y.C. Lee, J. A. Zasadzinski, and A.J. Waring. Design and performance of an integrated fluorescence, polarized fluorescence, and Brewster angle microscope/Langmuir trough assembly for the study of lung surfactant monolayers. *Rev Sci Instrum*, 68:2574, 1997.

[104] J. Meunier. Why a brewster angle microscope? *Colloid Surface A*, 171:33–40, 2000.

[105] L. Opilik, T. Bauer, T. Schmid, J. Stadler, and R. Zenobi. Nanoscale chemical imaging of segregated lipid domains using tip-enhanced Raman spectroscopy. *Phys Chem Chem Phys*, 13:9978–9981, 2011.

[106] L. J. Johnston. Nanoscale imaging of domains in supported lipid membranes. *Langmuir*, 23:5886–5895, 2007.

[107] A. Hassanzadeh and S. Mittler. Waveguide evanescent field fluorescence: high contrast imaging of a domain forming mixed lipid Langmuir-Blodgett monolayer mimicking lung surfactant. *J Biomed Opt*, 16:046022–1–4, 2011.

[108] H.M. Grandin, B. Stadler, M. Textor, and J. Voros. Waveguide excitation fluorescence microscopy: A new tool for sensing and imaging the biointerface. *Biosens Bioelectron*, 21:1476–1482, 2006.

[109] E.O. Potma and X. S. Xie. Detection of single lipid bilayers with coherent anti-Stokes Raman scattering (CARS) microscopy. *J Raman Spectrosc*, 34:642–650, 2003.

[110] S. Bernard, N. Felifj, S. Truong, P. Peretti, G. Lévi, and J. Aubard. Study of LangmuirBlodgett phospholipidic films deposited on surface

enhanced Raman scattering active gold nanoparticle monolayers. *Biopolymers*, 67:314–318, 2002.

[111] M.K. Weldon, V.R. Zhelyaskov, and M.D. Morris. Surface-enhanced Raman spectroscopy of lipids on silver microprobes. *Appl Spectrosc*, 52:265–269, 1998.

[112] J.R. Ferraro and K. Nakamoto. *Introductory Raman spectroscopy*. Academic Press, 2nd edition, 2003.

[113] W. Demtroder. *Laser Spectroscopy: Basic Concepts and Instrumentation*. Springer, 2nd edition, 1996.

[114] N. Stone. *Raman spectroscopy of biological tissue for application in optical diagnosis of malignancy*. PhD thesis, Cranfield University, 2001.

[115] D.L. Andrews and A.A. Demidov. *An Introduction to Laser Spectroscopy*. Kluwer Academic/Plenum publishers, 2nd edition, 2002.

[116] G. Placzek. Handbuch der radiologie. *Academische Verlag*, 6(526):12–18, 1934.

[117] D.I. Blokhistev. *Emission, absorption, and scaterring of light by atomic systems, in Principles of quantum mechanics*. Allyn and Bacon, 1964.

[118] P.F. Bernath. *Spectra of atoms and molecules*. Oxford University Press, 2nd edition, 2005.

[119] S. P. S. Porto and D. L. Wood. Ruby optical maser as a Raman source. *J Opt Soc Am*, 52:251, 1962.

[120] A. Weber, S. P. S. Porto, L. E. Cheesman, and J. J. Barrett. High-resolution Raman spectroscopy of gases with CW-laser excitation. *J Opt Soc Am*, 57:19–27, 1967.

[121] K. Kneipp, H. Kneipp, I. Itzkan, R.R. Dasari, and M.S. Feld. Ultrasensitive chemical analysis by Raman spectroscopy. *Chem Rev*, 99:2957–2976, 1999.

[122] M. Abramowitz and M. W. Davidson. Microscope objectives: Numerical aperture and resolution. "http://www.olympusmicro.com/primer/anatomy/numaperture.html", 2010.

[123] A.A. Michelson. On the application of interference-methods to spectroscopic measurements. *Philos Mag*, 31:256, 1891.

[124] R. J. Bell. *Introductory Fourier Transform Spectroscopy*. Academic Press Inc. Ltd., 1972.

[125] F.L. Pedrotti and L.S. Pedrotti. *Introduction to Optics*. Prentice-Hall, 1987.

[126] E. Hecht. *Optics*. Addison Wesley, 4th edition, 2002.

[127] D. Schräder and B.S. Moore. Nomenclature, symbols, units, and their usage in spectrochemical analysis-XVIII: Laser-based molecular spectroscopy for chemical analysis-Raman scattering processes (IUPAC recommendations 1997). *Pure & Appl Chem*, 69(7):1451–1468, 1997.

[128] P. Jacquinot and C.J. Dufour. Condition optique d'emploi des cellules photo-électriques dans les spectrographes et les interfèrométres. *Journal Recherche du Centre National Recherche Scientifique Laboratorie Bellevue*, 6:91–103, 1948.

[129] J.B. Slater, J. M. Tedesco, R. C. Fairchild, and I. R. Lewis. *Handbook of Raman Spectroscopy: from the research laboratory to the process line.* Dekker, M., 2001.

[130] C. J. H. Brenan. Enviromental isolation platform for microrobot system development. *Rev Sci Instrum*, 63:1143754, 1992.

[131] P. Tran. *Live cell imaging: a laboratory manual*. Cold Spring Harbor Laboratory Press, 2005.

[132] A. D. McNaught and A. Wilkinson. *Compendium of Chemical Terminology*. Blackwell Science, 2nd edition, 1997.

[133] P. Latham, Y. Morita, N. Massa, and T. Jeong. Photodetector characteristics. "http://cord.org/cm/leot/Module4/module4.htm".

[134] D. Litwiller. CMOS vs. CCD: maturing technologies, maturing markets. "http://www.dalsa.com/corp/markets/ccd_vs_cmos.aspx", 2005.

[135] J. Baudot, W. Dulinski, M. Winter, R. Barbier, E. Chabanat, P. Depasse, and N. Estre. Photon detection with CMOS sensors for fast imaging. *Nucl Instrum Meth A*, 604:111–114, 2009.

[136] P. J. Treado and M. P. Nelson. *Handbook of Raman spectroscopy: from the research laboratory to the process line*. M. Dekker, 2001.

[137] M. Delhaye and P. Dhamelincourt. *J Raman Spectrosc*, 3:33–43, 1975.

[138] G. J. Puppels, T. C. Bakker Schut, N. M. Sijtsema, M. Grond, F. Maraboeuf, C. J. Grauw de, C. G. Figdor, and J. Greve. Application of Raman microspectroscopic and Raman imaging techniques for cell biological studies. *J Molec Struct*, 347:477–484, 1995.

[139] R. Salzer, G. Steiner, H. H. Mantsch, J. Mansfield, and E.N. Lewis. Infrared and Raman imaging of biological and biomimetic samples. *Fresenius J Anal Chem*, 366:712–716, 2000.

[140] J. Barbillat, E. Da Silva, and B. Roussel. Demonstration of low-frequency performance and microanalysis capability of multi-channel Raman spectroscopy with near-infrared excitation. *J Raman Spectrosc*, 22:383–391, 1991.

[141] C.L. Jahncke, M. A. Paesler, and H. D. Hallen. Raman imaging with near-field scanning optical microscopy. *Appl Phy Lett*, 67:2483–2485, 1995.

[142] M. Larraona-Puy, A. Ghita, A. Zoladek, W. Perkins, S. Varma, I.H. Leach, A.A. Koloydenko, H. Williams, and I. Notingher. Development of Raman micro-spectroscopy for automated detection and imaging of basal cell carcinoma. *J Biomed Opt*, 14:054031 1–10, 2009.

[143] S. Schlücker, M. D. Schaeberle, S. W. Huffman, and I. W. Levin. Raman microspectroscopy: A comparison of point, line, and wide-field imaging methodologies. *Anal Chem*, 75:4312–4318, 2003.

[144] J. Hutchings, C. Kendall, N. Shepherd, B. Smith, H. Barr, and N. Stone. Rapid Raman microscopic imaging for potential histological screening. *Proc SPIE*, 6853, 2008.

[145] A. Zoladek, F. C. Pascut, P. Patel, and I. Notingher. Non-invasive time-course imaging of apoptotic cells by confocal Raman micro-spectroscopy. *J Raman Spectroc*, 42:251–258, April 2011.

[146] C. Krafft, T. Knetschke, R.H.W. Funk, and R. Salzer. Identification of organelles and vesicles in single cells by Raman microspectroscopic mapping. *Vib Spectrosc*, 38:85–93, 2005.

[147] P.G. Etchegoin and E. Le Ru. *Surface enhanced Raman spectroscopy: analytical, biophysical and life science applications*. Wiley-VCH, 2010.

[148] P. F. Liao and A. Wokaun. Lightning rod effect in surface enhanced Raman scattering. *J Chem Phys*, 76:751–752, 1982.

[149] Y.F. Huang, H.P. Zhu, G.K. Liu, D.Y. Wu, B. Ren, and Z.Q. Tian. When the signal is not from the original molecule to be detected: Chemical transformation of para-aminothiophenol on Ag during the SERS measurement. *J Am Chem Soc*, 132:9244–9246, 2010.

[150] E.C. Le Ru. Discussion by email.

[151] R. Aroca, editor. *Surface enhanced vibrational spectroscopy*. John Wiley and Sons, 2006.

[152] J.R. Lombardi, R. L. Birke, and G. Haran. Single molecule SERS spectral blinking and vibronic coupling. *J Phys Chem C*, 115:4540–4545, 2011.

[153] Y. Maruyama, M. Ishikawa, and M. Futamata. Thermal activation of blinking in SERS signal. *J Phys Chem B*, 108:673–678, 2004.

[154] E. Blackie. *Quantification of the Enhancement Factor in Surface-Enhanced Raman Scattering*. PhD thesis, Victoria University of Wellington, 2010.

[155] E.C. Le Ru and P.E. Etchegoin, editors. *Principles of surface enhanced Raman spectroscopy and related plasmonic effects*. Elsevier, 2009.

[156] E.C. Le Ru, E. Blackie, M. Meyer, and P.G. Etchegoin. Surface enhanced Raman scattering enhancement factors: A comprehensive study. *J Phys Chem C*, 111:13794–13803, 2007.

[157] E.C. Le Ru and P.G. Etchegoin. Phenomenological local field enhancement factor distributions around electromagnetic hot spots. *J Chem Phys*, 130:181101, 2009.

[158] V. J. Morris, A. R. Kirby, and A. P. Gunning. *Atomic force microscopy for biologists*. Imperial College Press, 2009.

[159] B. Cappella and G. Dietler. Force-distance curves by atomic force microscopy. *Surf Sci Reports*, 34:1–3, 5–104, 1999.

[160] H.J. Butt, B. Cappella, and M. Kappla. Force measurements with the atomic force microscope: Technique, interpretation and applications. *Surf Sci Reports*, 59:1–152, 2005.

[161] E.T. Castellana and P.S. Cremer. Solid supported lipid bilayers: From biophysical studies to sensor design. *Surf Sci Reports*, 61:429–444, 2006.

[162] C.G. Knight. *Liposomes: from physical structure to therapeutic applications*. Elsevier, 1981.

[163] M. Jurak and E. Chibowski. Wettability and topography of phospholipid DPPC multilayers deposited by spin-coating on glass, silicon, and mica slides. *Langmuir*, 23:10156–10163, 2007.

[164] A. Zoladek. *Confocal life imaging of live cells*. PhD thesis, School of Physics and Astronomy, The University of Nottingham, 2010.

[165] C.S. Sweetenham. *Raman spectroscopy methods for investigating supported lipid bilayers*. PhD thesis, School of Physics and Astronomy, The University of Nottingham, 2011.

[166] I. Horcas, R. Fernández, J.M. Gómez-Rodríguez, J. Colchero, J. Gómez-Herrero, and A. M. Baro. WSxM: A software for scanning probe microscopy and a tool for nanotechnology. *Rev Sci Instrum*, 78:013705, 2007.

[167] D. Necas and P. Klapetek. Gwyddion: an open-source software for SPM data analysis. *Cent Eur J Phys*, 10:181–188, 2012.

[168] P.R. Griffiths and A. De Haseth. *Fourier Transform Infrared Spectrometry*. John Wiley and Sons, 7th edition, 2007.

[169] R.L. McCreery, editor. *Raman spectroscopy for chemical analysis*. John Wiley and Sons, 2000.

[170] A. Savitzky and M.J. E. Golay. Smoothing and differentiation of data by simplified least squares procedures. *Anal Chem*, 36:1627 –1639, 1964.

[171] T. C. B. Schut, M. J. H. Witjes, H. J. C. M. Sterenborg, O. C Speelman, and. Marple T. Roodenburg, J. L. N., H. A. Bruining, and G. J. Puppels. In vivo detection of dysplastic tissue by Raman spectroscopy. *Anal Chem*, 72:6010–6018, 2000.

[172] J.T. Motz, S.J. Gandhi, O.R. Scepanovic, A.S. Haka, J. Kramer, R. Ramachandra, R. Dasari, and M.S. Feld. Real-time Raman system for in vivo disease diagnosis. *J Biomed Opt*, 10:031113, 2005.

[173] M. Brownhill. *Atomic force microscopy studies of supported biological molecules*. PhD thesis, School of Physics and Astronomy, The University of Nottingham, 2009.

[174] B.G. Frushour and J.L. Koenig. Raman scattering of collagen, gelatine and elastin. *Biopolymers*, 14(2):379–391, 1975.

[175] B. W. Barry, H. G. M. Edwards, and A. C. Williams. Fourier transform Raman and infrared vibrational study of human skin: Assignment of spectral bands. *J Raman Spectrosc*, 23:641–645, 1992.

[176] Z. Movasaghi, S. Rehman, and I.U. Rehman. Raman spectroscopy of biological tissues. *Appl Spectrosc Rev*, 42:493–541, 2007.

[177] A. T. Tu. *Raman spectroscopy in biology: principles and applications*. John Wiley and Sons, 1982.

[178] Bell S. E. J. Beattie, J. R. and B. W. Moss. A critical evaluation of Raman spectroscopy for the analysis of lipids: Fatty acid methyl esters. *Lipids*, 708:407–419, 2000.

[179] R. O. Duda, P.E. Hart, and D.G. Stork. *Pattern Classification*. John Wiley and Sons, 2nd edition, 2001.

[180] Gutierrez-Osuna. R. Introduction to pattern recognition.

[181] T. Hastie, R. Tibshirani, and J. Friedman. *The Elements of Statistical Learning Data Minining, Inference and Prediction*. Springer Series in Statistics, 2001.

[182] J. Rybczynski, U. Ebels, and M. Giersig. Large-scale, 2D arrays of magnetic nanoparticles. *Colloid Surface A*, 219:1–6, 2003.

[183] T.R. Jensen, G.C. Schatz, and R. P. Van Duyne. Nanosphere lithography: Surface plasmon resonance spectrum of a periodic array of silver nanoparticles by ultraviolet?Visible extinction spectroscopy and electrodynamic modeling. *J Phys Chem B*, 103:2394–2401, 1999.

[184] A.D. McFarland, M.A. Young, J.A. Dieringer, and R.P. Van Duyne. Wavelength-scanned surface-enhanced Raman excitation spectroscopy. *J Phys Chem B*, 109:11279–11285, 2005.

[185] Larsson. Conformation-dependent features in the Raman spectra of simple lipids. *Chem Phys Lipids*, 10:65, 1973.

[186] Y.Y. Luk, M. Kato, and M. Mrksich. Self-assembled monolayers of alkanethiolates presenting mannitol groups are inert to protein adsorption and cell attachment. *Langmuir*, 16:9604–9608, 2000.

[187] J.C. Hoogvliet and W.P. van Bennekom. Gold thin-film electrodes: an EQCM study of the influence of chromium and titanium adhesion layers on the response. *Electrochimica Acta*, 47:599–611, 2001.

[188] V. Cheng. Nanoscale pattern generation for use in surface plasmon resonances. Ira A. Fulton School of Engineering, Arizona State University, 2002.

[189] J. Lützenkirchena, R. Zimmermannb, T. Preocaninc, A. Filbya, T. Kupcika, D. Kttnerb, A. Abdelmonema, D. Schilda, T. Rabunga, M. Plaschkea, F. Brandensteind, C. Wernerb, and H. Geckeisa. An attempt to explain bimodal behaviour of the sapphire c-plane electrolyte interface. *Adv Colloid Interfac*, 157:61–74, 2010.

[190] X.-M. Lin, Y. Cui, Y.-H. Xu, B. Ren, and Z.-Q. Tian. Surface-enhanced Raman spectroscopy: substrate-related issues. *Anal Bioanal Chem*, 394:1729–1745, 2009.

[191] C. Farcau and S. Astilean. Probing the unusual optical transmission of silver films deposited on two-dimensional regular arrays of polystyrene microspheres. *J Opt A: Pure Appl Opt*, 9:S345–S349, 2007.

[192] J. P. Schmidt, S. E. Cross, and S. K. Buratto. Surface-enhanced Raman scattering from ordered Ag nanocluster arrays. *J Chem Phys*, 121:10657–10659., 2004.

[193] M. Osawa, N. Matsuda, K. Yoshii, and I. Uchida. Charge transfer resonance Raman process in surface-enhanced Raman scattering from p-aminothiophenol adsorbed on silver: Herzberg-Teller contribution. *J Phys Chem*, 98:12702–12707, 1994.

[194] D.Y. Wu, L.B. Zhao, X.M. Liu, R. Huang, Y.F. Huang, B. Ren, and Z.Q. Tian. Photon-driven charge transfer and photocatalysis of p-aminothiophenol in metal nanogaps: a DFT study of SERS. *Chem Commun*, 47:2520–2522, 2011.

[195] D. Maniu, V. Chis, M. Baia, F. Toderas, and S. Astilean. Density functional theory investigation of p-aminothiophenol molecules adsorbed on gold nanoparticles. *J Optoelectron Adv M*, 9:733–736, 2007.

[196] N. Mohri, M. Inoue, Y. Arai, and K Yoshikawa. Kinetic study on monolayer formation with 4-aminobenzenethiol on a gold surface. *Langmuir*, 11:1612–1616, 1995.

[197] C. L. Haynes and R. P. Van Duyne. Plasmon-sampled surface-enhanced Raman excitation spectroscopy. *J Phys Chem B*, 107:7426–7433, 2003.

[198] Seppo Lindroos and Markku Leskela. *Solution processing of inorganic material*. John Wiley and sons, 2009.

[199] G.V. Franks and Y. Gan. Charging behavior at the alumina-water interface and implications for ceramic processing. *J Am Ceram Soc*, 90:3373–3388, 2007.

[200] S. Chatterjeea, A.and Niwab and F. Mizukami. Structure and property correlation for Ag deposition on alpha–Al_2O_3–a first principle study. *J Mol Graph Model*, 23:447–456, 2005.

[201] J. Mou, J. Yang, and Z. Shao. Tris(hydroxymethyl)aminomethane ($C_4H_{11}N0_3$) induced a ripple phase in supported unilamellar phospholipid bilayers. *Biochemistry-US*, 33:4439–4443, 1994.

[202] W.A. Ducker and D.R. Clarke. Controlled modification of silicon nitride interactions in water via zwitterionic surfactant adsorption. *Colloid Surface A*, 93:275–292, 1994.

[203] O. Mori and T. Imae. Atomic force microscope observation of monolayers of arachidic acid, octadecyldimethylamine oxide, and their mixtures. *Langmuir*, 11:4779–4784, 1995.

[204] P. Martin and M. Szablewski. *Langmuir-Blodgett troughsoperating manual*. Nima Technology, 6th edition, 2001.

[205] A. Gopal and K.Y.C. Lee. Headgroup percolation and collapse of condensed Langmuir monolayers. *J Phys Chem B*, 110:22079–22087, 2006.

Appendix I

Linear discriminant Analysis (LDA)

On the one hand, this classification method can be derived by assuming that the feature vectors (measurements) $\mathbf{x}$ within each class $j = 1, \ldots, K$ are distributed according to (multivariate) Gaussian distribution [181]. A further assumption that all of these K distributions have the same covariance matrix results in the method being linear in the feature vector $\mathbf{x}$ [179]. In our specific case the feature vectors are p-dimensional vectors ($p = 5$), whose elements are the intensities of the 5 spectral bands which empirically showed maximum differences in the Raman spectra of the different classes. On the other hand, LDA also maximises a specific measure of class separation by projecting the features $\mathbf{x}$ onto a line in an optimally chosen direction $\mathbf{w}$. Note that $\mathbf{w}$ is also a p-dimensional vector. Specifically, suppose that we have n examples $\mathbf{x}_i$, $i = 1, 2, \ldots n$, where each $\mathbf{x}_i$ is of dimensions $p \times 1$. In the case of the dataset used for the model, $n = 329$, which is the total number of Raman spectra of the ensemble of epidermis, dermis, and BCC. Then, the linear transformation performed by LDA is of the form

$$\mathbf{y} = \mathbf{w}^t X,$$

where X is the $p \times n$ matrix with the feature vector $\mathbf{x}_i$ placed in its ith column, and $\mathbf{y}$ contains n (scalar) coordinates of the examples along the optimal direction $\mathbf{w}$. Let D_j be the subset of the examples corresponding to class j. For each class, these examples are $\mathbf{x_i} \epsilon D_j$. In our practical case, 2 class LDA is performed, i.e. $j = 2$. Thus, for the first LDA, D_1 represents the subset whose elements x_i correspond to the Raman spectra of the ensemble of BCC and epidermis. Similarly, for the first LDA, D_2 is the subset formed by the dermis spectra. For the second LDA, the elements of D_1 and D_2 are the spectra of BCC and epidermis, respectively. In order to find the line where class separation is maximum, a function J_w is defined. The required line

would be obtained by maximizing J_w, also known as the criterion function. J_w is the ratio of the between-class scatter S_b and the within-class scatter S_w. The within-class scatter defines the scatter of samples $\mathbf{x}_i$ around their respective means $\boldsymbol{\mu_j}$. The matrix S_w is

$$S_w = \sum_{1}^{j=2} S_{D_j} \tag{7.5}$$

where $S_{D_j}, , j = 1, 2$ are the scatter matrices for each class. They are defined as

$$S_{D_j} = \sum_{i}^{n} (\mathbf{x_i} - \boldsymbol{\mu_j})(\mathbf{x_i} - \boldsymbol{\mu_j})^t \tag{7.6}$$

where $\boldsymbol{\mu_j}, , j = 1, 2$ is the p-dimensional vector containing the five means of intensities of the previously mentioned optimal spectral bands.

$$\boldsymbol{\mu_j} = \frac{1}{n_j} \sum_{i, \mathbf{x_i} \epsilon D_j}^{n} \mathbf{x_i} \tag{7.7}$$

The between-class scatter matrix S_b is

$$S_b = \sum_{j} (\boldsymbol{\mu_1} - \boldsymbol{\mu_2}) (\boldsymbol{\mu_1} - \boldsymbol{\mu_2})^t \tag{7.8}$$

S_b can be considered as the covariance of the dataset formed by the means of each class (note that the difference between the covariance matrix and the scatter matrix is that the latter is not normalised to the number of examples). In summary, J_w can be expressed in terms of the scatter matrices as:

$$J_w = \frac{\mathbf{w^t} S_b \mathbf{w}}{\mathbf{w}^t S_w \mathbf{w}} \tag{7.9}$$

Note that J_w is expressed as a function of the coordinates of the new space, as we want to find the maximum class separation of the projection of the data in the direction $\mathbf{w}$. Thus, just $\mathbf{w^t} S_b \mathbf{w}$ is the projection of S_b in the new space and the same relation holds for $\mathbf{w^t} S_w \mathbf{w}$. For J_w to be maximum, the following criterion has to be satisfied [180] :

$$\left({S_w}^{-1} S_b\right) \mathbf{w} - \lambda \mathbf{w} = 0 \tag{7.10}$$

Equation 7.10 is the eigenvalue problem, were λ are the eigenvalues (simple and real) and $\mathbf{w}$ the associated eigenvectors. Therefore the unitary vector defining the optimal direction is the eigenvector which satisfies equation 7.10.

In this thesis only the non-zero eigenvalues are considered. Zero eigenvalues correspond to the degenerate case in which the projection of the feature vector in the new space falls in the origin (without any separation among the projections and therefore not satisfying the criterion of maximum separation among classes). The eigenvalue equation is solved with basic algebra, by the characteristic polynomial equation. Knowing the value of the non-zero λ, the correspondent eigenvectors can be calculated. In the analysis presented in this thesis two consecutive LDAs are performed. Therefore, the model returns sequentially two eigenvectors corresponding to the directions in which the class separation is maximised. Projecting the feature vector in both directions will give two coordinates for each measurement. Thus, each measurement can be represented by these coordinates in a 2D plot. Line boundaries are drawn in this 2D scatter plot. The threshold depends on the target sensitivity.

Appendix II

Electronic circuits of the wide-field Fourier transform Raman spectroscopic instrument

Figures 7.36-7.38 are schematics of the circuits used, and were made with PSpice software (Cadence Design Systems, USA). Firstly, a current-to-voltage converter was designed to transform the photocurrent into a voltage signal. A diagram of the circuit is shown in Figure 7.36. The circuit uses a pin p-n

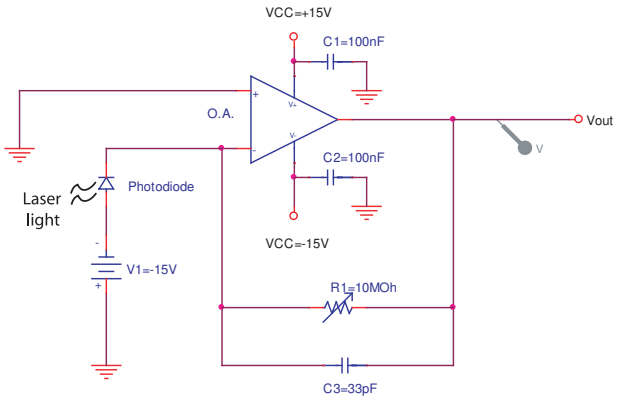

Figure 7.36: Circuit1. Current-to-voltage conversion circuit.

junction photodiode (S5973-02, Hamamatsu Photonics, Japan) in photoconductive mode and an operational amplifier (OA) (OP97, Analog Devices). The output voltage generated from the circuit was:

$$V_{out} = R1.I_{photocurrent} \tag{7.11}$$

Peak-to-peak voltage of the V_{out} needs to be 5 V. As $I_{photocurrent}$ is very small, feedback resistors of the order of MΩ were required, − see eq. (7.11) −. Note that the intensity of the laser photocurrent will be 10^8 times larger than the Raman signal. The use of a potentiometer helped to optimise the signal output.

In order to amplify the output signal, the output of circuit 1 was introduced into circuit 2 (see Figure 7.37) using an OA in its non-inverting form and non-saturated (linear) mode (INA118P, National Semiconductor, USA). The variable resistor R3 allows the adjustment of the system gain.

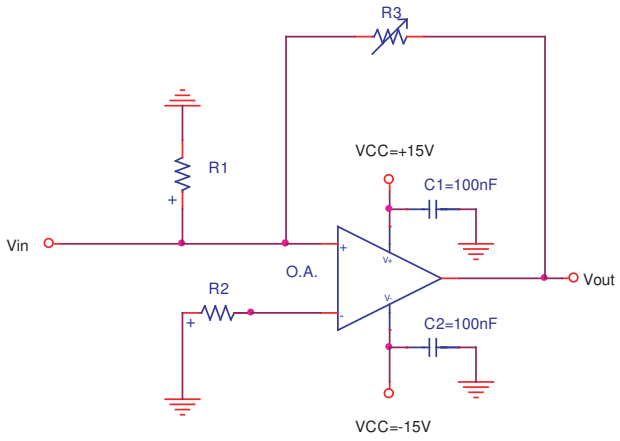

Figure 7.37: Circuit2. Signal amplification circuit.

Finally, the amplified sinusoidal signal was introduced into circuit 3 (see Figure 7.38) where, using an OA as a comparator, the signal was transformed into a square or TTL signal. A variable threshold voltage allowed controlling of the width of the square signal. Circuit 3 also included an amplifier to ensure the output was a TTL signal of 5 V.

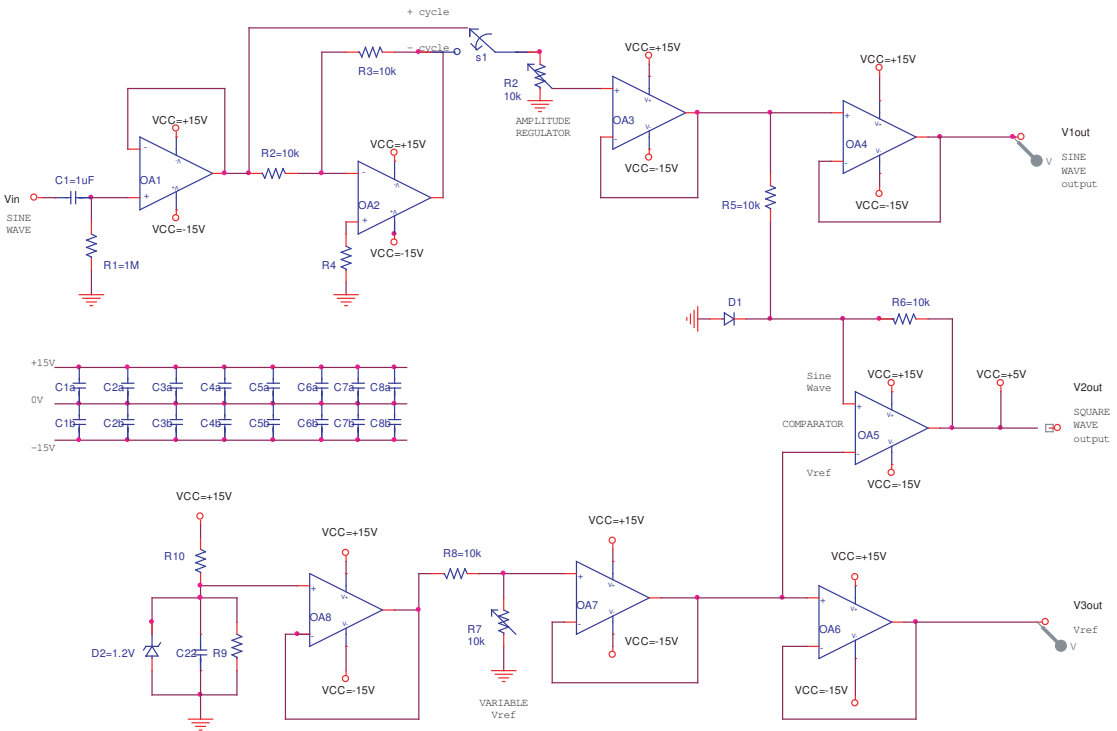

Figure 7.38: Circuit3. Sine-to-TTL signal conversion circuit.

Apendix III

Geometrical calculations of the surface of an individual metal nanostructure of the NSL fabricated substrate.

For each metallic nanostructure (MN) forming the NSL-substrates the surface exposed to laser illumination is approximately the surface area of a truncated triangular pyramid without its bottom triangular base, (see Figure 7.39). According

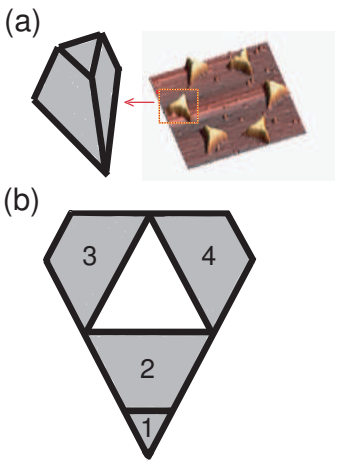

Figure 7.39: (a) A triangular truncated pyramid without its bottom base is the geometrical model chosen for the metallic nanostructures. (b) The total area of a metallic nanostructure is the grey-coloured surface of the truncated pyramid. Number 1 corresponds to the top triangular base of the truncated pyramid, and it is approximately equal to each one of the triangles of the 2-dimensional lattice of Figure 7.40.

to Figure 7.40 the area in the transversal plane occupied by the 6 MNs within the hexagonal unit cell of the lattice is the difference between the surface of the hexagon and the surface occupied by the beads. The area of the beads is 6 thirds of a circle plus a complete circle of diameter D ($D = 2R$). By basic geometry the area of the regular hexagon A_{hex} is $A_{hex} = \frac{3\sqrt{3}}{2}D^2$. In the horizontal section of the lattice represented in Figure 7.40 the area covered by a single MN can be calculated. The area occupied by the beads correspond to the white region within the hexagonal unit cell and it is

$$A_{beads} = (3/4)\pi D^2 \tag{7.12}$$

Figure 7.40: In the top transversal plane of the NSL substrates, there are 6 metallic nanostructures in a hexagonal cell. R is the radius of the inner circle, corresponding to a bead that has been removed.

The area from Figure 7.40 occupied by a single MN and referred to from now onwards in this appendix as A_{mn1} is

$$A_{mn1} = \frac{1}{4}\left(\sqrt{3} - \frac{\pi}{2}\right) D^2 \tag{7.13}$$

Defining a constant $B_1 = \left(\sqrt{3} - \frac{\pi}{2}\right)^{1/2}$ eq. 7.13 can be rearranged to read,

$$A_{mn1} = \left(\frac{1}{2} B_1 D\right)^2 \tag{7.14}$$

For a D of 384 nm, the surface of the hexagonal cell in the 2D lattice occupied by each MN is 5.94×10^3 nm^2.

Consider the largest equilateral triangle that fits in the 2D shape of the MN as represented in Figure 7.41.

Figure 7.41: Area of the largest equilateral triangle that fits in the 2D shape of the MN.

In first place, the mentioned equilateral triangle will be used as the top base or smallest triangular base of the truncated pyramid. The bottom base (whose area would not be considered in the total area of the 3D metal nanostructure model) corresponds to the red equilateral triangle whose vertices are KLM following the notation of Figure 7.42. These vertices are the edges of the curved shape corresponding to the "empty space" among the 3 circumferences centred at B, E and G in Figure 7.42. Note that in Figure 7.42, the top base has not been drawn for clearness of the figure, as it was already sketched in Figure 7.41. The area of the red triangle KLM is a fourth of the area of the black triangle BEG, whose side is known an equal to the diameter D, and its height is H.

From now onwards in this appendix the subindeces 1 and 2 will be used to refer to the top and bottom bases of the truncated pyramid, respectively. From elementary

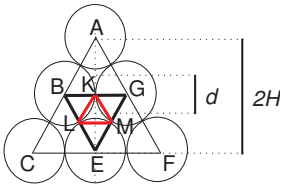

Figure 7.42: Top view of the substrates. Inside the triangle ACF there are four truncated pyramids. In the example the central truncated pyramid is chosen. Its two bases (bottom and top, respectively) correspond to the minimum outer, and maximum inner equilateral triangles fitting in the curved shape KLM, or "empty space" among the 3 circumferences centred at B, E and G. The red equilateral triangle whose vertices are KLM is the bottom base. The top base has not been drawn for clearness of the figure, as it was already sketched in Figure 7.41. Note that the area of the red triangle KLM, is a fourth of the area of the black triangle BEG, whose side is known an equal to the diameter D and its height is H.

geometry the surface area of the truncated pyramid without the bottom base, and with the area of its top base defined as A_1 is,

$$A_{total} = A_{lat} + A_1 \tag{7.15}$$

Where A_{lat} is the lateral area of the truncated pyramid, mathematically described by

$$A_{lat} = \frac{P_1 + P_2}{2} a_p \tag{7.16}$$

P_1 and P_2 are the perimeters of the top and bottom bases of the truncated pyramid, respectively, and a_p is the apothem of the pyramid, defined as

$$a_p = \sqrt{t^2 + [a_{p2} - a_{p1}]^2} \tag{7.17}$$

where t is the height of the truncated pyramid which in the SERS-active substrates corresponds to the thickness of the layer of silver deposited by metal evaporation. a_{p1} and a_{p2} are the apothems of the triangles corresponding to the top and bottom bases of the truncated pyramid, respectively. If both bases of the truncated pyramid are equilateral triangles their apothems satisfy:

$$a_{pi} = \frac{\sqrt{3}}{6} l_i, , i = 1, 2 \tag{7.18}$$

where l_i is the side of the corresponding ith triangle. The areas of the triangles can be expressed as

$$A_i = \frac{\sqrt{3}}{4} ({l_i}^2), , i = 1, 2 \tag{7.19}$$

Therefore,

$$l_i = \frac{2}{3^{1/4}} \sqrt{A_i}, , i = 1, 2 \tag{7.20}$$

And the perimeters of the triangles are,

$$P_i = 3l_i, , i = 1, 2. \tag{7.21}$$

From Figure 7.42, some geometrical considerations can be inferred which allow the calculation of the base areas (A_i), sides (l_i), base perimeters (P_i), base apothems (ap_i), apothem of the truncated pyramid (ap), and final total area of the truncated pyramid (A_{total}). Also, the distance d is defined as the distance between the centres of 2 top triangular bases of area A_1 belonging to two consecutive truncated pyramids. It can be deduced from

$$2H = 3d \tag{7.22}$$

Thus,

$$d = \frac{2}{3}H = \frac{D}{\sqrt{3}} \tag{7.23}$$

From Figure 7.42, the length of the side l_2 of the bottom base can be directly identified with the radii of the beads, i.e., $l_2 = R$. The height H of the black triangle BEG of Figure 7.42, whose area is 4 times the area of the bottom base, can be trivially calculated by the theorem of Pythagoras:

$$D^2 = H^2 + R^2 \tag{7.24}$$

and thus, $H = \sqrt{3}\frac{D}{2}$. Therefore, the area of the triangle BEG is

$$A_{BEG} = \frac{DH}{2} \tag{7.25}$$

The area A_2 of the bottom base of the truncated pyramid, i.e. the area of the red equilateral triangle KLM in Figure 7.42 is

$$A_2 = \frac{DH}{8} \tag{7.26}$$

and expressing H in terms of D

$$A_2 = \left(3^{1/2}\right) 2^{-4} D^2 \tag{7.27}$$

The only variables would be the diameter D of the spheres and the thickness t of the silver layer deposited. The apothem a_{p2} of the bottom base can be expressed as

$$a_{p2} = 3^{-1/2} 2^{-2} D \tag{7.28}$$

The apothem a_{p1} of the top triangular base can be deduced with few geometrical calculations. The notation used is indicated in Figure 7.43. In the figure point C is the center of both triangular bases: top (triangle NPQ) and bottom (triangle KLM). The difference between the apothems of both triangles is the segment $\bar{SF}$. But $\bar{SF} = \bar{SO} - \bar{OF}$, where $\bar{SO}$ is the radius R of the beads and $\bar{OF} = \bar{OM}\cos\pi/6$, i.e. $\bar{OF} = \frac{\sqrt{3}}{2}R$. Then,

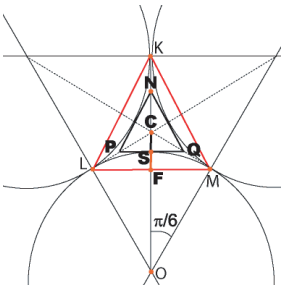

Figure 7.43: Top view of the substrates. Point C is the center of both triangular bases: top (triangle NPQ) and bottom (triangle KLM). The difference between the apothems of both triangles is the segment SF.

$$\bar{SF} = R\left(1 - \frac{\sqrt{3}}{2}\right) \tag{7.29}$$

The apothem a_{p1} of the small triangle NPQ, or top base is

$$a_{p1} = a_{p2} - \bar{SF} = \left(\frac{1}{2\sqrt{3}} - 1 + \frac{\sqrt{3}}{2}\right)\frac{D}{2} \tag{7.30}$$

The area A_1 of the top base of the truncated pyramid is

$$A_1 = 3^{3/2}\left(\frac{1}{2\sqrt{3}} - 1 + \frac{\sqrt{3}}{2}\right)^2 \frac{D^2}{4} \tag{7.31}$$

In addition, the apothem of the pyramid in terms of t and D and the constant B_1 previously defined is,

$$a_p = \sqrt{t^2 + \bar{SF}^2} = \sqrt{t^2 + \left(1 - \frac{\sqrt{3}}{2}\right)^2 \frac{D^2}{4}} \tag{7.32}$$

The perimeters of the top and bottom triangles are,

$$P_1 = 6\sqrt{3}a_{p1} = 3\left(2 - \sqrt{3}\right)D \tag{7.33}$$

$$P_2 = \frac{3}{2}D \tag{7.34}$$

The lateral area A_{lat} of the truncated pyramid is

$$A_{lat} = B_2\sqrt{t^2 + \left(1 - \frac{\sqrt{3}}{2}\right)^2 \left(\frac{D^2}{4}\right)}D \tag{7.35}$$

where the constant B_2 is defined as $B_2 = \frac{3}{4}\left(5 - 2\sqrt{3}\right)$. Then the total area of the truncated pyramid can be calculated by eq. 7.15. However, at this stage it is important to consider which area to take for the top base. So far, we have calculated either the area A_1 of the maximum inner triangle fitting in the real curved shape in eq. 7.31 and also, the whole area of the real curved shape A_{mn1} in eq. 7.14. Particularising for a diameter of the beads $D = 384$ nm and layer of silver deposited $t = 25$ nm, $A_1 = 4.58 \times 10^3$ nm^2 and $A_{mn1} = 5.94 \times 10^3$ nm^2. Therefore, A_1 is the 77 % of the real area of silver illuminated by the laser in a 2D horizontal cross-section at a height of 25 nm. For calculating the total area A_{total} of the model, A_{mn1} is used instead of A_1. Thus, the final expression for the total surface area of the truncated pyramid in terms of the diameter D of the spheres, the thickness t of the silver layer deposited, and the two constants B_1, and B_2 introduced for simplicity is,

$$A_{total} = B_2 D\sqrt{t^2 + \left(1 - \frac{\sqrt{3}}{2}\right)^2 \frac{D^2}{4} + \left(\frac{1}{2}B_1 D\right)^2} \tag{7.36}$$

Giving to B_1 and B_2 decimal values, $B_1 = 0.40$ and $B_2 = 1.15$. From eq. 7.36 the total surface area A_{total} of the metallic nanostructure illuminated by the laser is $A_{total} = 2.18 \times 10^4$ nm^2. This value is 2.4 times larger than the result calculated by Sweetenham [165] for the same substrates modelling the pyramids as truncated tetrahedrons, which was reported to be 9066 nm^2 using the formula taken from reference [197]. In order to validate the model described in this appendix a simulation written in MATLAB by J. Stirling was compared with the real substrate pattern measured experimentally with the AFM. Figure 7.44 shows the high visual agreement of the model (b) and experiment (a). The model image is a front view of a 3D simulation. Note that in this image the area of the top base of the pyramids is considered as an equilateral triangle and has not a curved shape, in contrast with the finer corrected model.

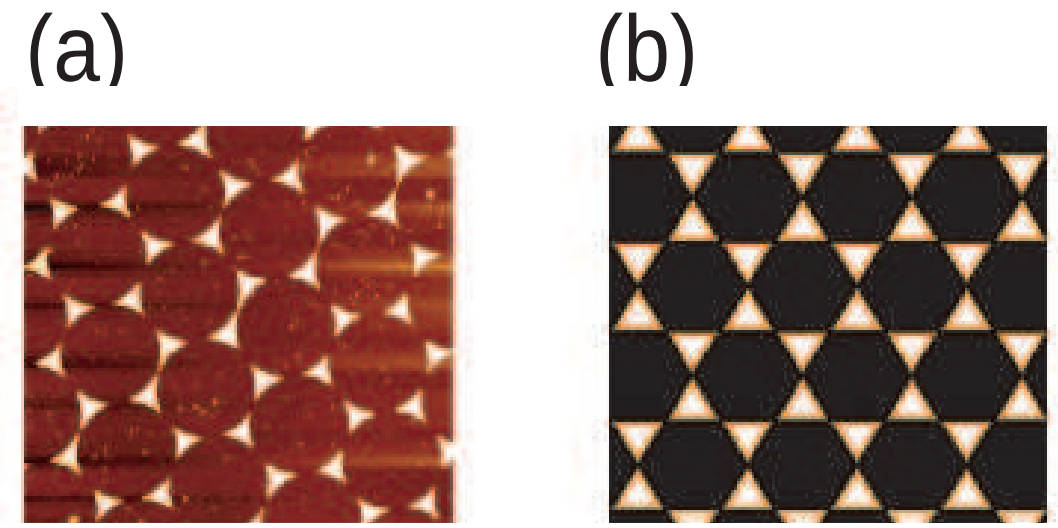

Figure 7.44: (a) AFM height image of the NSL substrates. (b) Simulation of a substrate with the model of truncated pyramids. Note that in this image the area of the top base of the pyramids is considered as a triangle and has not a curved shape. (b) is courtesy of J. Stirling.